Effects of baryons on the dark matter distribution in cosmological hydrodynamical simulations

MATTHIEU SCHALLER

Effects of baryons on the dark matter distribution in cosmological hydrodynamical simulations

Matthieu Schaller

Abstract

Simulations including solely dark matter performed over the last three decades have delivered an accurate and robust description of the cosmic web and dark matter structures. With the advent of more precise cosmological probes, planned and ongoing, and dark matter detection experiments, this numerical modelling has to be improved to incorporate the complex non-linear and energetic processes taking place during galaxy formation. We use the "Evolution and Assembly of GaLaxies and their Environment" (EAGLE) suite of cosmological simulations to investigate the effects of baryons and astrophysical processes on the underlying dark matter distribution. Many effects are expected and we investigate (i): the modification of the profile of halos from the Navarro-Frenk-White profile shape found in collisionless simulations, including the changes in the dark matter profiles themselves, (ii) the changes of the inner density profiles of rich clusters, where observations have suggested a deviation from the standard cold dark matter paradigm, (iii) the offset created by astrophysical process between the centre of galaxies and the centre of the dark matter halo in which they reside and, (iv) the changes in the shape of the dark matter profile due to baryons in the centre of Milky Way halos and the impact these changes have on the morphology of the annihilation signal that could be observed as an indirect proof of the existence of dark matter. In all cases we find that the baryons play a significant role and change the results found in collisionless simulations dramatically. This highlights the need for more simulations like EAGLE to better understand and analyse future cosmology surveys. We also conduct a thorough study of the hydrodynamics solver parameters used in these simulations, assess their impact on the simulated galaxy population and show how robust some of the EAGLE results are against such variations.

Effects of baryons on the dark matter distribution in cosmological hydrodynamical simulations

by Matthieu Schaller

A thesis submitted to the University of Durham
in accordance with the regulations for
admittance to the Degree of Doctor of Philosophy.

Department of Physics
University of Durham
June 2015

Contents

List of Figures

List of Tables

Declaration

The work described in this thesis was undertaken between November 2011 and June 2015 while the author was a research student under the supervision of Prof. Carlos S. Frenk, Prof. Richard G. Bower and Prof. Tom Theuns in the Department of Physics at the University of Durham. This work has not been submitted for any other degree at the University of Durham or any other University.

Chapters 3 - 7 have all been submitted for publication in the form of papers to Monthly Notices of the Royal Astronomical Society (MNRAS):

- *The EAGLE simulations of galaxy formation: the importance of the hydrodynamics scheme.*
  Matthieu Schaller, Claudio Dalla Vecchia, Joop Schaye, Richard G. Bower, Tom Theuns, Robert A. Crain, Michelle Furlong, Ian G. McCarthy, *MNRAS* 2015, Volume 454, Issue 3, pp. 2277-2291,
  ARXIV:1509.05056

- *Baryon effects on the internal structure of ΛCDM halos in the* EAGLE *simulations.*
  Matthieu Schaller, Carlos S. Frenk, Richard G. Bower, Tom Theuns, Adrian Jenkins, Joop Schaye, Robert A. Crain, Michelle Furlong, Claudio Della Vecchia, Ian G. McCarthy, *MNRAS* 2015, Volume 451, Issue 2, pp. 1247-1267, ARXIV:1409.8617

- *The effect of baryons on the inner density profiles of rich clusters.*
  Matthieu Schaller, Carlos S. Frenk, Richard G. Bower, Tom Theuns, James W. Trayford, Robert A. Crain, Michelle Furlong, Joop Schaye, Claudio Della Vecchia, Ian G. McCarthy, *MNRAS* 2015, Volume 452, Issue 1, pp. 343-355, ARXIV:1409.8297

- *The offsets between galaxies and their dark matter in ΛCDM.*
  Matthieu Schaller, Andrew Robertson, Richard Massey, Richard G. Bower,

Vincent R. Eke, *MNRAS* 2015, Volume 453, Issue 1, pp. L58-L62, ARXIV:1505.05470

- *Dark matter annihilation radiation in hydrodynamic simulations of Milky Way haloes.* **Matthieu Schaller**, Carlos S. Frenk, Tom Theuns, Francesca Calore, Gianfranco Bertone, Nassim Bozorgnia, Robert A. Crain, Azadeh Fattahi, Julio F. Navarro, Till Sawala, Joop Schaye , *MNRAS* submitted, ARXIV:1509.02166

Acknowledgements

I would like to thank my supervisors Carlos Frenk, Richard Bower and Tom Theuns for their help and guidance over the course of my PhD. The extensive knowledge of the topic and general science practice experience of Carlos, Richard's endless enthusiasm and Tom's detailed knowledge of simulation software have all been crucial to the construction of this work and to my education. The extended EAGLE team is also to be thanked for their various contributions to the discussions and simulations. Rob Crain and Michelle Furlong deserve a special recognition for the support and help they provided when I joined the team and their extensive dedication around-the-clock to assist me and to run, debug and improve simulations. I would also like to thank Joop Schaye for all the constructive comments and criticisms brought to my work. Finally, I would like to thank Lydia Heck for her help with the computer resources and for putting up with all my demands.

Over the last four years, I have had the chance to share offices with formidable people that have all kept me going and bore with my ranting at computers and software not doing what they should. So, thank you Claudia, Alex I, Alex II, Tamsyn, Jascha, Flora, Will, Bruno and Hou Jun. I have also learned a lot and enjoyed the company of too many people for this short acknowledgement but Charles, Peter, James, Violeta, Mathilde, Sownak, Andrew, Mark and Paddy have all contributed in their own way to making my time in Durham as great as it gets. Let's not forget my time in college for which Cameron and Hao deserve a special mention.

Finally, I would like to thank my family for having always supported my interest in physics and astronomy even if the topic is not their main interest.

This work was supported by the European Research Council under the ERC Grant agreements GA 267291 "Cosmiway" and GA 238356 "Cosmocomp".

Chapter 1 | *Introduction*

1.1 Cosmology, Dark matter and Galaxy formation

Over the course of the 20^{th} century a combination of theoretical breakthroughs and careful observations has allowed cosmologists to paint a comprehensive picture of our Universe and its evolution on the largest scales. Several independent lines of evidence have been used to support the construction of the "Lambda Cold Dark Matter" (ΛCDM) cosmogony. This model describes accurately the evolution of the Universe and of its content over the past 13.7 billion years that separate the epoch of inflation from the present (Komatsu et al., 2011; Planck Collaboration et al., 2014). However successful this model is, it suffers from the fact that the nature of its two major ingredients, the cold dark matter (CDM) and the cosmological constant Λ, are still unknown. Shedding light on those two components, that dominate the energy budget of the Universe today, is one of the major tasks for scientists in the 21^{st} century.

Hot Big Bang model

The development of our current cosmological model started, in the 1930s, with the observational evidence that galaxies were, on average, receding from us at a pace proportional to their distance. These results could be explained, within the framework of general relativity, using the models developed by Friedmann, Lemaître, Robertson and Walker that described an expanding Universe given by a metric of the form

$$\mathrm{d}s^2 = c^2\mathrm{d}t^2 - a(t)^2\left(\frac{\mathrm{d}r^2}{1-kr^2} + r^2\mathrm{d}\Omega^2\right), \tag{1.1}$$

where $a(t)$ is the time dependent scale factor of the Universe and k its curvature. More recent measurement of the motion of galaxies and other tracers show that at the present time the constant of proportionality between distance and recession velocity takes the value $H_0 \equiv H(t=0) \equiv \dot{a}(t=0)/a(t=0) \approx 70\ \mathrm{km/s/Mpc}$.

A direct consequence of the expansion of the Universe is that it was more dense and hotter in the distant past. Looking back at the time where $a(t)$ was less than $1/1000$ of its current value, the Universe was filled with a plasma of protons, electrons and photons, cooling down with the expansion of the Universe. At a redshift $z \equiv 1/a(t) - 1 \approx 1100$, the photons had redshifted enough such that the Universe became transparent and letting the photons of the plasma travel freely through space, transporting the imprints of this primordial state. The measurement of this radiation (now shifted to microwave frequencies due to the expansion of the Universe and called the cosmic microwave background, CMB) in 1964 by Penzias & Wilson essentially confirmed the Big Bang theory as the underlying cosmological paradigm.

In parallel to these measurements, theoretical calculations, based on the work of Alpher, Bethe & Gamow, predicted the relative abundance of elements heavier than hydrogen that should be produced in the hot and dense plasma filling the Universe in the first minutes of its existence. The observational estimation of the abundance of elements in the Universe, later confirmed this scenario, leading to a third piece of evidence favouring the Big Bang model over the competing steady-state theories.

Cosmologists then turned towards more precise measurements of the parameters describing our Universe. Using modern notation, the evolution of the scale factor with time can be related to the content of the Universe (Friedmann equations) as follows:

$$\frac{H^2(t)}{H_0^2} = \Omega_\mathrm{r} a(t)^{-4} + \Omega_\mathrm{m} a(t)^{-3} + \Omega_\mathrm{k} a(t)^{-2} + \Omega_\Lambda, \tag{1.2}$$

where the different Ω's represent the present day density of radiation, matter, spatial curvature and vacuum cosmological constant respectively. Determining these

quantities with precision allows for a full description of the evolution of the largest scales of the Universe and exquisite precision has been reached in the last few years through the measurement of the CMB.

The ΛCDM paradigm and CMB experiments

The era of precision cosmology started with the COBE satellite mission (Smoot et al., 1992) measuring the large scale temperature fluctuations of the CMB. These fluctuations were found to be anisotropic enough to allow for the growth of structures through gravitational instability, provided the Universe contained enough dark matter. A wealth of information can be obtained by measuring the angular power spectrum of the fluctuations in the temperature maps of the CMB. These acoustic peaks correspond to the oscillations in the matter-radiation fluid that was filling the Universe at the epoch of recombination. The first peak, located at an angle $\theta \sim 1^\circ$ on the sky, is the fundamental mode of sound waves that had the time to oscillate once between entering the sound horizon and the time of recombination (see e.g. Hu & Dodelson, 2002, for a review). Precise measurements of the position of this peak (de Bernardis et al., 2000; Hanany et al., 2000; Komatsu et al., 2011; Planck Collaboration et al., 2014), have confirmed that the Universe is spatially flat on large scales ($k = 0$ in equation 1.1). Using the information locked in the second peak, specifically by comparing its amplitude to the first peak, one can constrain the density of baryons at the time of recombination. Similarly, the next acoustic peaks contain information about the quantity of dark matter found in the Universe. The picture that has emerged is that our Universe is filled (in terms of energy-density) with $\sim 4.5\%$ of baryons, $\sim 27\%$ of dark matter and $\sim 68.5\%$ of dark energy, in a form compatible with a cosmological constant (Planck Collaboration et al., 2014).

Supernoave and BAO tests

The presence of dark energy as the dominant component was, however, first firmly established using measurements at low redshifts of standard candles. Type Ia Su-

pernovae (SNe) are extremely bright, hence detectable far beyond the local volume. They also display a standardizable evolution of their luminosity with time, allowing observers to get their intrinsic brightness by measuring the evolution of their light curve only. Measurements of Type Ia SNe by Riess et al. (1998) and Perlmutter et al. (1999) showed that the Universe is currently undergoing a phase of accelerated expansion, making the necessity for dark energy as an important component widely accepted.

Another test of the ΛCDM paradigm comes from the evolution of the acoustic oscillations between the redshift of recombination and the current time. These so-called Baryon Acoustic Oscillations (BAO) have been predicted to leave an imprint in the distribution of matter at low redshift on scales of $\sim 150\ \mathrm{Mpc}$. Measurements using the 2dF (Cole et al., 2005) and SDSS (Eisenstein et al., 2005) galaxy surveys have shown that these oscillations are indeed present, confirming the model of matter-photon plasma filling the Universe before recombination as well as confirming the late time acceleration inferred from the SNe and CMB data. A large range of other cosmological probes (strong and weak lensing, cluster counts, ...) have since been used to test the validity of the ΛCDM model and obtain independent constraints on its parameters. The paradigm is being tested is being tested on increasingly smaller scales with each new generation of probes and the influence of the non-linear processes of galaxy formation start to play a significant role in the uncertainty budget. These processes, occurring on scales ($\sim 1\ \mathrm{Mpc}$) where gravity is not the dominant force any more, will now to be constrained by the theory of galaxy formation in order for precision cosmology probes to disentangle the potential deviations from ΛCDM from the expected non-linearities due to baryonic processes.

Dark matter

Dark matter is the dominant matter component entering the ΛCDM model. Although being hypothesised in the 1930's the dark matter model has only taken its current form following the work of Peebles (1982), that proposed that dark matter is made of fundamental weakly interacting massive particles (WIMPs). These subatomic particles would only interact very weakly with their environment, making their detection in experiments extremely difficult. A large number of theoretical candidates have been put forward as potential WIMPs over the years. The neutralino predicted by super-symmetry models (see Jungman et al., 1996, for a review) has been favoured for many years, although the recent results from the LHC are starting to put strong constraints on the model parameter space. The detection of a dark matter particle would be the holy grail of cosmology, leading to the confirmation that the cold (or slightly warm) dark matter model is indeed the paradigm governing the laws of nature.

There are three main types of experiments currently ongoing to shed some light on the nature of dark matter. Particle accelerators could produce WIMPs in their collisions. Such a result would allow experimentalists to study and understand the properties of this particle. However, this would not necessarily imply that the identified particle is the one that makes up 27% of the Universe's content. Direct detection experiments complement this approach by attempting to measure the recoil of atoms following the collision with a dark matter particle. With a positive result, this type of experiment would show that we are surrounded by dark matter particles but would not necessarily allow phenomenologists to decide which (if any) of the many theorised particles is the dark matter. Those two types of experiments are hence complementary and will hopefully provide results in the near future. The third type of experiment attempts to detect, in the sky, the signal resulting from the annihilation of WIMPs. Most particle candidates (such as Majorana particles) could interact with themselves and annihilate into photons. Observing an excess of photons above all other known astrophysical sources, in regions where

large amounts of dark matter is expected, would be a smoking gun for the existence of such a kind of dark matter particle. Unlike the other two types of experiments this technique relies heavily on the understanding of the astrophysical processes occurring at the centre of galaxies, where the dark matter density is the highest.

Effects of baryons and of galaxy formation

With the precision of both the cosmological probes and dark matter detection experiments now requiring to take into account the astrophysical processes, the theorists have had to start improving the models of galaxy formation and make predictions for its effect on the dark matter. Following the seminal work of White & Rees (1978), it is now widely accepted that galaxies form at the centre of dark matter haloes that have collapsed from the primordial perturbations imprinted in the CMB. Haloes grow by accreting material and by merging with other haloes, leading to a hierarchical formation of structures[1]. The pristine gas falling onto haloes will shock at the virial radius when encountering the hotter medium (virialised gas) present in the haloes. This hotter medium is in hydrostatic equilibrium, balancing the gravitational collapse by pressure support. The gas is then going to cool thorough radiative processes and hence, losing its pressure support, will move towards the centre of the halo. Conservation of angular momentum then leads to the formation of a disk in which stars will be able to form, leading to the creation of disk galaxies (e.g. Mo et al., 1998).

The processes leading to the formation of stars are complex and involve a large range of scales, from the size of a galactic arm generating turbulence in the gas to the size of a single star, many orders of magnitude smaller. Observationally, the star formation rate of a galaxy is found to be well described by the Kennicutt-Schmidt law that relates the star formation rate to the gas surface density (Kennicutt, 1998) or possibly to the surface density of H_2 gas (Kennicutt et al., 2007). Over the course of their evolution the stars will release gas enriched in metals by nucleosynthesis

[1]Note, however, that if dark matter was warm and not cold, this scenario would be reversed on the smallest scales, with larger haloes forming first

(see for instance Portinari et al., 1998, for a set of stellar evolution tracks) into the interstellar medium (ISM), which will then increase the cooling rate of the ISM, leading to increased star formation. At the same time, a small fraction of the stars will explode in the form of supernovae and release large amounts of energy (in the form of heat) into the ISM. Together with radiation pressure and stellar winds, these explosions will disrupt some of the dense gas, reducing the star formation rate and will drive galactic winds outside the disks, ejecting material into the haloes and beyond. The galaxies will hence grow at a rate set by the balance between infalling material and ejection of material as a result of star formation (White & Frenk, 1991). More massive, elliptical, galaxies are later formed by the merging of galaxies, creating the population of galaxies that is observed today (e.g. GAMA, Driver et al., 2011). Observations have also shown that galaxies host supermassive black holes in their centres (e.g. Kormendy & Richstone, 1995; Magorrian et al., 1998). These black holes are responsible for the injection of large amounts of energy into the ISM and haloes through jets, winds and radiation. This energy significantly impacts the state of the gas by blowing large X-ray cavities (e.g. Rafferty et al., 2006) and reduces the star formation rate of the galaxies hosting the most active of these black holes (Bower et al., 2006).

The understanding of all these processes and their interaction in a cosmological context is crucial to estimate their effect on the cosmological probes and on the dark matter experiments. This task is made very challenging for the theorists as the large range of scales interacting and the non-linearity of most equations make the search for precise solutions extremely demanding.

1.2 The role of simulations

A lot of models have been proposed over the years to describe the processes taking place during galaxy formation. Some models also attempt to present a comprehensive picture of how galaxies form. These models are useful as they can help theorists understand in simple terms parts of the processes that are relevant. But,

as was discussed above, the processes taking place span a large range of scales, are highly non-linear and coupled with each other, making a simple but comprehensive solution difficult to reach analytically. Numerical simulations have thus to be used in order to track the evolution of the different species and how they interact over cosmic history.

Dark matter only simulations

Cosmological simulations are used to probe the non-linear regime of structure formation with the collapse of structures and formation of the cosmic web. Early simulations considered solely the gravitational interactions, which is the only relevant force acting on very large scales and considered all matter to be collisionless. In some sense, these simulations can be understood as an extension of perturbation theory calculations and as such have a high predictive power. Simulations of this kind by Davis et al. (1985) and Frenk et al. (1988) established the cold dark matter paradigm as a viable model in which galaxies can form. Improving over this, many generations of simulations in larger and larger volumes with increasing mass resolution showed that the entire observed cosmic web could faithfully be reproduced in ΛCDM (e.g. Springel et al., 2006; Klypin et al., 2011). Similarly, using simulations of individual haloes, theorists have shown that the dark matter follows a universal Navarro-Frenk-White (NFW) profile (Navarro et al., 1996b; Navarro et al., 1997; Navarro et al., 2010) and have been characterising the abundance and distribution of substructures within these haloes very precisely (Springel et al., 2008a; Gao et al., 2012b).

Galaxies and Halo Occupation Distribution

Using these Dark Matter Only (DMO) simulations it is then possible to include statistically some of the physical processes discussed above and populate the simulated haloes with galaxies. The simplest way of performing this is arguably to use the Halo Occupation Distribution (HOD) technique (e.g. Berlind & Weinberg, 2002). By assuming a functional form for the mean number of galaxies occupying

simulated haloes one can construct mock universes with proxies for real galaxies populating virtual haloes. A popular variant of HOD is abundance matching in which the galaxies are assigned to haloes based on their abundance (and so indirectly on their mass in the simplest models, e.g. Moster et al. (2013); Behroozi et al. (2013)). These models can produce realistic mock universes, very useful tools for the analysis of large survey data, but do not provide theorists with information on the processes that take place during galaxy formation nor do they incorporate the back reaction on the dark matter that the baryons have.

Semi-Analytic Models

More advanced models, called Semi-Analytic Models (SAMs) attempt to describe the processes taking place to form galaxies as a set of coupled differential equations (White & Frenk, 1991; Cole et al., 2000; Bower et al., 2006; Guo et al., 2011; Henriques et al., 2015). These describe the galaxies as a whole (i.e. only describe their internal structures very coarsely) and use the underlying dark matter distribution given by DMO simulations as a canvas on which the processes occur. These models rely heavily on free parameters that are adjusted such that the model reproduces some observational properties, usually low-redshift galaxy luminosity or stellar mass functions. Once the underlying DMO simulation has been run, these models do not require large computational resources to run and full exploration of the free parameter space is possible, allowing very good fits to the observational data to be obtained. They also allow one to analyse rapidly a large range of processes and assess their relevance for galaxy formation. One of the limitation of these models is that the properties of the galaxies can only be made dependent on the properties of the dark matter halo hosting them. They also cannot modify the underlying dark matter distribution nor include any spatial information about the gas distribution. Finally, the interactions between the feedback from star formation and the gas in the ISM or halo cannot be followed properly and are hence left as crude models. Despite these shortcomings, the SAMs have proved to be extremely valuable tools that are now central to the analysis of surveys for cosmology. Future cosmology

missions, such as EUCLID (Laureijs et al., 2011), will require $\mathcal{O}(10^4)$ mock surveys generated from SAMs to construct the error correlation matrices needed to understand fully the data. Such task is beyond the ability of current hydrodynamics simulations and considerable effort is spent by the cosmology community on these models.

Hydrodynamical simulations

Hydrodynamical simulations attempt to simulate both the dark matter and the baryons together from the early Universe to the present day. These simulations are much more demanding in terms of computational ressources and have only reached levels of accuracy comparable with the SAMs in the last few years. Tracking the baryons in the simulation allows the simulators to obtain spatial information about the galaxies but also to follow the interaction between the different components and the back reaction of the baryons on the dark matter. These simulations also include models for the processes that cannot be followed because they occur on scales too small for the hydrodynamics solver. However, some processes involving gas physics such as the mixing of cold gas into hot haloes or the ram pressure stripping of gas taking place around satellites in clusters can be entirely and, in principle, accurately followed by the solver and do not require models as in the SAMs. However processes such as star formation or accretion of gas onto supermassive black holes cannot be followed with current simulations since they occur on scales much too small for the solvers, at least in the case of cosmological simulations that simultaneously follow the evolution of large scale structures. These processes take place on scales $\ll 1$ pc whilst volumes of size > 100 Mpc are required to be able to sample a representative part of the galaxy population. Accurately following more than 8 orders of magnitude in length is currently out of reach of simulators and will probably remain so for many more years.

Subgrid models

Subgrid models are employed to simulate the processes that occur on the scales that cannot be tracked by the solvers. These models can roughly be split into two categories. Some models can be constrained directly from observations or from fundamental physics. For instance the cooling of gas in the presence of radiation can be computed (at least in principle) from quantum mechanics and the resulting rates then directly imported into the simulations (see for instance the CLOUDY code Ferland et al., 1998). Similarly, star formation taking place in the disks of galaxies can be modelled by creating a model that reproduces directly the observational results of Kennicutt (1998). Those two subgrid models are hence constrained and cannot be arbitrarily be modified by simulators.

In contrast, the feedback from star formation or AGN is only poorly understood and many different models exist in the literature. Some inject energy in the ISM, some inject momentum, some inject both or add radiation pressure. The amount of energy or momentum injected can also be varied sometimes as a function of halo mass (inspired by the success of SAMs) or as function of local quantities or redshift. Unfortunately these uncertain parts of the subgrid parametrisation seem to dominate the uncertainty budget of the whole modelling (see for instance Schaye et al. (2010), Scannapieco et al. (2012), Vogelsberger et al. (2013) and chapter 3 of this thesis).

Summary of recent results

Over the last 15 years, the accuracy of the hydrodynamical simulations has dramatically increased. Simulations such as the one of Pearce et al. (2001) and Springel & Hernquist (2003) were able to reproduce roughly the cosmic star formation history of the Universe. The use of AGN feedback later allowed the study of the build-up of the galaxy stellar mass function (Oppenheimer et al., 2010), whilst Crain et al. (2009) focused on the differences in environment. The large set of simulations in the OWLS suite (Schaye et al., 2010) allowed for a comprehensive study of the processes

necessary to reproduce the star formation history of the Universe. The shaping of the galaxy stellar mass function at $z = 0$ was then achieved by Puchwein & Springel (2013), whilst Le Brun et al. (2014) managed to reproduce the X-ray properties of galaxy clusters and groups. Following this, two big collaborations attempted to calibrate their subgrid models to reproduce both the low redshift universe and its evolution through time. The ILLUSTRIS (Vogelsberger et al., 2013, 2014; Genel et al., 2014) and EAGLE (Schaye et al., 2015; Crain et al., 2015) simulations both achieve this goal using different numerical techniques (SPH for EAGLE, see chapters 2 and 3, and AREPO (Springel, 2010b) for ILLUSTRIS) and different subgrid prescriptions and parametrizations. These two simulations represent the current state-of-the-art in the field of numerical cosmology and have already proved very valuable tools for the understanding of galaxy formation and the effects of baryons on dark matter.

Future prospects

This new generation of simulations, calibrated to observables, allows the theorists to analyse how and when the different processes take place. The large number of observables they reproduce (see section 2.3 for EAGLE) suggest that the right balance between the baryonic effects has been found, meaning that the response of the dark matter could be comparable to what takes place in nature. These simulations can hence be used to answer questions such as:

- Do the energetic winds, ejecting material far from the galaxies, affect the halo masses and halo growth? Can this be an issue for precision cosmology probes attempting to measure the halo mass function?
- How do baryons affect the profile of halos? Do the very energetic feedback events taking place in galaxies affect the dark matter distribution? Strong and weak lensing cosmological probes rely on our understanding of the matter distribution in haloes. Have baryons changed that picture?
- Are the dark matter profiles flattened in their centre as a consequence of AGN

and stellar feedback in massive galaxies? If not, can observational biases reconcile the simulated profiles with the interpretation of observational data?

- Where are the galaxies located in their halos? How close to the centre are they? Alternative models of dark matter predict an offset between the dark matter and the stars. Could baryonic processes lead to similar offsets in a ΛCDM universe

- If the dark matter particles can annihilate, what is the expected morphology of the signal from the centre of the Milky Way? Have baryonic effects modified the predictions based on DMO simulations?

These questions will be adressed in this work and the importance of using hydrodynamics simulations for precision cosmology and dark matter detection experiments will be highlighted. This thesis is based on the results of the EAGLE simulations, which will be described extensively in the next two chapters.

1.3 Thesis outline

The remainder of this thesis is organised as follows. Chapter 2 introduces the EAGLE simulation and summarizes some of the main results obtained thus far. The subgrid model is presented as well as the calibration process. Chapter 3 is dedicated to the analysis of the impact of the hydrodynamics solver on the results of the simulation. By comparing the reference model and a variation using an older hydrodynamics solver, we attempt to quantify how important the accuracy of the hydrodynamics solver is in simulating the galaxy population. In chapter 4, we start the analysis of the effect of baryons on the dark matter distribution by studying the density profiles of haloes in the EAGLE simulation. We find that the total matter density is well fit by a universal profile whose parameters scale with halo mass and that the dark matter is only affected by baryons in a narrow range of halo masses. Chapter 5 continues the analysis of density profiles by focusing on galaxy clusters. Our findings are compared to observational results and reasons for the

discrepancies are discussed. In chapter 6, we investigate the offset between the centre of the light distribution of galaxies and the centre of their host dark matter halo. Such offsets are expected in alternative models of dark matter and it is hence crucial to provide a prediction for this quantity for pure cold dark matter with only astrophysical processes creating an offset. Chapter 7 uses higher resolution simulations within the EAGLE suite to investigate the dark matter distribution near the centre of simulated Milky Way galaxies, in order to provide templates for the analysis of the γ-ray excess, thought to be the result of dark matter annihilation. Finally in chapter 8 we summarize our findings and discuss future avenues that could be explored in order to improve on the current results.

As the chapters 3 to 7 have all been designed to be self-contained, they each contain a short introduction to the topic and a description of the EAGLE simulation suite.

Chapter 2

The EAGLE *suite of simulations*

The results presented in this thesis are based on the "Evolution and Assembly of GaLaxies and their Environment" (EAGLE) suite of cosmological simulations. These simulations include cosmological periodic volumes, calibrated to reproduce the low redshift galaxy population, as well as zoom-in re-simulations of local group environments. The simulations have been introduced by Schaye et al. (2015) and Crain et al. (2015) as well as Sawala et al. (2014a) for the local group zooms.

Schaye et al. (2015) discussed the limitations of such cosmological simulations due to the limited resolution and the absence of proper treatment of the ISM physics. They argued that the free parameters that enter the model hence had to be calibrated against some observations. In the case of EAGLE these are the $z = 0.1$ stellar mass function, the relation between galaxy mass and size and the relation between galaxy stellar and supermassive black hole masses. EAGLE improved upon earlier simulations by proposing a treatment of stellar and AGN feedback in which thermal energy is injected into the gas without the need to turn off cooling or decouple hydrodynamical forces, allowing winds to develop without predetermined speed or mass loading factors. As a consequence of the calibration process, the observed galaxy stellar mass function is reproduced to $\lesssim 0.2$ dex over the full resolved mass range, 10^8 M$_\odot$ $< M_* \leq 10^{11}$ M$_\odot$, a level of agreement close to that attained by semi-analytic models, and unprecedented for hydrodynamical simulations.

The exploration of parameters for the model was presented by Crain et al. (2015) who showed, using 13 simulations in the EAGLE suite, how the feedback parameters impact the low redshift galaxy population and how imposing that the simulated galaxies follow the observed mass-size relation is crucial to reproduce the

growth of the population over cosmic time. This was achieved by imposing a dependence on the local gas density of the intensity of the feedback. Stellar feedback events taking place in high density gas are made more efficient to compensate for the numerical losses.

Using the same code, Sawala et al. (2014a) simulated local group environments at much higher resolution ($\sim 200\times$ better in mass). They showed that the simulation setup, without any recalibration of the parameters, was able to reproduce the observed luminosity function of satellites, a task that had not been achieved previously, leading to the infamous "missing satellite" and "too big too fail" problems that were supposedly challenging the ΛCDM paradigm. This exercise demonstrated the importance of baryonic effects (here mainly stellar feedback and reionisation) on the small scale properties of a ΛCDM universe.

The remainder of this chapter is dedicated to the technical description of the EAGLE simulation code with a special emphasis on the subgrid models. The details of the hydrodynamics scheme are presented in chapter 3, where its impact on the simulated population of galaxies is also discussed.

The author of this thesis is one of the 'builders' of the EAGLE simulation. This implies that the author has been involved in the project from an early stage, participating in the scientific discussion and the development of the subgrid model as well as taking part in the design of the optimisations to the code that were required in order to perform the main simulation. The author has also been involved in the running of the simulation, both during the calibration phase taking place on the PRACE Tier 0 machine, Curie, in Paris, and during the actual production runs that took place on the Cosma-5 machine in Durham. This also involved post-processing the simulations with the halo and subhalo finder as well as preparing analysis software to be used by the collaborators involved in projects exploiting the large volume of data that came out of the simulations.

2.1 Gravity and Hydrodynamics solver

Initial conditions

The EAGLE simulations assume a flat ΛCDM universe, using the best-fitting parameters to the first data release of the *Planck* survey (Planck Collaboration et al., 2014); $\Omega_\Lambda = 0.693$, $\Omega_m = 0.307$, $\Omega_b = 0.048$, $\sigma_8 = 0.8288$, $n_s = 0.9611$ and $H_0 = 67.77$ km s^{-1} Mpc^{-1}. From these ΛCDM parameters, an initial power spectrum using Gaussian initial conditions has been produced with the public real-space white noise field PANPHASIA (Jenkins, 2013). Together with the linear transfer functions assuming the same ΛCDM parameters, particle displacements and velocities have been computed at $z = 127$ using second-order Langrangian perturbation theory (Jenkins, 2010).

Dark matter and gravity

In simulations, dark matter is modelled as a collisionless fluid, interacting solely through gravity. Its motion is hence governed by the collisionless Boltzmann equation (e.g. Binney & Tremaine, 1987). The peculiar gravitational potential $\Phi(\mathbf{r})$ is evaluated in comoving coordinates

$$\nabla^2\Phi(\mathbf{r}) = 4\pi G a^2 \left(\rho(\mathbf{r}) - \bar{\rho}\right), \tag{2.1}$$

where $\bar{\rho}$ is the mean density of the Universe and a is the expansion factor. These two coupled equations are solved in simulation codes by discretising the fluid into N particles. As the scales involved and the magnitude of the fields do not require the use of general relativity, the gravity force acting on a given particle i of mass m_i is simply given by the Newtonian formula:

$$\mathbf{F}(\mathbf{r}_i) = \sum_{j=1, j\neq i}^{N-1} \frac{G m_i m_j}{|\mathbf{r}_j - \mathbf{r}_i|^3}(\mathbf{r}_j - \mathbf{r}_i). \tag{2.2}$$

In practical cases, the number of particles, N, is very large, making an evaluation of this sum a computationally challenging task. Alternative methods must

hence be employed to approximate this sum. Over the years, multiple techniques (see review by Dehnen & Read, 2011) have been developed to reduce the computational cost of this operation. The most commonly used of them being particle-mesh (PM) codes (Klypin & Shandarin, 1983; White et al., 1983), tree codes (Barnes & Hut, 1986) and tree-PM codes (Bode et al., 2000; Bagla, 2002). The EAGLE code, based on the GADGET code (last described in Springel, 2005) uses the tree-PM technique. Long range forces and periodic forces are obtained by mapping the density field onto a regular mesh and solving the Poisson equation (eq. 2.1) directly in Fourier space. The short range interactions are computed using an octree. The volume is recursively subdivided into a hierarchy of cells or nodes. Cells that are close enough will allow their particles to interact directly using a direct summation algorithm whilst the interactions between particles in distant cells are replaced by interactions between particles and multipole moments of the density field in the cells. The difficulty is then to define when two cells are close and hence decide when to apply either of the two approximations. In GADGET, a condition based on the size of the cell s, distance to the cell d and mass of the cell M is used and reads

$$\frac{GM}{d^2}\left(\frac{s}{d}\right)^2 \geq \theta|\mathbf{a}|, \tag{2.3}$$

where $\mathbf{a}$ is the acceleration of the particle at the previous time-step and $\theta \approx 0.7$ is a tolerance parameter. Studies of convergence, such as the work of Power et al. (2003), have shown that this criterion provides sufficient accuracy and that results are well converged when applying it.

Hydrodynamics solver

In cosmological simulations, the gas is usually assumed to be an inviscid fluid (away from shocks) obeying Euler's equations. Various techniques have been proposed to evolve these equations forward in time. They can be grouped in two categories. The first one uses a mesh (regular or not) to solve the equations using finite volume techniques. The second category uses particles to discretize the

fluid and smoothing functions to interpolate the quantities between these particles. This Smoothed Particle Hydrodynamics (SPH) technique (see Price, 2012; Springel, 2010a, for reviews), pioneered by Lucy (1977) and Gingold & Monaghan (1977), is fully conservative and can easily be coupled to a tree code (Hernquist & Katz, 1989). The fluid is discretised into point mass particles, which transport the properties of the fluid, making the whole scheme particularly interesting when matter clusters in small regions as is the case in cosmological simulations. Continuous fluid properties, such as the density or pressure are computed by interpolating the particle properties over a finite neighbourhood, using a kernel function, $W(|\mathbf{r}_i - \mathbf{r}_j|, h)$, depending solely on the separation of particles i and j and a smoothing length, h. In practice, this smoothing length adapts itself to the local density of particles, giving more resolution in the regions of space where more matter is clustered. The density of the fluid can be constructed at any point using this smoothing kernel and reads

$$\rho(\mathbf{r}_i) = \Sigma_j m_j W(|\mathbf{r}_i - \mathbf{r}_j|, h). \tag{2.4}$$

Given an equation of state for the gas (usually $P = \rho(\gamma - 1)u$ with $\gamma = 5/3$ and u the internal energy of the gas), the pressure P can be derived, which will then allow computation of the forces that will act on the particles and set their accelerations. In parallel, another thermodynamic quantity is evolved, either the entropy s or the internal energy u. As this scheme is fully conservative and completely inviscid, the key difficulty of the technique is to apply the right amount of viscosity around shocks. Similarly some thermal conductivity terms are often added to the equations. Authors advocate many different recipes for these two key components and a full description of the available terms and their shortcomings is beyond the scope of this work. A comprehensive description of the variant of SPH used in the EAGLE code is presented in chapter 3, where a discussion of its effects in the simulated galaxy population can be found.

2.2 Subgrid models

The subgrid model in EAGLE is an improved version of that used in the GIMIC and OWLS simulations (Crain et al., 2009; Schaye et al., 2010).

Equation of state for the ISM

As for all cosmological simulations, the resolution of the runs in the EAGLE suite is too low to allow for a proper treatment of the processes occurring in the ISM, especially in the cold phase ($T \ll 10^4$ K), where the Jeans mass is of order 1 M$_\odot$ and hence far below the mass contained in one resolution element. The ISM and the star formation that takes place is thus evolved in the simulation using a subgrid model. To prevent the fragmentation of gas and capture the unresolved turbulence, we impose an equation of state $P_{\rm eos} \propto \rho^{\gamma_{\rm eos}}$ for the gas with $\rho > 0.1$ cm^{-3} and normalised to $T_{\rm eos} = 8000$ K at the density threshold. By choosing $\gamma_{\rm eos} = 4/3$, we ensure that the ratio of the Jeans length of the gas to the SPH kernel radius is independent of density, suppressing spurious fragmentation of the gas to sizes that cannot be resolved numerically (Schaye & Dalla Vecchia, 2008).

Star formation

Star formation can take place in high density cold gas, leading to a threshold in hydrogen number density for star formation n_* below which star formation is strongly suppressed by the radiation field (e.g. Bigiel et al., 2008). As the transition from the warm neutral phase of the ISM to the cold molecular phase is metallicity (and dust) dependent, we use a metallicity-dependent threshold as proposed by Schaye (2004):

$$n_*(Z) = \min\left[0.1\left(\frac{Z}{0.002}\right)^{-0.64}, 10\right] \text{ cm}^{-3}, \tag{2.5}$$

where Z is the metal mass fraction of the gas (hereafter metallicity). To prevent star formation in low-overdensity environments at high redshift, we impose another

numerical threshold and only allow star formation in regions with an overdensity $\delta > 57.7$.

The star formation rate is then computed following the pressure-law scheme of Schaye & Dalla Vecchia (2008). Assuming that the star-forming gas is self-gravitating, the Kennicutt-Schmidt star formation law (Kennicutt, 1998) can be rewritten in terms of the local gas pressure P:

$$\dot{m}_* = m_{\rm g} A \left(1\ {\rm M}_\odot\ {\rm pc}^{-2}\right)^{-n} \left(\frac{\gamma}{G} f_{\rm g} P\right)^{(n-1)/2}, \tag{2.6}$$

where $\gamma = 5/3$ is the polytropic index of the gas, $f_{\rm g}$ is the gas fraction (which we take to be 1). The remaining coefficients A and n are taken directly from observations and read $A = 1.515 \times 10^{-4} {\rm M}_\odot\ {\rm yr}^{-1}\ {\rm kpc}^{-2}$ and $n = 1.4$. We adjusted the value of A of Kennicutt (1998) to convert from the Salpeter initial mass function (IMF) assumed in the observations to the Chabrier (2003) IMF used in our simulations.

Stellar evolution and enrichment

Once the stars are formed, they are treated as a simple stellar population with a Chabrier IMF spanning the range $0.1 - 100\ {\rm M}_\odot$. The stars then follow the stellar tracks of Portinari et al. (1998) and will enrich the ISM following the implementation of Wiersma et al. (2009b). Eleven elements are tracked individually and the mass losses through AGB stars, type Ia and type II supernovae are computed and injected in the ISM. These elements later influence the radiative heating and cooling rate of the gas. These rates are computed on an element-by-element basis by interpolating between tables generated by CLOUDY (Ferland et al., 1998, version 07.02). These tables give the cooling rates as a function of density, temperature and redshift for a gas in ionisation equilibrium, in the optically thin regime exposed to the CMB and UV/X-ray background given by Haardt & Madau (2001). The details of the implementation are given in Wiersma et al. (2009a). In addition to the contribution from the various background radiations, we inject $2\ {\rm eV}$ of thermal energy per proton at $z = 11.5$ to mimic the effects of HI reionisation. This instantaneously heats the gas to $\sim 10^4$ K. The HeII reionisation is implemented by injecting energy

over a broad redshift range using a Gaussian function centred at $z = 3.5$ and with a standard deviation of $\sigma_z = 0.5$. The thermal history of the gas in the intergalactic medium hence reproduces the one inferred from observations by Schaye et al. (2000).

Stellar feedback

When the stellar particles reach an age of 3×10^7 yr the stars contained in their single stellar population that have $M > 6\ \mathrm{M}_\odot$ will explode as type II supernovae and release $\approx 10^{51}$ erg per supernova. The injection of this energy in the ISM is done following Dalla Vecchia & Schaye (2012). The gas surrounding the stellar particles is heated to a temperature ΔT, chosen to be large enough to erase the numerical losses created by the cooling in the unresolved parts of the ISM. They showed that heating a single gas particle in an SPH neighbourhood leads to efficient feedback if the density is below a certain threshold

$$n_{\mathrm{H,tc}} = 10\ \mathrm{cm}^{-3} \left(\frac{T}{10^{7.5}\ \mathrm{K}} \right)^{3/2} \left(\frac{m_g}{10^6 \mathrm{M}_\odot} \right)^{-1/2}, \tag{2.7}$$

where T is the temperature of the gas after the injection of energy. This estimate assumes that the cooling is dominated by Bremsstrahlung and is hence valid only for temperatures above the regime where metal-line cooling dominates. The radiative losses can be reduced by using higher temperatures, but at the cost of creating a more stochastic injection of energy. The number of particles that are heated per feedback event is given by

$$\langle N_{\mathrm{heat}} \rangle = 1.3 \left(\frac{\Delta T}{10^{7.5}\ \mathrm{K}} \right)^{-1}. \tag{2.8}$$

Setting $\Delta T \gg 10^{7.5}$ K will lead to a low number of particles being heated per event. We hence set $\Delta T = 10^{7.5}$ K to allow for efficient feedback in as dense environment as possible (equation 2.7) whilst heating at least one particle on average per feedback event (equation 2.8). While the choice of ΔT allows us to suppress numerical losses, the physical efficiency of feedback can be controlled by injecting more or less energy per feedback event. In practice, we multiply the 10^{51} erg

per supernova by a factor $f_{\rm th}$. This parameter is designed to represent the states of the ISM in which the supernova energy is injected. As the exact state of the ISM is unresolved by our simulation, this parameter $f_{\rm th}$ is our main subgrid model parameter and the calibration process advocated by Schaye et al. (2015) uses this handle to achieve the goal of matching given observational data sets. In the case of the EAGLE simulations, we use (in the reference EAGLE model) a function for $f_{\rm th}$:

$$f_{\rm th} = f_{\rm th,min} + \frac{f_{\rm th,max} - f_{\rm th,min}}{1 + \left(\frac{Z}{Z_\odot}\right)^{n_Z} \left(\frac{n_{\rm H,birth}}{n_{\rm H,0}}\right)^{-n_n}}, \tag{2.9}$$

where $n_{\rm H,birth}$ and Z are the density and metallicity of the gas surrounding the stellar particle, $n_{\rm H,0} = 0.67\ {\rm cm}^{-3}$, $n_Z = n_n = 2/\ln 10$ and the minimal and maximal values are set to $f_{\rm th,min} = 0.3$ and $f_{\rm th,max} = 3$ respectively. The construction and motivation for this parametrisation are given in Crain et al. (2015). This form of $f_{\rm th}$ implies a larger coupling of the supernova energy to the ISM in low metallicity environments. Similarly, the efficiency of feedback is enhanced in high density environments when compared to low density regions. As argued by Crain et al. (2015), this compensates for the numerical losses in very high density regions and the dependence of $f_{\rm th}$ on the gas density is weaker at higher resolution.

Supermassive black holes

The growth of black holes (BH) and the associated activity leading to the quenching of star formation in large galaxies is modelled using two prescriptions. Firstly, the injection of BH seeds, their evolution, mergers and accretion is modelled following the recipe of Rosas-Guevara et al. (2015), itself an evolution of the models of Springel et al. (2005) and Booth & Schaye (2009). Secondly, the injection of energy generated by the AGN activity is implemented following Booth & Schaye (2009). In summary, seed BHs of mass $m_{\rm BH} = 1.475 \times 10^5\ {\rm M}_\odot$ are injected in haloes (identified by the FoF algorithm, see below) more massive than $1.475 \times 10^{10}\ {\rm M}_\odot$[1] that

[1]Note that we use h-free units here for consistency with the rest of the text. The BH seed mass and minimal halo mass are $10^5\ {\rm M}_\odot/h$ and $10^{10}\ {\rm M}_\odot/h$ respectively.

do not already contain a BH. They are then allowed to grow and merge with other BHs if they are separated by less than three gravitational softening lengths and if their relative speed is lower than the circular velocity at the distance separating them. This velocity threshold delays the merger event and delays merging during the initial instants of a galaxy merger. Gas is accreted onto black holes using a rate computed as the minimum of two values, the Eddington rate:

$$\dot{m}_{\rm Edd} = \frac{4\pi G m_{\rm BH} m_{\rm p}}{\epsilon_{\rm r}\sigma_T c}, \tag{2.10}$$

and a modified Bondi & Hoyle (1944) rate:

$$\dot{m}_{\rm accr} = \frac{4\pi G^2 m_{\rm BH}^2 \rho}{(c_{\rm s}^2 + v^2)^{3/2}} \times \min\left[(c_{\rm s}/v_\phi)^3/C_{\rm visc}, 1\right]. \tag{2.11}$$

In these equations, σ_T is the Thomson scattering cross-section, m_p is the proton mass, $\epsilon_r = 0.1$, the radiative efficiency of the accretion disk, c_s the sound speed of the gas and v its velocity with respect to the BH. The Bondi-Hoyle accretion is modified to take into account the rotational velocity v_ϕ of the gas around the BH as proposed by Rosas-Guevara et al. (2015). $C_{\rm visc}$ is a parameter that is adjusted in the calibration process and that can be understood as the effective viscosity of the subgrid accretion disk. The Ref model of EAGLE uses $C_{\rm visc} = 2\pi$. Note that the first term contains no proportionality factor α of the kind used in many alternative implementations (e.g. Vogelsberger et al., 2013, use a factor $\alpha = 100$). AGN feedback is implemented using a single mode in which energy is injected thermally in a stochastic way very similar to the implementation of feedback from star formation (Booth & Schaye, 2009). Each BH has an energy reservoir that increases after each time step by $\epsilon_{\rm f}\epsilon_{\rm r}\dot{m}_{\rm accr}\Delta t$ until the BH has stored enough energy to heat at least one SPH particle to a temperature $\Delta T_{\rm AGN} = 10^{8.5}$ K. The feedback efficiency $\epsilon_{\rm f}$ is set to 0.15. Each SPH particle within the neighbourhood of the BH can then probabilistically be heated and the reservoir's energy is reduced by the corresponding amount of injected energy. Larger values of $\Delta T_{\rm AGN}$ reduce the radiative losses in the ISM that follow an AGN event but also make the activity more intermittent.

Halo identification

Haloes were identified using the Friends-of-Friends (FoF) algorithm (Davis et al., 1985), and bound structures within them were then identified using the SUBFIND code (Springel et al., 2001; Dolag et al., 2009). A sphere centred at the minimum of the gravitational potential of each subhalo is grown until the mass contained within a given radius, R_{200}, reaches $M_{200} = 200\,(4\pi\rho_{\rm cr}(z)R_{200}^3/3)$, where $\rho_{\rm cr}(z) = 3H(z)^2/8\pi G$ is the critical density at the redshift of interest.

2.3 Other scientific results from EAGLE

As discussed above, the EAGLE simulation has been calibrated to reproduce the low-redshift stellar mass function, the relation between galaxy size and mass as well as the relation between galaxy and supermassive black hole masses. Using the simulation and some of its variations, a number of studies have explored some of the properties of the galaxy population and gas distribution that had not been considered during the calibration process. We summarize here some of the key findings that have been published thus far.

The author of this thesis has been actively taking part in the analysis and the scientific discussions that led to these results and is a co-author of the resulting publications. These results will not be discussed further in this work.

- Furlong et al. (2015) explored the population of galaxies at $z > 0.1$ and showed that the simulated stellar mass function evolved in a fashion similar to what is inferred from observational data. They also showed how the cosmic star formation rate density evolves with time and discussed possible reasons for the discrepancy seen between the simulated evolution and the observed one.

- Trayford et al. (2015) used simple stellar population models and dust models to infer the luminosity and colour of the simulated galaxies. They showed that the simulated galaxy population is in broad agreement with observations. This result suggests that EAGLE galaxies at $z = 0.1$ have ages, metal-

licities and levels of obscuration that are comparable to those of observed galaxies.

- Velliscig et al. (2015) used the simulation to study the alignment and shape of the dark matter, stellar and gas distributions. They found that overall, galaxies align well with local distribution of the total (mostly dark) matter. However, the stellar distributions on galactic scales exhibit a median misalignment of about $45-50^{\circ}$ with respect to their host haloes. This result directly impacts lensing measurements and hence should be taken into account for cosmological probes.

- Rahmati et al. (2015) studied the distribution of HI gas around galaxies at redshifts $z \sim 2-4$. They showed that the EAGLE simulation reproduces both the observed global column density distribution function of HI and the observed radial covering fraction profiles of strong HI absorbers around galaxies and bright quasars.

- Lagos et al. (2015) investigated the abundance of H_2 gas in the simulation using state-of-the-art post-processing techniques. Their main result is that the simulations reproduce the observed scaling relations between the mass of H_2 and the stellar mass, star formation rate and stellar surface density, a result particularly remarkable since it involves no adjustable parameters.

- Bahe et al. (submitted) explored the HI gas distribution in low-redshift simulated galaxies and compared it to observations. They found that the HI mass-size relation is close to, but slightly steeper than, the observed one. These results may be compromised by the presence of large HI holes, likely to be a consequence of the feedback model of the simulation, that are not observed in nature.

- Using higher resolution zoom-in simulations of local group environments with the EAGLE code, Sawala et al. (2015) showed that the baryonic processes have a large impact on the low-mass end of the relation between halo

and galaxy masses. They showed that only a small fraction of the low-mass haloes host galaxies, hence breaking the monotonic relation usually assumed between halo and stellar mass.

- Sawala et al. (2014b) then investigated, in these zoom-in simulations, which of the haloes of a given mass host a galaxy and showed that it was not a random subset of haloes, but rather only haloes that grew fast enough to host a galaxy before reionization. As a consequence, they found that satellite haloes are populated more frequently than field haloes. This makes dwarf galaxies a highly biased tracer population of the underlying dark matter distribution.

- Oman et al. (2015) used the same zoom-in simulation and the main EAGLE simulation to investigate rotation curves of galaxies and suggested that the large variety of curves seen in nature could not easily be reconciled with the results of simulations, since these do not display the same scatter. They proposed that observational biases could be the source of the observed diversity, which should be confirmed in the future by producing mock observations of the simulated galaxies.

These early results suggest that the EAGLE simulation is a very valuable tool to study galaxy formation and to understand and follow the non-linear processes taking place. Many further studies are currently being undertaken, using the simulation, to explore all corners of galaxy formation. These should hopefully make this simulation an important milestone in our understanding of the physics taking place. This will be helped by the public release of the galaxy catalogues, allowing astrophysicists outside of the collaboration to directly analyse the wealth of information currently awaiting to be exploited.

Chapter 3

Importance of the hydrodynamics scheme

3.1 Introduction

Over the last decade, cosmological hydrodynamical simulations have started to play a major role in the study of galaxy formation. Recent simulations are able to cover the large dynamical range required to study the large-scale structure dominated by dark matter as well as the centres of halos where baryon physics dominates the evolution. Comparisons of such simulations with observations show broad agreement and help confirm the predictions of the ΛCDM paradigm (e.g. Vogelsberger et al., 2014; Schaye et al., 2015).

Galaxy formation arises as mixture of complex processes and the numerical requirements to simulate all of the relevant scales are enormous. A direct consequence of this is the need to model some of the unresolved processes with subgrid prescriptions. Other processes, taking place on larger scales, can in principle be followed accurately by numerical hydrodynamics solvers. The shocking of cold gas penetrating halos or the turbulence generated by supernova activity within galaxies are examples of the processes that can be treated by the hydrodynamics solvers. Conversely, the accretion of gas onto black holes and the formation and evolution of stars are examples of processes that occur on scales that are too small to be simulated jointly with the large scale environment.

For the processes that can be simulated using standard numerical solvers, the main question is how the various parameters that enter hydrodynamics solvers affect the formation of galaxies in the simulations. For example, it has been reported that different numerical techniques and choices of parameters affect the disrup-

tion of a cold gas blob in a low-density hot medium, a case directly relevant the accretion of gas and satellite of galaxies (Frenk et al., 1999; Marri & White, 2003; Okamoto et al., 2003; O'Shea et al., 2005; Agertz et al., 2007; Wadsley et al., 2008; Mitchell et al., 2009; Kereš et al., 2012; Sijacki et al., 2012). In principle, these numerical parameters can be set by performing controlled numerical experiments for which the solution is known. In the case of simulations using Smoothed Particle Hydrodynamics (SPH) (Lucy, 1977; Gingold & Monaghan, 1977) (see Springel, 2010a; Price, 2012, for reviews) as a solver, the free parameters relate to the treatment of shocks, artificial viscosity and conduction. Performing tests such as Sedov explosions or Kelvin-Helmoltz instabilities (e.g. Price, 2008; Read et al., 2010; Springel, 2010b; Hu et al., 2014; Hopkins, 2015; Beck et al., 2015) allows the simulator to decide on the best values for the parameters. However, it is unclear whether there is a single set of values that is suitable for all problems and whether these parameter values are also the best choice when performing simulations of very hot and diffuse conditions, such as the ones found in the hot haloes of galaxies (e.g. Sembolini et al., 2015). Similarly, the large gap in resolution between these controlled experiments and cosmological simulations makes the extrapolation of the solver's behaviour a difficult task. The correct treatment of entropy jumps in shocks or of the spurious viscosity that can appear in rotating disks can have direct consequences for the population of simulated galaxies.

In their comprehensive study of galaxy formation models, Scannapieco et al. (2012) used multiple hydrodynamics solvers coupled to multiple sets of subgrid models to study the formation of galaxies in a single halo and the impact of the choices in the solvers. One of their main findings was that the variations in the hydrodynamics solvers led to much smaller changes in the final results than the changes in the subgrid model parameters. This was especially the case for the prescription of feedback, which can change the final galaxy tremendously (Schaye et al., 2010; Haas et al., 2013; Vogelsberger et al., 2013). A more controlled experiment was performed by Kereš et al. (2012) who compared two hydrodynamics solvers but used only a simplified model of galaxy formation and found very little

difference despite the large gap in accuracy between the hydro solvers tested.

Building on those studies, we attempt to quantify the impact of the uncertainties in the implementation of the hydrodynamics solvers on a simulated galaxy population. The EAGLE simulation project (Schaye et al., 2015; Crain et al., 2015) used a state-of-the art implementation of SPH, called ANARCHY (Dalla Vecchia (in prep.), see also appendix A of Schaye et al. (2015)) and the time-step limiter of Durier & Dalla Vecchia (2012). EAGLE's subgrid model parameters were calibrated to reproduce the observed local Universe population of galaxies. In this study, we vary the hydrodynamics solver. In particular, we use the flavour of SPH implemented in the GADGET code (Springel, 2005) and compare the resulting galaxy population to the one in the reference EAGLE simulation and to those in simulations with weaker/stronger stellar feedback and to runs without AGN feedback. Since EAGLE broadly reproduces the galaxy population, our test is especially relevant and allows us to disentangle the effects of the hydro solver from the effects of the subgrid model.

This chapter is structured as follows. In section 3.2 the EAGLE model and the two flavours of SPH that we consider are described. Section 3.3 discusses the impact of the hydrodynamics solver on the simulated galaxies whilst Section 3.4 presents differences in the gas properties of the haloes. A summary of our findings can be found in Section 3.5.

Throughout this chapter, we assume a *Planck2013* flat ΛCDM cosmology (Planck Collaboration et al., 2014) ($h = 0.6777$, $\Omega_b = 0.04825$, $\Omega_m = 0.307$ and $\sigma_8 = 0.8288$) and express all quantities without h factors.

3.2 The EAGLE simulations

The EAGLE set consists of a series of cosmological simulations with state-of-the-art subgrid models and smoothed particle hydrodynamics. The simulations have been calibrated to reproduce the observed stellar mass function and galaxy mass-size relation at $z = 0.1$. The simulations also broadly reproduce a large variety of

other observables such as the Tully-Fisher relation and specific star formation rates (Schaye et al., 2015), the H_2 and HI properties of galaxies (Lagos et al. (2015), Bahe et al. (submitted)), the evolution of the galaxy stellar mass function (Furlong et al., 2015), the column density distribution of intergalactic metals (Schaye et al., 2015; Rahmati et al., 2015) and galaxy rotation curves (Schaller et al., 2015a).

The EAGLE simulations discussed in this chapter follow $752^3 \approx 4.3 \times 10^8$ dark matter particles and the same number of gas particles in a 50^3 Mpc^3 cubic volume[1] from ΛCDM initial conditions. Note that the simulation volumes considered here are eight times smaller than the main 100^3 Mpc^3 EAGLE run. The mass of a dark matter particle is $m_{\rm DM} = 9.7 \times 10^6$ M$_\odot$ and the initial mass of a gas particle is $m_{\rm g} = 1.8 \times 10^6$ M$_\odot$. The gravitational softening length is 700 pc (Plummer equivalent) in physical units below $z = 2.8$ and set to 2.66 kpc (comoving) at higher redshifts. The simulations were run with a heavily modified version of the GADGET-3 N-body tree-PM and SPH code, last described in Springel (2005). The changes include the introduction of the subgrid models described in the next subsection as well as the implementation of the ANARCHY flavour of SPH, whose impact on the simulation outcome is the topic of this chapter. In the next subsections we will describe the subgrid model used in the EAGLE simulations with a special emphasis on those aspects of the model that are directly impacted by the hydrodynamic scheme. For the sake of completeness, we will then describe both the standard GADGET and ANARCHY flavours of SPH.

3.2.1 Subgrid models and halo identification

The subgrid model is an improved version of that used in the GIMIC and OWLS simulations (Crain et al., 2009; Schaye et al., 2010). Radiative cooling is implemented using element-by-element rates (Wiersma et al., 2009a) for the 11 most important metals in the presence of the CMB and UV/X-ray backgrounds given by Haardt & Madau (2001). To prevent artificial fragmentation, the cold and dense gas is placed on an equation of state $P_{\rm eos} \propto \rho^{4/3}$ that is designed to mimic the mixture

[1]Note that the units do not have factors of h.

of phases in the interstellar medium (ISM) (Schaye & Dalla Vecchia, 2008). Star formation is implemented using a pressure-dependent prescription that reproduces the observed Kennicutt-Schmidt star formation law (Schaye & Dalla Vecchia, 2008) and uses a threshold that captures the metallicity dependence of the transition from the warm, atomic to the cold, molecular gas phase (Schaye, 2004). Star particles are treated as single stellar populations with a Chabrier (2003) IMF evolving along the tracks provided by Portinari et al. (1998). Metals from supernovae and AGB stars are injected into the ISM following the model of Wiersma et al. (2009b) and stellar feedback is implemented by injecting thermal energy into the gas as described in Dalla Vecchia & Schaye (2012). The amount of energy injected into the ISM per feedback event is dependent on the local gas metallicity and density in an attempt to take into account the unresolved structure of the ISM (Schaye et al., 2015; Crain et al., 2015). Supermassive black hole seeds are injected in halos above $10^{10}h^{-1}\mathrm{M}_{\odot}$ and grow through mergers and accretion of low angular momentum gas (Rosas-Guevara et al., 2015; Schaye et al., 2015). AGN feedback is performed by injecting thermal energy into the gas directly surrounding the black hole (Booth & Schaye, 2009; Dalla Vecchia & Schaye, 2012).

The subgrid model was calibrated (by adjusting the intensity of stellar feedback and the accretion rate onto black holes) so as to reproduce the present day stellar mass function and galaxy sizes (Schaye et al., 2015). As discussed by Crain et al. (2015), this latter requirement is crucial to obtain a galaxy population that evolves with redshift in a similar fashion to the observed populations (Furlong et al., 2015).

Haloes were identified using the Friends-of-Friends (FoF) algorithm (Davis et al., 1985), and bound structures within them were then identified using the SUBFIND code (Springel et al., 2001; Dolag et al., 2009). A sphere centred at the minimum of the gravitational potential of each subhalo is grown until the mass contained within a given radius, R_{200}, reaches $M_{200} = 200\,(4\pi\rho_{\rm cr}(z)R_{200}^3/3)$, where $\rho_{\rm cr}(z) = 3H(z)^2/8\pi G$ is the critical density at the redshift of interest.

3.2.2 SPH implementations

All simulations that are compared in this study use the Gadget-3 code. We use both the default flavour of SPH documented in Springel (2005) and the more recent flavour nicknamed ANARCHY (Dalla Vecchia (in prep.), see also appendix A of Schaye et al. (2015)) implemented as a modification to the default code. For completeness, we describe both sets of hydrodynamical equations in this section without derivations. For a comprehensive description and a motivation, see the review by Price (2012) and the description of the alternative SPH formalism used in ANARCHY by Hopkins (2013, 2015). A similar formulation to ANARCHY is presented in Hu et al. (2014). Note that apart from the differences highlighted in this section, the codes (and parameters) used for both types of simulations are identical.

Default Gadget-2 SPH

In its default version, GADGET-2 uses the fully conservative SPH equations introduced by Springel & Hernquist (2002). We will label this "GADGET SPH" in the remainder of this chapter and restrict our discussion of the model to the 3D case. As in any flavour of SPH, the starting point is a the choice of a smoothing function to reconstruct field quantities at any point in space from a weighted average over the surrounding particles. In the case of gas density, at position $\mathbf{x}_i$. the equation reads

$$\rho_i = \sum_j m_j W\left(|\mathbf{x}_i - \mathbf{x}_j|, h_i\right), \tag{3.1}$$

where $W(|\mathbf{r}|, h)$ is the spherically symmetric kernel function. In the case of GADGET, the M_4 cubic B-spline function is used and reads

$$W(r,h) = \frac{8}{\pi h^3} \begin{cases} 1 - 6\left(\frac{r}{h}\right)^2 + 6\left(\frac{r}{h}\right)^3 & \text{if} \quad 0 \leq r \leq \frac{h}{2} \\ 2\left(1 - \frac{r}{h}\right)^3 & \text{if} \quad \frac{h}{2} < r \leq h \\ 0 & \text{if} \quad r > h. \end{cases}$$

The smoothing length h_i of a particle is obtained by requiring that the weighted

number of neighbours

$$N_{\rm ngb} = \frac{4}{3}\pi h_i^3 \sum_j W\left(|\mathbf{x}_i - \mathbf{x}_j|, h_i\right) \tag{3.2}$$

of the particle is close to a pre-defined constant; $N_{\rm ngb} = 48$ in our case. Note, however, that contrary to what is often written in the literature, GADGET defines the smoothing length as the cut-off radius of the kernel and not as the more physical FWHM of the kernel function (Dehnen & Aly, 2012).

The quantity integrated in time alongside the velocities and positions of the particles is the entropic function[2] $A_i = P_i/\rho_i^\gamma$, defined in terms of the pressure P_i and polytropic index γ. The equations of motion are then given by

$$\frac{\mathrm{d}\mathbf{v}_\mathrm{i}}{\mathrm{dt}} = -\sum_j m_j \left[\frac{P_i}{\Omega_i \rho_i^2}\nabla_i W_{ij}(h_i) + \frac{P_j}{\Omega_j \rho_j^2}\nabla_i W_{ij}(h_j)\right], \tag{3.3}$$

where Ω_i, accounts for gradient in the smoothing length,

$$\Omega_i = 1 + \frac{h_i}{3\rho_i}\sum_j m_j \frac{\partial W_{ij}(h_i)}{\partial h} \tag{3.4}$$

and $W_{ij}(h_i) \equiv W(\mathbf{x}_i - \mathbf{x}_j, h_i)$. In the absence of radiative cooling or thermal diffusion terms, the entropic function of each particle is a constant in time. Only cooling, feedback events (see the previous section) and shocks will change the entropic function.

In order to capture shocks, artificial viscosity is implemented by adding a term to the equations of motion (3.3) to evolve the entropic function accordingly:

$$\begin{aligned}
\frac{\mathrm{d}\mathbf{v}_\mathrm{i}}{\mathrm{dt}} &\overset{\text{visc.}}{=} -\frac{1}{4}\sum_j m_j \Pi_{ij} \nabla \overline{W}_{ij}\left(f_i + f_j\right) \\
\frac{\mathrm{dA}_\mathrm{i}}{\mathrm{dt}} &\overset{\text{visc.}}{=} \frac{1}{8}\frac{\gamma-1}{\rho_i^{\gamma-1}}\sum_j m_j \Pi_{ij}\left(\mathbf{v}_i - \mathbf{v}_j\right)\cdot\nabla\overline{W}_{ij}\left(f_i + f_j\right),
\end{aligned}$$

with $\overline{W}_{ij} \equiv (W_{ij}(h_i) + W_{ij}(h_j))$ and the viscous tensor (Π_{ij}) and shear flow switch f_i defined below. Following Monaghan (1997), the viscous tensor, which plays the

[2]This quantity is not the thermodynamical entropy s but a monotonic function of it.

role of an additional pressure in the equations of motion, is defined in terms of the particle's sound speed, $c_i = \sqrt{\gamma P_i/\rho_i}$, as

$$\Pi_{ij} = -\alpha \frac{(c_i + c_j - 3w_{ij})\, w_{ij}}{\rho_i + \rho_j}, \tag{3.5}$$

$$w_{ij} = \min\left(0, \frac{(\mathbf{v}_j - \mathbf{v}_i)\cdot(\mathbf{x}_i - \mathbf{x}_j)}{|\mathbf{x}_i - \mathbf{x}_j|}\right) \tag{3.6}$$

with the dimensionless viscosity parameter set to the commonly used value of $\alpha = 2$ in our simulations. Finally, to prevent the application of viscosity in the case of pure shear flows, the switch proposed by Balsara (1995) is used:

$$f_i = \frac{|\nabla \cdot \mathbf{v}_i|}{|\nabla \cdot \mathbf{v}_i| + |\nabla \times \mathbf{v}_i| + 10^{-4} c_i/h_i}, \tag{3.7}$$

with the last term in the denominator added to avoid numerical instabilities. The divergence and curl of the velocity field are computed in the standard SPH way (e.g. Price (2012)).

Anarchy SPH

The first change in ANARCHY with respect to GADGET is the choice of kernel function. More accurate estimators for both the field quantities and their derivatives can be obtained by using Wendland (1995) kernels (Dehnen & Aly, 2012). ANARCHY uses the C_2 kernel. This kernel function is not affected by pairing instability, which occurs when high values of $N_{\rm ngb}$ are used with spline kernels. It reads

$$W(r,h) = \frac{21}{2\pi h^3} \begin{cases} \left(1 - \frac{r}{h}\right)^4 \left(1 + 4\frac{r}{h}\right) & \text{if} \quad 0 \leq r \leq h \\ 0 & \text{if} \quad r > h. \end{cases}$$

To keep the effective resolution of the simulation similar between the two flavours of SPH, we use $N_{\rm ngb} = 58$ with this kernel. This yields the same kernel FWHM as obtained for the cubic kernel[3] with $N_{\rm ngb} = 48$.

[3]Expressing our resolution in terms of the local inter-particle separation (Price, 2012; Dehnen & Aly, 2012) gives $\eta = \mathrm{FWHM}(W(r,h))/\Delta x = 1.235$ for both kernels.

The equations of motion used in the ANARCHY flavour of SPH are based on the Pressure-Entropy formulation of Hopkins (2013), a generalisation of the earlier solutions of Ritchie & Thomas (2001), Read et al. (2010) and Saitoh & Makino (2013). The two quantities carried by particles that are integrated forward in time are again the velocity and the entropic function. Alongside the density, which is computed in the usual way (Eq. 3.1), two additional smoothed quantities are introduced in this formulation of SPH: the weighted density

$$\bar{\rho}_i = \frac{1}{A_i^{1/\gamma}} \sum_j m_j A_j^{1/\gamma} W\left(|\mathbf{x}_i - \mathbf{x}_j|, h_i\right) \tag{3.8}$$

and its associated weighted pressure: $\bar{P}_i = A_i \bar{\rho}_i^{\gamma}$. Despite having the same units as the regular density, its weighted counterpart should only be understood as an intermediate quantity entering other equations and should not be used as the gas density. Using these two new quantities, the equation of motion for the particle velocities becomes

$$\begin{aligned} \frac{\mathrm{d}\mathbf{v}_\mathrm{i}}{\mathrm{dt}} &= -\sum_j m_j \left[\frac{A_j^{1/\gamma}}{A_i^{1/\gamma}} \frac{\bar{P}_i}{\bar{\rho}_i^2} \Omega_{ij} \nabla_i W_{ij}(h_i) + \right. \\ &\left. \frac{A_i^{1/\gamma}}{A_j^{1/\gamma}} \frac{\bar{P}_j}{\bar{\rho}_j^2} \Omega_{ji} \nabla_j W_{ij}(h_j) \right] \end{aligned} \tag{3.9}$$

with the terms accounting for the gradients in the smoothing length reading

$$\Omega_{ij} = 1 - \frac{1}{A_i^{1/\gamma}} \left(\frac{h_i}{3\rho_i} \frac{\partial \bar{P}_i^{1/\gamma}}{\partial h_i} \right) \left(1 + \frac{h_i}{3\rho_i} \right)^{-1}. \tag{3.10}$$

The use of the smoothed quantities, $\bar{P}_i$ and $\bar{\rho}_i$, in the equations of motion smooths out the spurious pressure jumps appearing at contact discontinuities in older formulations of SPH (Saitoh & Makino, 2013; Hopkins, 2013).

As in all versions of SPH, artificial viscosity has to be added to capture shocks. In the ANARCHY formulation of SPH, this is done following the method of Cullen & Dehnen (2010). Their scheme is the latest iteration of a series of improvements to the standard (Monaghan, 1997) viscosity term that started with the proposal

of Morris & Monaghan (1997) to assign individual viscosities α_i to each particle. Improving on the work of Rosswog et al. (2000), Price (2004) and Wetzstein et al. (2009), Cullen & Dehnen (2010) proposed a differential equation for α_i that is solved alongside the equations of motion (Eqn. 3.9):

$$\dot{\alpha}_i = 2l v_{\mathrm{sig},i} \left(\alpha_{\mathrm{loc},i} - \alpha_i\right) / h_i, \tag{3.11}$$

with $l = 0.01$ and the signal velocity $v_{\mathrm{sig},i}$ introduced below. The local viscosity estimator $\alpha_{\mathrm{loc},i}$ is given by

$$\alpha_{\mathrm{loc},i} = \alpha_{\mathrm{max}} \frac{h_i^2 S_i}{v_{\mathrm{sig},i}^2 + h_i^2 S_i}, \tag{3.12}$$

where $\alpha_{\mathrm{max}} = 2$ and $S_i = \max\left(0, -\frac{d}{dt}\left(\nabla \cdot \mathbf{v}_i\right)\right)$ is the shock detector. After passing through a shock, $S_i = 0$ and hence $\alpha_{\mathrm{loc},i} = 0$, leading to a decrease in α_i. We impose $\alpha_i > \alpha_{\mathrm{min}} = 0.05$ to facilitate particle re-ordering. The signal velocity is constructed to capture the maximal velocity at which information can be transferred between particles whilst remaining positive:

$$v_{\mathrm{sig},i} = \max_{|\mathbf{x}_{ij}| \leq h_i} \left(\frac{1}{2}\left(c_i + c_j\right) - \min(0, \mathbf{v}_{ij} \cdot \hat{\mathbf{x}}_{ij}) \right), \tag{3.13}$$

with $\hat{\mathbf{x}}_{ij} = (\mathbf{x}_i - \mathbf{x}_j)/|\mathbf{x}_i - \mathbf{x}_j|$ and $\mathbf{v}_{ij} = \mathbf{v}_j - \mathbf{v}_i$.

The individual viscosity coefficients α_i are then combined to enter the equations of motion in a similar way as in the GADGET formulation. Equations 3.5 and 3.6 are replaced by:

$$\Pi_{ij} = -\frac{\alpha_i + \alpha_j}{2} \frac{\left(c_i + c_j - 3w_{ij}\right) w_{ij}}{\rho_i + \rho_j}, \tag{3.14}$$

$$w_{ij} = \min\left(0, \frac{\left(\mathbf{v}_j - \mathbf{v}_i\right) \cdot \left(\mathbf{x}_i - \mathbf{x}_j\right)}{|\mathbf{x}_i - \mathbf{x}_j|}\right). \tag{3.15}$$

Note that contrary to Hu et al. (2014) we do not implement expensive matrix calculations (Cullen & Dehnen, 2010) for the calculation of the velocity divergence time derivative entering the shock detector S_i as we found that using the standard SPH expressions was sufficient for the accuracy we targeted.

The last improvement included in the ANARCHY flavour of SPH is the use of some entropy diffusion between particles. SPH is by construction non-diffusive (Price, 2012) and does, hence, not incorporate the thermal conduction that may be required to faithfully reproduce the micro-scale mixing of gas phases. We implement a small level of numerical diffusion following the recipe of Monaghan (1997) and Price (2008), but use the entropy and not the internal energy as the thermodynamic variable that is diffused. More specifically, the equation of motion for the entropy includes a new term that reads

$$\frac{\mathrm{dA_i}}{\mathrm{dt}} \overset{\mathrm{diff.}}{=} \frac{\gamma-1}{\bar{\rho}^{\gamma-1}} \sum_j \alpha_{\mathrm{diff},ij} v_{\mathrm{diff},ij} \frac{m_j}{\rho_i+\rho_j} \left(\frac{\bar{P}_i}{\bar{\rho}_i} - \frac{\bar{P}_j}{\bar{\rho}_j}\right) \overline{W}_{ij}, \tag{3.16}$$

with the diffusion velocity given by $v_{\mathrm{diff},ij} = \max(c_i + c_j + (\mathbf{v}_i - \mathbf{v}_j)\cdot(\mathbf{x}_i - \mathbf{x}_j) \,/\, |\mathbf{x}_i - \mathbf{x}_j| \,, 0)$ and the diffusion coefficient by $\alpha_{\mathrm{diff},ij} = \frac{1}{2}(\alpha_{\mathrm{diff},i} + \alpha_{\mathrm{diff},j})$. The individual diffusion coefficients are evolved alongside the other thermodynamic variables following the differential equation

$$\alpha_{\mathrm{diff},i} = \beta \frac{h_i \nabla_i^2 \left(\bar{P}_i/\bar{\rho}_i\right)}{\sqrt{\bar{P}_i/\bar{\rho}_i}}, \tag{3.17}$$

where we adopted $\beta = 0.01$ as this value only leads to a small amount of diffusion and does not require a specific limiter in the presence of a gravitational field. We further impose $0 < \alpha_{\mathrm{diff},i} < 1$, but note that the upper limit is rarely reached, even for large discontinuities.

3.2.3 Thermal energy injection and time-step limiter

A crucial aspect of the stellar feedback implementation used in EAGLE and described in Dalla Vecchia & Schaye (2012) is the instantaneous injection of large amounts of thermal energy Δu in the ISM. This injection is performed by raising the temperature of a the gas particle by $\Delta T = 10^{7.5}$ K, a value much larger than the average temperature of the warm ISM. In the GADGET formulation of SPH, this is implemented by changing the entropy A_i of a particle. In the case of ANARCHY, the situation is more complex since the densities themselves are weighted by the

entropies which implies that a change in the entropy will affect both quantities entering the equations of motion of all the particles in a given neighbourhood. Hence, changing the internal entropy of just one single particle will *not* lead to the correct change of energy (across all particles in the simulation volume) of the gas. The thermal energy injected in the gas will be different (typically lower) from what is expected by a simple rise in A_i, leading to a seemingly inefficient feedback event.

This problem is alleviated in the EAGLE code by the use of a series of iterations during which the values of A_i and ρ_i are changed until they have converged to value where the total energy injection is close to the imposed value:

$$A_{i,n+1} = \frac{(\gamma-1)(u_{\rm old}+\Delta u)}{\bar{\rho}_{i,n}^{\gamma-1}},$$
$$\bar{\rho}_{i,n+1} = \frac{\bar{\rho}_{i,n}A_n^{1/\gamma} - m_i W(0,h_i)A_{i,n}^{1/\gamma} + m_i W(0,h_i)A_{i,n+1}^{1/\gamma}}{A_{i,n+1}^{1/\gamma}}.$$

This approximation is only valid for reasonable values of Δu and only leads to the injection of the correct amount of energy if the energy is injected into one particle in a given neighbourhood, as is the case in most stellar feedback events. When large amounts of energy are injected into multiple neighbouring particles, as can happen in some AGN feedback events, this approximation is not sufficient to properly conserve energy (across all particles in a given kernel neighbourhood). To avoid this, we limit the number of particles being heated at the same time to 30% of the AGN's neighbours. If this threshold is exceeded, the time step of the BH is decreased and the remaining energy is kept for injection at the next time step. Isolated explosion tests have shown that this limit leads to the correct amount of energy being distributed.

As was pointed out by Saitoh & Makino (2009), the conservation of energy in SPH following the injection of large amounts of energy requires the reduction of the integration time-step of the particles receiving energy as well as those of its direct neighbours. This was further refined by Durier & Dalla Vecchia (2012) who demonstrated that energy conservation can only be achieved if the time-step of the

particles is updated according to their new hydrodynamical state. This latter time-step limiter is applied in both the GADGET-SPH and ANARCHY-SPH simulations used in sections 3.3 and 3.4 of this chapter. We discuss its influence on galaxy properties in subsections 3.3.1 and 3.3.2.

3.3 Galaxy population and evolution through cosmic time

As discussed by Schaye et al. (2015) and Crain et al. (2015), the subgrid models of stellar and AGN feedback are only an incomplete representation of the physical processes taking place in the unresolved multiphase ISM. In particular, because radiative losses and momentum cancellation associated with feedback from star formation and AGN in the multiphase interstellar medium cannot be predicted from first principles, the simulations cannot make ab initio predictions for the stellar and black hole masses. In a fashion similar to the semi-analytic models, the subgrid models for feedback in the EAGLE simulations have therefore been calibrated to reproduce the $z = 0.1$ galaxy stellar mass function and, the relations between galaxy size and mass and between the mass of the central supermassive black hole and the galaxy. The details of this calibration procedure are described in Crain et al. (2015). In this section, we will present the basic properties of our simulated galaxy population when the hydrodynamic scheme is changed back to the commonly used GADGET-SPH formalism. We will specifically focus on the galaxy stellar mass function and on the galaxy sizes before turning towards the star formation rates.

We stress that the model parameters have not been recalibrated when switching our hydrodynamics scheme back to GADGET-SPH.

3.3.1 The galaxy stellar mass function

In Fig. 3.1, we show the stellar mass function at $z = 0.1$ of our simulated galaxies computed in spherical apertures of 30 kpc around the centre of potential of the haloes. As discussed by Schaye et al. (2015), this choice of aperture gives a simple way to distinguish the galaxy and the ICL. The blue and red lines correspond to our simulations with the ANARCHY and GADGET flavours of SPH, respectively. We use dashed lines when fewer than 10 objects populate a (0.2 dex) stellar mass bin and dotted lines when the galaxy mass drops below our resolution limit (see Schaye et al. (2015) for resolution considerations). The two hydrodynamic schemes lead to a very similar GSMF with significant differences only appearing at $M_* > 2 \times 10^{11}$ M$_\odot$, where the small number of objects in the volume forbids a strong interpretation of the deviation. The white circles and grey squares correspond to the observationally inferred GSMFs from the GAMA (Baldry et al., 2012) and SDSS (Li & White, 2009) surveys, respectively. The two simulated galaxy populations undershoot the break of the stellar mass function in a similar fashion and are in a similarly good agreement ($\lesssim 0.2$ dex) with the data. The choice of hydrodynamics solver seems to have little impact on the mass and abundance of galaxies in our cosmological simulations. We re-iterate that there has been no recalibration of the subgrid parameters between the GADGET and ANARCHY simulations.

In order to compare the contribution of hydrodynamics uncertainties to the uncertainties arising from the subgrid models, we show using green and yellow lines two additional models using the ANARCHY flavour of SPH but with feedback from star formation injecting half and twice as much energy, respectively. These simulations are the models WeakFB and StrongFB introduced by Crain et al. (2015) and reduced or increased the number of feedback events taking place, whilst keeping the amount of energy injected per event constant. They have been run in smaller volumes (25^3 Mpc^3), leading to poorer statistics at the high-mass end. These changes in the amount of energy injected in the ISM lead to much larger differences in the GSMF than changing the flavour of SPH used for the simulation. The large impact of variations of the subgrid model for stellar feedback on the simulated population

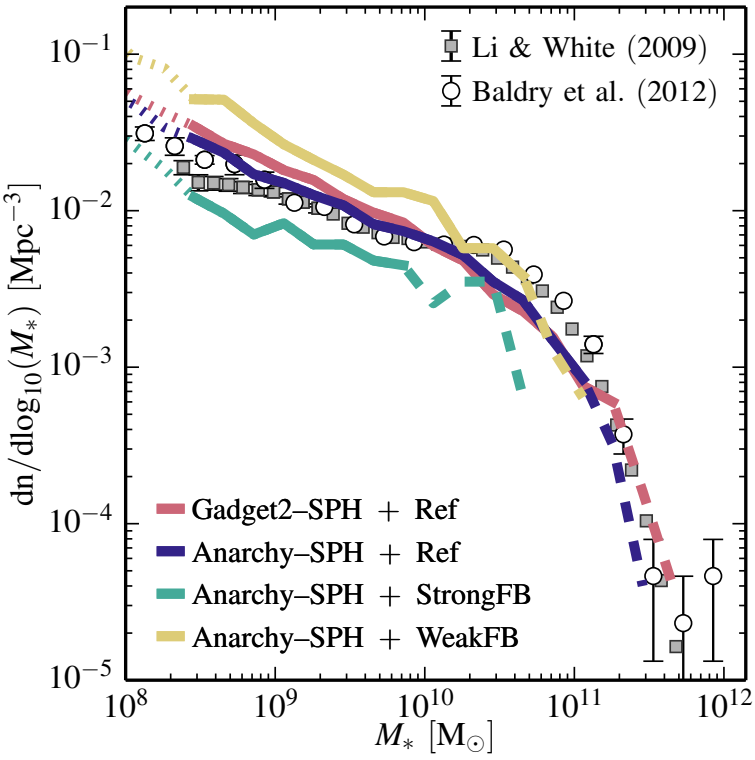

Figure 3.1: The $z = 0.1$ GSMF of the L050N0752 simulations using ANARCHY SPH (blue line, the EAGLE default) and GADGET SPH (red line). Curves are drawn with dotted lines where galaxies are comprised of fewer than 100 star particles, and dashed lines where the GSMF is sampled by fewer than 10 galaxies per 0.2 dex mass bin. Data points show measurements with 1σ error bars from the SDSS (Li & White, 2009, filled squares), and GAMA (Baldry et al., 2012, open circles) surveys. The yellow and green lines show the GSMF of the L025N0376 simulations with twice weaker and twice stronger feedback from star formation respectively, in a smaller 25^3 Mpc^3 volume. The differences due to the choice of hydrodynamical scheme are smaller than the differences due to uncertainties in the sub-grid modelling.

and on single galaxies can also be appreciated from the large range of outcomes of the different models in the OWLS suite (Schaye et al., 2010; Haas et al., 2013) and AQUILA projects (Scannapieco et al., 2012). Our work, however, uses a higher resolution than was accessible in the OWLS suite for $z = 0$ and contrary to AQUILA uses a cosmological volume and can hence study the effect of the hydrodynamics scheme from dwarf galaxies to group-sized haloes. The study of Kereš et al. (2012), which compared the AREPO (Springel, 2010b) and GADGET-SPH hydro solvers but using simple subgrid models, came to the same conclusion: the choice of hydrodynamics scheme has little impact on the stellar mass function of simulated galaxies. The source terms arising from the physical modelling of the unresolved processes in the ISM clearly dominate the uncertainty budget.

We now turn to the impact of the time-step limiter on the simulated galaxy population. As was demonstrated by Durier & Dalla Vecchia (2012), the absence of a time-step limiter leads to the non-conservation of energy during feedback events. The energy of the system after the injection is larger than expected. This implies that a simulation without time-step limiter will have a spuriously high feedback efficiency. In order to test this, we ran a simulation in a $25^3\ \mathrm{Mpc}^3$ volume using the Ref subgrid model and the ANARCHY-SPH scheme but with the (Durier & Dalla Vecchia, 2012) time-step limiter switched off. Since this simulation volume is too small to be representative, it is more informative to study the relation between halo mass and stellar mass.

In Fig. 3.2, we show the relation between halo mass (M_{200}) and galaxy formation efficiency (M_*/M_{200}) for central galaxies at $z = 0.1$. As for all other figures, the blue and red lines correspond to the ANARCHY-SPH and GADGET-SPH simulations respectively both using the time-step limiter. We show the simulation using twice stronger and twice weaker feedback with a green and yellow line respectively. These are the same simulations that were shown in Fig. 3.1. The stronger feedback from star formation leads to a lower stellar mass formed in a given halo than in the Ref model, as was discussed by Crain et al. (2015). As expected from the GSMF, galaxy formation efficiency is strongly moderated by the feedback pa-

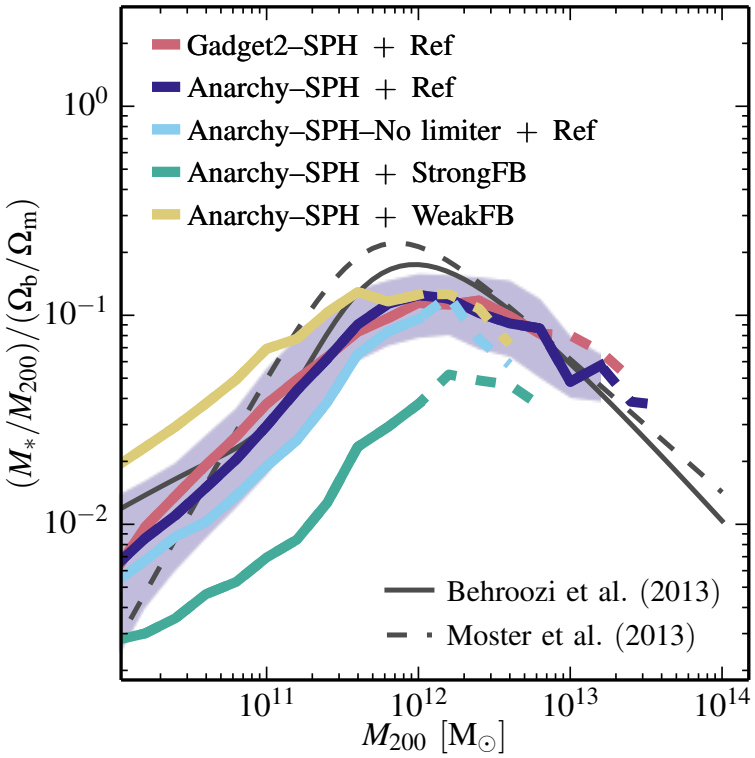

Figure 3.2: The median ratio of the stellar and halo mass of central galaxies, as a function of halo mass M_{200} and normalised by the cosmic baryon fraction at $z = 0.1$ for both the L050N0752 ANARCHY SPH (blue line) and GADGET SPH (red line) simulations. Curves are drawn with dashed lines where the GSMF is sampled by fewer than 10 galaxies per bin. The 1σ scatter about the median of the ANARCHY run is denoted by the blue shaded region. The solid and dashed grey lines show the multi-epoch abundance matching results of Behroozi et al. (2013) and Moster et al. (2013) respectively. The yellow and green lines show the GSMF of the L025N0376 simulations with twice weaker and twice stronger feedback from star formation respectively. The cyan line corresponds to the simulation using the ANARCHY formulation of SPH and reference subgrid model, but without the time-step limiter. The absence of the time-step limiter artificially increases the efficiency of the feedback and has a greater impact than the choice of hydro solver.

rameters. Finally, we show in cyan the simulation using the Ref subgrid model but without the time-step limiter. This simulation displays a lower stellar mass in a given halo than its counterpart using the limiter. This indicates that the feedback was indeed more efficient at quenching star formation in that simulation. This is a purely numerical effect that has to be corrected by the use of small time-steps in regions where feedback takes place. Note that the impact of the time-step limiter is much larger than the differences due to the hydrodynamics solver, but smaller than the effect of doubling/halving the feedback strength.

3.3.2 The sizes of galaxies

Crain et al. (2015) showed that matching the observed GSMF does not in general lead to a realistic population of galaxies. Alongside the galaxy masses the galaxy sizes were therefore considered in the EAGLE project during the calibration process of the parameters of the subgrid model for stellar feedback. Crain et al. (2015) demonstrated that feedback from star formation is less efficient at quenching the galaxies if the feedback occurs in dense regions of the ISM. This would lead to galaxies that are too compact and with a specific star formation rate at low redshift lower than observations. As a consequence, they also showed that selecting model parameters that lead to galaxies with sizes in agreement with observational data was necessary to obtain a realistic population of galaxies across cosmic time. Assessing the dependence of the galaxy sizes on the hydrodynamics scheme is, hence, crucial.

In Fig. 3.3, we show the sizes of the galaxies in both the ANARCHY-SPH and GADGET-SPH simulations. The observational data sets from Shen et al. (2003) (SDSS, black line) and Baldry et al. (2012) (GAMA, white circles) are shown for comparison. The sizes of the simulated galaxies are computed following McCarthy et al. (2012). We fit a Sérsic profile to the projected, azimuthally-averaged surface density profiles. We then extract the half-mass radius of the galaxy, R_{50}, from this profile when integrated to infinity. To match the observational selection of Shen et al. (2003), we select only galaxies that have a Sérsic index $n_{\rm s} < 2.5$. We use

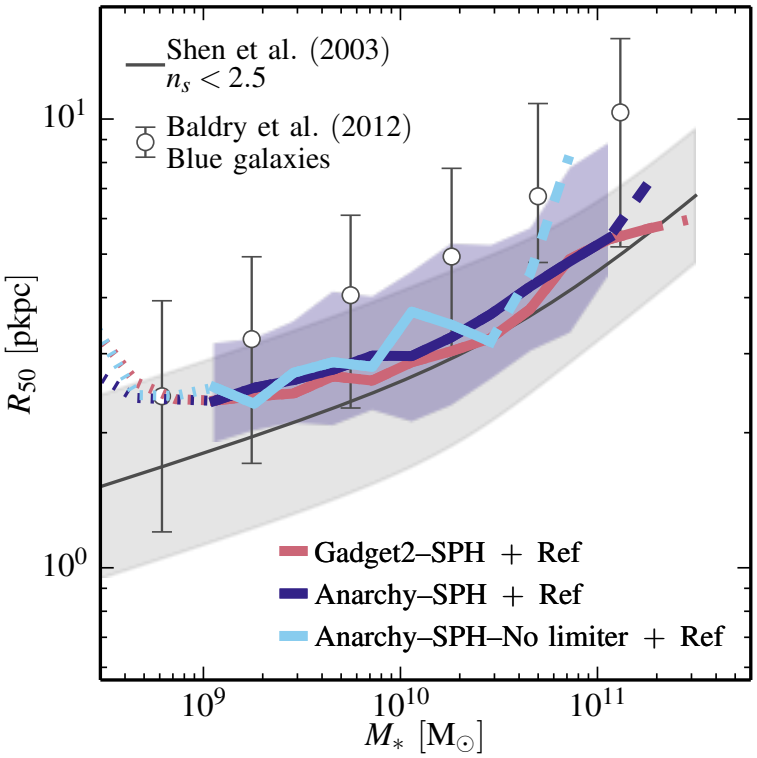

Figure 3.3: The sizes, at $z = 0.1$, of disc galaxies in the L050N0752 ANARCHY SPH (blue line) and GADGET SPH (red line) simulations and ANARCHY SPH model without time-step limiter (cyan line). Size, R_{50}, is defined as the half-mass radius of a Sérsic profile fit to the projected, azimuthally-averaged stellar surface density profile of a galaxy, and those with Sérsic index $n_s < 2.5$ are considered disc galaxies. Curves show the binned median sizes, and are drawn with dotted lines below a mass scale of 600 star particles, and using a dashed line style where sampled by fewer than 10 galaxies per 0.2 dex mass bin. The 1σ scatter about the median of the ANARCHY run is denoted by the blue shaded region. The solid grey lines show the median and 1σ scatter of sizes for $n_s < 2.5$ galaxies inferred from SDSS data by Shen et al. (2003), whilst white circles with error bars show sizes of blue galaxies inferred by Baldry et al. (2012) from GAMA data. All simulations reproduce the $z = 0.1$ galaxy sizes.

dashed lines where the (0.2 dex) mass bins containing fewer than 10 objects and dotted lines for galaxies that are represented by less than 600 star particles. The 1σ scatter around the mean in the ANARCHY-SPH simulation is shown as the blue shaded region for the mass bins that are both well resolved and well sampled. The GADGET-SPH simulation presents a similar scatter.

Both simulations reproduce the observed galaxy size-mass relation. The simulated galaxies lie within $0.1 - 0.2$ dex of either of the two data sets. As was the case for the GSMF, the galaxy sizes are unaffected by the specific details of the hydrodynamics scheme. This implies that the two hydro schemes have similar energy losses in dense gas regions where feedback takes place. Differences much larger than this can be seen when the subgrid model parameters are varied, even if one requires the GSMF to match observations (Crain et al., 2015).

When considering the galaxy masses, we found that not using the Durier & Dalla Vecchia (2012) time-step limiter led to an increase of the feedback efficiency although the magnitude of the effect was small compared to that of doubling the feedback energy. As galaxy sizes was our second diagnostic, we also consider the effect of switching off this limiter on the sizes of our simulated galaxies. This model is shown as a cyan line in Fig. 3.3. The oscillations seen in the curve are due to the smaller volume used for this simulation. The sizes of the galaxies are close to or slightly larger than the ones in the default simulation. This is in agreement with Crain et al. (2015), who found stronger feedback leads to galaxies with larger radii (see also Sales et al. (2010)). The absence of limiter increases the efficiency of feedback but only by a small amount, leading to galaxy sizes being nearly unchanged.

Crain et al. (2015) also showed that using more efficient stellar feedback lead (among other things) to higher SSFRs, lower passive fractions and lower metallicities. We have verified that turning off the time-step limiter has the same qualitative effects. We will not consider the effect of turning off the limiter further in the rest of this chapter.

3.3.3 The star formation rate of galaxies

We now turn to the star formation rates of galaxies. This quantity was not used in the parameter calibration process of the ANARCHY-SPH run (i.e. the default EAGLE) and is an important independent diagnostic of the success of the simulation. Furthermore, since the ISM dictates the star formation rate of galaxies, changes in the way the equations of hydrodynamics are solved may lead to changes in the SFRs.

In Fig. 3.4, we show the star formation rate per unit volume. The blue and red lines again correspond to the ANARCHY and GADGET flavours of SPH, respectively. Observational data from Rodighiero et al. (2010), Karim et al. (2011), Cucciati et al. (2012) and Bouwens et al. (2012) are also shown. Where applicable, the data has been corrected for our adopted cosmology and IMF as described in Furlong et al. (2015). In agreement with the data, Both simulations display a rise in the star formation rate density at high redshifts and a fall at $z \lesssim 2$. As was discussed by Furlong et al. (2015), the constant offset in star formation rate of ≈ 0.2 dex between the simulations and observations leads to 20% less stars being formed over the cosmic history, in good agreement with the $z = 0.1$ GSMF (Fig. 3.1), whose "knee" the simulations undershoots.

The simulation using the GADGET version of SPH predicts a higher cosmic star formation rate density than its ANARCHY counterpart between redshifts 2 and 6 but this does not lead to a large difference in stellar mass formed by $z = 2$. However, the higher star formation rate seen at $z < 1$ is significant and the smaller decrease between $z = 1$ and $z = 0$ implies a star formation rate that is 65% higher by $z = 0$ in the simulation using the GADGET formulation of SPH. This higher star formation rate can be tentatively related to the large number of high-mass galaxies seen in the GSMF of this simulation and could, hence, indicate a lower quenching efficiency of the AGN activity in the largest haloes. An extreme version of a model with a low quenching efficiency in large haloes is given by a model without AGN feedback. Such a model, using the ANARCHY flavour of SPH, is shown, using the yellow line in Fig. 3.4. The excess star formation at $z < 2$ is, much larger than in the GADGET-

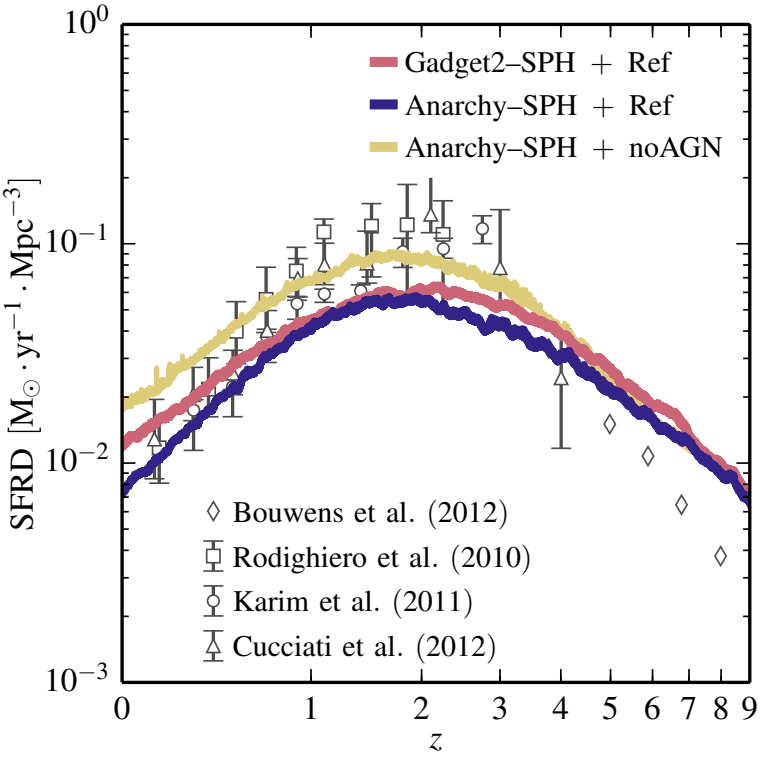

Figure 3.4: The evolution of the cosmic star formation rate density in both the L050N0752 ANARCHY SPH (blue line) and GADGET-2 SPH (red line) simulations. The data points correspond to observations from (Karim et al., 2011, radio), (Rodighiero et al., 2010, 24 μm), (Cucciati et al., 2012, FUV) and (Bouwens et al., 2012, UV). The decline in the star formation rate density from $z = 2$ to $z = 0$ is less pronounced in the GADGET run, leading to a 65% higher star formation rate density at $z = 0$. For comparison, a model without AGN feedback (yellow line) is shown. The star formation rate density in that model has a low-redshift slope similar to that of the GADGET simulation.

SPH based run with AGN, but the slope is similar and not steep enough compared to the observational data.

Whether the excess star formation rate at low redshift may be due to large haloes can be confirmed by looking at the specific star formation rate (SSFR) of the simulated galaxies. This quantity is shown in Fig. 3.5 as a function of mass. We limit our selection to star-forming galaxies by excluding objects with $\dot{M}_*/M_* < 0.01\ \mathrm{Gyr}^{-1}$. As was the case for the stellar mass of the galaxies, we measure the SFR within a $30\ \mathrm{kpc}$ spherical aperture. The red and blue lines show the mean SSFR in the simulations using the GADGET and ANARCHY flavours of SPH respectively. As for other figures, the lines are dashed when a given mass bin is sampled by fewer than 10 objects. The blue shaded region indicates the 1–σ scatter in the ANARCHY-based simulation. The GADGET-based simulation displays a scatter of the same magnitude. For comparison, we show the SSFR inferred from observations in the SDSS field by Gilbank et al. (2010) (white squares) and in the GAMA survey by Bauer et al. (2013) (grey circles). Simulated galaxies with masses $M_* \sim 10^{11}\mathrm{M}_\odot$ are in agreement with the data, whilst lower-mass objects exhibit a specific star formation rate lower than observed with the discrepancy reaching $\sim 0.3\ \mathrm{dex}$ at $M_* \sim 10^9\mathrm{M}_\odot$. Schaye et al. (2015) showed that most of this discrepancy goes away if the resolution of the simulation is increased. Both the GADGET and ANARCHY simulations show the same discrepancy with the data at low masses.

At the upper end of the mass spectrum the two simulations do, however, differ. The star formation rate of galaxies with $M_* \gtrsim 2 \times 10^{10}\mathrm{M}_\odot$ is significantly larger for the GADGET formulation of SPH. At $M_* \sim 10^{11}\mathrm{M}_\odot$, the discrepancy is $0.3\ \mathrm{dex}$.

Complementary to the SSFR of the star forming galaxies, the passive fraction provides a good diagnostic of the efficiency with which SF is quenched in large galaxies. This quantity is shown in Fig. 3.6 for both our simulations. Galaxies are considered passive if their SSFR is smaller than $0.01\ \mathrm{Gyr}^{-1}$, which is an order of magnitude below the observed median SSFR for star forming galaxies at that redshift. For comparison, the data points show the fractions inferred from SDSS data by Gilbank et al. (2010) and Moustakas et al. (2013). We only show points for the

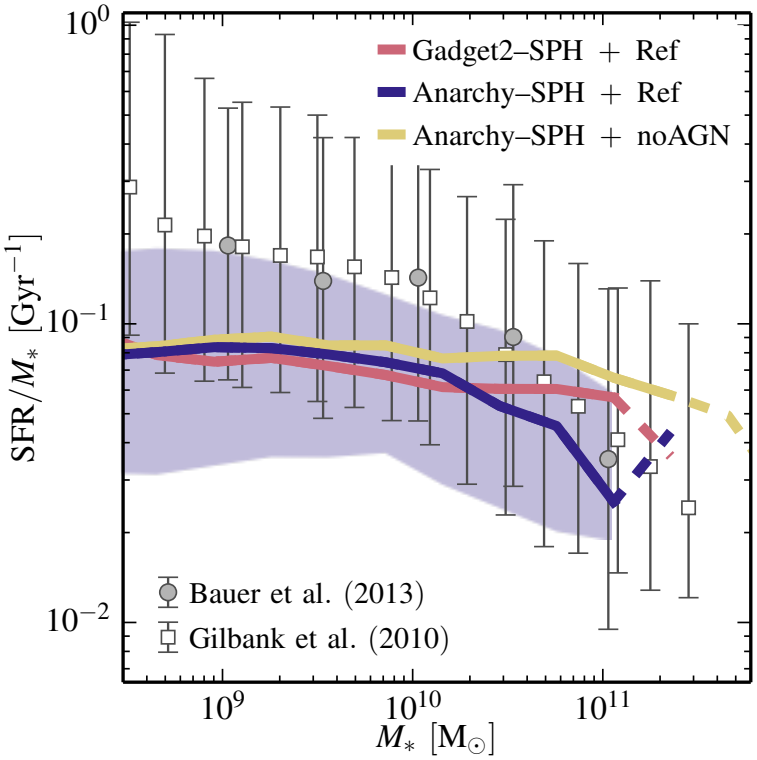

Figure 3.5: The median specific star formation rate $\dot{M}_*/M_*$, of star-forming galaxies ($\dot{M}_*/M_* > 0.01$ Gyr^{-1}) as a function of stellar mass at $z = 0.1$ in the L050N0752 ANARCHY SPH (blue line) and GADGET-2 SPH (red line) simulations. Dashed line styles are used where the simulation is sampled by fewer than 10 galaxies per 0.2 dex mass bin. The 1σ scatter about the median of the ANARCHY run is denoted by the blue shaded region. Observational data points with error bars correspond to the median and 1σ scatter of the SSFR from SDSS by (Gilbank et al., 2010, grey circles) and GAMA by (Bauer et al., 2013, white squares). Galaxies with $M_* > 2 \times 10^{10}$M$_\odot$ have a significantly higher specific star formation rate in the GADGET SPH simulation than in the ANARCHY SPH one, but the decrease is smaller than when AGN activity is turned off (yellow line).

simulated population at masses for which there are at least 100 particles at the median SSFR (see Schaye et al. (2015)). The two simulations present a very different behaviour for galaxies with $M_* \gtrsim 2 \times 10^{10}\mathrm{M}_\odot$. Whilst the ANARCHY-SPH simulation follows the trend seen in the observational data (albeit with a transition mass slightly too large), the GADGET-SPH simulation shows a constant passive fraction of $\sim 15\%$ at masses up to $M_* = 2{\times}10^{11}\mathrm{M}_\odot$. At larger masses, the fraction is 0, implying that all galaxies are star-forming, in disagreement with the data that indicates that almost all galaxies ($> 80\%$) of that mass range are passive. Note, however, that there are only 20 galaxies with $M_* > 10^{11}\mathrm{M}_\odot$ in the simulation volume and that the fractions displayed in Fig. 3.6 are, hence, affected by small number statistics. Since the ANARCHY and GADGET simulations use the same initial conditions, the comparison between the two schemes is, however, still meaningful. The comparison with a simulation using ANARCHY but excluding AGN feedback (yellow line) has qualitatively a similar effect as switching off AGN feedback.

The shortage of passive galaxies in the GADGET simulation at the high-mass end of the galaxy population and the higher SSFR for high-mass objects both indicate that the star formation quenching processes are inefficient in the largest haloes. This higher star formation rate at low redshift in high-mass haloes leads to an increase of the stellar mass of massive galaxies as was hinted by the difference in the GSMF between the two simulations at $z = 0.1$ (Fig. 3.1). AGN feedback, which is the main source of quenching in our model for galaxies with $M_* \gtrsim 2 \times 10^{10}\mathrm{M}_\odot$, seems to be insufficiently effective at quenching star formation in large haloes.

It is worth mentioning that we cannot eliminate the possibility that a re-calibration of the subgrid parameters could bring the GADGET simulation into agreement with the data. By changing the frequency of the AGN events or the temperature at which the gas is heated during such an event, it might be possible to quench star formation in large galaxies even when the GADGET formulation of SPH is used. It is, however, unclear if this could be achieved and whether subgrid parameters should be used to compensate for the shortcomings of a particular hydro scheme. Similarly, simulations run at different resolutions might lead to different conclu-

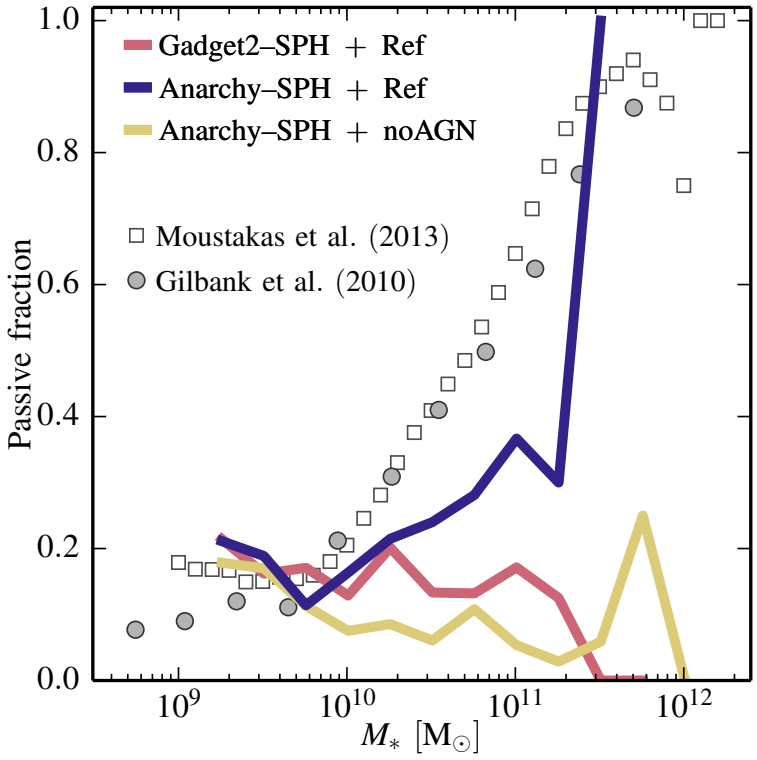

Figure 3.6: The fraction of passive galaxies ($\dot{M}_*/M_* < 0.01$ Gyr^{-1}) at $z = 0.1$ in both the L050N0752 ANARCHY SPH (blue line) and GADGET SPH (red line) simulations. We only show mass bins that correspond to 100 or more star-forming particles for the median SSFR. The grey circles and white squares correspond to the passive fraction inferred from the SDSS data by Gilbank et al. (2010) and by Moustakas et al. (2013). The passive fraction is far too low for galaxies with $M_* \gtrsim 2 \times 10^{10}M_\odot$ in the GADGET simulation, in a similar fashion to the simulation without AGN feedback (yellow line).

sions (if the subgrid parameters are kept fixed). Note that simulations run at a lower resolution (such as the low-redshift versions of OWLS Schaye et al. (2010) and cosmo-OWLS (Le Brun et al., 2014)) have fewer resolution elements in the haloes and may hence not suffer as much from the lack of phase mixing. A full exploration of the subgrid model parameter space or a comprehensive resolution study are, however, beyond the scope of the present chapter.

The effectiveness of the AGN feedback can be related to the state of the gas surrounding the galaxies and in the whole halo. The difference can be understood as follows. The accretion of cold gas onto the galaxies from filaments is the key source of fresh material from which stars can be formed in those haloes. The AGN will sustain a hot halo in which these filaments will dissolve. It is likely that the spurious surface tension that plagues the density-entropy formulation of SPH used in GADGET does not leave the gas in the hot halo in a state where the AGN activity can be effective at stopping star formation. An example of these issues would be that the inability for dense gas blobs to dissolve in a hot halo medium (see for instance the "blob test" problem by Agertz et al. (2007)) could allow cold pristine gas in filaments to survive the hot bubbles created by the AGN activity and feed the galaxy with gas ready to form stars. The better phase-mixing ability of the ANARCHY formulation of SPH is more effective at disrupting infalling filaments and preventing them from reaching the galaxies, making the AGN-driven bubbles effective at stopping star formation. In this scenario, the issue is not generated by an AGN being unable to sustain a hot halo (we will show that hot haloes are present in both cases), it is rather that the pristine gas forms clumps that are unstable and cool rather than being mixed in. The next section explores more the differences in gas properties of the two simulations.

3.4 Large- and small-scale gas distribution

In the previous section, we showed that the masses and sizes of galaxies are only marginally affected by the improvements to the hydrodynamics scheme made in

the ANARCHY flavour of SPH. We also showed, however, that the star formation rate in massive galaxies is significantly affected by these same improvements and argued that some of the differences might be directly related to the way in which the different SPH schemes treat the gas in large haloes. In this section, we explore this possibility by studying the state of the gas both outside and inside haloes. We will especially focus on the largest systems, where the dynamical time is similar to the cooling time, and hence the hydrodynamic forces become important.

3.4.1 Gas in large-scale structures

A simple diagnostic of the state of the gas in a simulation is the distribution of the SPH particles or grid cells in the density-temperature plane. The different components (ISM, IGM, etc.) can then be identified and their relative abundance in terms of mass or volume estimated. Since the ANARCHY and GADGET formulations behave differently when different phases are in contact or in the presence of a shock, it is worth analysing the differences created by those schemes. In order to minimize the impact of the subgrid models on the distribution of the gas, we start by looking at the gas in the inter-halo medium, i.e. the gas outside of haloes. Most of the gas that is located outside of haloes has never been in contact with star forming regions or with the winds driven by AGN and star formation. We are hence focusing on the pristine gas before it falls onto haloes. This should allow us to consider differences driven mostly by the two flavours of the hydrodynamics scheme.

The haloes have been identified using the FoF algorithm and are hence typically larger than the commonly given virial radii. This ensures that we are not considering particles that are gravitationally bound to any resolved haloes. In both our simulations, we only identify haloes that have more than 32 particles, effectively imposing a minimum halo mass of $M_{\rm FoF} = 3.1 \times 10^8 {\rm M}_\odot$. This analysis is resolution dependent via the definition of the minimum halo mass resolved by the simulation. If the resolution were increased, one would find smaller haloes, meaning that some of the particles that we identify as being outside of any halo will become part of small haloes. However, small haloes are unlikely to host large amounts of star for-

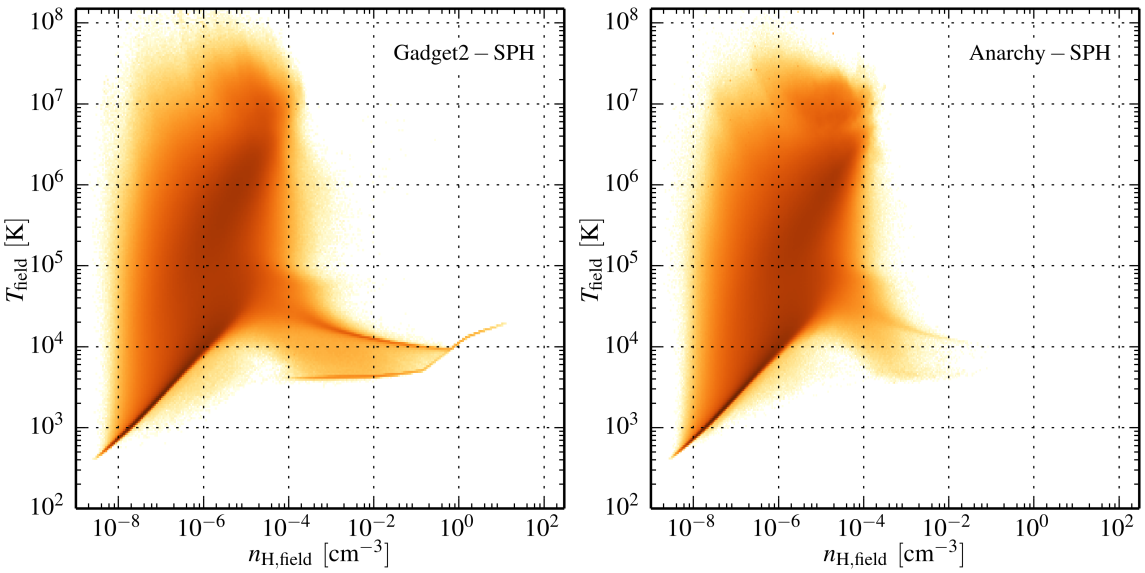

Figure 3.7: The mass-weighted distribution of gas outside of collapsed structures in the density-temperature plane. The left panel shows the $z = 0$ distribution for the GADGET SPH simulation whereas the right panel shows the equivalent distribution for the ANARCHY SPH simulation. The GADGET SPH run displays high-density gas on the imposed equation of state whilst there is no gas in the ANARCHY SPH run above a density of $n_{\rm H} > 10^{-1}{\rm cm}^{-3}$. Dense star forming gas is mixing with the lower density higher temperature medium in the ANARCHY SPH run, whilst the artificial surface tension introduced by the GADGET SPH formulation forbids this gas from dissolving and leads to star formation outside of the haloes.

mation and drive enrichment and feedback. As both simulations have been run at the same resolution with the same initial conditions, the same objects will collapse and form haloes, ensuring that our one-to-one comparison is not compromised by the potential presence of smaller unresolved structures.

In Fig. 3.7, we show the distribution of the gas outside of all FoF groups in the density-temperature plane at $z = 0$ for the GADGET-SPH left panel) and ANARCHY-SPH (right panel). The low-density material ($n_{\rm H} < 10^{-4}$ cm^{-3}) is in a very similar state in both simulations with an extended distribution of diffuse material spanning more than 4 orders in magnitude in temperature. The highest temperature material has been heated by feedback activity and blown out of

the haloes in both simulations. Differences start to appear at intermediate densities ($10^{-4}\ \mathrm{cm}^{-3} < \mathrm{n_H} < 10^{-1}\ \mathrm{cm}^{-3}$). A lot more mass resides in that regime in the simulation using the GADGET formulation of SPH. Because of the artificial surface tension appearing in GADGET-SPH between different phases in contact discontinuities, this dense gas is unable to properly mix with the lower density, higher temperature material surrounding it. In the ANARCHY simulation, the use of both the Pressure-Entropy formulation of the SPH equations and of a (small numerical) diffusion term has allowed this dense gas to dissolve into its surroundings. The difference is even more striking at higher densities ($n_\mathrm{H} > 10^{-1}\ \mathrm{cm}^{-3}$), where no gas is present in the ANARCHY simulation, whilst a significant amount is present in the GADGET one. This difference is especially important since, depending on its metallicity, some of this dense gas may be star-forming. Star formation is hence taking place outside of collapsed structures in the simulation using GADGET. Interestingly, this high-density gas also has a high metallicity ($Z \gtrsim 0.1 Z_\odot$). This gas has thus been ejected from haloes after having been enriched by star formation. In ANARCHY-SPH, similar material would likely be dissolved into the lower-density medium either, outside haloes or in winds inside haloes.

3.4.2 Extragalactic gas in haloes

Within haloes differences in the density-temperature diagram are best quantified by looking at the distribution of star forming gas. We define the IntraGroup Medium (IGrM) as the gas within R_{200} but outside of $30\ \mathrm{kpc}$ masks placed at the centre of each subhalo. This excludes the gas present in the ISM or close to galaxies and should leave us with a reasonable definition of the IGrM.

In Fig. 3.8, we show the star formation rate of the IGrM as a function of the halo mass M_{200} at $z = 0.1$ for objects extracted from the ANARCHY simulation (blue squares) and GADGET-SPH simulation (red circles). At masses $M_{200} \gg 10^{12}\mathrm{M}_\odot$ the simulation using the GADGET formulation of SPH contains haloes with a higher star formation rate in the IGrM than the ANARCHY simulation. The higher fraction of dense gas ($n_\mathrm{H} > 10^{-1}\ \mathrm{cm}^{-3}$) in the GADGET simulation leads to a higher IGrM

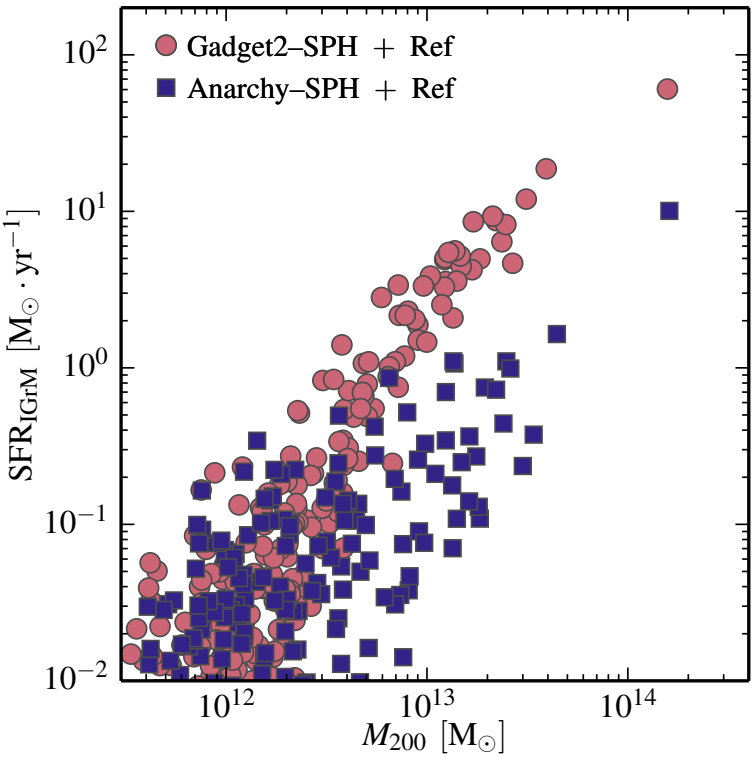

Figure 3.8: The star formation rate of the inter-group medium (IGrM) as a function of halo mass at $z = 0.1$ for the L050N0752 ANARCHY SPH (blue squares) and GADGET SPH (red circles) simulations. The IGrM is forming significantly more stars in group- and cluster-mass haloes ($M_{200} > 5 \times 10^{12}\mathrm{M_\odot}$) in the run using the GADGET SPH scheme.

star formation rate. The specific star formation of the IGrM corresponds to $\approx 5 \times 10^{-3}$ Gyr^{-1} in the GADGET simulation and is more than an order of magnitude lower ($\approx 4 \times 10^{-4}$ Gyr^{-1}) for ANARCHY. Although, these values are low when compared to the typical values for galaxies (see Fig. 3.5), the presence of significant star formation in the IGrM indicates that the AGN activity or gravitational heating is not effective enough at quenching star formation in the largest haloes.

As the haloes in the GADGET-based simulation exhibit more star formation in their IGrM and, it is interesting to investigate how the dense gas is distributed spatially. To this end, we selected the most massive halo ($M_{200} \approx 2 \times 10^{14}\mathrm{M}_{\odot}$) in both simulations and constructed column density maps of the gas. As we are mainly interested in the dense gas and to increase the clarity of the maps, we only select the gas with $n_{\mathrm{H}} > 10^{-2}$ cm^{-3}. As discussed above, the behaviour of warm diffuse medium is similar in both formulations of the SPH equations and can hence be safely discarded here.

These dense gas column density maps are shown in Fig. 3.9 for the GADGET (left panel) and ANARCHY (right panel) simulations. The large dashed circles indicate the position of the spherical overdensity radius, $R_{200} \approx 1.1$ Mpc, whilst the small solid circles indicate the innermost 100 kpc, where the effects of the central galaxies on the gas will be maximized. We will not consider this central region in the remainder of this subsection since, as was discussed in section 3.3, in this region the differences are likely to be smaller than the ones induced by small variations in the subgrid parameters.

The difference between the two maps is striking. The halo from the GADGET simulation contains a large number of dense clumps of gas at all radii, as was found in the simulations of Kaufmann et al. (2009). These clumps can be seen even inside the inner 100 kpc where feedback from both the AGN and star formation might be expected to disrupt them. These nuggets of dense gas also accompany the in-falling satellites. The map extracted from the ANARCHY simulation is much smoother and dense gas is found mostly in the wakes of in-falling satellite galaxies following their stripping. ANARCHY's ability to mix phases in contact discontinuity allows dense

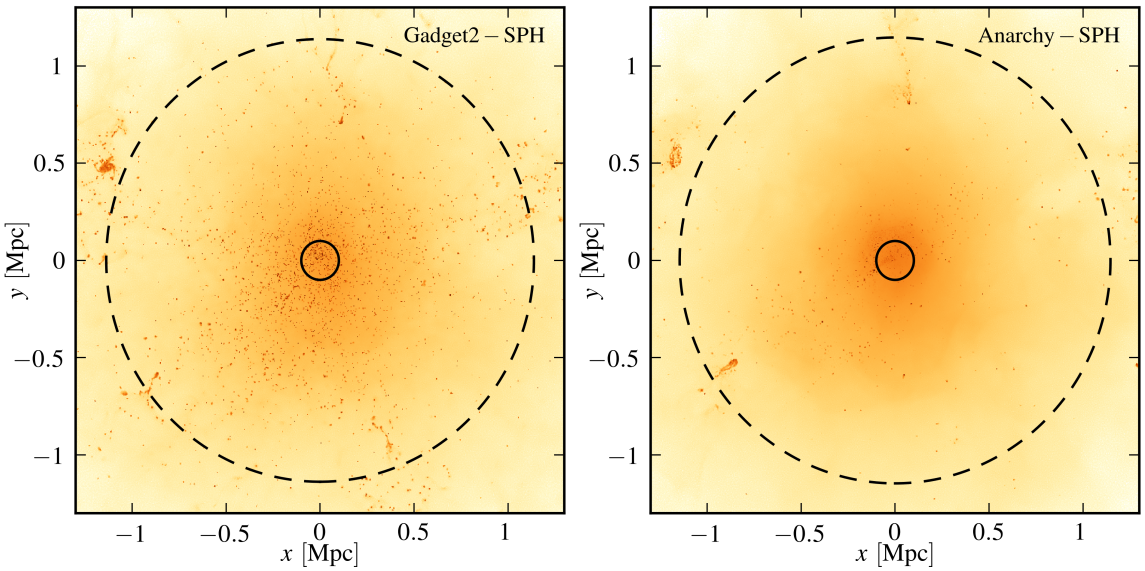

Figure 3.9: Maps of the column density of dense gas ($n_{\rm H} > 0.01\ {\rm cm}^{-3}$) in the largest haloes ($M_{200} \approx 2 \times 10^{14} {\rm M}_{\odot}$) of the L050N0752 GADGET SPH (left panel) and ANARCHY SPH (right panel) simulations. The large dashed circle shows the location of the overdensity radius R_{200}, whilst the small solid circle in the centre encloses the inner $100\ {\rm kpc}$. The halo in the GADGET SPH run contains a significant number of dense clumps of gas, as was found by Kaufmann et al. (2009) in their simulations, while its counterpart in the ANARCHY SPH run displays a much smoother gas distribution. The spurious surface tension appearing in the GADGET formulation of SPH makes it difficult for the dense gas stripped from the in-falling satellites to be disrupted and mixed into the IGrM.

clumps to get dissolved into the hot halo, whereas the spurious surface tension that appears between phases in GADGET SPH allows them so survive and perhaps even grow. Since some clumps reach densities that exceed the threshold for star formation, some of them will increase the SF rate of the IGrM. The flavour of SPH has, here, a direct consequence on the observables extracted from the simulation.

An other observable that may be affected by the choice of hydrodynamics scheme is the gas fraction. In Fig. 3.10, we show the result of mock X-ray observations of our haloes. Following the method described in Le Brun et al. (2014), we realise mock X-ray observations of our haloes and, assuming hydrostatic equilibrium, infer the halo mass and gas fraction following the same analysis applied to observational data. For comparison, we show data from Vikhlinin et al. (2006), Maughan et al. (2008), Sun et al. (2009), Pratt et al. (2009) and Lin et al. (2012). We only selected clusters at $z < 0.25$. As was discussed by Schaye et al. (2015), the simulation using the ANARCHY flavour of SPH (blue squares), the Ref model of EAGLE, overshoots the data. This indicates either that the amount of X-ray gas in these haloes is too high or that the gas is in the wrong thermodynamic state. This motivated Schaye et al. (2015) to introduce an alternative model (labelled AGNdT9) for which the mock-observation inferred gas fractions are in better agreement with the data. This model uses more sparse, but also more energetic AGN heating event and is shown in Fig. 3.10 using yellow triangles[4].

Interestingly, the EAGLE Ref model using the GADGET version of SPH (red triangles) yields results that are very similar to the improved AGNdT9 model combined with ANARCHY-SPH. The gas fractions are in reasonable agreement with the observational data. The analysis of the dense gas maps and the following discussion indicates that this better agreement is mostly accidental and not a success of the model. The X-ray inferred gas fractions are driven down by a change in the gas mass in the haloes but also by the presence of cold and dense gas in the IGrM

[4]We note that the column density of dense gas map (Fig. 3.9) of the largest halo in this model is very similar to the one using the Ref model and ANARCHY code (right panel). There is no large pool of dense gas clumps floating in the halo.

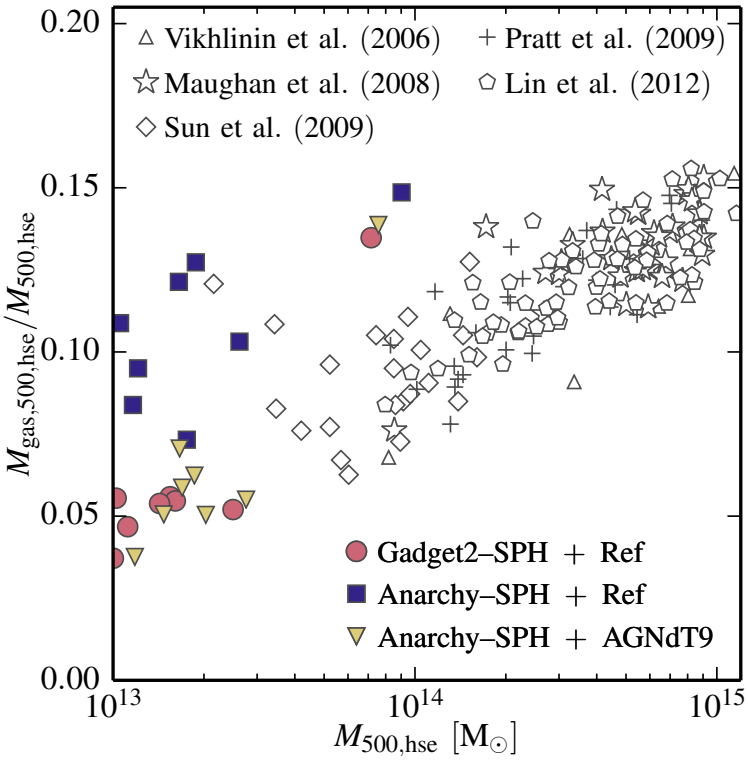

Figure 3.10: The $z = 0$ gas fractions within $R_{500,\rm hse}$ as a function of $M_{500,\rm hse}$ inferred from virtual X-ray observations of the L050N0752 ANARCHY SPH (blue squares) and GADGET SPH (red circles) simulations. Data points correspond to measurements from Vikhlinin et al. (2006) (triangles), Maughan et al. (2008) (stars), Sun et al. (2009) (diamonds), Pratt et al. (2009) (crosses) and Lin et al. (2012) (pentagons). The ANARCHY SPH Ref model overpredicts the gas fractions for group-sized objects but this can be solved by using the AGNdT9 model (yellow triangles). The haloes of the GADGET SPH run are in better agreement with the data as a result of their higher fraction of cold gas that artificially reduces the X-ray inferred gas fractions.

that does not emit any X-ray and hence artificially reduces the inferred gas masses. The cold clumps lead to the star formation seen in Fig. 3.7. We note, however, that these spurious undisrupted clumps of dense gas are unlikely to affect simulations of the IGrM done at lower resolution such as those of McCarthy et al. (2010) or Le Brun et al. (2014).

The significant difference in star formation rates in massive haloes seen between the two formulations of SPH can have consequences on quantities that are directly observable. An example of such an observable is the I-band luminosity of the clusters (e.g. Sanderson et al., 2013). For galaxies with similar masses and metallicities (as is the case when comparing matched pairs of galaxies extracted from both our simulations), a higher I-band luminosity indicates a younger population of stars and a higher star formation rate over the last billion years. In Fig. 3.11, we show the I-band luminosity as a function of halo mass $M_{500,\mathrm{hse}}$. The values are computed by generating mock-observations of our haloes as described by Le Brun et al. (2014). Their procedure allows us to compute the halo mass and radius assuming hydro-static equilibrium as is done in observations of actual clusters. The (Cousin) I-band luminosity is computed within $R_{500,\mathrm{hse}}$, the overdensity radius inferred by assuming in the mock observations by assuming hydrostatic equilibrium. For comparison, we show observational data taken from Sanderson et al. (2013), Gonzalez et al. (2013) and Kravtsov et al. (2014) as well as the SDSS image stacking result of Budzynski et al. (2014). In all cases we selected only clusters at $z < 0.25$.

As expected from the previous analysis of the star formation rates, we find that the I-band luminosity in the groups and clusters extracted from the simulation using the GADGET flavour of SPH is higher than when using ANARCHY. It is also higher than the observational data as expected from our analysis of the specific star formation rate and the passive fraction for massive ($M_* > 10^{11}\mathrm{M}_\odot$) galaxies. In the same figure, we also show the cluster luminosities extracted from the simulation using the AGNdT9 model and the ANARCHY SPH scheme. The I-band luminosity as a function of mass for that model is very similar to the one obtained using the Ref model. The differences between the GADGET and ANARCHY based simulations

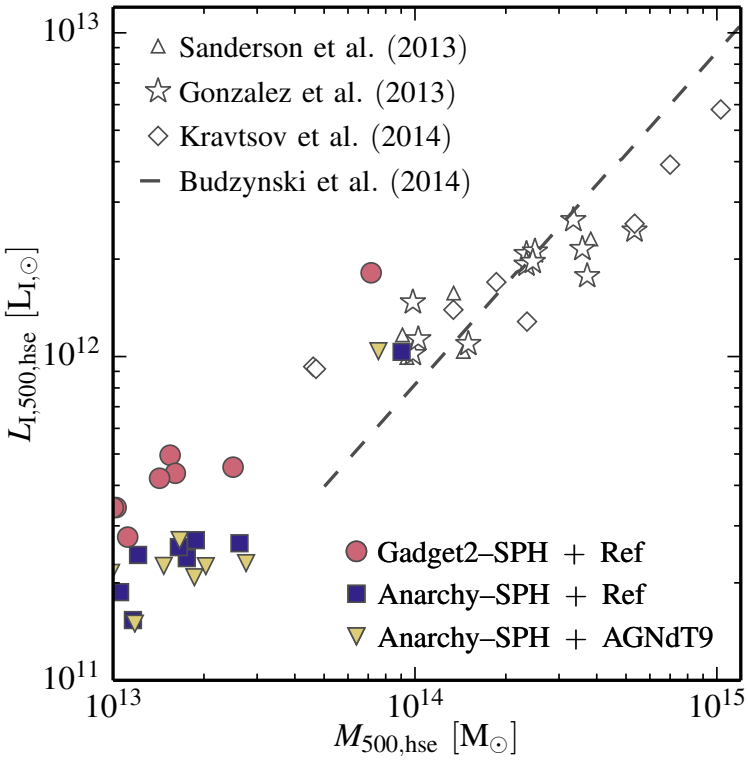

Figure 3.11: I-Band luminosity within $R_{500,\mathrm{hse}}$ as a function of $M_{500,\mathrm{hse}}$ at $z = 0$ in the L050N0752 ANARCHY SPH (blue squares) and GADGET SPH (red circles) simulations. Data points correspond to the observations of Sanderson et al. (2013) (triangles), Gonzalez et al. (2013) (stars), Kravtsov et al. (2014) (diamonds) and the dashed line represents the SDSS image stacking results of Budzynski et al. (2014). Where necessary, observations were converted to the I-band following Le Brun et al. (2014). The yellow triangles show the haloes extracted from the L050N0752 ANARCHY SPH run with an improved AGN model (AGNdT9). The GADGET SPH run overestimates the I-band luminosity in the group- and cluster-size objects as expected from the absence of passive galaxies in that simulation.

are much larger. However, as discussed earlier, changing the model parameters for feedback from star formation will have a larger effect.

3.4.3 ISM and CGM gas

We now turn to the gas inside galaxies or in their direct vicinity. The state of this gas will retain some of the properties of the IGrM but will also be directly affected by the subgrid models.

We first focus on the cold and dense phase of the gas. With the help of careful simulations using radiative transfer, Rahmati et al. (2013) showed that cold ($T < 10^{4.5}$ K) and dense ($n_{\rm H} > 0.01$ cm^{-3}) gas was a good proxy for HI gas. They provide a fitting function to compute HI but for the purpose of this chapter, setting the HI fraction to 1 for all this cold and dense gas is a sufficiently good proxy. In Fig. 3.12, we show the mass function of the HI gas in the ANARCHY (blue line) and GADGET (red line) simulations. We use dashed lines when the mass bins contain fewer than 10 objects and dotted lines when the HI mass corresponds to fewer than 300 SPH particles. We measured the HI mass using fixed spherical apertures placed at the centre of each subhalo in order to only select the gas in the ISM and circumgalactic medium (CGM). As a point of reference, we show the best-fitting Schechter functions to the data of Haynes et al. (2011) (ALFALFA survey) and Zwaan et al. (2003) (HIPASS survey). As expected from the non-disruption of cold gas in the hot halo, there is an over-abundance of massive HI objects in the simulation using the GADGET variant of SPH. Whilst the simulation using ANARCHY is in reasonable agreement with the observations, the same model using GADGET overshoots the break in the mass function and vastly over-predicts the abundance of HI clouds of mass $M_{\rm HI} > 10^{10}$ M$_\odot$. Both simulations under-predict the abundance of low mass ($M_{\rm HI} \lesssim 2 \times 10^9$ M$_\odot$) HI clouds. As is shown by Crain et al. (in prep) for ANARCHY, this is a resolution effect. Simulations run with both flavours of SPH exhibit the same behaviour in that regime and can then likely be rescued in a similar way by increased resolution. The discrepancy at the high-mass end is another sign that the densest gas clumps found in the group and cluster-like haloes are not

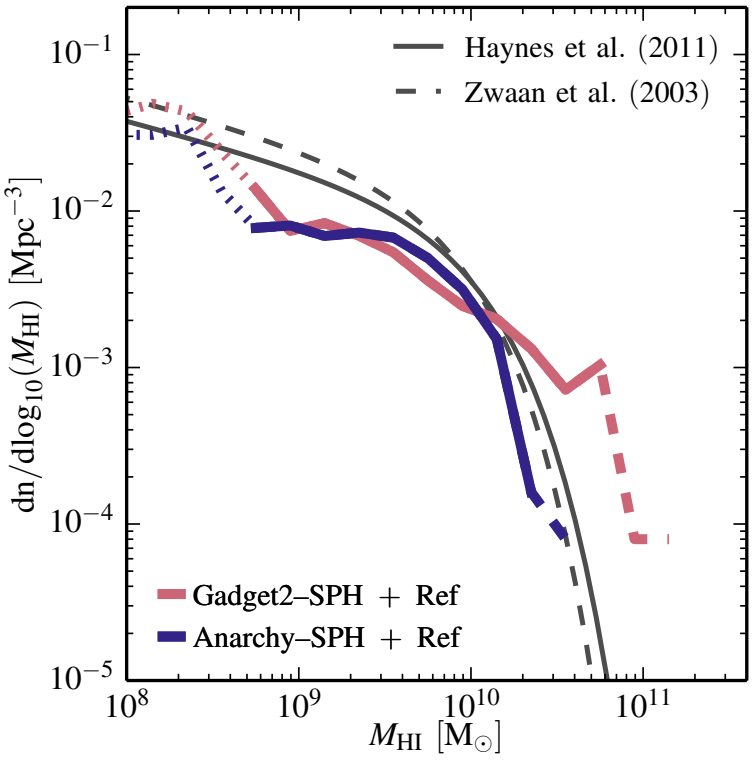

Figure 3.12: The mass function of HI-like gas (gas with $n_{\mathrm{H}} > 0.01$ cm^{-3}, T $< 10^{4.5}$ K) in the L050N0752 ANARCHY SPH (blue line) and GADGET SPH (red line) simulations. Curves are drawn with dotted lines below a mass scale of 300 star particles, and a dashed line style where sampled by fewer than 10 galaxies per 0.2 dex mass bin. The solid and dashed grey lines show the best-fitting Schechter fits to the ALFALFA data by Haynes et al. (2011) and HIPASS data by Zwaan et al. (2003), respectively. The simulation using the GADGET SPH formulation overestimates the abundance of massive HI clouds.

disrupted by the hot halo. They also seem to survive AGN activity and the effect of stellar feedback. These large pools of cold gas in massive haloes are not observed and are likely to be responsible for the spurious star formation seen in the largest galaxies (Figs. 3.5 and 3.6). We note that a modification of the AGN subgrid model could disrupt those clouds without breaking other constraints imposed on the model. However, it seems unlikely that this purely numerical issue can be completely alleviated. Furthermore, the abundance of spurious cold clumps will increase with the resolution (as larger fluctuations in the density distribution can be sampled), implying that the AGN activity needed to suppress them will also have to be modified. One possible solution would be the increase of the heating temperature $\Delta T_{\rm AGN}$ to larger values but that would also lead to a poorer time sampling and much rarer events. A temperature increase is also likely to lead to other numerical issues since only very short time-steps could then be used for the gas phase in order to properly propagate the resulting shock waves.

Another consequence of the presence of large pools of dense gas inside galaxies is the lower efficiency of feedback that this creates. A feedback event taking place in a medium with a density higher than the threshold given by equation 2.7 will experience numerical radiative losses and potentially do only little work on the gas. This will hence, limit the quenching efficiency of this feedback. For our choice of parameters, this threshold is $n_{\rm H,tc} = 6.1\ {\rm cm}^{-3}$ (Eqn. 2.7). In Fig. 3.13, we show the distribution of densities of the medium in which stars are born and hence will attempt to quench through feedback. The red and blue solid lines correspond to the simulations using GADGET-SPH and ANARCHY-SPH respectively. To better highlight the differences, we also show the cumulative distributions using dashed lines. The threshold for efficient feedback is depicted as a vertical dotted line. Crain et al. (2015) studied this distribution for different subgrid models in the EAGLE suite and found that it was a powerful diagnostic to discriminate between models that do or do not present over-cooling problems.

The simulation using GADGET as its hydro solver displays a slightly larger fraction of stars born in environments where the feedback will be inefficient (especially

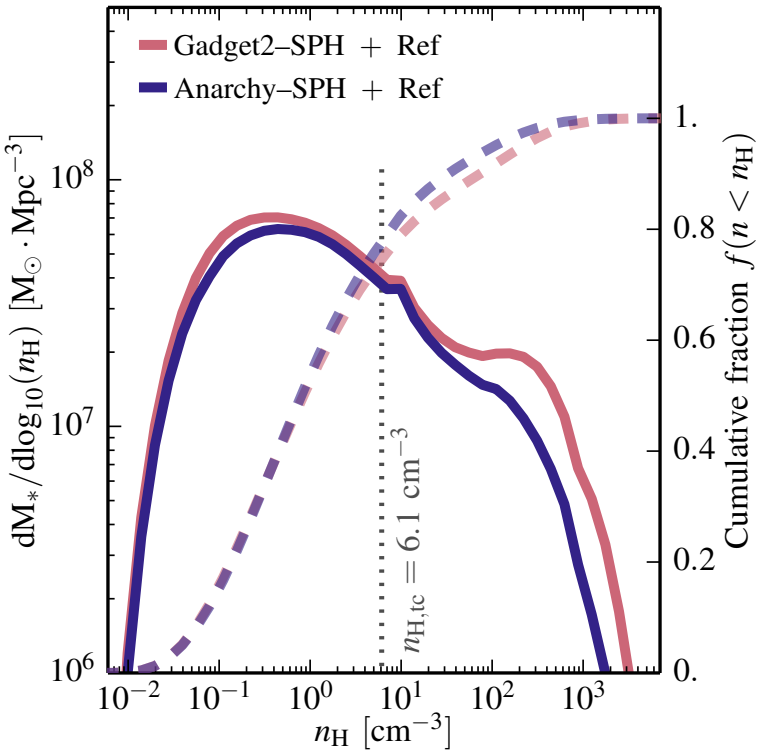

Figure 3.13: Differential (solid lines, left axis) and cumulative (dashed lines, right axis) distribution of the densities of SPH particles at the instant they were converted to star particles, in both the L050N0752 ANARCHY SPH (blue) and GADGET SPH (red) simulations. The vertical dotted line indicates the critical density for numerically efficient feedback $n_{\mathrm{H,tc}} = 6.1\ \mathrm{cm}^{-3}$ (equation 2.7). The simulation using the GADGET SPH formulation forms a larger fraction of its stars in denser environments, where the thermal feedback is numerically inefficient.

at $n_{\rm H} > 20\,{\rm cm}^{-3}$). The difference with the ANARCHY simulation is smaller than the differences seen between various subgrid models. This is expected since a large difference in this distribution will lead to a large difference in the galaxy mass-size relation as well as in the build-up of stellar mass across cosmic time (Crain et al., 2015). The larger fraction of stars formed in dense medium is a sign that the star formation rates in the run using GADGET-SPH will be higher as the quenching efficiency of feedback is lower. So, not only is the AGN feedback ineffective at disrupting dense gas clouds, it also impacts the quenching efficiency of the stellar feedback. The hot halo prevents the accumulation of cold gas in the central galaxies only if this in-falling material can dissolve in the IGrM. If this dense material penetrates the galaxy, stellar feedback taking place in the clumps will be less efficient. This may explain why galaxies with $M_* \approx 3 \times 10^{10}{\rm M}_\odot$, that are typically by a combination of both stellar and AGN feedback, display a higher SFR in the GADGET simulation than in the ANARCHY based one.

3.5 Summary & Conclusion

The aim of this study was to investigate the effects of the improved hydrodynamics solver and time stepping used for the EAGLE suite of simulations (Schaye et al., 2015; Crain et al., 2015). By running the same simulation without re-calibrating the subgrid model parameters with both EAGLE's ANARCHY and the standard GADGET formulations of the SPH equations, we were able to isolate the effects of the hydrodynamics solver. Thanks to the use of the pressure-entropy formulation of SPH (Hopkins, 2013), of a more stable kernel function (Dehnen & Aly, 2012), of a small amount of numerical diffusion (Price, 2008) and of an improved viscosity switch (Cullen & Dehnen, 2010), the ANARCHY flavour of SPH is able to reproduce a large set of hydrodynamical tests more accurately than the GADGET flavour (Dalla Vecchia (in prep.)). The better mixing of gas phases implied by this changes as well as the improved treatment of viscosity in shear flows are likely to affect the simulation of haloes and galaxies. Our analysis of the differences can be summarized as

follows:

1. Except for the most massive objects, the masses and sizes of the simulated galaxies are largely unaffected by the choice of SPH flavour. Uncertainties in the subgrid parameters lead to much larger differences.

2. The absence of the Durier & Dalla Vecchia (2012) time-step limiter leads to somewhat more efficient feedback, as expected from the non-conservation of energy occurring in feedback events when the limiter is neglected.

3. The star formation rates of galaxies in small haloes, where the cooling time is smaller than the dynamical time, are unaffected by the change of hydrodynamics scheme. However, in haloes where those time scales are similar, the star formation rates are higher in the simulation using GADGET SPH. These differences in behaviour can be related to the lower quenching power of the AGN activity in that simulation. The lack of phase mixing, coming from the spurious artificial surface tension appearing at contact discontinuities, prevents cold dense gas from dissolving into the hot halo.

4. This cold dense gas then reaches the central galaxies and leads to increased star formation in both the central galaxies and intragroup medium. This also leads to a lower hot gas fraction in the haloes.

Our results indicate that the improved hydrodynamics scheme plays a significant role in the parts of cosmological simulations where the cooling time exceeds the dynamical time, such as in hot hydrostatic gas haloes. Our results are resolution dependent and it is possible that simulations performed at much higher resolution will be more sensitive to the accuracy of the hydrodynamics solver. Finally, we also stress that some of the differences between the simulations could potentially be cancelled by changing the value of some of the subgrid parameters.

Chapter 4

Baryon effects on the internal structure of ΛCDM halos

4.1 Introduction

The development of efficient computational techniques and the growing availablity of computing power over the past three decades have made it possible to simulate the evolution of representative cosmological volumes at high enough resolution to follow the formation of cosmic structures over many orders of magnitude in mass.

One of the best established and most robust results from this programme is the characterization of the density structure of dark matter (DM) halos in equilibrium whose spherically averaged density profile, $\rho(r)$, is nearly universal in shape and obeys simple scaling relations (Navarro et al., 1996b; Navarro et al., 1997). The functional form of this "NFW" radial profile is independent of mass, formation redshift, and cosmological parameters and has the form:

$$\frac{\rho(r)}{\rho_{\rm cr}} = \frac{\delta_{\rm c}}{(r/r_{\rm s})\,(1+r/r_{\rm s})^2}, \tag{4.1}$$

where $\rho_{\rm cr}$ is the critical density of the Universe, $\delta_{\rm c}$ a characteristic density and $r_{\rm s}$ a characteristic radius. Navarro et al. (1997) showed that these two scale parameters are strongly correlated and that the characteristic density is proportional to the density of the universe at the time when the halo was assembled. This proportionality constant or, equivalently, the proportionality constant between halo mass

and concentration has been studied by many authors (e.g. Avila-Reese et al., 1999; Jing, 2000; Bullock et al., 2001; Eke et al., 2001; Zhao et al., 2003; Neto et al., 2007; Duffy et al., 2008; Gao et al., 2008; Navarro et al., 2010; Ludlow et al., 2014; Dutton & Macciò, 2014). The validity of the model is well established and a physical understanding of the universality of the profile is beginning to emerge (Ludlow et al., 2013; Correa et al., 2015a,b).

The nearly scale-free behaviour induced by gravity applies only to halos made entirely of DM. In practice, halos of mass above $\sim 10^9\ \mathrm{M}_\odot$ participate in the process of galaxy formation. The cooling and dissipation of gas in these halos introduces a characteristic scale that breaks self-similarity (White & Rees, 1978; White & Frenk, 1991) and the subsequent formation of stars can deepen the potential well and modify the structure of the halo in this region.

One of the early models of the effects of baryon collapse on the structure of a halo, making use of adiabatic invariants, concluded that halos would become denser in their centres (Blumenthal et al., 1986). These simple models, however, were later shown not to match hydrodynamic simulations and led to a more general framework for calculating adiabatic contraction based on the average radial distribution of particles (Gnedin et al., 2004; Gustafsson et al., 2006). The parameters of this model, however, have been shown to depend on halo mass, redshift and on the details of the hydrodynamic simulation, making analytical descriptions of adiabatic contraction complex and uncertain (Duffy et al., 2010).

Baryons, however, can also produce the opposite effect and induce expansion rather than contraction of the halo. Using idealized hydrodynamic simulations, Navarro et al. (1996a) showed that the rapid expulsion of gas that had previously cooled to very high density near the centre of a halo could generate a central core. Subsequent work using cosmological simulations has confirmed and extended this result (e.g. Read & Gilmore, 2005; Dehnen, 2005; Mashchenko et al., 2006; Governato et al., 2010; Pontzen & Governato, 2012; Teyssier et al., 2013; Martizzi et al., 2013).

The structure of the inner halo is often used as a test of the ΛCDM paradigm

(e.g. Sand et al., 2002; Gilmore et al., 2007). Such tests, however, tend to compare observations of halos which have galaxies within them with results from simulations of pure dark matter halos (Newman et al., 2013a). For the tests to be meaningful, accurate and reliable calculations of how baryons affect the structure of the halos are essential. Such calculations are also of major importance for efforts to detect DM experimentally, either directly in the laboratory, or indirectly through the products of particle decay or annihilation.

Simulating the evolution of the visible components of the universe is a much more complex task than simulating the evolution of the DM because baryons undergo a variety of astrophysical processes many of which are relatively poorly understood. The resolution that is attainable even with the largest computers today is insufficient for an *ab initio* calculation of most of these processes which, as a result, need to be treated through parametrized "subgrid" models added to the coupled hydrodynamical and gravitational evolution equations. These models describe the effects of radiative cooling, star formation, feedback from energy liberated during the evolution of stars and supermassive black holes growing at the centres of galaxies. Simulations that include some or all of these processes have shown that significant changes can be induced in the total masses of halos (Sawala et al., 2013, 2014a; Cusworth et al., 2014; Velliscig et al., 2014; Vogelsberger et al., 2014) and in their inner structure (e.g. Gnedin et al., 2004; Pedrosa et al., 2009; Duffy et al., 2010; Pontzen & Governato, 2012; Brook et al., 2012; Di Cintio et al., 2014).

In this chapter we investigate how baryon physics modifies the structure of DM halos in the Evolution and Assembly of Galaxies and their Environment (EAGLE) cosmological hydrodynamical simulations (Schaye et al., 2015). An important advantage of these simulations is that they give a good match to the stellar mass function and and to the distribution of galaxy sizes over a large range of stellar masses ($(10^8 - 10^{11.5})$ $\mathrm{M}_\odot$). Furthermore, the relatively large volume of the reference EAGLE simulation provides a large statistical sample to derive the halo mass function in the mass range $(10^9 - 10^{14})$ $\mathrm{M}_\odot$ and to investigate the radial density profiles of halos more massive than $10^{11}\mathrm{M}_\odot$.

This chapter is organised as follows. In Section 4.2 we introduce the simulations and describe the selection of halos. In Section 4.3 we focus on the change in the mass of halos induced by baryon processes and the effect this has on the halo mass function. In Section 4.4 we analyse the radial density profile of the halos and decompose them according to their different constituents. We fit the total matter profile with a universal formula that accounts for deviations from the NFW profile and show that the best fit parameters of these fits correlate with the mass of the halo. Our main results are summarized in Section 4.5. All our results are restricted to redshift $z = 0$ and all quantities are given in physical units (without factors of h).

4.2 The simulations

The simulations analysed in this chapter were run as part of a Virgo Consortium project called the Evolution and Assembly of Galaxies and their Environment (EAGLE; Schaye et al. 2015). The EAGLE project consists of simulations of ΛCDM cosmological volumes with sufficient size and resolution to model the formation and evolution of galaxies of a wide range of masses, and also include a counterpart set of dark matter-only simulations of these volumes. The galaxy formation simulations include the correct proportion of baryons and model gas hydrodynamics and radiative cooling. State-of-the-art subgrid models are used to follow star formation and feedback processes from both stars and AGN. The parameters of the subgrid model have been calibrated to match certain observables as detailed in Schaye et al. (2015). In particular, the simulations reproduce the observed present day stellar mass function, galaxy sizes and many other properties of galaxies and the intergalactic medium remarkably well. These simulations also show the correct trends with redshift of many galaxy properties (Schaye et al., 2015; Furlong et al., 2015).

The simulations were run using an extensively modified version of the code GADGET-3 (Springel et al., 2008a), which is essentially a more computationally efficient version of the public code GADGET-2 described in detail by Springel (2005).

GADGET uses a Tree-PM method to compute the gravitational forces between the N-body particles and implements the equations of hydrodynamics using Smooth Particle Hydrodynamics (SPH, Monaghan, 1992; Price, 2012).

The EAGLE version of GADGET-3 uses an SPH implementation called ANARCHY (Dalla Vecchia in prep.), which is based on the general formalism described by Hopkins (2013), with improvements to the kernel functions (Dehnen & Aly, 2012) and viscosity terms (Cullen & Dehnen, 2010). This new implementation of SPH alleviates some of the problems associated with modelling contact discontinuities and fluid instabilities. As discussed by Dalla Vecchia (in prep.), the new formalism improves on the treatment of instabilities associated with cold flows and filaments and on the evolution of the entropy of hot gas in halos. The timestep limiter of Durier & Dalla Vecchia (2012) is applied to ensure good energy conservation everywhere, including regions disturbed by violent feedback due to supernovae and AGN. The impact of this new hydrodynamics scheme on our galaxy formation model is discussed in Chapter 3.

The analysis in this chapter focusses on two simulations: the Ref-L100N1504 simulation introduced by Schaye et al. (2015), which is the largest EAGLE simulation run to date, and its counterpart dark matter-only simulation, DM-L100N1504. To investigate smaller mass halos and test for convergence in our results we also analyse the higher resolution Recal-L0025N0752 simulation (and its dark matter-only counterpart) in which some of the sub-grid physics parameters were adjusted to ensure that this calculation also reproduces the observed galaxy stellar mass function, particularly at the low-mass end, as discussed by (Schaye et al., 2015). We will refer to the two simulations with baryon physics as "EAGLE" simulations and to the ones involving only dark matter as "DMO" simulations.

The main EAGLE simulation models a cubic volume of side-length $100\ \mathrm{Mpc}$ with 1504^3 gas and 1504^3 dark matter particles to redshift $z = 0$. A detailed description of the initial conditions is given in Schaye et al. (2015). Briefly, the starting redshift was $z = 127$; the initial displacements and velocities were calculated using second order Lagrangian perturbation theory with the method of Jenkins

(2010); the linear phases were taken from the public multiscale Gaussian white noise field, Panphasia (Jenkins, 2013); the cosmological parameters were set to the best fit ΛCDM values given by the *Planck-1* data (Planck Collaboration et al., 2014): $[\Omega_{\rm m}, \Omega_{\rm b}, \Omega_\Lambda, h, \sigma_8, n_s] = [0.307, 0.04825, 0.693, 0.6777, 0.8288, 0.9611]$; and the primordial mass fraction of He was set to 0.248. These choices lead to a dark matter particle mass of $9.70 \times 10^6 {\rm M}_\odot$ and an initial gas particle mass of $1.81 \times 10^6 {\rm M}_\odot$. We use a comoving softening of 2.66 kpc at early times, which freezes at a maximum physical value of 700 pc at $z = 2.8$. The Recal-L0025N0752 simulation follows 752^3 gas and 752^3 DM particles in a 25 Mpc volume assuming the same cosmological parameters. This implies a DM particle mass of $1.21 \times 10^6 {\rm M}_\odot$ and an initial gas mass of $2.26 \times 10^5 {\rm M}_\odot$. The softening is 1.33 kpc initially and reaches a maximum physical size of 350 pc at $z = 0$.

The DMO simulations, DM-L100N1504 and DM-L0025N0752, follow exactly the same volume as EAGLE, but with only 1504^3 and 752^3 collisionless dark matter particles, each of mass $1.15 \times 10^7 {\rm M}_\odot$ and $1.44 \times 10^6 {\rm M}_\odot$, respectively. All other cosmological and numerical parameters are the same as in the EAGLE simulation.

4.2.1 Baryonic physics

The baryon physics in our simulation correspond to the *Ref* EAGLE model. The model, fully described in Schaye et al. (2015), is summarized here for completeness.

Star formation is implemented following Schaye & Dalla Vecchia (2008). A polytropic equation of state, $P \propto \rho^{4/3}$, sets a lower limit to the gas pressure. The star formation rate per unit mass of these particles is computed using the gas pressure using an analytical formula designed to reproduce the observed Kennicutt-Schmidt law (Kennicutt, 1998) in disk galaxies (Schaye & Dalla Vecchia, 2008). Gas particles are converted into stars stochastically. The threshold in hydrogen density required to form stars is metallicity dependent with lower metallicity gas having a higher threshold, thus capturing the metallicity dependence of the ${\rm HI} - {\rm H}_2$ phase transition (Schaye, 2004).

The stellar initial mass function is assumed to be that of Chabrier (2003) in the

range $0.1\mathrm{M}_\odot$ to $100\mathrm{M}_\odot$ with each particle representing a single age stellar population. After 3×10^7 yrs all stars with an initial mass above $6\mathrm{M}_\odot$ are assumed to explode as supernovae. The energy from these explosions is transferred as heat to the surrounding gas. The temperature of an appropriate amount of surrounding gas is raised instantly by $10^{7.5}$ K. This heating is implemented stochastically on one or more gas particles in the neighbourhood of the explosion site (Dalla Vecchia & Schaye, 2012). This gas, once heated, remains coupled in a hydrodynamic sense with its SPH neighbours in the ISM, and therefore exerts a form of feedback locally that can affect future star formation and radiative cooling.

The energy injected into the gas corresponds to 10^{51} erg per supernovae times a dimensionless efficiency factor, f_E, that depends on the local gas metallicity and density. The construction of f_E and its impact on galaxy formation is discussed thoroughly by Schaye et al. (2015) and Crain et al. (2015). For a gas of metallicity, Z, and hydrogen number density, n_H, the efficiency in the reference model is:

$$f_\mathrm{E} = 0.3 + 2.7S\left(X; w\right),$$

where $w = 2/\ln 10$,

$$X = 3.35\left(\frac{Z}{0.1Z_\odot}\right)\left(\frac{0.1\ \mathrm{cm}^{-3}}{n_\mathrm{H}}\right),$$

and $S(X; w)$ is a convenient sigmoid function which varies between 0 and 1, and which we will need again in the following section. We define the sigmoid function for $x \geq 0$, $w > 0$ as

$$S(X; w) = \frac{X^w}{1 + X^w}. \tag{4.2}$$

As X varies from zero to infinity, the sigmoid function $S(X; w)$ smoothly varies between 0 and 1, taking the value of $\frac{1}{2}$ when the argument $X = 1$. The parameter w controls the rapidity of the transition between the asymptotes.

Besides energy from star formation, the star particles also release metals into the ISM through three evolutionary channels: type Ia supernovae, winds and supernovae from massive stars, and AGB stars using the method discussed in Wiersma et al. (2009b). The yields for each process are taken from Portinari et al. (1998),

Marigo (2001) and Thielemann et al. (2003). Following Wiersma et al. (2009a), the abundances of the eleven elements that dominate the cooling rates are tracked. These are used to compute element-by-element dependent cooling rates in the presence of the Cosmic Microwave Background and the ultraviolet and X-ray backgrounds from galaxies and quasars according to the model of Haardt & Madau (2001).

For halos whose masses first exceed $M_{\rm FOF} = 10^{10}h^{-1}{\rm M}_{\odot}$ (≈ 1500 dark matter particles, see section 4.2.2), black hole (BH) sink particles are placed at the centre of the halos. The BHs are then allowed to grow through gas accretion and by merging with other BHs using methods based on those introduced by Springel et al. (2005) and Booth & Schaye (2009). The gas surrounding a BH is accreted at a rate given by the Bondi-Hoyle formula (Bondi & Hoyle, 1944) unless the viscous timescale of the gas around the BH is larger than the Bondi time, in which case the accretion rate is reduced by a factor proportional to the cube of the ratio of the local sound speed and the rotation velocity (Rosas-Guevara et al., 2015). For a BH of mass, $M_{\rm BH}$, surrounded by gas at density, ρ, velocity with respect to the BH, v, and sound speed, $c_{\rm s}$, the accretion rate is:

$$\dot{m}_{\rm BH} = \frac{4\pi G M_{\rm BH}^2 \rho}{(c_{\rm s}^2 + v^2)^{3/2}} \cdot \begin{cases} \frac{1}{C_{\rm visc}} \left(\frac{c_{\rm s}}{V_\phi}\right)^3 & \text{if} \quad C_{\rm visc} V_\phi^3 > c_{\rm s}^3 \\ 1 & \text{if} \quad C_{\rm visc} V_\phi^3 \leq c_{\rm s}^3 \end{cases},$$

where V_ϕ is the circular speed of the gas at the Bondi radius and $C_{\rm visc} = 2\pi$ in the reference simulation.

Feedback due to AGN activity is implemented in a similar way to the feedback from star formation described above. The fraction of the accreted rest mass energy liberated by accretion is $\epsilon_r = 0.1$, and the heating efficiency of this liberated energy (i.e. the fraction of the energy that couples to the gas phase) is $\epsilon_f = 0.15$. Gas particles receiving AGN feedback energy are chosen stochastically and their temperature is raised by $10^{8.5}$ K.

These models of supernova and AGN feedback are extensions of the models developed for the Virgo Consortium projects OWLS (Schaye et al., 2010) and GIMIC (Crain et al., 2009). The values of the parameters were constrained by matching key

observables of the galaxy population including the observed $z \approx 0$ galaxy stellar mass function, galaxy sizes and the relation between black hole and stellar mass (Crain et al., 2015).

4.2.2 Halo definition and selection

Halos were identified using the Friends-of-Friends (FOF) algorithm on all dark matter particles adopting a dimensionless linking length, $b = 0.2$ (Davis et al., 1985). We then applied the SUBFIND algorithm, which is built into GADGET-3 (Springel et al., 2001; Dolag et al., 2009), to split the FOF groups into self-bound substructures. A sphere is grown outwards from the potential minimum of the dominant subgroup out to a radius where the mean interior density equals a target value. This target value is conventionally defined in units of the critical density, $\rho_{\rm cr}(z) = 3H^2(z)/8\pi G$. With our choice of cosmology, at $z = 0$ we have $\rho_{\rm cr} = \rho_{\rm cr}(0) = 127.5\ {\rm M}_\odot\ {\rm kpc}^{-3}$. A halo of mass, $M_{\rm X}$, is then defined as all the mass within the radius, $R_{\rm X}$, for which

$$\frac{3M_{\rm X}}{4\pi R_{\rm X}^3} = {\rm X}\rho_{\rm cr}({\rm z}) \tag{4.3}$$

Commonly used values are ${\rm X} = 200$, 500 and 2500, leading to the definition of the mass, M_{200}, and the radius, R_{200}, and similar definitions for other values of X.

In the particular case of the virial radius, $R_{\rm vir}$, one can use the spherical top-hat collapse model to derive the value of X (Eke et al., 1996). We use the fitting formula given by Bryan & Norman (1998):

$${\rm X} = 18\pi^2 + 82\left(\Omega_{\rm m}({\rm z}) - 1\right) - 39\left(\Omega_{\rm m}({\rm z}) - 1\right)^2, \tag{4.4}$$

where

$$\Omega_{\rm m}(z) = \Omega_{\rm m}\left(1+z\right)^3\left(\frac{H_0}{H(z)}\right)^2, \tag{4.5}$$

and $H(z)$ is the value of the Hubble parameter at redshift z which, in a flat Universe, is

$$H(z) = H_0\sqrt{\Omega_{\rm m}(1+z)^3 + \Omega_\Lambda}. \tag{4.6}$$

In the case of the *Planck1* cosmology, at $z = 0$, ${\rm X} = 102.1$, giving $M_{\rm vir} = M_{102}$ and $R_{\rm vir} = R_{102}$.

We define the circular velocity, $V_{\rm X}$, as

$$V_{\rm X} = \sqrt{\frac{GM_{\rm X}}{R_{\rm X}}}. \tag{4.7}$$

We only consider halos with more than 200 particles within R_{200}, implying a limit, $M_{200} \gtrsim 2.5 \times 10^8 {\rm M}_\odot$, in our joint analysis of the two EAGLE simulations. For specific properties that depend on the internal structure of the halo we adopt more conservative limits as described in section 4.4.

4.2.3 Matching halos between the two simulations

The EAGLE and DMO simulations start from identical Gaussian density fluctuations. Even at $z = 0$ it is possible, in most cases, to identify matches between halos in the two simulations. These matched halos are comprised of matter that originates from the same spatial locations at high redshift in the two simulations. In practice, these identifications are made by matching the particle IDs in the two simulations, as the values of the IDs encode the Lagrangian coordinates of the particles in the same way in both simulations.

For every FOF group in the EAGLE simulation, we select the 50 most bound dark matter particles. We then locate those particles in the DMO simulation. If more than half of them are found in a single FOF group in the DMO simulation, we make a link between those two halos. We then repeat the procedure by looping over FOF groups in the DMO simulation and looking for the position of their counterparts in the EAGLE simulation. More than 95% of the halos with $M_{200} > 2 \times 10^{10} {\rm M}_\odot$ can be matched bijectively, with the fraction reaching unity for halos above $7 \times 10^{10} {\rm M}_\odot$ in the L100N1504 volumes. Similarly, 95% of the halos with $M_{200} > 3 \times 10^9$ can be matched bijectively in the L0025N0752 volumes.

4.3 Halo masses and content

Previous work comparing the masses of halos in cosmological galaxy formation simulations with matched halos in counterpart dark matter-only simulations have

found strong effects for all but the most massive halos (e.g. Cui et al., 2012; Sawala et al., 2013). Sawala et al. (2013) found that baryonic effects can reduce the masses of halos by up to 25% for halo masses (in the dark matter only simulation) below $10^{13}\mathrm{M}_{\odot}$. (They did not include AGN feedback in their simulation.) A similar trend was observed at even higher masses by Martizzi et al. (2013), Velliscig et al. (2014), Cui et al. (2014) and Cusworth et al. (2014) using a variety of subgrid models for star formation and stellar and AGN feedback. All these authors stress that their results depend on the details of the subgrid implementation used. This is most clearly shown in Velliscig et al. (2014), where the amplitude of this shift in mass is shown explicitly to depend on the subgrid AGN feedback heating temperature, for example. Hence, it is important to use simulations that have been calibrated to reproduce the observed stellar mass function.

In this section we find that similar differences to those seen before occur between halo masses in the EAGLE and DMO models. These differences are of particular interest because EAGLE reproduces well a range of low-redshift observables of the galaxy population such as masses, sizes and star formation rates (Schaye et al., 2015), although the properties of clusters of galaxies are not reproduced as well as in the Cosmo-OWLS simulation (Le Brun et al., 2014) analyzed by Velliscig et al. (2014).

4.3.1 The effect of baryon physics on the total halo mass

In this section we compare the masses of halos in the EAGLE and DMO simulations combining our simulations at two different resolutions. To minimise any possible biases due to incomplete matching between the simulations, we only consider halos above $3 \times 10^{9}\mathrm{M}_{\odot}$ (in DMO), since these can be matched bijectively to their counterparts in more than 95% of cases.

Fig. 4.1 shows the ratio of M_{200} for matched halos in the EAGLE and DMO simulations as a function of M_{200} in the DMO simulation. The black filled circles correspond to the geometric mean of the ratios in each logarithmically spaced mass bin. The choice of a geometric mean is motivated simply by the fact that its reciprocal

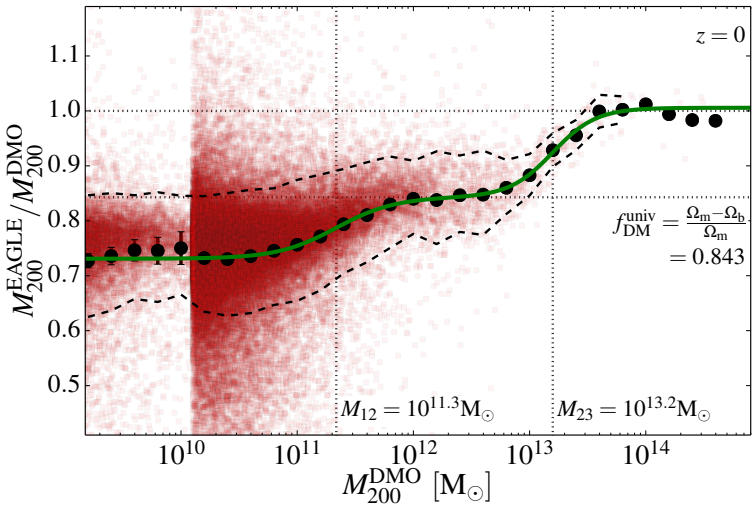

Figure 4.1: The ratio of the masses of the matched halos in the EAGLE and DMO simulations. The red squares show values for individual halos and the black filled circles values binned by DMO halo mass. Halos with $M_{200}^{\rm DMO} < 10^{10.1}{\rm M}_\odot$ come from the high resolution simulations. The binned points are the geometric average of the individual ratios with the error bars at $M_{200}^{\rm DMO} < 10^{10.1}{\rm M}_\odot$ indicating the uncertainty arising from the low number of halos in the high-resolution simulation. The black dashed lines placed above and below the black points show the geometrical 1σ scatter for each bin. The lower horizontal grey dotted line indicates the universal dark matter fraction $f_{\rm DM} = 1 - f_{\rm b} = (\Omega_{\rm m} - \Omega_{\rm b})/\Omega_{\rm m} = 0.843$. The upper dotted line marks unity. The green solid line is the function of Eqn. 4.10 fitted to the binned ratios. The vertical dotted lines mark the values of the fitting parameters M_{12} and M_{23}.

is the geometric mean of $M_{200}^{\rm DMO}/M_{200}^{\rm EAGLE}$, which is also a quantity of interest.

The halos in EAGLE are typically lighter than their DMO counterparts. There appear to be three distinct regimes in Fig. 4.1 . At the low mass end, $M_{200} < 5 \times 10^{10}$ M$_\odot$, $M_{200}^{\rm EAGLE}/M_{200}^{\rm DMO}$ drops to ~ 0.72. This is less than one minus the universal baryon fraction, $f_{\rm DM}$, so not only have the baryons been removed but the dark matter has also been disturbed. The reduction in mass due to the loss of baryons lowers the value of R_{200} and thus the value of M_{200}. However, this reduction in radius is not the sole cause for the reduction in halo mass: the amount of mass within a fixed physical radius is actually lower in the simulation with baryons because the loss of baryons, which occurs early on, reduces the growth rate of the halo (Sawala et al., 2013). At higher masses, stellar feedback becomes less effective, but AGN feedback can still expel baryons and the ratio rises to a plateau of ~ 0.85 between $M_{200}^{\rm DMO} = 10^{12}$ M$_\odot$ and 5×10^{12} M$_\odot$. Finally, for the most massive halos ($M_{200} > 10^{14}$ M$_\odot$) not even AGN feedback can eject significant amounts of baryons from the halos and the mass ratio asymptotes to unity.

Sawala et al. (2013) proposed a fitting function to the ratio of M_{200} in simulations with and without baryons from the GIMIC project (Crain et al., 2009). Their study focused mostly on lower-mass objects and subhalos, but included enough large halos to sample the high-mass end of the relation. Their four parameter fitting function can be written as:

$$\frac{M_{200}}{M_{200}^{\rm DMO}} = a + (b-a)S\left(\frac{M_{200}^{\rm DMO}}{M_t}; w\right), \tag{4.8}$$

where S is a sigmoid function that varies smoothly between 0 and 1, and is defined in Eqn. 4.2. The best-fit parameter values in Sawala et al. (2013) are: $(a, b, \log_{10}(M_t/{\rm M}_\odot), w)$ = $(0.69, 0.98, 11.6, 0.79)$. The values of a and b correspond to the low- and high-mass asymptotes, respectively.

Velliscig et al. (2014) used a similar fitting function to summarise the results of their study, again with four parameters, which can be written as:

$$\frac{M_{200}}{M_{200}^{\rm DMO}} = a\left(\frac{b}{a}\right)^{S\left(M_{200}^{\rm DMO}/M_t; w\right)}, \tag{4.9}$$

where exactly the same sigmoid function is used to interpolate between the two asymptotic values, a and b, but now in a geometric rather than arithmetic fashion. The functional forms of Eqns. 4.8 and 4.9 are virtually identical as, in practice, the ratio b/a is never far from unity.

It is quite clear, however, from Fig. 4.1 that a single sigmoid function does not reproduce the behaviour we observe particularly well: the ratio shows three, not two, distinct plateaux. The simulations used by Sawala et al. (2013) did not include AGN feedback and so did not show the change in mass arising from this form of feedback. In contrast, the simulations used by Velliscig et al. (2014) did not have sufficient numerical resolution to see the asymptotic low-mass behaviour determined by stellar feedback.

To fit our results, we use a double sigmoid:

$$\begin{aligned}\frac{M_{200}}{M_{200}^{\rm DMO}} = r_1 \quad &+ \quad (r_2 - r_1) S\left(\frac{M_{200}^{\rm DMO}}{M_{12}}; t_{12}\right) \\ &+ \quad (r_3 - r_2) S\left(\frac{M_{200}^{\rm DMO}}{M_{23}}; t_{23}\right), \end{aligned} \tag{4.10}$$

where the seven parameters can be interpreted as follows: r_1, r_2 and r_3 are the values of the ratios corresponding to the three distinct plateaux; the mass scales, M_{12} and M_{23}, are the mid-points between regimes 1 and 2, and 2 and 3 respectively; and the parameters, t_{12} and t_{23}, control the rapidity of each transition.

The green curve in Fig. 4.1 shows the best fitting curve to the black binned data points. The fit was obtained by a least-squares minimisation for all seven parameters assuming Poisson uncertainties for each mass bin. Adopting a constant error instead gives very similar values for all parameters. The values of the two transition masses, M_{12} and M_{23}, are shown as vertical dotted lines in Fig. 4.1. The best-fitting parameters are given in Table 4.1. Note that the value of r_3 is, as expected, very close to unity.

The value of the first transition mass, $M_{12} = 10^{11.35}\mathrm{M}_\odot$, is similar to that reported by Sawala et al. (2013) who found $M_t = 10^{11.6}\mathrm{M}_\odot$ for the GIMIC simulations. The second transition, $M_{32} = 10^{13.2}\mathrm{M}_\odot$, is located well below the range of values found by Velliscig et al. (2014) ($10^{13.7}\mathrm{M}_\odot$ -$10^{14.25}\mathrm{M}_\odot$). However, as Schaye et al. (2015) have

Table 4.1: Best fitting parameters to the black points in Fig. 4.1 using Eqn. 4.10, and their uncertainties which are taken to be the diagonal elements of the covariance matrix of the least-squares fitting procedure.

Parameter	Value	1–σ fit uncertainty
r_1	0.7309	± 0.0014
r_2	0.8432	± 0.0084
r_3	1.0057	± 0.0024
$\log_{10}(M_{12}/\mathrm{M}_\odot)$	11.33	± 0.003
$\log_{10}(M_{23}/\mathrm{M}_\odot)$	13.19	± 0.029
t_{12}	1.721	± 0.045
t_{23}	2.377	± 0.18

shown the AGN feedback in the few rich clusters formed in the EAGLE volume may not be strong enough, as evidenced by the fact that this simulation overestimates the gas fractions in clusters, whereas the $400\ \mathrm{Mpc/h}$ Cosmo-OWLS simulation used by Velliscig et al. (2014) reproduces these observations (Le Brun et al., 2014).

A simulation with stronger AGN feedback, EAGLE-AGNdT9, which gives a better match to the group gas fractions and X-ray luminosities than EAGLE, was discussed by Schaye et al. (2015) . Applying the same halo matching procedure to this simulation and its collisionless dark matter-only counterpart, we obtain slightly different values for the best-fitting parameters of Eqn. 4.10. The difference is mainly in the parameters, M_{23} and t_{23}, which describe the high-mass end of the double-sigmoid function. In this model, the transition occurs at $\log_{10}\left(M_{23}/\mathrm{M}_\odot\right) = 13.55 \pm 0.09$, closer to the values found by Velliscig et al. (2014). The width of the transition, however, is poorly constrained, $t_{23} = 3.0 \pm 12.7$, due to the small number of halos (only eight with $M_{200,\mathrm{DMO}} > 2 \times 10^{13}\mathrm{M}_\odot$) in this simulation which had only an eighth the volume of the reference simulation.

As Velliscig et al. (2014) did, we provide a fit to the scatter in the log of the ratio about the mean relation, valid over the range where appropriately constraining data are available:

$$\sigma\left(\log_{10}(M_{200}^{\mathrm{DMO}})\right) = 0.044 - 0.015\log_{10}\left(\frac{M_{200}^{\mathrm{DMO}}}{10^{12}\mathrm{M}_\odot}\right). \tag{4.11}$$

The scatter is about 10% for a halo mass of $10^{12}\mathrm{M}_\odot$ and decreases with mass. The slope in the relation is approximatively a factor of two greater than that found for the AGN models of Velliscig et al. (2014).

4.3.2 The halo mass function

The effect of baryons on the halo mass function can be seen in Fig. 4.2. The red and green lines in the top panel show the mass functions in the EAGLE and DMO simulations. The ratio of the two functions (bottom panel) shows an almost constant shift over most of the plotted mass range, $M_{200}/\mathrm{M}_\odot = 10^9 - 10^{13}$, as expected from Fig. 4.1. The relatively small volume of the EAGLE simulation does not sample the

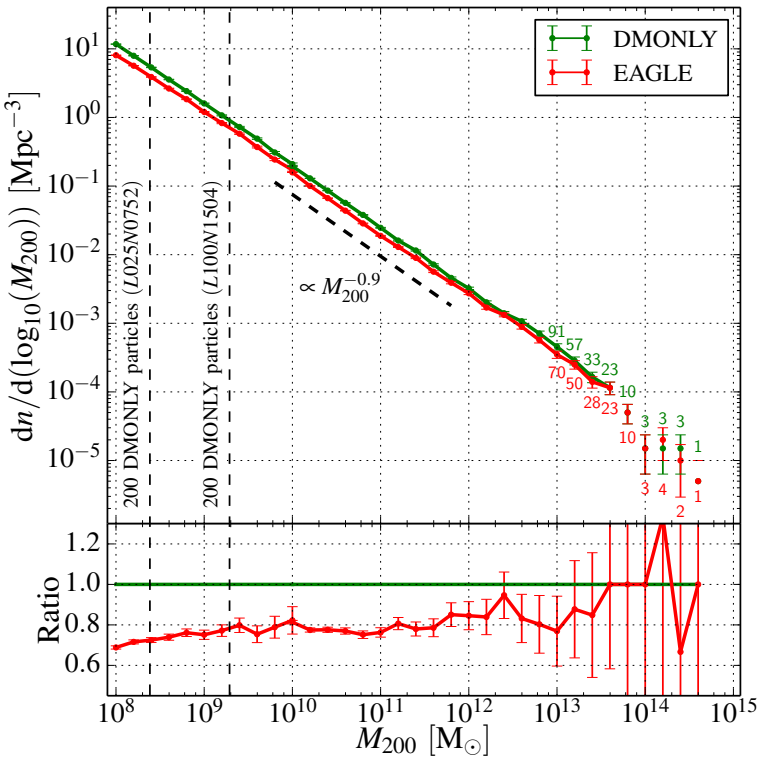

Figure 4.2: Top panel: the abundance of halos at $z = 0$ as a function of the mass, M_{200}, in the EAGLE (red curve, lower line) and DMO (green curve, upper line) simulations. The high resolution volume is used for $M_{200}^{\rm DMO} < 10^{10.1}{\rm M}_{\odot}$. The resolution limits for both simulations are indicated by the vertical dashed lines on the left, and the number of halos in sparsely populated bins is given above the Poisson error bars. Bottom panel: the ratio of the mass functions in the EAGLE and DMO simulations.

knee of the halo mass function well, but extrapolating the fit to the mass ratios of Eqn. 4.10 to higher masses, together with results from previous studies (Cusworth et al., 2014; Martizzi et al., 2013; Velliscig et al., 2014), suggests that the differences vanish for the most massive objects. Studies that rely on galaxy clusters to infer cosmological parameters will need to take account of the effects of the baryons, particularly for clusters of mass $M_{200} \lesssim 10^{14}\mathrm{M}_{\odot}$.

4.3.3 Baryonic and stellar fractions in the EAGLE simulation

We have shown in the previous subsection that for all but the most massive examples, halo masses are systematically lower when baryonic processes are included. In this subsection we examine the baryonic content of halos in the EAGLE simulation. We restrict our analysis to the L100N1504 volume.

Fig. 4.3 shows the mass fractions of baryons and stars within R_{200} as a function of the halo mass, M_{200}, in the EAGLE simulation. The baryon fraction increases with halo mass and approaches the universal mean value, $f_{\mathrm{b}}^{\mathrm{univ}} \equiv \Omega_{\mathrm{b}}/\Omega_{\mathrm{m}}$, for cluster mass halos. The gas is the most important baryonic component in terms of mass over the entire halo mass range. At a much lower amplitude everywhere, the stellar mass fraction peaks around a halo mass scale of $2 \times 10^{12}\mathrm{M}_{\odot}$ where star formation is at its least inefficient.

The baryon fractions are much lower than the universal value for all but the most massive halos. For Milky Way sized halos, we find $f_{\mathrm{b}}/f_{\mathrm{b}}^{\mathrm{univ}} \approx 0.35$. It is only for group and cluster sized halos, whose deeper gravitational potentials are able to retain most of the baryons even in the presence of powerful AGN, that the baryon fraction is close to $f_{\mathrm{b}}^{\mathrm{univ}}$. The baryon fractions of the halos extracted from the EAGLE-AGNdT9 model (which provides a better match to X-ray luminosities; Schaye et al. 2015) are presented in Appendix A.

The stellar mass fraction is never more than a few percent. At the peak, around $M_{200} \approx 2 \times 10^{12}\mathrm{M}_{\odot}$, it reaches a value of ~ 0.023. Multiplying the stellar fraction by the halo mass function leads to an approximate stellar mass function, which is close to the actual one (published in Schaye et al. 2015), after a fixed aperture correction

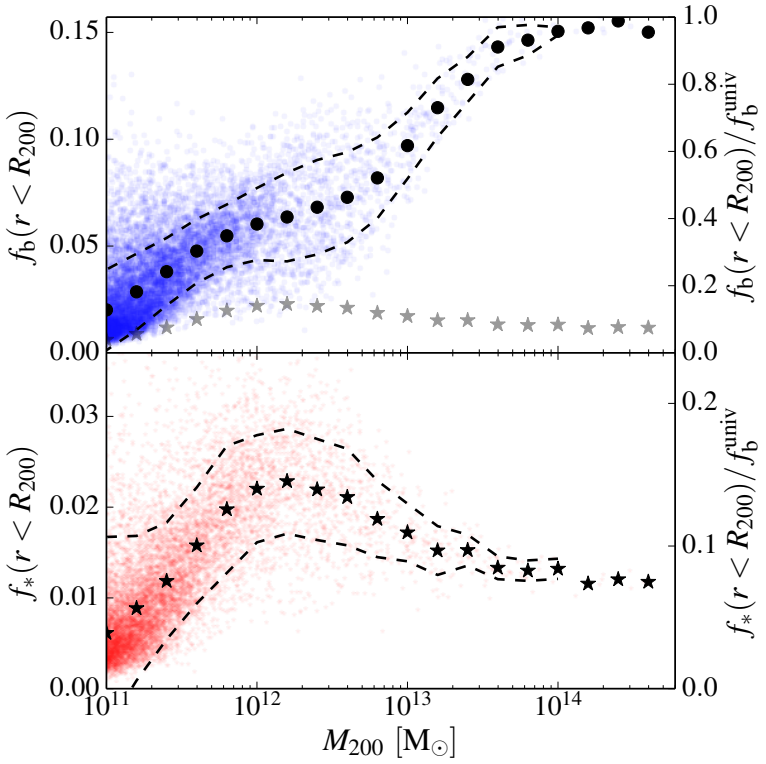

Figure 4.3: Baryon fraction, $f_{\rm b} = M_{\rm b}/M_{200}$ (top panel), and stellar fraction, $f_* = M_*/M_{200}$ (bottom panel), within R_{200} as a function of M_{200}. The right-hand axis gives the fractions in units of the universal mean value, $f_{\rm b}^{\rm univ} = 0.157$. The solid circles in the top panel and the stars in the bottom panel show the mean value of the fractions binned by mass. The dashed lines above and below these symbols show the RMS width of each bin with more than three objects. The stellar fractions are reproduced as grey stars in the top panel.

is applied to mimic observational measurements. As may be seen in both panels, there is significant scatter in the baryonic and stellar fractions, with variations of a factor of a few possible for individual halos.

While the baryonic and stellar fractions are low within R_{200}, they are much higher in the inner regions of halos as shown in Fig. 4.4, where these fractions are now plotted within $0.05R_{200}$, a scale commensurate with the sizes of galaxies both in EAGLE and in the real universe. Within this radius the fractions rise above the cosmic mean for halos in the mass range $5 \times 10^{11}\mathrm{M}_{\odot} < M_{200} < 2 \times 10^{13}\mathrm{M}_{\odot}$. The central parts of these halos contain a large fraction of baryons. In agreement with observations of the nearby universe, the most important contribution to the mass on these scales is from stars rather than gas. Another notable feature is that the most massive halos are baryon poor in their central regions, reflecting the regulation by AGN feedback.

4.4 Halo profiles

In this section we explore the effects of baryons on halo profiles restricting the analysis to halos with more than 5000 particles within $R_{\rm vir}$, which corresponds to a halo mass of about $5 \times 10^{10}\mathrm{M}_{\odot}$ in the L100N1504 simulation and $6 \times 10^{9}\mathrm{M}_{\odot}$ in the L050N0752 simulation. The stellar masses found in the EAGLE simulation for halos of this mass are consistent with observational expectations based on abundance matching (Schaye et al., 2015). Halos smaller than this typically have fewer than the hundred star particles, which Schaye et al. (2015) showed to be a necessary criterion for many applications. This limit of 5000 in the number of particles is intermediate between those used in other studies. It is similar to the number adopted by Ludlow et al. (2013) and lower than the number adopted by Neto et al. (2007) and Duffy et al. (2008, 2010) (10000 particles), but higher than the number adopted by Gao et al. (2008); Dutton & Macciò (2014) (3000 particles) or Macciò et al. (2007) (250 particles). There are 22867 halos with at least 5000 particles in the Ref-L100N1504 EAGLE simulation and 2460 in the Recal-L0025N0752 simulation.

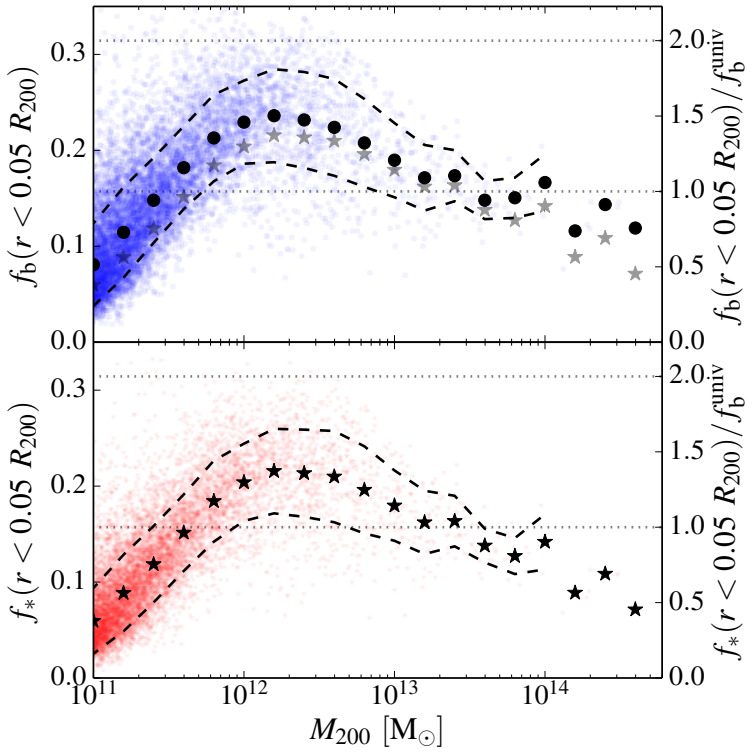

Figure 4.4: Same as Fig. 4.3 but for the mass contained within 5% of R_{200}. Note the different scale on the ordinate axis. The dotted horizontal lines mark one and two times the universal baryon fraction.

We define *relaxed* halos as those where the separation between the centre of the potential and the centre of mass is less than $0.07R_{\rm vir}$, as proposed by Macciò et al. (2007). Neto et al. (2007) used this criterion, and also imposed limits on the substructure abundance and virial ratio. Neto et al. (2007) found that the first criterion was responsible for rejecting the vast majority of unrelaxed halos. Their next most discriminating criterion was the amount of mass in substructures. In common with Gao et al. (2008), here we use stacked profiles. Hence, individual substructures, which can be important when fitting individual halos, have a small effect on the average profile. We therefore do not use a substructure criterion to reject halos. Our relaxed sample includes 13426 halos in the L100N1504 simulation and 1590 in the L0025N0752 simulation. We construct the stacked halos by coadding halos in a set of contiguous bins of width $\Delta \log_{10}(M_{200}) = 0.2$.

The density and mass profiles of each halo and of the stacked halos are obtained using the procedure described by Neto et al. (2007). We define a set of concentric contiguous logarithmically spaced spherical shells of width $\Delta \log_{10}(r) = 0.078$, with the outermost bin touching the virial radius, $R_{\rm vir}$. The sum of the masses of the particles in each bin is then computed for each component (dark matter, gas, stars, black holes) and the density is obtained by dividing each sum by the volume of the shell.

4.4.1 Resolution and convergence considerations

Determining the minimum radius above which the results are robust and reliable is non-trivial. For DM-only simulations, Gao et al. (2008) showed that the best fit NFW profiles are sensitive to this choice and it is, therefore, important to estimate this minimum converged radius accurately. For DM-only simulations the thorough resolution study of (Power et al., 2003, P03) suggests a convergence radius, R_{P03}, based on the two-body relaxation timescale of particles orbiting in the gravitational potential well. This criterion can be written as:

$$0.6 \leq \frac{\sqrt{200}}{8}\sqrt{\frac{4\pi\rho_{\rm cr}}{3m_{\rm DM}}}\frac{\sqrt{N(<R_{P03})}}{\ln N(<R_{P03})}R_{P03}^{3/2}, \tag{4.12}$$

where $N(< r)$ is the number of particles of mass, $m_{\rm DM}$, within radius r.

While this criterion could be applied to the DMO simulation, the situation for the EAGLE simulation is more complex since, as discussed by Schaye et al. (2015), the concept of numerical convergence for the adopted subgrid model is itself ill defined. One option would be simply to apply the P03 criterion, which is appropriate for the DMO simulation, to both simulations. Alternatively, we could apply the criterion to the dark matter component of the halos in the baryon simulation or to all the collisionless species (stars, dark matter and black holes). Neither of these options is fully satisfactory but, in practice, they lead to similar estimates for R_{P03}. For the smallest halos of the L100N1504 simulation considered in this section, we find $R_{P03} \approx 5.1$ kpc whereas for the largest clusters we obtain $R_{P03} \approx 3.5$ kpc.

The original P03 criterion ensures that the mean density internal to the convergence radius, $\bar{\rho} = 3M(r < R_{P03})/4\pi R_{P03}^3$, is within 10% of the converged value obtained in a simulation of much higher resolution. As the magnitude of the differences between the EAGLE and DMO profiles that we see are significantly larger than 10% typically, we can relax the P03 criterion somewhat. Reanalysing their data, we set the coefficient on the left-hand side of Eqn. 4.12 to 0.33, which ensures a converged value of the mean interior density at the 20% level. With this definition, our minimal convergence radius $r_{\rm c}$ takes values between 4 kpc and 2.9 kpc for halos with $M_{200} \sim 10^{11}{\rm M}_\odot$ up to $M_{200} \sim 10^{14}{\rm M}_\odot$. Similarly, in the L025N0752 simulation our modified criterion gives $r_{\rm c} \approx 1.8$ kpc. Note that despite adopting a less conservative criterion than P03, the values of $r_{\rm c}$ are always greater than the Plummer equivalent softening length where the force law becomes Newtonian, $2.8\epsilon = 1.96$ kpc in the L100N1504 simulation and 0.98 kpc in L0025N0752 simulation.

The validity of our adopted convergence criterion can be tested directly by comparing results from our simulations at two different resolutions. Specifically, we compare our two simulations of $(25$ Mpc$)^3$ volumes, L025N0752, and L025N0376 which has the same initial phases as L025N0752 but the resolution of the reference, L100N1504, simulation. In the language of Schaye et al. (2015), this is a *weak* con-

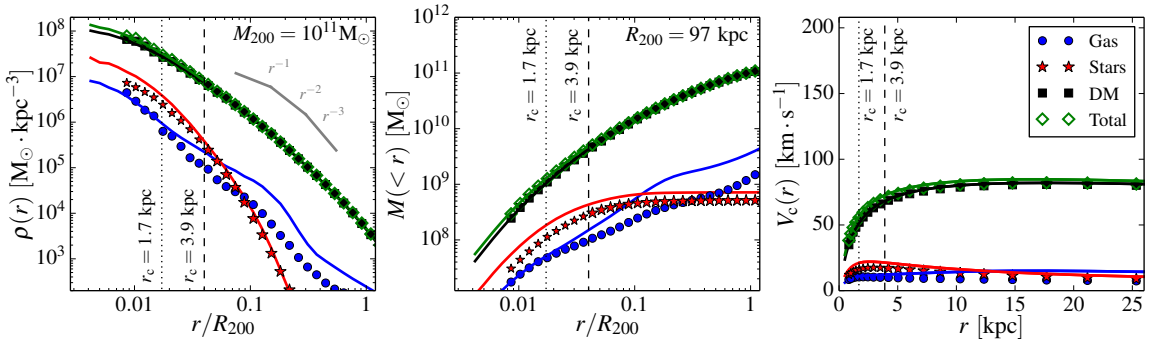

Figure 4.5: From left to right: the density, mass and circular velocity profiles of a stack of the 44 relaxed halos of mass $10^{11}\mathrm{M}_\odot$ at $z = 0$ that are present in both the L0025N0752 simulation (lines) and the L0025N0376 simulation (symbols). Profiles of total matter (green), dark matter (black), gas (blue) and the stellar component (red) are shown for both resolutions. The vertical dashed and dotted lines show the resolution limits, r_c, derived from our modified P03 criterion for the L0025N0376 and L0025N0752 simulations respectively; data point are only shown at radii larger than the Plummer equivalent force softening. The dark matter, total matter and stellar profiles are well converged even at radii smaller than r_c, indicating that this convergence cirterion is very conservative when relaxed halos in a narrow mass range are averaged together. Convergence is much poorer for the subdominant gas distribution at large radii.

vergence test since the parameters of the subgrid models have been recalibrated when increasing the resolution.

Fig. 4.5 shows the stacked profiles of the 44 relaxed halos of mass $10^{11}\mathrm{M}_{\odot}$ present in both the L025N0376 and L025N0752 simulations. This mass bin contains enough halos for the stacks not to be dominated by Poisson noise and the halos are large enough to contain more than 5000 particles in the lower resolution simulation. The three panels show density, contained mass and circular velocity profiles respectively, using symbols for the default resolution and lines for the higher resolution simulation. As may be seen, the stacked dark matter and total matter profiles are very well converged over most of the radial range, both in terms of the integral quantities, $M(r)$ and $V_{\rm c}(r)$, and in terms of the differential quantity, $\rho(r)$. The dashed and dotted vertical lines show the convergence radius, $r_{\rm c}$, for the default and high resolution simulations respectively, computed following the procedure described above.

The dark matter and total matter profiles converge well down to much smaller radii than $r_{\rm c}$ implying that this limit is very conservative. This is a consequence of comparing stacked rather than individual halos since the stacks tend to average deviations arising from the additional mass scales represented in the high resolution simulation. We conclude from this analysis that the total matter and dark matter profiles of stacked halos are well converged in our simulations and that we can draw robust conclusions about their properties for $r > r_{\rm c}$ in both the L100N1504 and L0025N0752 simulations.

The gas profiles in these simulations display a much poorer level of convergence. The disagreement between the two simulations increases at radii larger than $r > r_{\rm c}$. However, since the mass in gas is negligible at all radii and at all halo masses, the poor convergence of the gas profiles does not affect our conclusions regarding the dark and total matter profiles. We defer the question of the convergence of gaseous profiles to future studies and simulations.

4.4.2 Stacked halo density and cumulative mass of relaxed halos

Having established a robust convergence criterion for stacked halos we now analyse their profiles extracting halos of mass $M_{200} \geq 10^{11}\mathrm{M}_{\odot}$ from the L100N1504 simulation and halos of mass $10^{10}\mathrm{M}_{\odot} \leq M_{200} \leq 10^{11}\mathrm{M}_{\odot}$ from the L0025N0376 simulation.

Fig. 4.6 shows the stacked profiles for five different halo mass bins. The left-hand column shows that the DM is the dominant component of the density of halos of all masses outside about one percent of R_{200}. Inside this radius the stellar component begins to contribute and even dominate in the case of halos with mass $\gtrsim 10^{12}\mathrm{M}_{\odot}$. Considering only the baryonic matter, the inner radii are dominated by stars, but gas dominates outside of $\sim 0.1R_{200}$, as we already saw in Fig. 4.3. In halos of Milky Way size ($M_{200} \sim 10^{12}\mathrm{M}_{\odot}$) the density profile of the gas is roughly isothermal with $\rho(r) \propto r^{-2}$. The stars exhibit a steep profile, $\rho(r) \propto r^{-3} - r^{-4}$, in the region where this is resolved ($r > r_{\mathrm{c}}$). The resolution of our simulations is not sufficient to enable the discussion of the stellar profile in the central part of the galaxies, within $\sim 3\,\mathrm{kpc}$ of the centre of potential.

The shape of the dark matter profiles in the EAGLE simulation are typically very close to those obtained in the DMO simulation. The profiles depart from the DMO shape in halos with $M_{200} \gtrsim 10^{12}\mathrm{M}_{\odot}$, where the slope in the inner regions (below $0.1R_{200}$) is slightly steeper. This indicates that some contraction of the dark matter has taken place, presumably induced by the presence of baryons in the central region.

The *total* density profiles of the EAGLE halos also closely resemble those of the DMO simulation. This follows because the DM dominates over the baryons at almost all radii. In halos with a significant stellar fraction, the total profile is dominated by the stars within $\sim 0.01R_{200}$. This creates a total inner profile that is steeper than in the DMO simulations. The stellar contribution is dominant only in the first few kiloparsecs almost independently of the halo mass. Given that DMO halos have profiles similar to an NFW profile, this implies that the total profile will be closer to an NFW for more massive halos because the stars will only be important inside

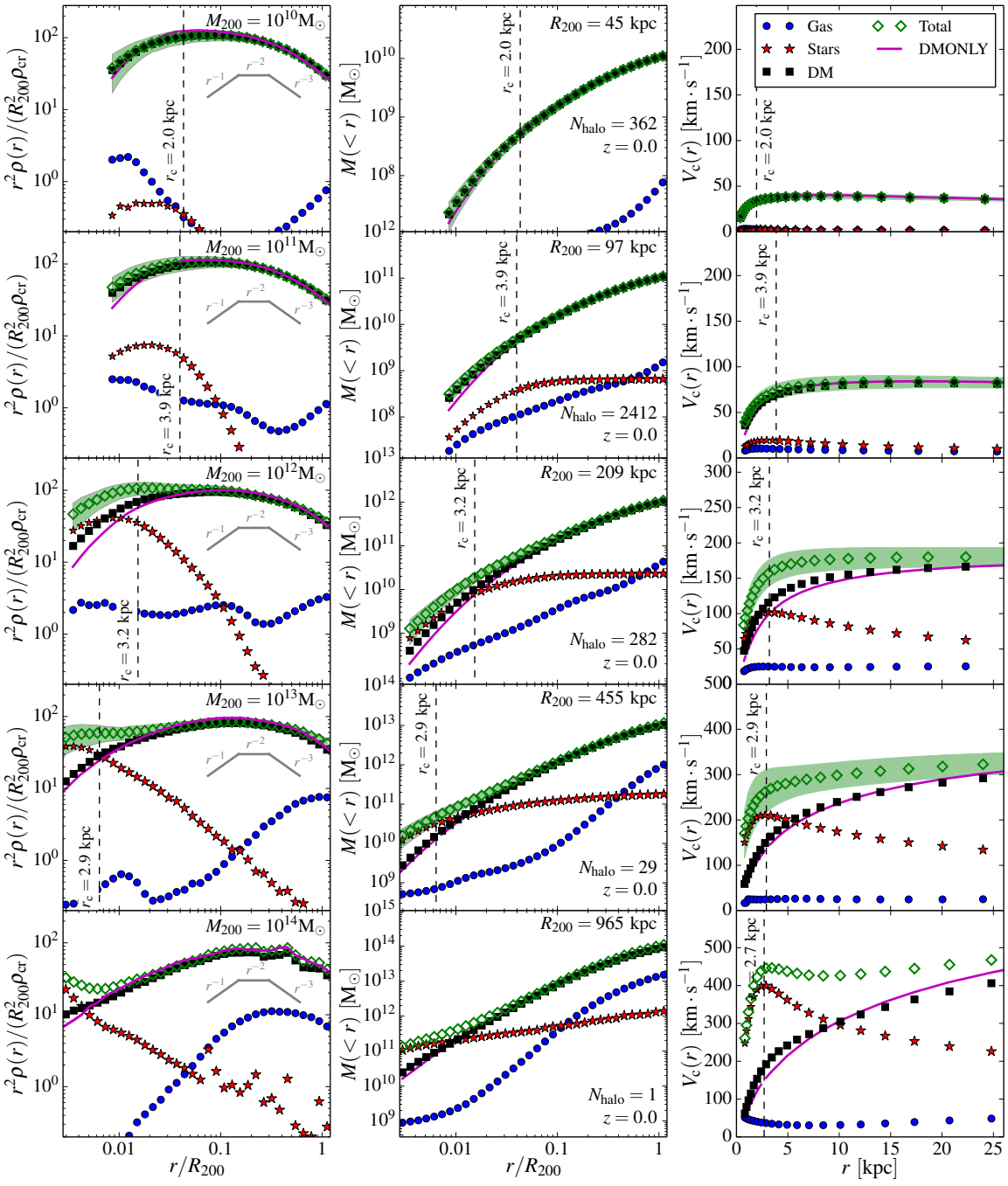

Figure 4.6: From left to right: the density, mass and circular velocity profiles for stacks of relaxed halos in different mass bins at $z = 0$. From top to bottom: bins centred on $M_{200} \approx 10^{10}\mathrm{M}_\odot$, $10^{11}\mathrm{M}_\odot$, $10^{12}\mathrm{M}_\odot$, $10^{13}\mathrm{M}_\odot$ and $10^{14}\mathrm{M}_\odot$. Profiles of the total matter (green diamonds), dark matter (black squares), gas (blue circles) and stellar component (red stars) are shown for the halos extracted from the EAGLE simulation.

Figure 4.6: (continued) Profiles extracted from halos of similar mass in the DMO simulation are shown with a magenta solid line on all panels. The RMS scatter of the total profile is shown as a green shaded region. The vertical dashed line shows the (conservative) resolution limit, r_c, introduced in the previous subsection; data are only shown at radii larger than the force softening. The number of halos in each mass bin is indicated in the middle panel of each row. The density profiles have been multiplied by r^2 and normalized to reduce the dynamic range of the plot and to enable easier comparisons between different halo masses. Note that following the analysis of Section 4.3.1, matched halos are not guaranteed to fall into the same mass bin. The oscillations seen in the profiles of the two highest mass bins, which have only a few examples, are due to the object-to-object scatter and the presence of substructures.

a smaller fraction of the virial radius. This is most clearly seen in the $10^{14}\mathrm{M}_{\odot}$ halo where the profile is dominated by the DM and follows the NFW form down to $0.01R_{200}$. Similarly, in the smallest halos, $M_{200} \approx 10^{10}\mathrm{M}_{\odot}$, the baryon content is so low that the total matter profile behaves almost exactly like the dark matter profile and is hence in very good agreement with dark matter-only simulations.

It is also interesting to note the absence in our simulations of DM cores of size $0.5 - 2$ kpc such as have been seen in simulations with different subgrid models (e.g. Navarro et al., 1996a; Read & Gilmore, 2005; Mashchenko et al., 2006; Pontzen & Governato, 2012, 2014) even though such cores would have been resolved in our simulations. As first shown by Navarro et al. (1996a), density cores can be generated by explosive events in the central regions of halos when gas has become self-gravitating. Our simulations include violent feedback processes but these are not strong enough to generate a core or even a systematic flattening of the inner DM profile. We cannot, of course, rule out the possibility that the central profile could be modified even with our assumed subgrid model in higher resolution simulations.

4.4.3 Halo circular velocities

The right-hand column of Fig. 4.6 shows the rotation curves. Those for Milky Way mass halos display a flat profile at radii greater than 10 kpc as observed in our galaxy and others (e.g. Reyes et al., 2011). The dominant contribution of the DM is clearly seen here. The stellar component affects only the first few kiloparsecs of the rotation curve. The rotation curves of halos with a significant (> 0.01) stellar fraction (i.e. halos with $M_{200} > 3 \times 10^{11}\mathrm{M}_{\odot}$) have a higher amplitude than the corresponding DMO stacked curves at small radii $r \lesssim 10$ kpc. The combination of the stellar component and contraction of the inner dark matter halo leads to a maximum rotation speed that is $\approx 30\%$ higher in the EAGLE simulation compared to that in DMO.

To assess whether the circular velocity profiles for the galaxies in the EAGLE simulation are realistic, we compare them to a sample of observed disc galaxies. We

use the data from Reyes et al. (2011), who observed a sample of 189 spiral galaxies and used Hα lines to measure the rotation curves. From their SDSS $r-$band magnitudes and $g-r$ colours, we derive the stellar masses of their galaxies using the M_*/L scaling relation of Bell et al. (2003). We apply a -0.1 dex correction to adjust these stellar mass estimates from their assumed 'diet Salpeter' IMF to our adopted Chabrier (2003) IMF, and apply the extinction correction from Dutton et al. (2011) to convert our masses to the MPA/JHU definitions (Bell et al., 2003) (See McCarthy et al. (2012) for the details.).

In Fig. 4.7 we show the circular velocities of our sample of relaxed halos binned by the stellar mass contained within an aperture of 30 kpc, as used by Schaye et al. (2015) who already compared the predicted maximum circular velocities to observations. The simulated galaxies match the observations exceptionally well, both in terms of the shape and the normalisation of the curves. For all mass bins up to $M_* < 10^{11}\mathrm{M}_\odot$, the EAGLE galaxies lie well within the scatter in the data. Both the shape and the amplitude of the rotation curves are reproduced in the simulation. The scatter appears to be larger in the real than in the simulated population, particularly in the range $10.5 < \log_{10} M_*/\mathrm{M}_\odot < 10.75$ (lower left panel), but the outliers in the data might affected by systematic errors (Reyes et al., 2011) arising, for instance, from the exact position of the slit used to measure spectral features or from orientation uncertainties.

The rotation curves for the highest stellar mass bin in the simulation, $M_* > 10^{11}\mathrm{M}_\odot$, show a clear discrepancy with the data. Although the general shape of the curves is still consistent, the normalisation is too high. Part of this discrepancy might be due to the selection of objects entering into this mass bin. The data refer to spiral galaxies, whereas no selection besides stellar mass has been applied to the sample of simulated halos. This highest mass bin is dominated by elliptical objects in EAGLE. Selecting spiral-like objects (in a larger simulation) may well change the results at these high stellar masses. A more careful measurement of the rotation velocities in the simulations in a way that is closer to observational estimates (e.g. by performing mock observations of stellar emission lines) might also reduce the

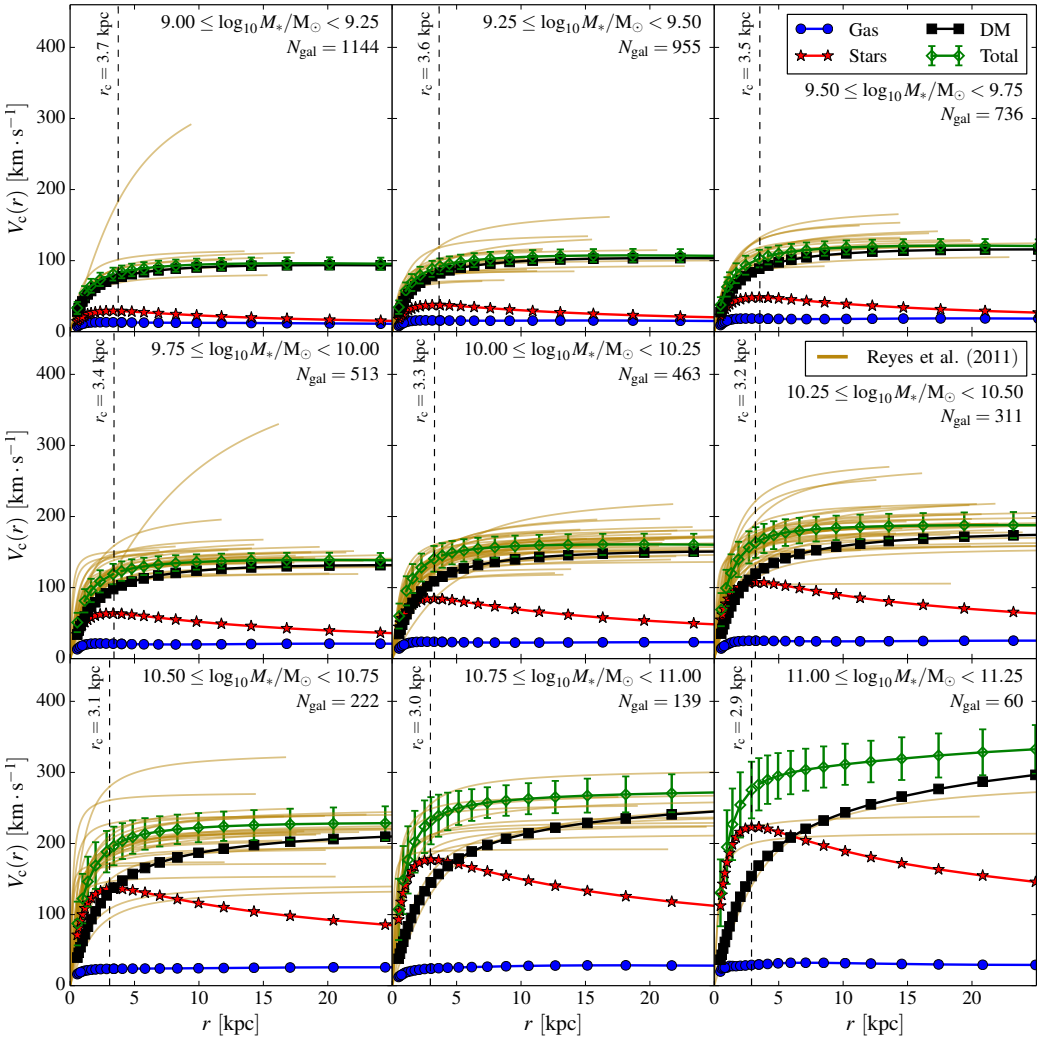

Figure 4.7: Simulated circular velocity curves and observed spiral galaxy rotation curves in different stellar mass bins. The green diamonds with error bars correspond to the total circular velocity and the RMS scatter around the mean. The black squares, red stars and blue circles represent the mean contributions of dark matter, star and gas particles respectively. The dashed vertical line is the conservative resolution limit, r_c. The background brown curves are the best-fit Hα rotation curves extracted from Reyes et al. (2011). We plot their data up to their $i-$band measured isophotal R_{80} radii.

discrepancies. We defer this, more careful, comparison to future work.

At all masses beyond the convergence radius the dominant contribution to the rotation curve comes from the dark matter. For the highest mass bins the stellar contribution is very important near the centre and this is crucial in making the galaxy rotation curves relatively flat. As already seen in the previous figure, the contribution of gas is negligible.

4.4.4 An empirical universal density profile

It is well known that the density profiles of relaxed halos extracted from dark matter only simulations are well fit by the NFW profile (Eqn. 4.1) at all redshifts down to a few percent of the virial radius (Navarro et al., 1997; Bullock et al., 2001; Eke et al., 2001; Navarro et al., 2004; Shaw et al., 2006; Macciò et al., 2007; Neto et al., 2007; Duffy et al., 2008; Ludlow et al., 2013; Dutton & Macciò, 2014). The total matter profiles shown in Fig. 4.6 for the EAGLE simulation follow the NFW prediction in the outer parts, but the inner profile is significantly steeper than the NFW form, which has an inner slope ($\rho(r \rightarrow 0) = r^{-\eta}$ with $\eta \approx 1$). The deviations from an NFW profile can be quite large on small scales.

To show this, we fit the total mass profiles using the fitting procedure defined by Neto et al. (2007). We fit an NFW profile to the stacked profiles over the radial range $[0.05, 1]R_{\rm vir}$, shown respectively as blue dashed curves and filled circles in Fig. 4.8. This choice of minimum radius is larger than the conservative convergence radius given by version of the Power et al. (2003) criterion that we adopted in the previous section. As described in Section 4.4.2, the bins are spherical and spaced logarithmically in radius.

The Neto et al. (2007) fit is performed by minimizing a χ^2 expression with two free parameters, $r_{\rm s}$ and $\delta_{\rm c}$, characterising the NFW profile, over a set of $N_{\rm b}(= 17)$ radial bins. We use the Levenberg & Marquart method to minimize the RMS deviation, $\sigma_{\rm fit}$, between the binned logarithmic densities $\rho_{\rm i}$ and the NFW profile $\rho_{\rm NFW}$:

$$\sigma^2_{\rm fit} = \frac{1}{N_{\rm b} - 1} \sum_{i=1}^{N_{\rm b}} \left(\log_{10} \rho_{\rm i} - \log_{10} \rho_{\rm NFW}(\delta_{\rm c}, r_{\rm s})\right)^2 . \tag{4.13}$$

Note that the bins are weighted equally.

The best-fit profile for each stacked halo mass bin is shown in Fig. 4.8 as a blue dashed line. The NFW profile is a very good fit to the filled circles, confirming that the outer parts of the halos are well described by this profile within R_{200}. However, the NFW profile is clearly a poor fit at small radii ($r \lesssim 0.05 R_{\rm vir}$) for halos with a significant stellar mass, i.e. for halos above $\sim 3 \times 10^{11} \mathrm{M}_{\odot}$, as expected from Fig. 4.6, due to the increased contribution of the stars and the subsequent contraction of the DM profile. For halo masses above $10^{12} \mathrm{M}_{\odot}$, the discrepancy between the NFW prediction and the actual total mass density profile reaches factors of two close to the resolution limit .

When multiplied by r^2, the NFW profile reaches a maximum at $r = r_{\rm s}$. For $M_{200} > 3 \times 10^{11} \mathrm{M}_{\odot}$ the profiles do not display a single sharp maximum but rather a broad range of radii at almost constant $r^2 \rho(r)$, i.e. a quasi isothermal profile. For $M_{200} \gtrsim 3 \times 10^{13} \mathrm{M}_{\odot}$, the difference is even more striking as a second maximum appears at small radii. We will explore alternative fitting formula in what follows, but it is clear that a fitting formula describing the most massive halos will require several parameters to work well.

In their detailed study, Navarro et al. (2004) explored the use of a more general class of profiles, where the slope varies with radius as a power law. This alternative profile was originally introduced by Einasto (1965) to model old stellar populations in the Milky Way, and so Navarro et al. (2004) called it the "Einasto profile":

$$\rho(r) = \rho_{-2} \exp\left[-\frac{2}{\alpha}\left(\left(\frac{r}{r_{-2}}\right)^{\alpha} - 1\right)\right], \tag{4.14}$$

which can be rewritten as

$$\frac{\mathrm{d} \ln \rho(\mathrm{r})}{\mathrm{d} \ln \mathrm{r}} = -2\left(\frac{r}{r_{-2}}\right)^{\alpha}, \tag{4.15}$$

to highlight that the slope is a power-law of radius. Navarro et al. (2004) showed that halos in DMO simulations are typically better fit by the Einasto profile and that the value of the power law parameter, $\alpha \approx 0.17$, can be used across the whole simulated halo mass range. This was confirmed by Gao et al. (2008) and Duffy

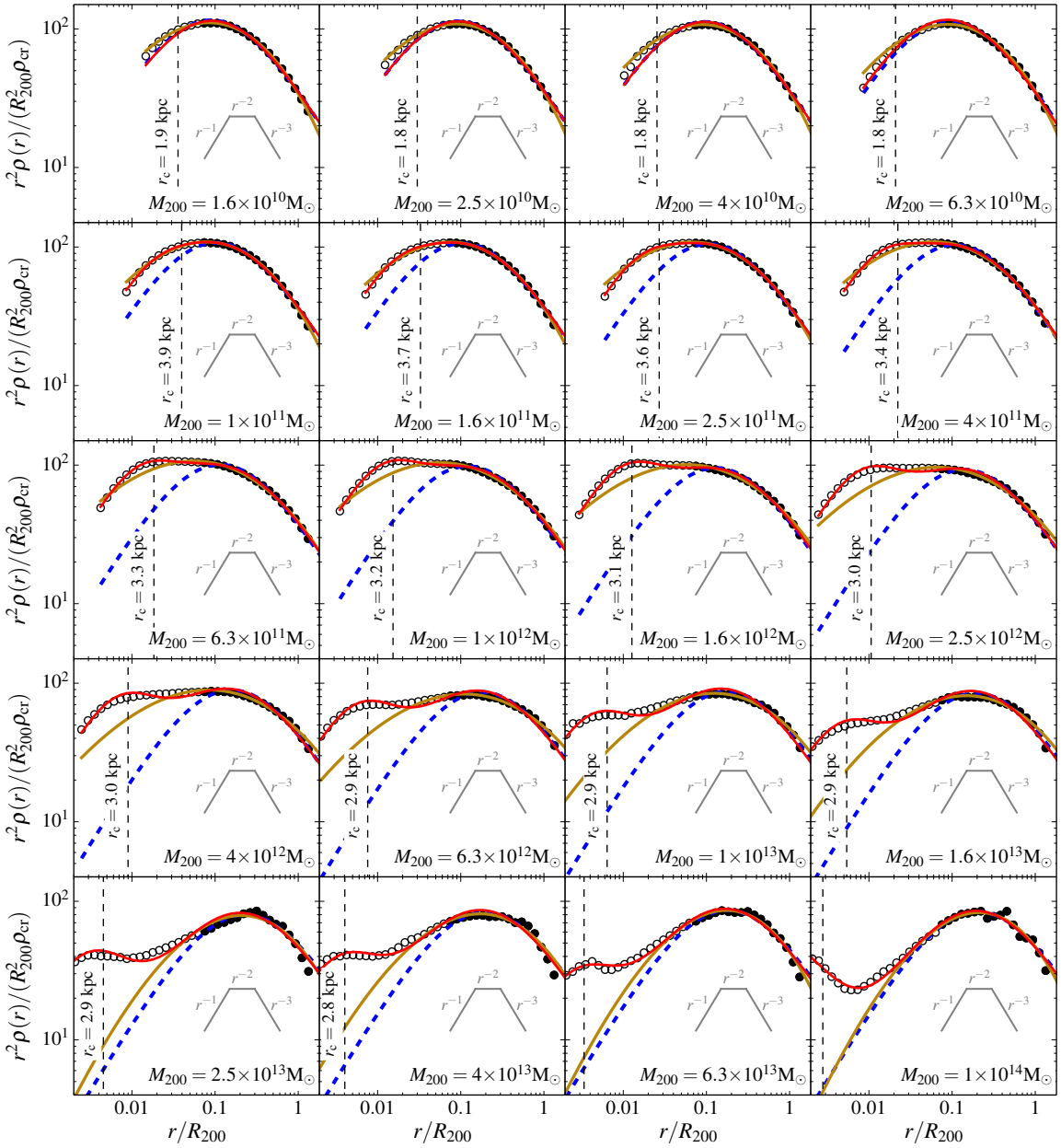

Figure 4.8: Stacked density profiles of the total mass normalized by the average R_{200} radius and scaled by r^2 for halos of different masses. The filled circles are the data points used to fit an NFW profile following Neto et al. (2007), i.e. radial bins above data points below it are shown using fainter symbols. The blue dashed lines correspond to the NFW fit to the filled circles, while the brown lines correspond to an Einasto profile fit to all radial bins down to the convergence radius, r_c. The red solid line is the best-fit profile given by Eqn. 4.16, which includes an NFW contribution for the outer parts of the halos and an additional contribution around the centre to model the baryons. The best-fitting parameters for each mass bins are given in Table 4.2.

et al. (2008) who found a weak dependence of α on the peak-height parameter. Gao et al. (2008) demonstrated that the Einasto profile is more robust to choices of the minimal converged radius, $r_{\rm c}$, improving the quality of the fit.

In the case of our sample of halos, the additional freedom to change the slope of the power law describing the density profile helps improve the fit. We use the same procedure as in the NFW case to find the best-fitting parameters $(r_{-2}, \rho_{-2}, \alpha)$ but instead of using only the radial bins with $r > 0.05R_{\rm vir}$, we use all bins with $r > r_{\rm c}$. The number of bins used is now a function of the halo mass. The resulting best-fit profiles are displayed in Fig. 4.8 as solid yellow lines. The fits are slightly better than in the NFW case simply because the rolling power law allows for a wider peak in $r^2\rho(r)$, but the Einasto profile is clearly unable to capture the complex behaviour seen in the profiles of the highest mass bins. The better fit quality is only incidental. Furthermore, if we had used the full range of radial bins for the NFW fitting procedure, we would have obtained similar fits as the two functions are very similar. Similarly, restricting the Einasto fit to the bins with $r > 0.05R_{\rm vir}$ yields a best fit profile (and $\sigma_{\rm fit}$) almost identical to the NFW ones shown by the dashed blue lines.

Clearly, in the presence of baryons, neither the NFW nor the Einasto profile faithfully represents the inner matter density profile. As Fig. 4.6 showed, the inner profile is shaped by both a substantial stellar contribution and the contraction of the dark matter associated with the elevated baryon fraction towards the centre. We find that the total profile can be fit everywhere by the following formula:

$$\frac{\rho(r)}{\rho_{\rm cr}} = \frac{\delta_{\rm c}}{(r/r_{\rm s})\left(1 + r/r_{\rm s}\right)^2} + \frac{\delta_{\rm i}}{(r/r_{\rm i})\left(1 + (r/r_{\rm i})^2\right)}. \tag{4.16}$$

The first term is the NFW profile, which we have shown gives a good fit to the outer, DM-dominated profile. The second term is NFW-like in that is shares the same asymptotic behaviour at small and large radii and has a slope of -2 at its scale radius, $r = r_{\rm i}$. We have found by trial and error that its sharper transition relative to the NFW profile between the asymptotic slope regimes of -1 and -3, which causes it to rise a factor of two above a corresponding NFW profile that shares the same

scale radius and asymptotic behaviour at small and large radii, make it particularly suitable for describing the deviations in the density profiles above an NFW profile seen in the central regions of the EAGLE halos.

We fit this profile using all the radial bins down to our resolution limit, $r_{\rm c}$. We rewrite expression (4.13) using our new profile and minimize $\sigma_{\rm fit}$ leaving the four parameters $(r_{\rm s}, \delta_{\rm c}, r_{\rm i}, \delta_{\rm i})$ free. The resulting fits are displayed in Fig. 4.8 as red solid lines. The values of the best-fitting parameters are given in Table 4.2. The fit is clearly of a much better quality than the NFW and Einasto formulas for the same set of radial bins.

For the lowest mass halos ($M_{200} < 6\times10^{10}{\rm M}_{\odot}$), this new profile does not provide a better $\sigma_{\rm fit}$ than a standard NFW profile does. This is expected since the baryons have had little impact on their inner structure. The values of $r_{\rm i}$ and $\delta_{\rm i}$ are, hence, not constrained by the fits. For these low mass stacks, we only provide the best-fitting NFW parameters in Table 4.2 instead of the parameters of our alternative profile.

The different features of the simulated halos are well captured by the additional component of our profile. We will demonstrate in the next sections that the additional degrees of freedom can be recast as physically meaningful quantities and that these are closely correlated with the halo mass. As in the case of the NFW profile, this implies that this new profile is effectively a one parameter fit, where the values of all the four parameters depend solely on the mass of the halo. It is worth mentioning that this profile also reproduces the trends in the radial bins below the resolution limit $r_{\rm c}$.

For completeness, we give the analytic expressions for both the enclosed mass, $M(r<R)$, and the gravitational potential, $\Phi(r)$, for the empirical profile of Eqn. 4.16,

$$\begin{aligned} M(r<R) &= 2\pi\rho_{\rm cr}\Bigg(2\delta_{\rm c}r_{\rm s}^3\left[\ln\left(1+\frac{R}{r_{\rm s}}\right)-\frac{R}{R+r_{\rm s}}\right] \\ &\quad +\delta_{\rm i}r_{\rm i}^3\ln\left(1+\frac{R^2}{r_{\rm i}^2}\right)\Bigg), \end{aligned} \tag{4.17}$$

Table 4.2: Best-fit parameters for the profile (Eqn. 4.16) for each stack of relaxed halos as plotted in Fig. 4.8. The tabulated values correspond to the black circles plotted in Figs. 4.13, 4.14 and 4.15. The first column gives the centre of the mass bin used for each stack and the last column the number of halos in each of the stacks. The concentration, c_{200}, and inner profile mass, $M_{\rm i}$, are defined, respectively, by Eqns. 4.19 and 4.21. For the halo stacks in the lowest mass bins, the profile 4.16 does not provide a better fit than a standard NFW. We hence only give the best-fitting parameters to the NFW fit.

M_{200} [$\mathrm{M}_\odot$]	R_{200} [kpc]	r_s [kpc]	c_{200} [$-$]	$\delta_{\rm c}$ [$-$]	$r_{\rm i}$ [kpc]	$\delta_{\rm i}$ [$-$]	$M_{\rm i}$ [$\mathrm{M}_\odot$]	$N_{\rm halo}$
1×10^{10}	45.4	4.2	10.7	5.2×10^4	–	–	–	362
1.6×10^{10}	52.8	4.8	11.0	5.5×10^4	–	–	–	231
2.5×10^{10}	61.4	5.7	10.7	5.2×10^4	–	–	–	153
4×10^{10}	70.8	6.7	10.5	5×10^4	–	–	–	96
6.3×10^{10}	83.5	9.8	8.5	2.7×10^4	2.01	1.25×10^5	5.66×10^8	96
1×10^{11}	97.4	11.7	8.3	2.5×10^4	2.23	1.53×10^5	9.44×10^8	2412
1.6×10^{11}	113.7	14.1	8.0	2.3×10^4	2.38	2.12×10^5	1.58×10^9	1657
2.5×10^{11}	132.6	17.2	7.7	2.1×10^4	2.59	2.85×10^5	2.74×10^9	1119
4×10^{11}	154.3	20.6	7.5	1.9×10^4	2.56	4.75×10^5	4.45×10^9	681
6.3×10^{11}	180.3	25.7	7.0	1.6×10^4	2.61	7.28×10^5	7.17×10^9	457
1×10^{12}	208.8	31.7	6.6	1.4×10^4	2.78	9.22×10^5	1.1×10^{10}	282
1.6×10^{12}	244.7	38.3	6.4	1.3×10^4	2.89	1.18×10^6	1.58×10^{10}	180
2.5×10^{12}	286.3	44.3	6.5	1.4×10^4	2.73	1.72×10^6	1.94×10^{10}	126
4×10^{12}	332.4	54.2	6.1	1.3×10^4	2.65	2.17×10^6	2.23×10^{10}	83
6.3×10^{12}	386.6	68.6	5.6	1.1×10^4	2.55	2.85×10^6	2.63×10^{10}	60
1×10^{13}	455.2	73.0	6.2	1.4×10^4	2.26	4.2×10^6	2.7×10^{10}	29
1.6×10^{13}	534.3	95.3	5.6	1.1×10^4	2.82	3.16×10^6	3.95×10^{10}	27
2.5×10^{13}	631.4	130.0	4.9	7.7×10^3	2.13	6.81×10^6	3.65×10^{10}	5
4×10^{13}	698.9	124.6	5.6	1.1×10^4	2.81	4.32×10^6	5.31×10^{10}	8
6.3×10^{13}	838.1	141.7	5.9	1.2×10^4	2.73	5.23×10^6	5.87×10^{10}	4
1×10^{14}	964.7	188.1	5.1	8.9×10^3	0.909	1.05×10^8	4.38×10^{10}	1

and

$$\Phi(r) = -4\pi G\rho_{\rm cr}\left(\frac{\delta_{\rm c}r_{\rm s}^3}{r}\ln\left(1+\frac{r}{r_{\rm s}}\right) + \delta_{\rm i}r_{\rm i}^2\left[\frac{\pi}{2} - \arctan\left(\frac{r}{r_{\rm i}}\right) + \frac{r_{\rm i}}{2r}\ln\left(1+\frac{r^2}{r_{\rm i}^2}\right)\right]\right). \quad (4.18)$$

The expressions for an NFW profile are recovered by setting $\delta_{\rm i} = 0$.

Finally, we stress that while this function provides an excellent fit to the results over the range of applicability the second term should not be interpreted as a description of the stellar profile. Rather, the second term models a combination of the effect of all components, including the contraction of the dark matter, and is only valid above our resolution limit which is well outside the stellar half-mass radius. Higher-resolution simulations, with improved subgrid models, would be needed to model accurately the stars and gas in these very inner regions.

4.4.5 Dark matter density profile

It is interesting to see whether the radial distribution of dark matter is different in the DMO and EAGLE simulations. In this subsection we look at the density profiles of just the DM in both the DMO and EAGLE simulations. In Fig. 4.9 we show the profiles of the stacked halos extracted from the DMO simulation for different halo mass bins. The dark matter outside $0.05R_{\rm vir}$ is well fit by the NFW profile, in agreement with previous work. The yellow curves show the best fit Einasto profile, and in agreement with many authors (Navarro et al., 2004; Gao et al., 2008; Dutton & Macciò, 2014) we find that the Einasto fit, with one extra parameter, provides a significantly better fit to the inner profile.

We show the stacked DM density profiles for the EAGLE simulation in Fig. 4.10 together with NFW and Einasto fits to the density at $0.05 \leq r/R_{\rm vir} \leq 1$. For the radii beyond $0.05R_{\rm vir}$ the NFW profile provides a good fit. The Einasto profile fits are better in the inner regions, but for the middle two mass bins ($10^{12}{\rm M}_\odot$ and $10^{13}{\rm M}_\odot$), the DM profile rises significantly above the Einasto fit. This rise coincides with a more pronounced feature in the total mass profile. The peak of the central

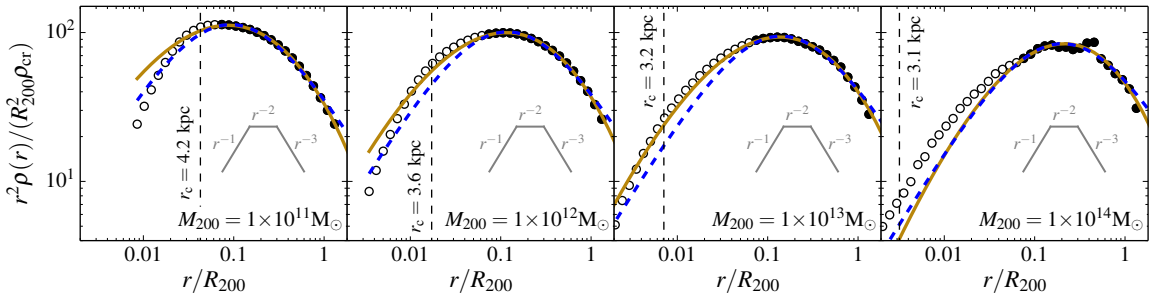

Figure 4.9: Stacked density profiles of the DMO halos normalized by the average R_{200} radius and scaled by r^2 for a selection of masses. The filled circles are the data points used to fit an NFW profile following Neto et al. (2007). The vertical line shows the resolution limit. Data points are only shown at radii larger than the Plummer-equivalent softening ($2.8\epsilon = 0.7$ kpc). The blue dashed and solid brown lines correspond, respectively, to the best-fit NFW and Einasto profiles to the filled circles. Only one halo contributes to the right hand panel.

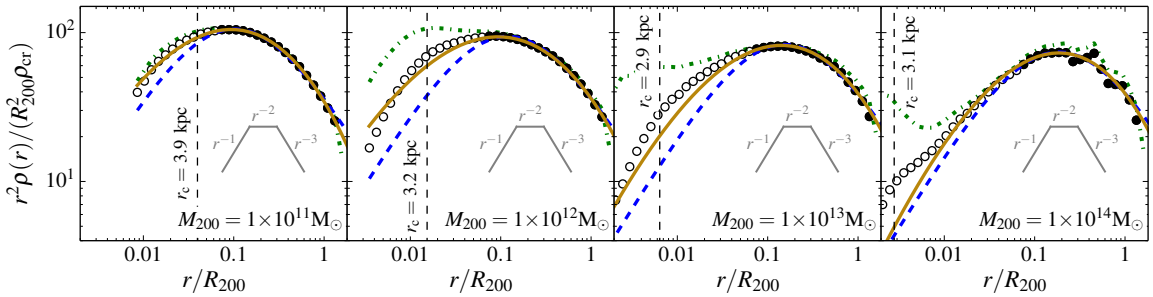

Figure 4.10: Stacked density profiles of the dark matter component of the EAGLE halos normalized by the average R_{200} radius and scaled by r^2 for a selection of halo masses. The green dash dotted line represents the total mass profile (from Fig. 4.8. The vertical line shows the resolution limit. Data points are only shown at radii larger than the Plummer-equivalent softening ($2.8\epsilon = 0.7$ kpc). The blue dashed lines and solid brown lines correspond, respectively, to the best-fit NFW and Einasto profiles to the filled circles.

stellar mass fraction occurs at this same halo mass scale, as shown in Fig. 4.4.

We conclude that the DM components of our simulated halos in both the DMO and EAGLE simulations are well described by an NFW profile for radii $[0.05R_{200} - R_{200}]$. For the DMO simulation an Einasto profile provides a better fit than an NFW profile at smaller radii. However, for the EAGLE simulation neither an NFW nor the Einasto profile provide a particularly good fit inside $0.05R_{\rm vir}$ for halos in the $10^{12}\mathrm{M}_{\odot}$ and $10^{13}\mathrm{M}_{\odot}$ mass bins, where the contribution of stars to the inner profile is maximum. For less massive and more massive halos than this both functions give acceptable fits.

In their detailed study of ten simulated galaxies from the MaGICC project (Stinson et al., 2013), Di Cintio et al. (2014) fitted (α, β, γ)-profiles (Jaffe, 1983) to the DM profiles of haloes in the mass range $10^{10}\mathrm{M}_{\odot} \leq M_{\rm vir} \leq 10^{12}\mathrm{M}_{\odot}$ and studied the dependence of the parameters on the stellar fraction. We leave the study of the DM profiles in the EAGLE halos to future work but we note that although in the small halo regime, $M_{200} \leq 10^{12}\mathrm{M}_{\odot}$, an (α, β, γ)-profile may be a good fit, the profiles of our most massive halos, $M_{200} \geq 10^{13}\mathrm{M}_{\odot}$, show varying slopes down to small radii, $r \leq 0.05R_{\rm vir}$, and are unlikely to be well fit by such a function as was already suggested by Di Cintio et al. (2014).

4.4.6 Halo concentrations

The concentration of a halo, $c_{\rm X}$, is conventionally defined by the ratio, $c_{\rm X} = R_{\rm X}/r_{\rm conc}$, where $R_{\rm X}$ is the radius within which mean internal density is $X\rho_{\rm cr}$, and $r_{\rm conc}$ is the radius at which the spherically averaged density profile (assumed monotonic) obeys

$$\frac{\mathrm{d}\ln\rho(r)}{\mathrm{d}\ln r} = -2. \tag{4.19}$$

For an NFW profile, $r_{\rm conc} = r_{\rm s}$, while for an Einasto profile $r_{\rm conc} = r_{-2}$. We set $\mathrm{X} = 200$.

Previous work (Navarro et al., 1997; Avila-Reese et al., 1999; Jing, 2000; Bullock et al., 2001; Eke et al., 2001; Zhao et al., 2003; Neto et al., 2007; Macciò et al., 2007;

Duffy et al., 2008; Gao et al., 2008; Dutton & Macciò, 2014) has shown that the concentration and the mass of relaxed halos are anticorrelated (at $z = 0$), and follow a power law of the form

$$c_{200} = A \left(\frac{M_{200}}{10^{14} h^{-1} \mathrm{M}_\odot} \right)^B , \tag{4.20}$$

where $A \approx 5$ and $B \approx -0.1$. The best-fit values of these parameters are sensitive to the cosmological parameters, particularly to the values of σ_8 and Ω_m (e.g. Duffy et al., 2008; Dutton & Macciò, 2014). The value of c_{200} at redshift zero is linked to the background density of the Universe at the time of formation of the halo (Navarro et al., 1997; Ludlow et al., 2013) which is affected by σ_8 and Ω_m. Higher values of these parameters lead to earlier halo formation times at a given mass and therefore higher concentrations. The concentrations of individual halos of a given mass scatter about the median value with an approximately log-normal distribution (Jing, 2000; Neto et al., 2007). The amplitude of this scatter decreases with halo mass (Neto et al., 2007).

While formally Eqn. 4.19 implicitly defines R_conc, it is impractical to apply a differential measure of the density to determine the concentrations of individual halos, even in simulations, because the density profiles are noisy and sensitive to the presence of substructures. In practice, the concentration is determined by fitting the spherically averaged density profile over a range of radii encompassing r_s with a model. This approach only works if the model provides a good description of the true halo profile over the fitted range. We have shown in Section 4.4.4 that the density profiles of halos in both the EAGLE and DMO simulations are well described by an NFW profile over the range $[0.05 - 1]R_\mathrm{vir}$, so we fit an NFW model over this range.

Fig. 4.11 shows the NFW concentration of relaxed halos as a function of halo mass for the DMO and EAGLE simulations. The top panel shows the DMO simulation. The black line is the best fit power law of Eqn. 4.20 to the solid black circles (corresponding to the stacks containing at least five halos) using Poissonian errors for each bin. We have verified that fitting individual halos (faint green circles in

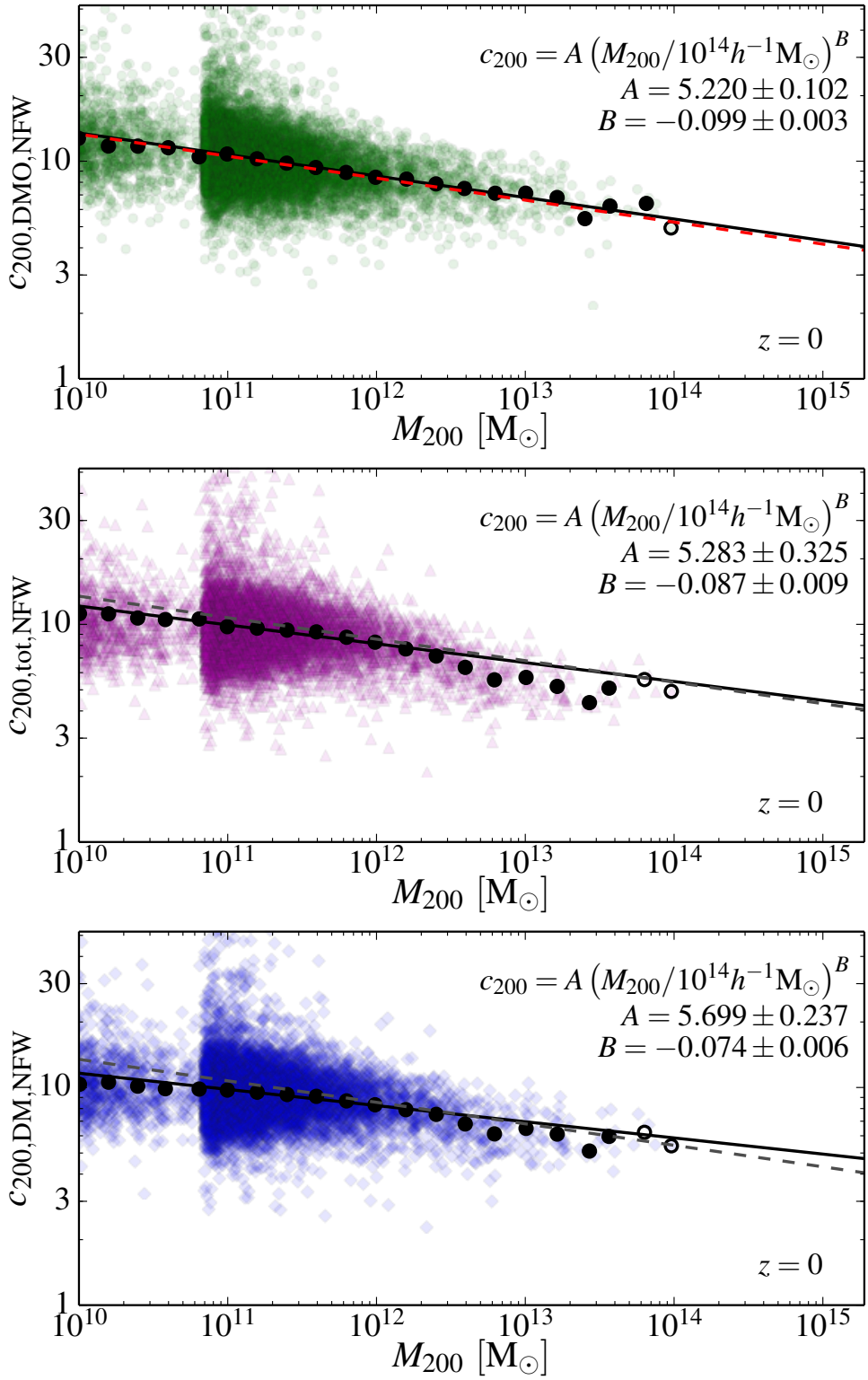

Figure 4.11: Halo concentration, c_{200}, as a function of mass M_{200}. The top panel shows the DMO simulation fit with the canonical NFW profile over the range $[0.05 - 1]R_{\mathrm{vir}}$. The middle panel shows the same fit applied to the total matter density profiles of the EAGLE halos.

Figure 4.11: (continued) The bottom panel shows the same fit to just the dark matter in the EAGLE halos. The faint coloured points in each panel are the values for individual halos and the black circles the values for the stacked profiles in each mass bin. Halos and stacks with $M_{200} < 6 \times 10^{10} \mathrm{M}_{\odot}$ are taken from the L0025N0752 simulation whilst the higher mass objects have been extracted from the L100N1504 simulation. The solid black line is the best-fit power law (Eqn. 4.20) to the solid black circles. The best-fit parameters are shown in each panel. The best-fit power law to the DMO halos is repeated in the other panels as a dashed line. The red dashed line on the first panel is the best-fit relation from Dutton & Macciò (2014).

Table 4.3: Best fitting parameters and their 1σ uncertainty for the mass-concentration relation (Eqn. 4.20) of the stacks of relaxed halos. The values correspond to those shown in the legends in Fig. 4.11. From top to bottom: NFW fit to the DMO halos, NFW fit to the total mass of the EAGLE halos, and NFW fit to the dark matter component of the EAGLE halos. All profiles were fit over the radial range $[0.05 - 1]R_{\rm vir}$. The uncertainties are taken to be the diagonal elements of the covariance matrix of the least-squares fitting procedure.

Fit	A	B
$c_{200,\rm DMO}$	5.22 ± 0.10	-0.099 ± 0.003
$c_{200,\rm tot,NFW}$	5.283 ± 0.33	-0.087 ± 0.009
$c_{200,\rm DM,NFW}$	5.699 ± 0.24	-0.074 ± 0.006

the same figure) returns essentially the same values of A and B. Table 4.3 lists the best-fitting values of these parameters. It is worth mentioning that the best-fitting power laws fit the halo stacks in the simulations equally well.

The mass-concentration relation of Dutton & Macciò (2014) is shown as a red dashed line in the top panel of Fig. 4.11. This fit is based on a series of DMO cosmological simulations of a ΛCDM model very similar to ours with the cosmological parameters values taken from the Planck Collaboration et al. (2014) data. Using several volumes at different resolutions, they were able to determine the concentration-mass relation over the range $10^{10}{\rm M}_\odot < M_{200} < 1.5 \times 10^{15}{\rm M}_\odot$ at $z = 0$. Fitting an NFW model to estimate the concentration, as we do here, they obtained

$$c_{200} = 5.05 \left(\frac{M_{200}}{10^{14} h^{-1} {\rm M}_\odot} \right)^{-0.101},$$

which agrees well with our results.

Not unexpectedly, given the sensitivity of the concentration to changes in the cosmological parameters, the values for the fit we obtain for the DMO simulation are significantly different from those reported by Neto et al. (2007), Macciò et al. (2007) and Duffy et al. (2008). Compared to the latter, the slope (B) is steeper and the normalisation (A) is higher. This change can be attributed mainly to changes in

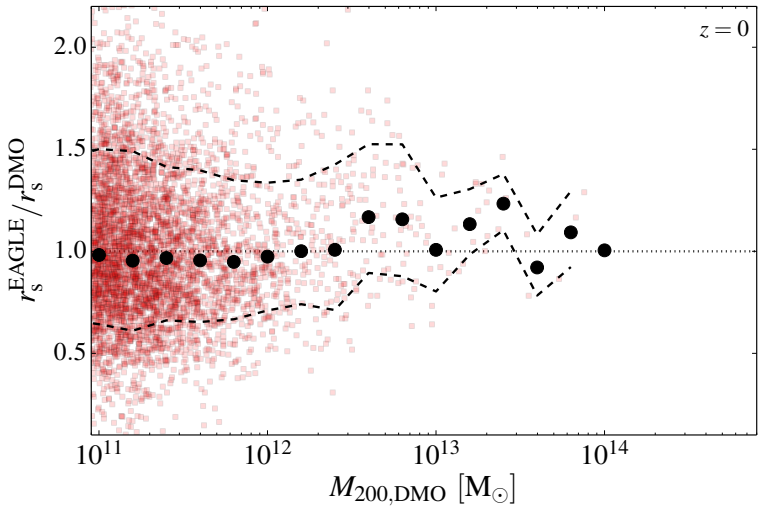

Figure 4.12: Ratio of NFW scale radii, $r_{\rm s}$, in matched relaxed halos in the DMO and EAGLE simulations. The black points are placed at the geometric mean of the ratios in each mass bin.

the adopted cosmological parameters $(\sigma_8, \Omega_{\rm m})$ which were $(0.796, 0, 258)$ in Duffy et al. (2008) and $(0.8288, 0.307)$ here.

The second panel of Fig. 4.11 shows the concentrations for the total matter density profiles of the EAGLE simulation obtained using the same fitting procedure. The best-fitting parameters for the mass - concentration relation are given in the second line of Table 4.3. Both the amplitude and slope are consistent with the values for the DMO simulation. As discussed in Section 4.3.1, matched halos in the DMO and EAGLE simulations have, on average, a lower mass in the EAGLE simulation. For the smallest halos, the average ratio is as low as 0.72. Because of this shift in mass, some difference in the concentration-mass relation might be expected between the two simulations but, since the value of the slope is small and $0.72^{-0.1} \simeq 1.04$, the effect on the amplitude is also small. A consequence of the shift in M_{200} is that the relative sizes of R_{200} for matched halos is $R_{200}^{\rm EAGLE}/R_{200}^{\rm DMO} \simeq 0.9$. In Fig. 4.12 we show that the mean ratio of $r_{\rm s}^{\rm EAGLE}/r_{\rm s}^{\rm DMO}$ for matched relaxed halos is also slightly below unity, so the net effect of those two shifts is that the concentrations are very similar in the two simulations.

Finally, the bottom panel of Fig. 4.11 shows the concentration of the DM only

component of EAGLE halos. We fit an NFW profile in the same way as for the total matter profiles in the panels above. As would be expected from the analysis of Fig. 4.8 and the fact that the outer parts of the dark halos are well described by the NFW profile, the same trend with mass can be seen as for the DMO simulation. The best-fitting power law to the mass-concentration relation is given at the bottom of Table 4.3. The values of the parameters are again close to the ones obtained for both the EAGLE and the DMO simulations.

We stress that the agreement between the EAGLE and DMO simulations breaks down if we include radii smaller than $0.05R_{\rm vir}$ in the fit. Hence, the mass - concentration relation given for EAGLE in Table 4.3 should only be used to infer the density profiles beyond $0.05R_{\rm vir}$.

4.4.7 Best-fit parameter values for the new density profile

We showed in Section 4.4.4 that the density profiles of halos in the EAGLE simulation are not well fit by an NFW profile in the inner regions, and we proposed Eqn. 4.16 as a new fitting formula for these profiles. This new profile has two lengthscales, $r_{\rm s}$ and $r_{\rm i}$, where the former describes the NFW-like outer parts of the halo, and the latter the deviations from NFW in the inner regions. For lower-mass halos these two lengths become similar, so both terms of the profile can contribute significantly to the density at all radii. We can still define the concentration of a halo in this model as $R_{200}/r_{\rm s}$, but we would expect to obtain a different mass-concentration relation from that for the dark matter-only case. Fig. 4.13 shows this relation for relaxed EAGLE halos. The anticorrelation seen when fitting an NFW profile is still present and we can use the same power-law formulation to describe the mass-concentration relation of our halo stacks. The values of the best-fit parameters, given in the figure, differ significantly from those obtained using the NFW fits listed in Table 4.3.

We now consider the two remaining parameters of the profile described by Eqn. 4.16. The inner component is characterized by two quantities, a scale radius, $r_{\rm i}$, and a density contrast, $\delta_{\rm i}$. We stress that this inner profile should not be inter-

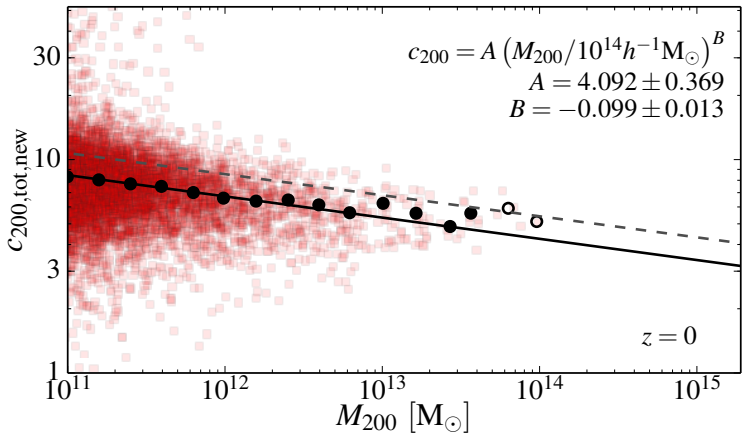

Figure 4.13: Halo concentration, c_{200}, as a function of mass, M_{200}, for the total matter density profiles of the EAGLE simulation using the fitting function of Eqn. 4.16 and the r_{s} parameter to define the concentration, $c_{200} = R_{200}/r_{\mathrm{s}}$. The colour points are for individual halos and the black circles for the stacked profiles in each mass bin. The solid black line is the best-fit power law (Eqn. 4.20) to the solid black circles. The best-fit values are given in the legend at the top right. The dashed line shows the best fitting power law to the halos extracted from the DMO simulation fitted using an NFW profile.

preted as the true underlying model of the galaxy at the centre of the halo. It is an empirical model that describes the deviation from NFW due to the presence of stars and some contraction of the dark matter. The profiles have been fit using the procedure described in Section 4.4.4 using all radial bins with $r > r_{\rm c}$.

The dependence of the $r_{\rm i}$ scale radius on the halo mass is shown in Fig. 4.14. The radius $r_{\rm i}$ is roughly constant over the entire halo mass range in the simulation. The scatter is large at all masses, but there is a weak trend with mass in the low-mass regime. This regime is, however, difficult to study as may be seen in the first few panels of Fig. 4.8: for the smallest halos, the effects due to baryons are small and the profile is thus closer to NFW than for the higher-mass bins.

The empirical profile (Eqn. 4.16) tends towards an NFW profile as $\delta_{\rm i} \to 0$ or $r_{\rm i} \to 0$. We find that, for the smallest halos, there is a degeneracy between these two parameters and the values of $r_{\rm i}$ and $\delta_{\rm i}$ can be changed by an order of magnitude (self-consistently) without yielding a significantly different $\sigma_{\rm fit}$ value. This is not a failure of the method but rather a sign that the baryonic effects on the profile shape become negligible for the lowest-mass haloes, at least for the range of radii resolved in this chapter.

Rather than working with the $\delta_{\rm i}$ and $r_{\rm i}$ parameters, we can combine them into a single parameter that reflects the additional mass contained in the central parts of the halo above and above that from the NFW component. Integrating the inner profile up to $r_{\rm i}$, we can obtain an estimate of this additional mass which we define as:

$$M_{\rm i} = (2\pi \ln 2)\rho_{\rm cr} r_{\rm i}^3 \delta_{\rm i} \approx 4.355 \rho_{\rm cr} r_{\rm i}^3 \delta_{\rm i}. \tag{4.21}$$

If $r_{\rm i}$ were really constant, then $M_{\rm i}$ would simply be a proxy for $\delta_{\rm i}$.

The mass, $M_{\rm i}$, is shown in Fig. 4.15 as a function of the halo mass, M_{200}. The black points corresponding to the stacked profiles lie in the middle of the relation for individual halos. The mass, $M_{\rm i}$, increases with halo mass. For halos with $M_{200} \lesssim 10^{12}{\rm M}_{\odot}$, the fraction, $M_{\rm i}/M_{200}$, increases with M_{200} highlighting that the effect of the baryons is more important for the bigger halos. This could have been expected by a careful inspection of Fig. 4.4, which shows that the central stellar and baryonic

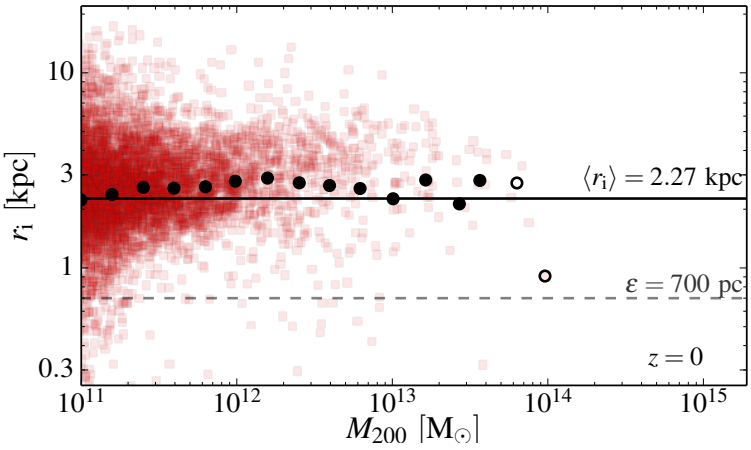

Figure 4.14: The characteristic radius, r_i, of the central component as function of halo mass (Eqn. 4.16) for halos in the EAGLE simulation. The red squares correspond to all the halos fitted individually and the overlaying black circles to the stacked halos in each mass bin. Stacks containing less than three objects are shown as open circles. The minimum Plummer-equivalent softening length ($\epsilon = 0.7$ kpc) is indicated by the grey dashed line at the bottom of the figure. The average value of the stacks with more than three objects is indicated by a solid black line.

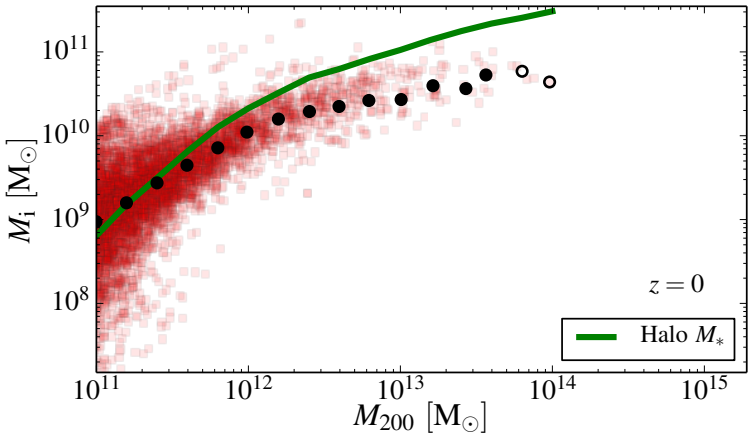

Figure 4.15: The mass, M_i, defined in Eqn. 4.21, as a function of halo mass, M_{200}. The red squares correspond to the individual halos and the overlaying black circles to the stacked profiles. The green solid line is the stellar mass - halo mass relation from the EAGLE simulation (Schaye et al., 2015).

fractions peak at $M_{200} \approx 10^{12}\mathrm{M}_{\odot}$. For larger halos, the M_{200}-$M_{\rm i}$ relation flattens reflecting the decrease in stellar fractions seen at the centre of the largest EAGLE halos.

To confirm this conjecture, we plot the stellar mass - halo mass relation for the EAGLE simulation as a solid green line in the same figure (Schaye et al., 2015)[1]. Neglecting the two highest mass bins (open circles), the similarity between this relation and our somewhat arbitrary definition of $M_{\rm i}$ seems to indicate that the stellar mass of the halos is related to this parameter. The definition of the mass, $M_{\rm i}$, could also be modified to take into account other properties of the galaxy in the halo. We could, for instance, include the galaxy size (half-stellar mass radius or half-light radius, for example) instead of $r_{\rm i}$ in the definition of $M_{\rm i}$. It would then be interesting to see how this newly defined mass correlates with the galaxy's stellar mass.

4.4.8 A non-parametric estimate of the concentration

The definition of concentration assumes that the halos are well fit by an NFW (or other) profile. This is the case for our sample of halos down to radii $\sim 0.05R_{\rm vir}$, so we can safely compute the concentration of these halos as $r_{\rm s} > 0.05R_{\rm vir}$ for almost all cases of interest. It is nevertheless worthwhile measuring a proxy for the concentration which does not rely on a specific parametrization of the profile. This is also more convenient for observational purposes, where a large range of radii are not always available to perform a fit. A simpler estimator of the concentration can then help constrain the models without making assumptions about the exact shape of the profile. This is particularly true for X-ray observations because it is difficult to detect X-ray emission all the way to the virial radius.

Such an estimator is given by the ratio of spherical over-density radii R_{500}/R_{2500} (e.g. Duffy et al., 2010). Both of these quantities can be obtained without assuming anything about the slope and functional form of the matter density profile. We show the value of this ratio as a function of the spherical enclosed mass, M_{500},

[1]Note that the EAGLE simulation reproduces abundance matching results (Schaye et al., 2015).

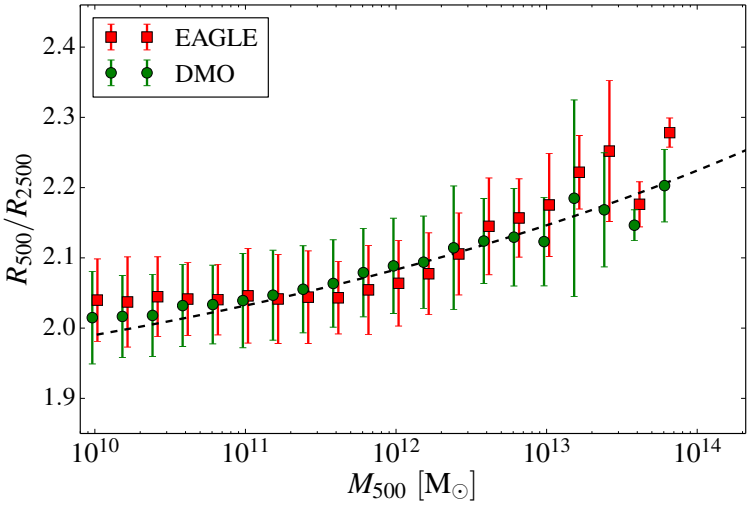

Figure 4.16: The average ratio of the R_{500} and R_{2500} radii as a function of halo mass, M_{500}, for both the EAGLE (red squares) and DMO (green circles) simulations.The error bars represent the 1σ scatter in the population. To ease the reading of the plot, the points with error bars have been artificially displaced by 0.02dex towards the left and right for the EAGLE and DMO results respectively. The black dashed line shows the expected relation for a NFW profile with the concentration-mass relation determined for the EAGLE simulation in Section 4.4.6.

in Fig. 4.16. The EAGLE and DMO simulations show the same trends and the differences between them are smaller than the scatter between individual halos. As could already be seen from the profiles in Figs. 4.6 and 4.8, the effect of modelling the baryons is concentrated at small radii, well within R_{2500}.

4.4.9 Limitations of the subgrid model

The convergence test in subsection 4.4.1 demonstrated that the simulation results of interest here are converged at radii, $r > r_c$ (given by a modified version of the criterion proposed by Power et al. 2003) and that even at smaller radii the profiles of stacked halos remain remarkably similar when the resolution is increased by a factor of 8 in particle mass. A halo of mass $M_{200} \approx 10^{11}\mathrm{M}_\odot$ is then resolved with $\mathcal{O}(10^5)$ particles and its stellar disk with $\mathcal{O}(10^3)$ particles, which is enough to sample star formation histories with good accuracy and obtain a realistic galaxy population (Schaye et al., 2015; Furlong et al., 2015; Crain et al., 2015).

An interesting aspect of our simulations is that no halos (of any mass) develop density cores in their central regions within the resolved radial range. By contrast, simulations of dwarf galaxies by a number of authors produce such cores (see Pontzen & Governato, 2014, for a review). As shown by Navarro et al. (1996a), a physical mechanism that can produce a flattening of the inner dark matter density profile is the sudden removal, in a starburst, of gas that had previously contracted enough to become self-gravitating, dominate the central gravitational potential and slowly drag dark matter in. The subsequent loss of binding energy from the central regions by the removal of that gas on a timescale shorter than the local dynamical time causes the dark matter to flow outwards resulting in a flattening of the profile to a degree that depends on the size and mass of the self-gravitating gas component. According to Pontzen & Governato (2014) a variant of this process is responsible for the formation of cores in the dwarf galaxy simulations of Governato et al. (2010) and related simulations (e.g. Brook et al., 2012; Di Cintio et al., 2014).

An important aspect of the simulations by Governato et al. (2010) and subse-

quent ones that also produced cores is that the assumed subgrid model adopts a higher density threshold for star formation ($10 - 100\ m_{\rm H} \cdot {\rm cm}^{-3}$) than we have assumed in EAGLE (a metallicity-dependent threshold with a value of $0.031\ m_{\rm H} \cdot {\rm cm}^{-3}$ at solar metallicity that traces the density above which a cold, molecular gas phase is expected to be present; see Schaye (2004); Schaye et al. (2015))[2]. Although even the high value assumed by Governato et al. (2010) is many orders of magnitude below the gas density in the star-forming cores of molecular clouds, it probably allows a substantial amount of gas to dominate the potential in the central regions prior to a starburst, as required for the Navarro et al. (1996a) mechanism to operate[3].

It is not obvious *a priori* which, if any, of the subgrid models for star formation used to date is more appropriate, but an important virtue of the EAGLE subgrid model is that it leads to a population of galaxies with properties that agree well with a large set of observations, from the regime of dwarf galaxies to the regime of galaxy clusters (Schaye et al., 2015; Furlong et al., 2015; Crain et al., 2015; Sawala et al., 2014a), chapter 5. None of the simulations that produce cores in the dark matter has yet been able to demonstrate such success. Indeed, other large cosmological simulations with different subgrid models to EAGLE such as "Illustris" do not appear to have produced density cores either Vogelsberger et al. (2014). In any event, the case for the existence of cores in real galaxies is still a matter of lively debate (e.g. Strigari et al., 2010, 2014, and references therein).

Finally, we stress that the conclusions in this chapter refer only to radii larger than $r > r_{\rm c} \approx 1.8\ {\rm kpc}$. Higher resolution simulations would be required to test whether our subgrid model can generate density cores on smaller scales than those resolved in the present work.

[2]A significant number of stars in EAGLE, however, form from gas at much higher densities that the threshold; see Crain et al. (2015)

[3]It is unclear whether cold, dense star-forming clouds in a multiphase interstellar medium McKee & Ostriker (1977) would contain enough mass to dominate the central potential of the halo.

4.5 Conclusions

The aim of this chapter was to characterize the mass density profiles of dark matter halos in a cosmological ΛCDM simulation, which includes dark matter and baryons, and in which the resulting galaxy population has realistic stellar masses and sizes; we also quantified the differences with halos in a dark matter-only simulation. We used the state-of-the-art EAGLE simulation from which we selected halos above $10^9\mathrm{M}_\odot$ to study changes in the mass, and above $10^{11}\mathrm{M}_\odot$ to study changes in the internal structure. Our results can be summarized as follows:

1. The mass, M_{200}, of halos is reduced by the inclusion of baryons and associated energy feedback effects. At the low mass end, feedback from star formation expels gas and this reduces the total mass, radius and growth factor of the halo; the reduction in mass can be as large as 30% for halos with $M_{200} \lesssim 10^{11}\mathrm{M}_\odot$. This reduction is progressively smaller for larger halos as the source of feedback shifts from star formation to AGN. In the EAGLE simulation there is virtually no effect for masses $M_{200} \gtrsim 10^{14}\mathrm{M}_\odot$, but the exact value of the mass at which this happens could be larger if, as suggested by Schaye et al. (2015), more effective AGN feedback is necessary than is present in EAGLE. The reduction in mass can be described by the double-sigmoid function of Eqn. 4.10, and the scatter around the mean by the formula of Eqn. 4.11.

2. The circular velocity curves of the EAGLE halos are in excellent agreement with observational data for galaxies with stellar mass ranging from $10^9\mathrm{M}_\odot$ to $5 \times 10^{11}\mathrm{M}_\odot$ (corresponding to halo masses in the range $10^{11} \lesssim M_{200}/\mathrm{M}_\odot \lesssim 10^{13}$).

3. The radial density profiles of EAGLE halos over the radial range $[0.05R_{\mathrm{vir}}, R_{\mathrm{vir}}]$ are very similar to the profiles of halos in dark matter-only simulations and are well described by the NFW formula. Halo concentrations estimated by fitting NFW profiles over this range are also very similar to the dark matter-only case.

4. The central regions of halos more massive than $M_{200} \gtrsim 10^{12}\mathrm{M}_{\odot}$, on the other hand, are dominated by the stellar component. The presence of these baryons causes a contraction of the halo, enhancing the density of dark matter in this region. The variation in profile shape is greatest for halos in the mass range $M_{200} = 10^{12}\mathrm{M}_{\odot} - 10^{13}\mathrm{M}_{\odot}$ where the stellar mass fraction peaks (as does the total baryonic mass fraction within $0.05R_{\mathrm{vir}}$

5. The radial density profiles of the EAGLE halos can therefore be well fit (over the radial range resolved in the simulation) by the sum of an NFW profile, which describes the outer, dark matter-dominated regions, and an NFW-like profile with a sharper bend, which describes the combined effect of the presence of stars and the contraction of the dark matter halo (Eqn. 4.16). Of the two additional parameters required in this fit, one, r_{i}, is approximately constant with halo mass, while the other one, the characteristic inner mass scale, M_{i}, scales with halo mass in a similar way to the stellar mass of the central galaxy.

The way in which galaxy formation affects the host halos is a problem that can only be reliably addressed with simulations of the kind we have described here. However, it is clear that the nature of these effects is sensitive to the way in which the baryon physics are implemented, particularly to the subgrid models for feedback from star formation and AGN. The EAGLE simulations have the great advantage that the subgrid models have been calibrated so that the simulation reproduces the local galactic stellar mass function as well as the distribution of galaxy sizes, and they also reproduce a wide variety of other observations. This lends a certain degree of credibility to our results and it would be interesting to compare them with other simulations that assume different subgrid models but achieve similarly good matches to observables over a large range of halo masses. A limited comparison of this kind is carried out in Appendix A.

The simulations investigated here do not have enough resolution to study dwarf galaxies for which there is much discussion regarding the formation of central cores

in the dark matter density distribution (for a review see Pontzen & Governato, 2014). However, the related high resolution simulations of the Local Group by Sawala et al. (2015), which use essentially the same subgrid models as EAGLE, do resolve dwarfs. The behaviour of these smaller halos simply continues to smaller masses the trends seen here: the halos become increasingly dark matter-dominated and remain well described by the NFW profile.

Chapter 5

The effect of baryons on the inner density profiles of rich clusters

5.1 Introduction

Simulations of structure formation in the cold dark matter (CDM) model predict that relaxed dark matter (DM) halos of all masses should have nearly self-similar spherically-averaged density profiles that are well described by a simple law with a central cusp, $\rho(r) \propto r^{-1}$, and a steeper slope, $\rho(r) \propto r^{-3}$, at large radii (Navarro et al., 1996b; Navarro et al., 1997). This Navarro-Frenk-White (NFW) profile provides a good approximation to halos in N-body simulations, in which the dark matter is treated as a collisionless fluid. Very high-resolution simulations of this kind have shown that the profiles are not always completely self-similar and that the inner slope could be shallower than the asymptotic NFW value (Navarro et al., 2004, 2010; Neto et al., 2007; Gao et al., 2008, 2012b; Dutton & Macciò, 2014). Despite these small variations, the form of the dark matter density profile is a robust and testable prediction of the CDM paradigm.

In the real world sufficiently massive halos contain baryons whose evolution might affect the density structure of the dark matter. Several processes have been proposed that could modify the central density profile, flattening it (Navarro et al., 1996a; Pontzen & Governato, 2012; Martizzi et al., 2012) steepening it (Blumenthal et al., 1986; Gnedin et al., 2004) or leaving it broadly unchanged (Laporte & White, 2015). Understanding the impact of these competing effects requires cosmological

hydrodynamical simulations (e.g. Duffy et al., 2010; Gnedin et al., 2011; Di Cintio et al., 2014; Vogelsberger et al., 2014), but these are far more challenging than N-body simulations and it is still unclear whether they can treat all the relevant scales and processes sufficiently accurately.

If the effects of baryons can be reliably established, the density profiles of halos could, in principle, reveal much about the nature of the dark matter. For example, if the dark were self-interacting rather than effectively collisionless, with a sufficiently large self-interaction cross-section, the inner halo density profile could be shallower than the NFW form even in the absence of baryonic effects (e.g. Spergel & Steinhardt, 2000; Vogelsberger et al., 2012; Rocha et al., 2013). Similarly, if dark matter particles decay or annihilate, they could produce potentially detectable particles or radiation whose intensity depends sensitively on the inner density profile.

From the observational point of view, studies of the inner dark matter density profiles have focussed on the two extremes of the halo mass distribution: dwarf galaxies and galaxy clusters. Dwarf galaxies (e.g. Walker & Penarrubia, 2011) are attractive because their very high mass-to-light ratios suggest that baryonic effects may have been unimportant. However, degeneracies in the analysis of photometric and kinematic data have so far led to inconclusive results (e.g. Strigari et al., 2010, 2014). Galaxy clusters are also attractive because baryons are relatively less important in the central regions than in L_* galaxies and their inner profiles can be probed by strong and weak lensing, as well as by the stellar kinematics of the central cluster galaxy.

Studies of the inner dark matter density structure in clusters have so far produced conflicting results. For example, Okabe et al. (2013) find that a sample of 50 clusters with good gravitational lensing data have density profiles that agree well with the NFW form from the inner $100h^{-1}$ kpc to the virial radius. Using X-ray observations, Pointecouteau et al. (2005), Vikhlinin et al. (2006) and Umetsu et al. (2014) similarly find that the total matter profile follows closely an NFW profile at $r \gtrsim 0.05R_{200} \approx 10 - 20$ kpc. On the other hand, combining strong and weak lensing with stellar kinematics, Sand et al. (2004) and Newman et al. (2013a,b) find that the

total central profile closely follows the NFW form but, once the contribution of the stellar component has been subtracted, the inferred dark matter density profile is significantly flatter than NFW.

Here we analyse a sample of massive clusters ($M_{200} \gtrsim 10^{14}\mathrm{M}_{\odot}$) from the "Evolution and assembly of galaxies and their environment" (EAGLE) cosmological hydrodynamical simulation (Schaye et al., 2015). This is one of a new generation of simulations which follow the evolution of relatively large volumes using the best current understanding of the physical processes responsible for galaxy formation. Since many of these processes cannot be resolved in these simulations, they are represented by 'subgrid' models which can be quite different in different simulations (e.g. Schaye et al., 2010; Scannapieco et al., 2012; Okamoto et al., 2014; Vogelsberger et al., 2014).

The EAGLE simulation is sufficiently realistic that it may be compared to a range of observed galaxy properties at different cosmic epochs. The galaxy population in the simulation shows broad agreement with basic properties such as the stellar mass function and star formation history, colour, size and morphology distributions, as well as scaling relations between photometric and structural properties (Schaye et al., 2015; Crain et al., 2015; Furlong et al., 2015; Trayford et al., 2015). In this chapter we focus on the effects of baryonic processes on the central density structure of the most massive galaxy clusters in the EAGLE simulation.

Our chapter is organized as follows: in Section 5.2, we briefly describe the EAGLE simulation; in Section 5.3, we measure the density profile of our simulated clusters; in Section 5.4 we focus on the inner profile slope and compare to recent observations; in Section 5.5 we carry out a more detailed comparison with the data of Newman et al. (2013b). We summarize our results in Section 5.6. Throughout this chapter, we assume values of the cosmological parameters inferred from the Planck satellite data for a ΛCDM cosmology (Planck Collaboration et al., 2014), the most relevant of which are: Hubble constant, $H_0 = 67.7$ km s^{-1}Mpc^{-1}; baryon and total matter densities in units of the critical density, $\Omega_\mathrm{b} = 0.0482$ and $\Omega_\mathrm{m} = 0.307$ respectively, and linear power spectrum normalization, $\sigma_8 = 0.829$.

5.2 The EAGLE simulations

The EAGLE set consists of a series of cosmological simulations with state-of-the-art treatments of smoothed particle hydrodynamics and subgrid models. The simulations reproduce the stellar mass function and other observed properties of the galaxy population at $z = 0$, and produce a reasonable evolution of the main observed galaxy properties over cosmic time (Schaye et al., 2015; Crain et al., 2015; Furlong et al., 2015).

In brief, the largest EAGLE simulation follows $1504^3 \approx 3.4 \times 10^9$ dark matter particles and the same number of gas particles in a 100^3 Mpc^3 cubic volume[1] from ΛCDM initial conditions generated using 2nd order Lagrangian perturbation theory (Jenkins, 2010) with the linear phases taken from the public multiscale Gaussian white noise field, PANPHASIA (Jenkins, 2013). The mass of a dark matter particle is $9.7 \times 10^6 \mathrm{M}_\odot$ and the initial mass of a gas particle is $1.8 \times 10^6 \mathrm{M}_\odot$. The gravitational softening length is 700 pc (Plummer equivalent). The simulation was performed with a heavily modified version of the GADGET-3 code last described by Springel (2005), using a pressure-entropy formulation of SPH (Hopkins, 2013) and new prescriptions for viscosity and thermal diffusion (Dalla Vecchia (in prep.), see also chapter 3) and time stepping (Durier & Dalla Vecchia, 2012). We now summarize the subgrid model.

5.2.1 Baryon physics

The subgrid model is an improved version of that used in the GIMIC and OWLS simulations (Crain et al., 2009; Schaye et al., 2010). Star formation is implemented using a pressure-dependent prescription that reproduces the observed Kennicutt-Schmidt star formation law (Schaye & Dalla Vecchia, 2008) and uses a threshold that captures the metallicity dependence of the transition from the warm, atomic

[1]Note that the units do not have factors of h.

to the cold, molecular gas phase (Schaye, 2004). Star particles are treated as single stellar populations with a Chabrier (2003) IMF evolving along the tracks provided by Portinari et al. (1998). Metals from AGB stars and supernovae (SNe) are injected into the interstellar medium (ISM) following the prescriptions of Wiersma et al. (2009b) and stellar feedback is implemented by injecting thermal energy into the gas as described in Dalla Vecchia & Schaye (2012). The amount of energy injected into the ISM by SNe is assumed to depend on the local gas metallicity and density in an attempt to take into account the unresolved structure of the ISM (Schaye et al., 2015). Supermassive black hole seeds are injected in halos above $10^{10}h^{-1}\mathrm{M}_{\odot}$ and grow through mergers and accretion of low angular momentum gas (Rosas-Guevara et al., 2015; Schaye et al., 2015). AGN feedback is modelled by the injection of thermal energy into the gas surrounding the black hole (Booth & Schaye, 2009; Dalla Vecchia & Schaye, 2012).

The subgrid model was calibrated (mostly by adjusting the intensity of stellar feedback and the accretion rate onto black holes) so as to reproduce the present day stellar mass function and galaxy sizes (Crain et al., 2015). The cooling of gas and the interaction with the background radiation is implemented following Wiersma et al. (2009a) who tabulate cooling and photoheating rates element-by-element in the presence of UV and X-ray backgrounds (Haardt & Madau, 2001).

Halos were identified using the Friends-of-Friends (FoF) algorithm (Davis et al., 1985) and bound structures within them were then identified using the SUBFIND code (Springel et al., 2001; Dolag et al., 2009). A sphere centred at the minimum of the gravitational potential of each subhalo is grown until the mass contained within a given radius, R_{200}, reaches $M_{200} = 200\,(4\pi\rho_{\rm cr}(z)R_{200}^3/3)$, where $\rho_{\rm cr}(z) = 3H(z)^2/8\pi G$ is the critical density at the redshift of interest.

5.2.2 Photometry

The luminosity and surface brightness of galaxies in the simulation are computed on a particle-by-particle basis as described by Trayford et al. (2015). The basic prescription for deriving the photometric attributes of each star particle is as follows.

Each star particle is treated as a single stellar population (SSP) of the appropriate age and metallicity as given by the simulation. The Bruzual & Charlot (2003, BC03) population synthesis model (assuming a Chabrier (2003) IMF for consistency with the simulation) gives the integrated spectrum of a SSP on a grid of age and metallicity. Using bilinear interpolation we estimate the radiated power in a particular band by integrating the spectrum through a filter transmission curve. (Before assigning broad-band luminosities, the metallicities are renormalised so that solar metallicity ($Z_\odot = 0.012$) is consistent with the older solar value assumed by BC03 ($Z_\odot = 0.02$)).

Because of the limited resolution of the simulation, a star particle represents a relatively large stellar mass. To mitigate discreteness effects, in each star formation event star particles with stellar ages $< 100\,\mathrm{Myr}$ are resampled from their progenitor gas particles and the currently star-forming gas in the subhalo in which the particle resides. Such resampling improves the match to the observed bimodality in galaxy colour-magnitude diagrams (Trayford et al., 2015). However, this treatment has very little impact on the properties of the brightest cluster galaxies (BCG) of interest here as their current star formation rates are negligible.

A modified Charlot & Fall (2000) dust model is used to attenuate the light emitted by star particles. The extinction is computed using a constant ISM optical depth and a transient molecular cloud component that disperses after $10\,\mathrm{Myr}$. We modified the model so that these values scale proportionally with galaxy metallicity according to the observed mass-metallicity relation of Tremonti et al. (2004). The resulting galaxy population gives a very good match to the observed luminosity function in various commonly used broad bands (Trayford et al., 2015).

5.3 The mass density profile of clusters

Our cluster sample consists of the six EAGLE halos of mass $M_{200} > 10^{14}\mathrm{M}_\odot$ (see Table 5.1), which we label Clusters 1 to 6. These clusters have moderate sphericity and would likely be considered relaxed in observational studies even if some of

Table 5.1: Properties of the six simulated clusters studied in this chapter. The stellar mass is measured within a $30\,\mathrm{kpc}$ spherical aperture. The baryon and stellar fractions are measured within R_{200} and are given in units of the universal baryon fraction, $f_\mathrm{b}^\mathrm{univ} = \Omega_\mathrm{b}/\Omega_\mathrm{m} = 0.157$.

Halo	M_{200} $[\mathrm{M}_\odot]$	R_{200} [kpc]	M_* $[\mathrm{M}_\odot]$	$f_\mathrm{b}/f_\mathrm{b}^\mathrm{univ}$	$f_*/f_\mathrm{b}^\mathrm{univ}$
1	1.9×10^{14}	1206	4.2×10^{11}	0.99	0.07
2	3.7×10^{14}	1518	3.5×10^{11}	0.94	0.08
3	3.0×10^{14}	1411	2.9×10^{11}	0.95	0.08
4	3.1×10^{14}	1422	4.5×10^{11}	0.97	0.07
5	2.0×10^{14}	1225	2.0×10^{11}	0.92	0.08
6	2.0×10^{14}	1229	3.7×10^{11}	0.93	0.08

them fail the strict relaxation criteria used in simulations (Neto et al., 2007). The stellar mass function of our cluster galaxies (including the BCG) provides a good match to observations (not shown here). Similarly, the sizes of cluster galaxies are in good agreement with observations. Thus, in many respects, the EAGLE rich cluster sample is quite realistic. It is worth mentioning that Schaye et al. (2015) showed that the gas fractions within R_{500} of the clusters in our sample may be too high when compared to observations. However, this small disagreement does not affect the results of this chapter where we focus on the very centres of the halos ($r \lesssim 20\,\mathrm{kpc}$) where the mass of gas is very small (see Fig. 5.2).

The main properties of our rich cluster sample are listed in Table 5.1. As shown by Schaye et al. (2015), the galaxy stellar masses are in good agreement with abundance matching relations (Moster et al., 2013). At the same time, the overall gas fractions within R_{200} are close to the cosmic mean, $f_\mathrm{b}^\mathrm{univ} = \Omega_\mathrm{b}/\Omega_\mathrm{m}$, as observed (Vikhlinin et al., 2006): the AGN feedback model has succeeded in suppressing star formation in the BCG without removing excessive amounts of gas from the halos.

A surface brightness map of Cluster 1 is shown in Fig. 5.1. The map is centred

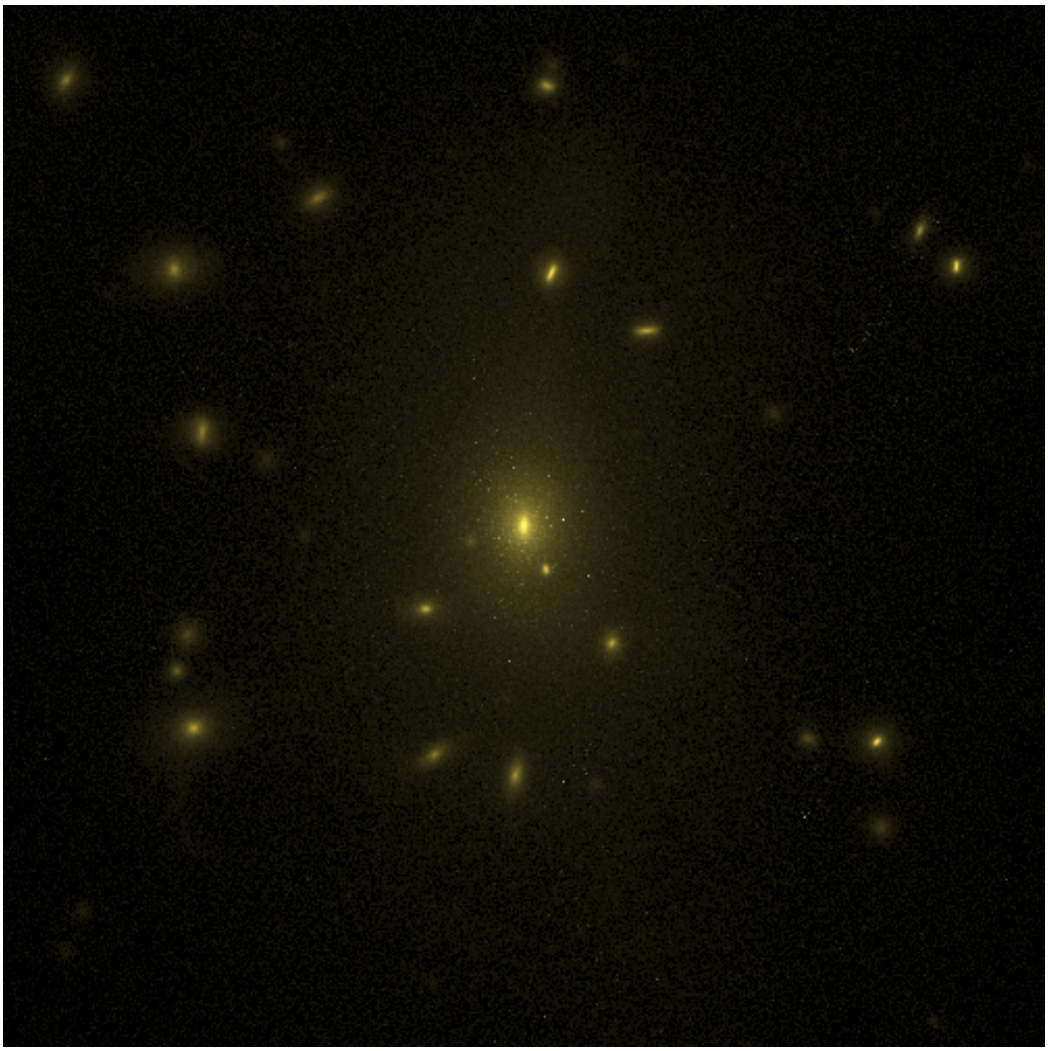

Figure 5.1: Surface brightness map of Cluster 1, using the SDSS ugr filter system. The map is $500\ \mathrm{kpc}$ on a side and has resolution of $1\ \mathrm{kpc}$. The central galaxy is easily visible and appears slightly elongated in projection. Satellite galaxies are also visible and cluster around the BCG.

on the centre of potential of the halo and shows a $500\ \mathrm{kpc} \times 500\ \mathrm{kpc}$ area of sky. Photometry for the model galaxies in the u, g and r-band SDSS filters (Doi et al., 2010) was obtained as described in Section 5.2.2. The surface brightness is then used to construct fake colour mock images following the method of Lupton et al. (2004). As can be seen, the central part of the halo seems spherical. The central galaxy is slightly prolate and the central satellite galaxies cluster around it roughly isotropically.

5.3.1 The mass density profiles of simulated halos

To study the density profiles of the EAGLE clusters, we bin the particles in logarithmically spaced radial bins centred on the minimum of the gravitational potential. We measure the dark matter, gas and stellar components separately and then sum all contributions to obtain the total mass profile. The result is shown in Fig. 5.2, where the six panels correspond to the six clusters of Table 5.1. In each panel, the green diamonds, black squares, red stars and blue circles represent the total mass, dark matter, stellar component and gas, respectively. The mass of each halo is indicated at the top of each panel. The dashed vertical lines show the radius, r_c, above which the profile is considered to have converged within 20% (Power et al., 2003; Schaller et al., 2015a). This is a conservative estimate of the convergence radius ($\sim 3.1\ \mathrm{kpc}$) and it is much larger than the Plummer-equivalent softening length ($\epsilon = 0.7\ \mathrm{kpc}$) often used as a rough estimate of the radius beyond which numerical effects become unimportant. Data points within this 'convergence radius' but at radii $r > \epsilon$ are shown using fainter symbols.

The dark matter dominates the density profiles at $r \gtrsim 8\mathrm{kpc}$. At smaller radii, the stellar component dominates and exceeds the dark matter density by up to an order of magnitude at the centre. The stellar density profiles are approximately constant power laws, $r^{-\alpha}$, with $\alpha \approx -3$ down to the very centre of the galaxy. The simulation does not resolve the centre of the BCG and the slopes measured there are probably affected by the force softening ($0.7\ \mathrm{kpc}$ at $z = 0$) used in the N-body solver. The peaks in the stellar components at large radii are caused by satellites

orbiting in the halo. The gas is subdominant at all radii, in particular in the central regions where the stellar densities are almost three orders of magnitude higher. The gas only dominates the baryon content at radii $r \gtrsim 50$ kpc. At radii larger than ~ 300 kpc, the gas profile has the same shape as the dark matter profile. The dark matter itself has the characteristic NFW shape, whose asymptotic behaviour is a power-law of slope -1 at the centre and a power law of slope -3 in the outer parts.

5.3.2 Fitting models to the simulated halos

The density profiles of relaxed dark matter halos in N-body simulations are well fit by the near-universal NFW profile which has the form:

$$\frac{\rho(r)}{\rho_{\rm cr}} = \frac{\delta_{\rm c}}{(r/r_{\rm s})\,(1+r/r_{\rm s})^2}, \tag{5.1}$$

(Navarro et al., 1996b; Navarro et al., 1997), where $\delta_{\rm c}$ is a characteristic amplitude and $r_{\rm s}$, a scale length that is often expressed in terms of the concentration, $c_{200} = R_{200}/r_{\rm s}$. Both $\delta_{\rm c}$ and c_{200} correlate with halo mass, M_{200}, so the NFW profile is fully specified by the halo mass. In our simulations, the cold gas and stars, which contribute only a small fraction of the total mass, are concentrated towards the centre, while the hot gas beyond the central regions closely follows the dark matter profile. Thus, even in the presence of baryons, the *dark matter* still closely follows an NFW profile. In the case of halos of mass $M_{200} \sim 10^{12} - 10^{13}{\rm M}_{\odot}$, the profile is slightly modified in the centre by a modest contraction due to the presence of stars (Duffy et al., 2010; Di Cintio et al., 2014; Schaller et al., 2015a).

Baryon contraction is less important in halos of mass $M_{200} \sim 10^{14}{\rm M}_{\odot}$ which are well fit by an NFW profile, as can be seen in Fig. 5.2, where the solid magenta line shows the best-fit NFW profile. The fit was performed using all radial bins from the resolution limit, $r_{\rm c} \sim 3$ kpc, to the virial radius, $R_{\rm vir} \sim 2$Mpc. We have checked that the best fitting parameter values are largely insensitive to the exact radial range used, provided that both the $\rho(r) \to r^{-1}$ and $\rho(r) \to r^{-3}$ regimes of the profile are well sampled. In all but one case, the magenta line closely tracks the

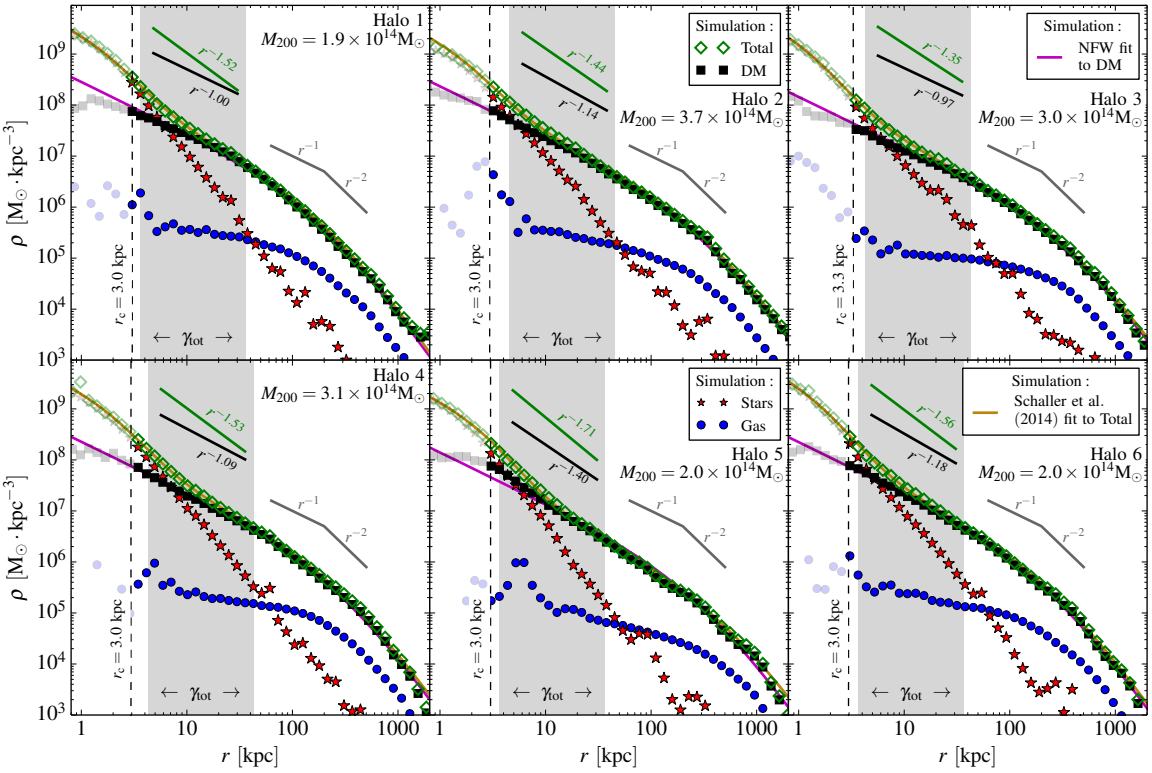

Figure 5.2: Radial density profiles of the six simulated clusters studied in this chapter (see Table 5.1). Green diamonds represent the total mass profile; the black squares, red stars and blue circles represent the dark matter, stellar and gas components respectively. The solid magenta and yellow lines are the best-fit NFW profile to the dark matter component and the best fit (Schaller et al., 2015a) profile (Eqn. 5.2) to the total mass distribution. The vertical dashed line in each panel shows the convergence radius, r_c, beyond which the density profile has converged to within 20%; data points within this radius are shown by fainter symbols. The grey shaded regions show the radial range over which the logarithmic slopes, $\gamma_{\rm tot}$ and $\beta_{\rm DM}$, of the total and DM profiles are measured. The values of the slopes are given above the simulation points. The DM halos are very well fit by NFW profiles and the total mass profiles only deviate from NFW in the central parts ($r \lesssim 10$ kpc), where the stellar component dominates. Note the similarities in the shapes of these six halos and the relatively small variations that occur mostly in the very central regions.

Table 5.2: Parameters of the best-fit NFW profiles (Eqn. 5.1) to the *dark matter* component of our halos.

Halo	M_{200} [$\mathrm{M}_\odot$]	R_{200} [kpc]	r_s [kpc]	c_{200}	δ_c
1	1.9×10^{14}	1206	199.2	6.1	1.1×10^4
2	3.7×10^{14}	1518	350.8	4.3	5.3×10^3
3	3.0×10^{14}	1411	452.0	3.1	2.5×10^3
4	3.1×10^{14}	1422	305.1	4.7	5.9×10^3
5	2.0×10^{14}	1225	331.1	3.7	3.3×10^3
6	2.0×10^{14}	1229	245.9	5.0	7.2×10^3

DM profile plotted as black squares. The exception is halo 5 (bottom row, middle panel) which shows a slight deviation from the NFW form in the radial range $3 - 7$ kpc, where some contraction is seen, possibly as a result of the recent accretion of a large substructure. The best-fit NFW parameters are listed in Table 5.2. The mean and scatter in concentration (nearly a factor of 2) of our halos are consistent with the results obtained for relaxed halos in the Millennium simulation by Neto et al. (2007), who found a concentration, $c_{200} = 4.51^{+0.71}_{-0.62}$, for halos of mass $M_{200} = 10^{14}\mathrm{M}_\odot$.

While the dark matter is well described by an NFW profile, the *total matter* profile in our halos is not. In our study of the entire halo population in the EAGLE simulation, we introduced the following fitting formula for the total matter (Schaller et al., 2015a):

$$\frac{\rho(r)}{\rho_\mathrm{cr}} = \frac{\delta_\mathrm{c}'}{(r/r_\mathrm{s}')\left(1 + r/r_\mathrm{s}'\right)^2} + \frac{\delta_\mathrm{i}}{(r/r_\mathrm{i})\left(1 + (r/r_\mathrm{i})^2\right)}. \tag{5.2}$$

The first term has the NFW form and describes the overall shape of the profile; the second term is a correction that reproduces the stellar cusps ($\rho_* \propto r^{-3}$), together with any dark matter contraction due to the presence of baryons. The dark yellow

Table 5.3: Parameters of the best-fit profiles of the form of Eqn. 5.2 (Schaller et al., 2015a) to the *total* matter distribution in our halo sample.

Halo	M_{200} $[\mathrm{M}_\odot]$	r'_s [kpc]	δ'_c	r_i [kpc]	δ_i
1	1.9×10^{14}	209.3	1.2×10^4	2.1	8.8×10^6
2	3.7×10^{14}	369.8	5.5×10^3	2.0	6.4×10^6
3	3.0×10^{14}	433.8	3.2×10^3	1.4	1.1×10^7
4	3.1×10^{14}	321.6	6.2×10^3	2.2	7.2×10^6
5	2.0×10^{14}	529.1	1.5×10^3	2.7	4.0×10^6
6	2.0×10^{14}	277.0	6.4×10^3	1.6	1.5×10^7

solid lines in the six panels of Fig. 5.2 show the best-fit profiles of this kind to each halo which, as may be seen from the figure, represent the data well over the entire resolved radial range. The best-fit parameter values are listed in Table 5.3.

5.4 The inner density profile

A testable prediction from simulations evolving only dark matter of the ΛCDM model is that the average slope of the inner mass profile ($r \ll r_\mathrm{s}$) should tend to the NFW value of -1. Steeper profiles might be explained by baryon effects causing some contraction. Significantly shallower profiles in massive halos, on the other hand, would be more difficult to explain. Explosive baryon effects could lower the inner dark matter density, and even induce cores, but only in dwarf galaxies (Navarro et al., 1996a; Read & Gilmore, 2005; Pontzen & Governato, 2014). In massive halos Martizzi et al. (2012) have argued that AGN feedback could introduce small (~ 10 kpc) cores, but it is unclear if this kind of feedback is compatible with the observed stellar masses of BCGs and the baryon fractions of clusters. Shallower inner profiles could also be generated if the dark matter is self-interacting (Vogelsberger et al., 2012; Rocha et al., 2013).

5.4.1 Total mass profiles: simulation results

A quantity that can be derived from observational data in selected samples of rich clusters is the *average logarithmic slope* of the inner density profile of the total mass, that is dark matter and baryons (e.g. Sand et al., 2004; Newman et al., 2013a):

$$\gamma_{\rm tot} \equiv -\left\langle \frac{d\log\rho_{\rm tot}(r)}{d\log r} \right\rangle_{r\in[0.003R_{200},0.03R_{200}]}, \tag{5.3}$$

where the average is over the radial range $[0.003R_{200}, 0.03R_{200}]$. It is important to recognize that the radial range typically probed by the data is *not* the asymptotic regime, $r \to 0$, where the NFW profile tends to $\rho(r) \propto r^{-1}$. Instead, in the region probed by observations, the NFW formula (Eqn. 5.1) predicts values of the inner slope significantly steeper than -1 (i.e. $\gamma_{\rm tot} > 1$):

$$\gamma_{\rm tot} = 1 + \log_{10}\left(\frac{(1+0.03c_{200})^2}{(1+0.003c_{200})^2}\right), \tag{5.4}$$

which, for the expected range of cluster concentrations ($c_{200} \in [3,5]$), gives $\gamma_{\rm tot} \approx 1.1$.

The radial range over which $\gamma_{\rm tot}$ is typically measured in observational studies is shown for our clusters as a grey shaded region in each panel of Fig. 5.2. The values of the slope predicted by our simulations in this range are shown above the data points. Values of $\gamma_{\rm tot}$ for our halo sample are plotted as a function of halo mass in Fig. 5.3 (large green diamonds), which also includes data for halos in the simulation volume that are less massive than those in our main sample (small green diamonds). The black dashed line shows the slope of the NFW profile obtained from Eqn. (5.4) and the mass-concentration relation of Schaller et al. (2015a). As a guide, we include two dashed-dotted lines showing where profiles may be considered to be "cuspy" ($\gamma_{\rm tot} > 1.5$) or "core-like" ($\gamma_{\rm tot} < 0.5$). The exact position of these lines is, of course, arbitrary.

The high mass tail of the cluster population is not represented in the limited volume of the EAGLE simulation. However, the general behaviour of massive clusters can be readily inferred from the trends seen for smaller halos. A halo of mass

$M_{200} \approx 2 \times 10^{15}\mathrm{M}_{\odot}$ has $R_{200} \approx 2$ Mpc and thus $\gamma_{\rm tot}$ is centred (logarithmically) around $r = 20$ kpc. In this region the profile is dominated by dark matter, even in the case of large, extended galaxies. Thus, $\gamma_{\rm tot}$ is unaffected by the BCG and directly reflects the slope of the DM profile which, as shown in chapter 4 showed has a slope close to or slightly steeper than the NFW value, as given by eq. 5.4. Thus, for halos of $M_{200} \approx 2 \times 10^{15}\mathrm{M}_{\odot}$ we expect $\gamma_{\rm tot} \approx 1.1$. This conclusion is consistent with the collisionless model of Laporte & White (2015) who also find slopes close to the NFW value for $M_{200} \sim 10^{15}\mathrm{M}_{\odot}$ clusters.

Based on this argument we can construct a simple model, consistent with the results for low mass halos, to extrapolate the slopes measured for the EAGLE clusters into the mass range appropriate to rich clusters. This model is designed to capture the general behaviour of $\gamma_{\rm tot}$ on mass scales larger than $M_{200} \approx 2 \times 10^{13}\mathrm{M}_{\odot}$. It assumes that the total matter profile is made up of an NFW dark matter halo plus a stellar component which, in order to be consistent with relevant observational analyses, we take to be a "dual pseudo isothermal elliptical mass distribution" (dPIE) (Elíasdóttir et al., 2007). The value of the halo mass determines the concentration of the halo and we infer the stellar mass of the central galaxy from abundance matching (e.g. Moster et al., 2013). For the dPIE profile, we adopt the mean scale radius and core radius of the best-fitting profiles for our BCGs and keep them fixed while varying the normalisation to match the stellar mass of interest. (We verified that varying the values of the parameters of this model does not affect our results.) In this way we construct the total mass profile and measure its slope, which we show as the green band in Fig. 5.3. The slopes of the total mass profiles of the largest EAGLE clusters plotted in Fig. 5.2 are slightly steeper than the NFW value over the radial range over which $\gamma_{\rm tot}$ is defined. This mostly reflects the contribution of stars to the inner matter density. By contrast, the values inferred for more massive clusters are closer to the NFW value.

We now turn to the slope of the dark matter profiles. Unlike the total mass profile, the dark matter profile cannot be measured directly from observations, but must instead be inferred through detailed modelling, which requires a number of

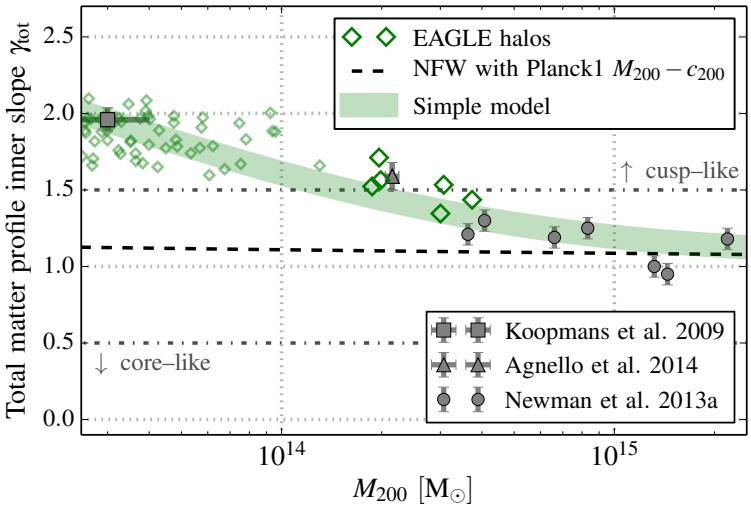

Figure 5.3: The logarithmic slope of the inner density profile of the *total* mass distribution, $\gamma_{\rm tot}$, as a function of halo mass, M_{200}. The dashed line shows the average slope of the NFW profile over the range in which $\gamma_{\rm tot}$ is defined. The large green diamonds represent the six EAGLE halos in our sample and the small green diamonds the smaller mass EAGLE halos. The grey symbols with error bars are the slopes measured by Koopmans et al. (2009) for 58 early type galaxies in the SLACS survey (square), the slope inferred by Agnello et al. (2014) from globular clusters orbits in M87 (triangle) and the slopes measured by Newman et al. (2013a) for seven massive clusters (circles). As a guide, the grey dash-dotted lines lines demarcate slopes that may be construed as "core-like" and "cuspy". The lower mass EAGLE clusters are cuspier than an NFW halo because of the contribution of the stellar component which, however, becomes increasingly less important for larger mass halos. The Newman et al. (2013a) data lie along the extrapolation of the trend seen in the EAGLE clusters.

assumptions. The dark matter profile in the simulations can, of course, be directly measured and the simulations can be used to test the consistency of the assumptions required in the modelling of the observational data.

The average slope of the dark matter density profile over the same radial range used to define $\gamma_{\rm tot}$ ($[0.003R_{200}, 0.03R_{200}]$) for our sample of simulated clusters is indicated by the black line in the grey shaded regions in Fig. 5.2 . Some observational analyses attempt to constrain the asymptotic slope, $\beta_{\rm DM}$, of a generalized NFW profile (gNFW):

$$\frac{\rho_{\rm gNFW}(r)}{\rho_{\rm cr}} = \frac{\delta_{\rm c}}{(r/r_{\rm s})^{\beta_{\rm DM}}(1+r/r_{\rm s})^{3-\beta_{\rm DM}}}. \tag{5.5}$$

This profile is often used to quantify deviations from the NFW form to which it reduces for $\beta_{\rm DM} = 1$ (Eqn. 5.1). We fit this profile to the dark matter of our simulated halos and plot the resulting values of $\beta_{\rm DM}$ as a function of halo mass, M_{200}, in Fig. 5.4, which is the dark matter analogue of Fig. 5.3. As may be seen, the EAGLE clusters (black squares) have inner slopes consistent with the NFW expectation (Eqn. 5.4). As was the case for the total matter profile, the inner dark matter profile slopes also show significant scatter, with $\beta_{\rm DM}$ varying by as much as ~ 0.4 for halos of similar mass.

5.4.2 Total mass profiles: overview of recent observational data

By combining different observational techniques, the *total* matter profile of clusters can be estimated. Two techniques have been used to probe the central mass distributions: strong lensing and modelling of the orbits of globular clusters (GC) or BCG stars. The former relies on a chance alignment of the cluster with a background galaxy and is, by nature, rare since only a few galaxy clusters present strong lensing arcs at the radii of interest. Similarly, the use of globular cluster (GC) orbits as tracers of the potential is limited to clusters that are close enough for the GCs to be unambiguously detected. Stellar velocity dispersion measurements of the central galaxy can also be used to constrain the mass near the centre of the halo

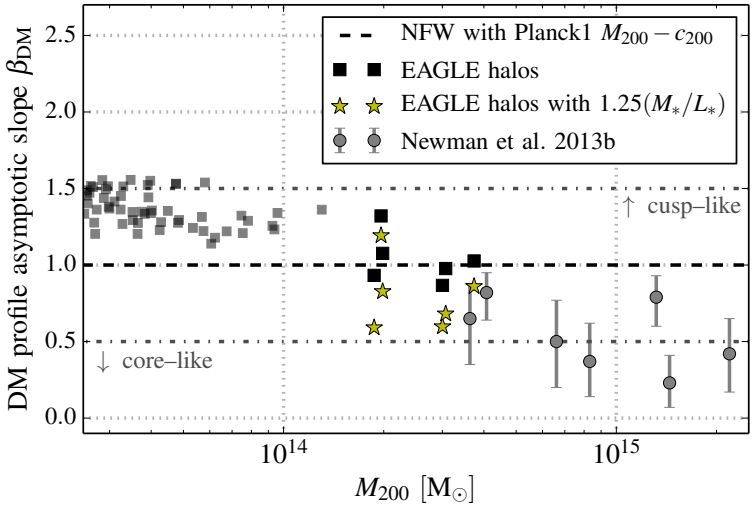

Figure 5.4: The asymptotic logarithmic slope of the inner dark matter density profile, $\beta_{\rm DM}$, as a function of halo mass, M_{200}. The dash-dotted line shows the NFW value of -1. The large black squares show the values measured for the six massive clusters in our EAGLE sample and the small black squares those measured for smaller EAGLE clusters. The yellow stars show the slopes that would be inferred for our sample if the stellar mass-to-light ratio is overestimated by 25% (see Section 5.5.3 for details). The grey circles with error bars are the values inferred by Newman et al. (2013b). As in Fig. 5.3, the grey dash-dotted lines lines demarcate slopes that may be construed as "core-like" and "cuspy".

but high-resolution spectroscopy is required. We will now compare our simulated cluster slopes to recent observational data. Although there is a wealth of data available for profiles at large radii, we focus exclusively on the inner regions which are the most sensitive to the nature of the dark matter.

The grey square with error bars at the low mass end of Fig. 5.3 shows the average slope measured for 58 early type galaxies in the SLACS survey by Koopmans et al. (2009) using a combination of strong lensing and stellar velocity dispersion measurements. Our simulation agrees perfectly with this data point. At the more massive end, Newman et al. (2013a) derived total mass profiles, $\rho_{\rm tot}(r)$, from projected mass profiles, which they estimated using strong and weak lensing data, together with the surface brightness and resolved stellar kinematics of the BCGs in a sample of seven clusters. The grey circles with error bars in Fig. 5.3 show their results. Five of these clusters have higher masses than the largest clusters in the relatively small EAGLE simulation volume, but the two lightest ones fall in the region represented in our simulation. Their values of $\gamma_{\rm tot}$ agree very well with those measured directly in our simulated clusters while the values for the more massive five lie in the region predicted by the simple model used to extrapolate the EAGLE results described in Section 5.4.1.

An independent measurement of the total inner density profile which does not rely on lensing data was carried out by Agnello et al. (2014) using the orbits of globular clusters in the halo of M87. The slope, $\gamma_{\rm tot}$, inferred from their best fitting broken power-law model is shown as a triangle with error bar in Fig. 5.3. This data point also agrees extremely well with the results for the EAGLE clusters.

We conclude that the inner density profiles of the *total* mass distribution in the EAGLE clusters are in good agreement with the best current data Koopmans et al. (2009); Newman et al. (2013a); Agnello et al. (2014). In both simulated and observed clusters, the inner profile slopes exhibit considerable scatter reflecting the variety of factors that affect the density structure, such as halo assembly history, shape and substructure distribution, BCG star formation and merger history, etc.

5.4.3 Dark matter density profiles

The situation is more complicated for the density profile of the dark matter since this is not directly accessible to observations. Instead, this profile must be inferred from a model to disentangle the contributions of the dark and visible components from the measured total mass profile. Wide radial coverage is needed fully to sample the two components and effect the decomposition. Strong lensing data seldom sample the range, $r \lesssim 10$ kpc, where the influence of baryons starts to play a role and so lensing data need to be supplemented by, for example, kinematical data for the stars of the BCG. Such data exist for only a handful of clusters (e.g. Sand et al., 2004; Newman et al., 2013a). The study by Newman et al. (2013a) is particularly interesting by virtue of the quality of the data and the comprehensive analysis performed. In the remainder of this chapter we will therefore focus on the comparison with these data.

The model assumed by Newman et al. (2013a) is a generalized NFW (gNFW) profile for the dark matter and a dPIE profile for the galaxy. The authors estimated the parameters values that minimize the difference between the model and the inferred lensing mass, the measured profiles of stellar velocity dispersion, $\sigma_{\rm l.o.s.}$, and surface brightness, S. In addition to the parameters describing the dark matter profile, the minimization procedure also constrains the stellar mass-to-light ratio, Υ_*. This is an important parameter since, at a given radius, it is degenerate with the dark matter mass: one can always trade dark matter for unseen stellar mass at that radius,

$$\rho_{\rm DM}(r) = \rho_{\rm tot}(r) - \Upsilon_* \cdot S(r). \tag{5.6}$$

This degeneracy can be broken by measuring the total density and surface brightness as a function of projected radius, R, and assuming that the stellar mass-to-light ratio is constant.

The values of $\beta_{\rm DM}$ (Eqn. 5.5) inferred by Newman et al. (2013b) for their sample of clusters are shown as grey circles in Fig. 5.4. The error bars indicate the 16th and 84th percentiles of the posterior distribution of $\beta_{\rm DM}$ returned by their model (not in-

cluding systematics). These lie well below the values for the EAGLE clusters (black squares) and are clearly inconsistent with them given the quoted errors. From our earlier discussion it seems unlikely that the discrepancy can be due to the slightly smaller masses of the EAGLE clusters compared to those in the observed sample, since the EAGLE clusters have dark matter inner slopes that are either close to or slightly steeper (due to contraction) than the NFW value. Thus, we conclude that profile slopes as shallow as those inferred by Newman et al. (2013b) are not present in ΛCDM simulations with the baryon physics modelled in EAGLE. This conclusion is surprising since the *total* mass profiles of the real and simulated clusters agree remarkably well. We will now discuss possible reasons for this apparent discrepancy.

5.5 Discussion

We saw in the preceding section that the inner slopes of the density profiles of the dark matter halos in the EAGLE clusters differ from the profiles inferred by Newman et al. (2013b) for their sample of seven clusters. There are several possible explanations for the discrepancy. One is that the simulations do not model the correct physics. This would be the case if the dark matter does not consist of cold collisionless particles but of particles that undergo self-interactions (e.g. Spergel & Steinhardt, 2000; Vogelsberger et al., 2012; Rocha et al., 2013). Cluster simulations would be required to determine whether the slopes found by Newman et al. can be explained for reasonable values of the self-interaction cross-section and a reasonable model for the baryonic physics.

Another possibility is that the dark matter is indeed cold and collisionless but the injection of energy from an AGN has flattened the NFW cusp. This is a scaled-up version of the mechanism originally invoked by Navarro et al. (1996a) to explain the possible existence of cores in dwarf galaxies. The simulations of Martizzi et al. (2012) show precisely this effect, but kiloparsec-scale cores are only produced by injecting very large amounts of AGN energy into the surrounding gas. Our sim-

ulations have weaker AGN feedback, as required to achieve a good match to the massive end of the observed stellar mass function, and do not produce cores. It is unclear if feedback as intense as that required by Martizzi et al. (2012) would lead to a similarly good match to the global properties of the galaxy population (Schaye et al., 2015; Crain et al., 2015; Furlong et al., 2015).

The disagreement between the inner dark matter profiles of the EAGLE clusters and of the clusters in the Newman et al. (2013b) sample could also be due to a mismatch between the directly observable quantities, $\sigma_{\rm l.o.s.}(R)$ and $S(R)$, and the corresponding quantities for the EAGLE clusters, or to systematic effects either in the selection of the observational sample or in the method used to inferred the inner dark matter slopes. We will now discuss these possibilities.

The most direct way to carry out the comparison would be to replicate the analysis of Newman et al. (2013a) on our simulated clusters. Unfortunately, the exact model and fitting pipeline used by them is not available to us and, as we will see below, the results are very sensitive to small changes in the assumption of the analysis pipeline. We therefore restrict our comparison to directly observable quantities and discuss how some of the assumptions made could impact the inferred values of $\beta_{\rm DM}$.

5.5.1 Surface brightness profiles

Stars are the dominant contributors to the density in the central regions of the EAGLE clusters and probably also in the real data. Clearly, if the surface brightness of the simulated clusters differed significantly from the observations, subtraction of this component could lead to different results for the slope of the dark matter profile in the two cases.

As discussed in Section 5.2.2, the luminosity of each stellar particle in the simulations is obtained from a Bruzual & Charlot (2003) population synthesis model assuming the Chabrier (2003) IMF. To compare our halos with observations, we derive magnitudes in the four HST filters (F606W, F625W, F702W and F850LP) used by Newman et al. (2013a). We placed our clusters at $z = 0.25$, the mean redshift of

that sample, by redshifting the spectra before applying the HST filters[2] and dimming the luminosities by a factor $(1+z)^{-4}$. To account for the somewhat smaller masses of the EAGLE clusters compared to those in the sample of Newman et al. (whose mean mass is $M_{200} = 1.03 \times 10^{15} \mathrm{M}_{\odot}$) we scaled up their surface brightnesses by a modest factor, $(M_{200}/1.03 \times 10^{15} \mathrm{M}_{\odot})^{1/6}$, derived assuming that the luminosity $L \propto M_{200}^{1/2}$ and that the stellar density remains constant in the narrow range or relevant halo masses[3]. We then chose 10,000 random lines-of-sight through each cluster and projected the particles along those axes onto the plane of the (virtual) sky. Finally, we binned the particles radially from the centre of the potential to derive the stellar surface brightness.

The surface brightness profiles of our six EAGLE clusters are plotted in Fig. 5.5. The solid lines show the mean profiles averaged over 10,000 lines-of-sight in the four different HST filters and the shaded regions the 1σ scatter around these values. The black symbols correspond to the measurements taken from Newman et al. (2013a) with physical radii derived from their angular sizes and redshift measurements. Although the EAGLE clusters have a slightly smaller total mass, the surface brightness of their central galaxies are in quite good agreement with those of the Newman et al. sample: the shapes of the profiles are somewhat different, with our clusters having a slightly shallower inner slope than the observed clusters.

A striking feature of Fig. 5.5 is the small scatter in the simulations for the different lines-of-sight. Near the centre the scatter is dominated by the presence of foreground satellites rather than by the orientation of the BCG. Another interesting feature is the large object-to-object variation, both in the simulations, where the central luminosities vary by around 0.8 mag, and in the observations, where the variation is even larger, almost 2 mag, with no apparent correlation with halo mass. Our simulated halos lie well within the observational scatter but themselves show somewhat smaller scatter. At large radii, 5 out of our 6 clusters appear to be slightly more luminous than the real clusters. However, this is the region where

[2]Effectively applying a reverse K-correction.

[3]Note that this is a more conservative rescaling factor than simply assuming $L \propto M_{200}$.

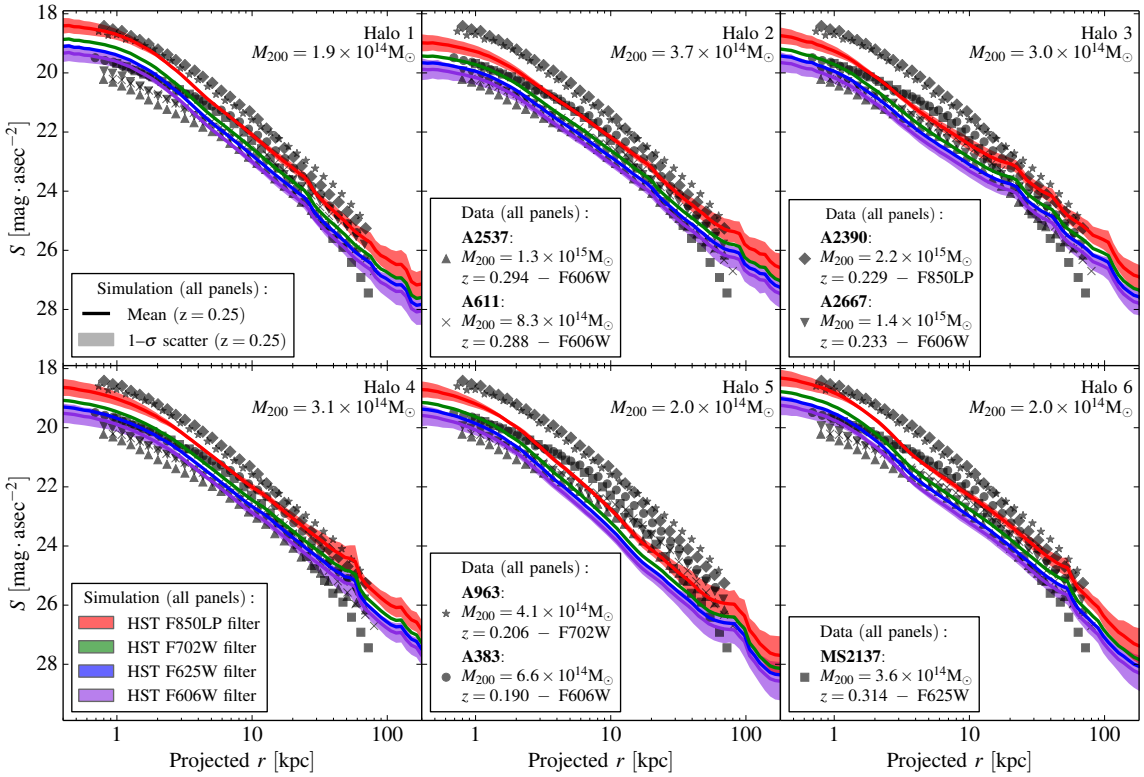

Figure 5.5: Surface brightness profiles of the six EAGLE clusters in our sample (placed at $z = 0.25$) in the four HST filters (from top to bottom: F850LP, F702W, F625W and F606W) used by Newman et al. (2013a) in AB magnitudes per arcsec^{-2}. The solid lines show the mean profile scaled by the factor, $(M_{200}/1.03 \times 10^{15} \mathrm{M}_\odot)^{1/6}$, averaged over 10,000 random lines-of-sight. The shaded regions show the 1σ scatter for the reddest and bluest filters. (The other filters have similar scatter.) The black symbols show the measured surface brightness profiles of the seven clusters observed by Newman et al. (2013a) whose redshifts are given in the legend together with the filter used. The clusters in the simulations have surface brightness profiles in reasonable agreement with those observed.

the observational data terminate and where background subtraction becomes significant.

We conclude that the surface brightness profiles of the EAGLE clusters are sufficiently similar to those of the Newman et al. (2013b) sample that differences in the starlight distribution cannot be the reason for the discrepancy between the dark matter profiles in the simulations and those inferred from the data.

5.5.2 Velocity dispersion profiles

The line-of-sight stellar velocity dispersion, $\sigma_{\rm l.o.s.}$, of our six halos as a function of projected radius is shown in Fig. 5.6. Since the EAGLE clusters are less massive than the clusters in the sample of Newman et al. (2013a), in order to facilitate a comparison, the velocity dispersions of the simulated clusters have been rescaled, as before, to the mean mass of the Newman et al. sample by multiplying the velocity dispersions by the corresponding factor $(M_{200}/1.03\times10^{15}{\rm M}_\odot)^{1/6}$ (assuming, here again, a constant stellar density in the centre of the galaxies).

The measured $\sigma_{\rm l.o.s.}$ is quite sensitive to the shape of the galaxy and the viewing angle. The axial ratios, of the six EAGLE BCGs (computed from the principal axes of the inertia tensor of the star particles $a>b>c$) are illustrated in Fig. 5.7 where the projection along the minor axis is shown at the top of each panel and the projection along the major axis at the bottom. Four of the six EAGLE clusters (1, 2, 5 and 6) are clearly prolate and the remaining two are close to spherical. We viewed the BCGs from 10,000 random directions placing an imaginary slit at a random angle on the plane of the sky centred on the halo potential minimum and measured the velocity dispersion of the stars as a function of projected radius, subtracting any bulk rotation.

As expected, the line-of-sight velocity dispersions increase with radius. In the inner regions ($r\lesssim10$ kpc) gravity is dominated by the stars. The 1σ scatter from the different viewing angles, shown as a grey shaded region in Fig. 5.6, is rather large at all radii for all objects, of order 10% or more for all but two of the halos. The black solid line shows $\sigma_{\rm l.o.s.}$ for a line-of-sight chosen along the major axis of

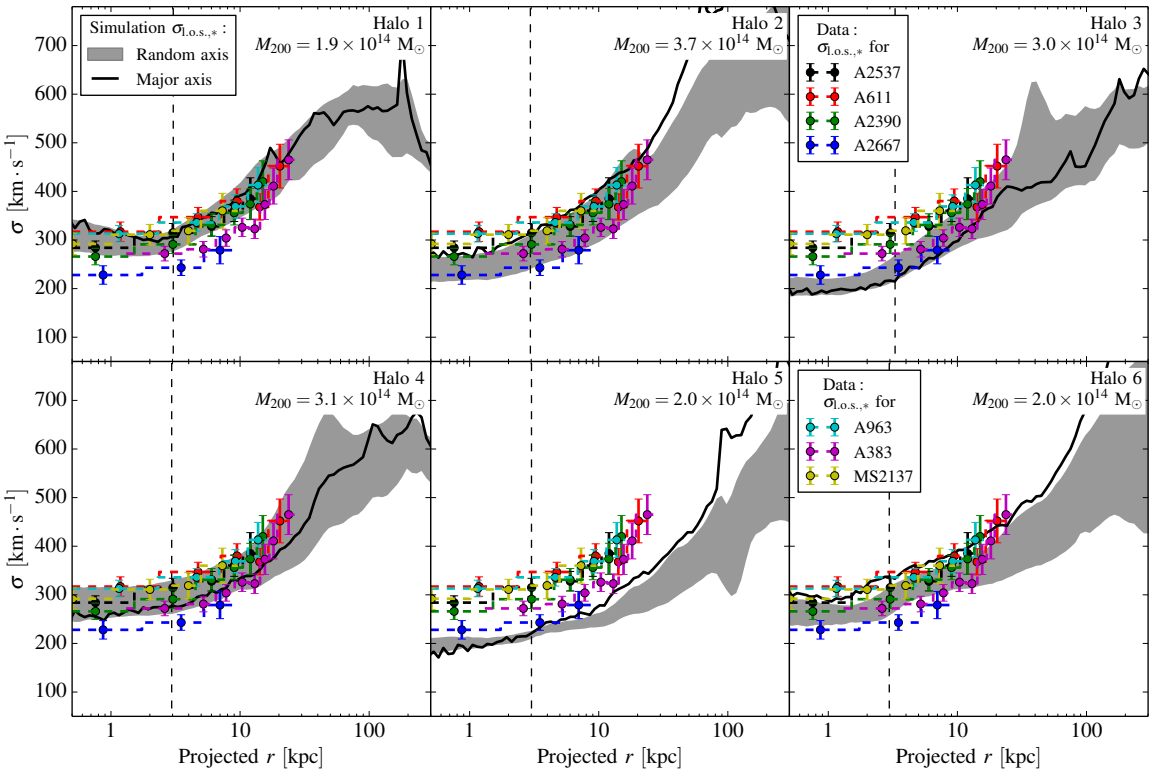

Figure 5.6: Stellar velocity dispersion along the line-of-sight as a function of projected radius for the six EAGLE clusters listed in Table 5.1. The dispersions have been rescaled by a factor $(M_{200}/1.03 \times 10^{15}\mathrm{M}_\odot)^{1/6}$ to correct for the slightly lower masses of these clusters compared to the mean of the observational sample of Newman et al. (2013a). The grey shaded region is the 1σ scatter obtained when looking at the halos from 10,000 random lines-of-sight. The black solid line is the profile as seen from a line-of-sight oriented along the galaxy's major axis. The vertical dashed line on each panel shows the 3D convergence radius, r_c. The coloured dashed lines with error bars are the measurements for the seven clusters observed by Newman et al. (2013a). In three of the six EAGLE halos the velocity dispersion profile measured along the major axis is biased high.

each BCG. In three of our six clusters (halos 2, 5 and 6) the velocity dispersion along this particular line-of-sight is biased high and, in two cases, it falls outside the 1σ scatter. As can be seen on Fig. 5.7, these are the three most prolate halos in our sample. A bias in the line-of-sight velocity dispersion is expected since orbits in prolate halos have larger velocities along the direction of elongation. These objects would nevertheless appear circular on the sky when viewed in this direction since the axis ratios b/c are close to unity. The three most spherical halos do not exhibit any particular bias when viewed along their major axis, as expected.

The line-of-sight velocity dispersion profiles of the seven clusters studied by Newman et al. (2013a) are shown as dashed colour lines with error bars in each panel of Fig. 5.6. The six rescaled EAGLE clusters have dispersions that fall within the scatter of the observational data. Thus, unless there is a strong orientation bias for the BCGs in the cluster sample of Newman et al. (2013a), a mismatch in velocity dispersion profile cannot be the cause of the difference between the slopes of the dark matter halos in the EAGLE clusters and those inferred by Newman et al.

Since the projected mass density of a prolate halo is also largest along its major axis, there is a potential and well-understood selection bias in samples of clusters selected for lensing studies. If the BCGs in the sample of Newman et al. (2013a) were prolate and preferentially viewed along their major axes, then, as shown in Fig. 5.6, the observed line-of-sight velocity dispersions would be biased high. This would lead to an overestimate of the mass enclosed within the radius sampled by the velocity dispersion data. In the absence of other information, it would not be possible to separate the relative contributions to this estimate from stars and dark matter. However, the available lensing data constrains the total mass (and, in the case of radial arcs, also the slope of the profile) in the central regions of the cluster. This, together with the inferred stellar profile, restricts the fits to the combined data and this could lead to an underestimate of the dark matter mass near the centre of the clusters.

Such an effect could explain the difference between the slopes of the dark matter profiles inferred by Newman et al. and those measured for the EAGLE clusters.

However, Newman et al. argue that their sample does not suffer from such a bias since the distribution of ellipticities in it is consistent with that of the BCG population as a whole. In the case of A383, for which the X-ray data indicate is elongated along the line-of-sight, they explicitly use a non-spherical model.

5.5.3 Mass-to-light ratio

As mentioned in Sec. 5.4.2, the stellar mass density at a given radius is degenerate with the dark matter mass density at that radius (Eqn. 5.6). In the simulations we know the stellar mass and so we can subtract it exactly from the total mass. The resulting value of the inner dark matter halo slope was shown in Fig. 5.4. By contrast, in the observational sample the stellar mass must be derived from an estimate of the stellar mass-to-light ratio, Υ_*.

Newman et al. (2013a,b) treated Υ_* as a parameter in their model over which they marginalize. The value of Υ_* is determined by the unknown IMF; In their Bayesian model, they adopt a prior distribution that effectively restricts the IMF to be between 1.5 times lighter than Chabrier and 2 times heavier than Salpeter. Despite this wide range, the posterior distribution of Υ_* is limited by the shape of the assumed prior in three out of the seven BCGs, suggesting that the mass-to-light ratio is not well constrained by the data. Had we in our simulations (which adopt a Chabrier IMF) subtracted a stellar mass inferred by incorrectly assuming a Salpeter IMF, we would have overestimated Υ_* by 65%. This would have led us to infer a negative slope for the inner dark matter density profile in three out of our six clusters, implying virtually no dark matter at their centres!

In Fig. 5.4 we show the effect of overestimating Υ_* by a much smaller factor of only 25%. The inferred slopes, shown by yellow stars, are significantly shallower than the true slopes and have more scatter. Such a relatively small systematic error would be sufficient to bring the inferred slopes in the simulations into agreement with the estimates of Newman et al. (2013b).

The estimate of Υ_* in the model of Newman et al. (2013b) requires the measurement of the line-of-sight velocity dispersion profile, $\sigma_{\rm l.o.s.}$, of the BCG, as a function

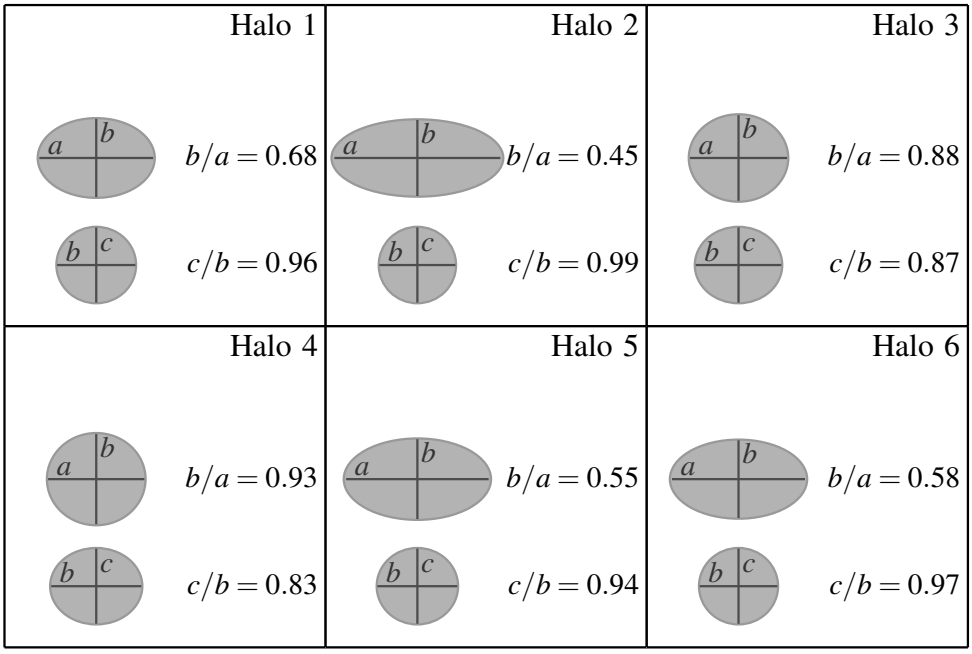

Figure 5.7: The projection of the central stellar component of the six EAGLE clusters along the minor axis (top ellipse in each panel) and major axis (bottom ellipse). The axes ratios are given next to each ellipse. Four of the galaxies are clearly prolate and the remaining two are slightly oblate. Prolate galaxies have velocity dispersions that are biased high (Fig. 5.6) when observed along their major axis.

of projected separation, R. In dynamical equilibrium, $\sigma_{\rm l.o.s.}$ is given by the Jeans Equation (e.g. Binney & Tremaine, 1987; Cappellari, 2008):

$$\sigma^2_{\rm l.o.s.}(R) = \frac{2G}{\Sigma_*(R)} \int_R^\infty \frac{\mathcal{F}(r,R,\beta)\rho_*(r)M_{\rm tot}(r)}{r^{2-2\beta}} {\rm d}r, \tag{5.7}$$

where $\rho_*(r)$ is the 3D density of tracers (the stars) whose surface density is $\Sigma_*(R)$; $M_{\rm tot}(r)$ is the total enclosed mass; $\beta = 1 - \sigma^2_\theta/\sigma^2_r$ is the velocity anisotropy parameter, here assumed to be independent of radius, with σ_r and σ_θ the radial and tangential velocity dispersions, respectively[4] and

$$\mathcal{F}(r,R,\beta) = \frac{R^{1-2\beta}}{2}\left[\beta B\left(\frac{R^2}{r^2};\beta+\frac{1}{2},\frac{1}{2}\right) - B\left(\frac{R^2}{r^2};\beta-\frac{1}{2},\frac{1}{2}\right) + \frac{\sqrt{\pi}\,(3-2\beta)\,\Gamma(\beta-\frac{1}{2})}{2\Gamma(\beta)}\right],$$

where $\Gamma(x)$ is the Gamma function and $B(z;a,b)$ is the incomplete Beta function. In the limit where $\beta \to 0$, $\mathcal{F}(r,R,\beta)$ reduces to

$$\lim_{\beta\to 0} \mathcal{F}(r,R,\beta) = \sqrt{r^2-R^2}.$$

In the more general case where β is a function of r, the problem of reconstructing the mass distribution becomes more complex. Solutions for specific forms of $\beta(r)$ have been derived by Mamon & Boué (2010).

In the Jeans equation the velocity anisotropy parameter and the mass are degenerate. In their analysis Newman et al. (2013a) assumed $\beta = 0$ i.e. isotropic orbits. This assumption is a source of a potentially significant systematic error which Newman et al. investigated. They found that if the orbits were mildly radially biased with a constant value of $\beta = +0.2$, then Υ_* would be overestimated by 30%. In our simulations we can calculate β directly for the stars in the model BCGs. The variation of β with radius is shown in Fig. 5.8. We find that, in general, β varies with radius over the range where Newman et al. obtained kinematical data. In two of our clusters, β is close to zero over this range, but in the other four, β becomes increasingly positive with radius, with a mean value of ~ 0.2 to 0.3. Complex features, which cannot be described by a simple linear form for $\beta(r)$ are also present,

[4]With this definition, $\beta = 0, 1$ and $-\infty$ correspond to isotropic, radially biased and circularly biased orbits respectively.

precluding the reconstruction of $M(r)$ from an assumed functional form for $\beta(r)$. It is also worth mentioning that the profile of $\beta(r)$ is uncorrelated with the shape of the BCGs: of the two cases with nearly isotropic orbits (halos 3 and 5), one is nearly spherical and the other very elongated (see Fig. 5.7).

In order to test the assumption of anisotropy, we inverted eq. 5.7 numerically. Extracting $\sigma_{\rm l.o.s.}(R)$, $\Sigma_*(R)$ and $\rho_*(r)$ from the simulated clusters we reconstructed $M_{\rm tot}(r)$ assuming $\beta = 0$ and compared the result to the actual value. We found that for this assumption the reconstruction overestimates the value of $M_{\rm tot}$ by factors ranging from 10% to over 100%. Repeating this analysis, this time assuming $\beta = 0.2$, led to errors of comparable size for the four halos that display an anisotropy profile differing significantly from $\beta(r) = 0.2$ (see Fig. 5.8). Thus, for most of our clusters, the analysis of Newman et al. (2013a) would have overestimated the stellar mass-to-light ratio by more than the 25% which, according to Fig. 5.4, would reconcile their results with our simulations. This test, however, does not take into account constraints on the *total* mass profile from lensing data at large radii, which could exaggerate the dependence of the inferred value of $M_{\rm tot}$ near the centre on the assumed value of β.

In real clusters additional uncertainties are introduced by factors such as an assumed form for the 3D stellar number density profile, $\rho_*(r)$, and an assumption for the value of the stellar mass-to-light ratio, Υ_*. This is mitigated by constraints on $M_{\rm tot}$ provided by lensing data although, in general, the lensing and kinematical data do not overlap sufficiently to separate the contributions from the stellar mass and the dark mass. In the model of Newman et al., Υ_* is coupled to other parameters such as the slope of the total mass profile, so that the effect on the quantity of interest, $\beta_{\rm DM}$, is difficult to anticipate without re-running their pipeline for different assumptions for the velocity anisotropy. For example, Newman et al. (2013b) tried a solution for the case of constant anisotropy, $\beta = 0.2$, and found an increase in $\beta_{\rm DM}$ of about 0.13, which would bring their data closer to our simulations. What we can say with certainty is that the kinematical model assumed by Newman et al. is not consistent with the EAGLE BCGs, offering a possible explanation for the dis-

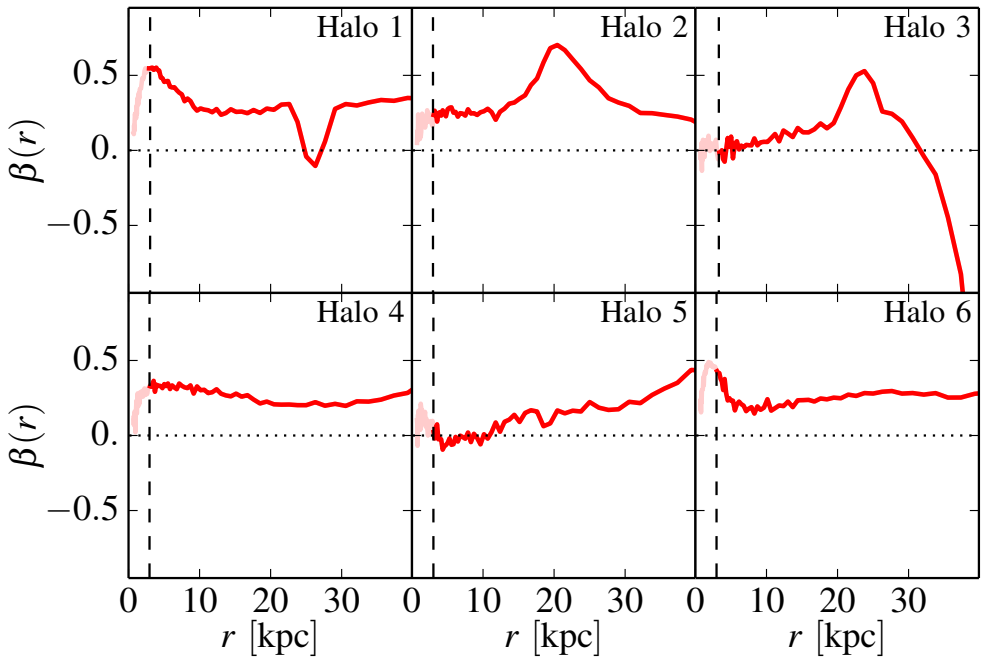

Figure 5.8: Stellar anisotropy profile $\beta(r)$ as a function radius for the six EAGLE clusters over the radial range relevant to the stellar kinematics analysis. The vertical dashed lines on each panel show the 3D convergence radius, r_c and the profiles at lower radii are shown using shaded lines. Two BCGs are consistent with $\beta = 0$ but would be better fit with a non-constant β. Ignoring complex features, the other four clusters present more radially biased orbits with $\beta(r) \approx 0.25$ A single profile shape for $\beta(r)$ cannot be used to characterize all six of our BCGs.

crepancy in the dark matter density slopes.

Constraining the anisotropy, β, in cases in which, as in our simulated clusters, it varies with radius is not straightforward. Yet, this is what is required in order to lift the degeneracy between anisotropy and mass which lies behind the degeneracy between Υ_* and the dark matter profile slope. The use of Integral Field Spectroscopy may help constrain this quantity in future studies.

5.6 Summary and conclusions

We have studied the density profiles of the six most massive clusters in the largest EAGLE simulation (Schaye et al., 2015). The EAGLE simulation was calibrated to provide a good match to the observed stellar mass function and galaxy sizes in the local universe, suggesting that it gives a realistic representation of the local galaxy population. Due to the relatively small volume of the simulation (100^3 Mpc^3), the clusters selected for this study tend to be somewhat less massive (mean $M_{200} = 2.6 \times 10^{14}\mathrm{M}_\odot$) than the seven clusters studied by Newman et al. (2013a) (mean $M_{200} = 1 \times 10^{15}\mathrm{M}_\odot$) to which we compare our results in particular detail, although the two lightest clusters in the observational sample have similar masses to the three most massive EAGLE clusters. For these clusters Newman et al. have obtained strong and weak lensing as well as stellar kinematical data for the BCGs.

The total mass density profile of the EAGLE clusters is dominated in the central parts ($r < 10$ kpc) by the BCG. The presence of the central galaxy makes the total mass profile steeper than an NFW profile near the centre. The inner slope of the total mass profile (defined as the average slope in the range $r = 4 - 35$ kpc) agrees remarkably well with the slopes measured by Newman et al. (2013a) for their clusters, with the corresponding slopes measured by Koopmans et al. (2009) for 58 early type galaxies in the SLACS survey, and with the slope inferred by Agnello et al. (2014) from the kinematics of globular clusters around M87.

The dark matter density profile of the EAGLE clusters is very well described by the NFW profile over the entire resolved radial range, $r = 3 - 2000$ kpc. By con-

trast, Newman et al. (2013b), after subtracting the contribution of the stars, inferred significantly shallower dark matter slopes for their clusters in the inner regions, in contradiction with our own results. This discrepancy is puzzling because, in addition to the total mass density profiles, the surface brightness and line-of-sight velocity dispersion profiles of the EAGLE clusters agree quite well with those of the Newman et al. clusters.

We have considered possible explanations for the discrepancy between the inner dark matter density profiles of the EAGLE clusters and those inferred by Newman et al. (2013b). A possible interpretation is that the simulations lack the correct physics, either because the dark matter is not collisionless (e.g. Spergel & Steinhardt, 2000; Vogelsberger et al., 2012; Rocha et al., 2013) or because extreme baryon processes not represented in our simulations have destroyed the inner dark matter cusps (Martizzi et al., 2012). Baryon effects associated with AGN in the EAGLE simulations are not strong enough to produce density cores; yet the simulation reproduces the exponential cut-off in the stellar mass function remarkably well.

An alternative explanation for the discrepancy is that the uncertainties in the determination of the inner dark matter density slope were underestimated by Newman et al. (2013b). In particular, their analysis relies on an accurate estimate of the stellar mass-to-light ratios of the BCGs. We showed that a systematic overestimation of this ratio by only 25% would reconcile the observational data with our results. An effect of this size could be produced if the measured stellar velocity dispersions were biased high as would be the case if the BCGs (which are all selected to be strong gravitational lenses) were prolate and preferentially viewed along their major axis. However, Newman et al. (2013a,b) have argued that such a selection bias is unlikely in their sample since the distribution of BCG ellipticities appears to be typical of a randomly oriented population.

Another possible source of systematic error in the estimate of the stellar mass-to-light ratio is the assumption made by Newman et al. (2013b) that the stars in the BCG have a uniform and isotropic distribution of orbits. In their paper, they showed that mildly radial orbits would lead to an overestimate of the stellar mass-

to-light ratio of 30%, sufficient, in principle, to account for the discrepancy with the NFW inner dark matter slopes of the EAGLE clusters. We find that just such a situation is present in four of our six clusters which show radially biased orbital distributions which vary with radius in a complicated way. However, in practice, the situation is not straightforward because the mass-to-light ratio in the model of Newman et al. is coupled to other parameters and is sensitive to the constraints on the total mass profile from lensing.

We can conclude, however, that systematic errors resulting from the assumptions made in the analysis of Newman et al. (2013b) could potentially be large enough to account for the shallow inner dark matter profiles that these authors infer for their clusters, in conflict with the cuspy profiles found for the EAGLE clusters. Unfortunately it is very difficult, if not impossible, to break the degeneracies inherent in stellar kinematical analyses with existing data. High resolution integral field spectroscopy of BCGs could prove helpful in future work.

Chapter 6

The offsets between galaxies and their dark matter in ΛCDM

6.1 Introduction

Observations of one (particularly well-constrained) galaxy in cluster Abell 3827 (redshift $z \approx 0.1$; Carrasco et al. 2010) revealed a surprising $1.62^{+0.47}_{-0.49}$ kpc (68% CL) offset between its dark matter and stars (Massey et al., 2015). Such offsets are not observed in isolated field galaxies (Koopmans et al., 2006; Gavazzi et al., 2007) [1]. However, offsets inside clusters are consistent with theoretical predictions from models of self-interacting dark matter (SIDM Spergel & Steinhardt, 2000). As galaxies move through a cluster core, interactions with the cluster's dark matter would create a friction and cause a galaxy's dark matter to lag slightly behind its stars (Massey et al., 2011; Kahlhoefer et al., 2014; Harvey et al., 2014), just like ram pressure causes gas to lag a long way behind stars in the Bullet Cluster (Clowe et al., 2004, 2006; Randall et al., 2008; Harvey et al., 2015). Simple simulations tailored

[1] A small number of galaxy quad lenses are not well-fitted by standard parametric models of dark matter centred on the optical emission. To fit lens RXS J1131, Claeskens et al. (2006) need to include a $0.044''$ offset or $m=4$ octupole term. With lens COSMOS J09593, Jackson (2008) achieved an acceptable goodness of fit only with a $0.063''$ offset and (an unrealistically large) external shear $|\gamma| = 0.25$. However, in these isolated lenses the cause of these poor fits is more likely to be local substructure (Hezaveh et al., 2013). An offset between mass and light would produce a relatively shallow core profile and possibly more detectable central images. Note also that the location of mass peaks is determined much more precisely by strong lensing than by weak lensing (George et al., 2012; Dietrich et al., 2012).

to Abell 3827 support this prediction (Kahlhoefer et al., 2015, although current results operate under the limited assumption that the galaxy is on first infall). Many particle physics models of dark matter naturally predict low level self-interactions (e.g. Tulin et al., 2013; Foot, 2014; Boddy et al., 2014; Hochberg et al., 2014; Cline et al., 2014; Khoze & Ro, 2014). If the interaction cross-section is considerable $\gtrsim 0.1\,\mathrm{cm}^2/\mathrm{g}$, it could also resolve small-scale issues in the predictions of non-interactive, cold dark matter (CDM) models (see review by Weinberg et al., 2015).

Cluster Abell 3827 was originally studied by Williams & Saha (2011) because its light distribution is interesting, with the intention of developing a lens analysis algorithm but not with the expectation of measuring an offset (L. Williams 2015, *pers. comm.*). This is the only galaxy for which an offset has been detected, but it may also be the only galaxy in a cluster for which such a small offset *could* have been detected. The measurement requires three chance circumstances, each individually rare.

- The cluster must gravitationally lens a well-aligned background galaxy with a complex morphology. The distribution of foreground dark matter (plus baryons) can be reconstructed from perturbations to this lensed image.

- The cluster must contain a bright galaxy near the Einstein radius. To enable precise measurements, it must intersect the lensed arcs and its mass must be a detectable fraction of the cluster. Since a single cD galaxy generally lies inside any Einstein rings, in practice, this means a cluster with multiple cDs.

- The cluster must be nearby, so small physical separations can be resolved. This reduces its efficiency as a gravitational lens.

The interpretation of the observed offset in such radical terms as SIDM is clouded by the possibility of alternative explanations. First, gravitational lensing is sensitive to the total mass distribution projected along the line of sight. The chance alignment of unrelated foreground/background structures has created apparently spurious features in other lens systems (Gray et al., 2001; Hoekstra, 2003; Host, 2012). In Abell 3827, projection effects do not appear to be an issue: of the four

galaxies at the centre of the cluster three have a total mass appropriate for their stellar mass, while the fourth (galaxy N1) has a low mass at the location of the stars, but a similarly appropriate total mass slightly offset. Had this been a chance projection, there would be mass at the location of N1 (because of its own, non-offset dark matter) plus a second mass peak (and probably a luminous source). These are not seen.

Second, a physical offset might arise even with collisionless dark matter, via the complex astrophysical processes operating in cluster core environments. Gas stripped from and trailing behind an infalling galaxy may self-gravitate and form new stars. This is not consistent with observations of Abell 3827, which has effectively zero star formation rate (Massey et al., 2015, Table 1). The different physical extent of dark matter and stars also leads to different dynamical friction, tidal gravitational forces, and relaxation times during mergers. Inside the complex distribution of Abell 3827, even normally linear effects like tidal forces could create or exacerbate small initial offsets. It could also be considered that the galaxy in question is undergoing one of two types of merger:

- Coincidentally with the galaxy's arrival near the cluster core , it has recently merged with a former satellite. The tightly-bound stars from the centre of the satellite have not yet had time to mix with the galaxy's stars, and remain as a second peak randomly located within the total system. Simulated analogues of this are not consistent with observations, because the observed galaxy is best-fit in all bands by a *single* Sersic profile (Massey et al., 2015, Table 1).

- The galaxy is about to merge with a more massive halo (the three more central galaxies of similar mass). In simulations, the dark matter from all the systems rapidly mix together into a single smooth halo. This is not consistent with observations, which still show the infalling galaxy's dark matter, *distinct from* and *further away from* the other galaxies' dark matter. [2].

[2]Allowing a distinct dark matter peak for N1 fits the observations with $\chi^2/\mathrm{dof} = 49.3/23$, Bayesian evidence $\log_{10}(E) = -26.4$, and lens-plane $\langle \mathrm{rms}_i \rangle = 0.26''$ (Massey et al., 2015, Table 3). A model without dark matter (but still stellar mass) is strongly disfavoured, with $\chi^2/\mathrm{dof} = 86.1/26$,

As a control test to determine whether more complex astrophysical effects could build an offset between galaxies and collisionless dark matter, we measure the 3D separation between galaxies' luminous and dark matter in the "Evolution and Assembly of GaLaxies and their Environments" (EAGLE) suite of hydrodynamical cosmological simulations (Schaye et al., 2015; Crain et al., 2015). These simulations have been calibrated to reproduce the mass and size of galaxies in the local Universe. These simulations also reproduce the observed low-redshift luminosity functions (Trayford et al., 2015) and produce an evolution of the galaxy mass function in broad agreement with observations (Furlong et al., 2015). They are hence, the perfect test-bed to predict the relative positions of galaxies' various components in a statistically meaningful way.

6.2 Method

In this section we describe briefly the cosmological simulations we analysed and the method used to infer the centre of luminous and dark matter in galaxies.

6.2.1 The simulation suite

In our study, we use the main EAGLE simulation (Ref-L100N1504) and to explore field galaxies, clusters and groups, and the higher resolution simulation (Recal-L025N0752) to understand the convergence of our results. These cosmological simulations use a state-of-the-art treatment of smoothed particle hydrodynamics and set of subgrid models. The full description of the model is given in Schaye et al. (2015) and the rationale for its parametrisation is presented in Crain et al. (2015); we only summarise here the aspects relevant to our study. The simulations assume collisionless dark matter, evolving in a flat ΛCDM cosmology with parameters from *Planck2013* (Planck Collaboration et al., 2014). The low (high) resolution initial conditions are generated at $z = 127$ using second-order Lagrangian perturbation theory in a 100^3 Mpc^3 (25^3 Mpc^3) volume with a dark matter particle

$\log_{10}(E) = -100.7$ and $\langle \mathrm{rms}_i \rangle = 0.34''$ (R. Massey 2015, *pers. comm.*).

mass of 9.7×10^6 $\mathrm{M}_\odot$ (1.2×10^6 $\mathrm{M}_\odot$) and initial gas particle mass of 1.8×10^6 $\mathrm{M}_\odot$ (2.2×10^5 $\mathrm{M}_\odot$). The particles are then evolved in time using the GADGET Tree-SPH code (Springel, 2005). The Plummer-equivalent gravitational softening is set to $\epsilon = 700$ pc ($\epsilon = 350$ pc at higher resolution).

The subgrid model in the EAGLE simulations includes element-by-element radiative cooling (Wiersma et al., 2009a), star formation obeying the Kennicutt-Schmidt relation (Schaye & Dalla Vecchia, 2008), enrichment of the ISM via stellar mass loss (Wiersma et al., 2009b), feedback from star formation (Dalla Vecchia & Schaye, 2012), gas accretion onto super-massive black holes and the resulting AGN feedback (Booth & Schaye, 2009; Rosas-Guevara et al., 2015).

6.2.2 Identification of galaxies and their locations

We find galaxies in the simulation via the SUBFIND algorithm (Springel et al., 2001; Dolag et al., 2009). We identify all galaxies with stellar mass $M_* > 10^9$ $\mathrm{M}_\odot$ at $z = 0$, both in the field and in groups or clusters.

We find the centre of galaxies' matter distributions using an iterative 'shrinking sphere'. We first identify all the star particles for each galaxy. We calculate their centre of mass and select only those particles within 90% of the maximal distance to the centre of mass. Repeating this process, the search radius and the number of considered particles decreases in subsequent iterations. This shrinking sphere procedure is repeated until the number of particles reaches 200. The centre of mass of this final set of particles is considered to be the centre of the galaxy's stellar distribution[3]. Similarly, we define the velocity of the stellar distribution as the mass weighted velocity of the particles selected in the final iteration of the procedure.

The same procedure is applied to each galaxy's dark matter particles, to calcu-

[3]As pointed out by Kahlhoefer et al. (2014, 2015), the choice of centroiding algorithm could produce varying results if dark matter does interact. Our identification of mass-weighted peaks in the stellar particles is both robust and the most comparable procedure to the identification of peaks in K-band luminosity-weighted observations (or other infrared bands in the absence of recent star formation).

late the centre of their dark matter distribution. Finally, the offset between the dark and luminous component is defined as the distance between those two centres. We have verified that our results are robust against variations of the parameters used in this procedure.

6.3 Offsets between dark matter and stars

In the EAGLE Ref-L100N1504 simulation there are 12776 galaxies with mass $M_* > 10^9$ $\mathrm{M}_\odot$, 1129 of which are satellites in clusters (halos with $M_{200} > 10^{14}$ $\mathrm{M}_\odot$), 3111 satellites in groups (halos with $M_{200} > 10^{13}$ $\mathrm{M}_\odot$) and 7391 are field galaxies. The higher resolution Recal-L025N0752 simulation contains 618 galaxies above our mass threshold. These four samples will be used to investigate environmental and resolution effects.

6.3.1 3D offset between dark matter and stellar components

The offsets between the centre of galaxies' dark matter and their stars for our four sub-samples of galaxies is shown in Fig. 6.1. The distributions are consistent with being randomly sampled from a Maxwellian with distribution parameter $\sigma = 196 \pm 2$ pc (main simulation) or $\sigma = 126 \pm 1$ pc (high resolution simulation). Arrows indicate the position of the 95 and 99.7 (2 and 3σ) percentiles. In both cases, the typical scatter is smaller than the gravitational softening length, indicated by a vertical dashed line.

The distribution of offsets in the Ref-L100N1504 main simulation is remarkably similar for field galaxies (top left panel) and satellite galaxies in groups or clusters (bottom panels). This indicates that, at our resolution, the offsets are not influenced by environmental effects. Fewer than 5% of all galaxies display an offset larger than the gravitational softening length. Offsets larger than 1 kpc are only found in 59 field galaxies (0.79%) and 17 satellites in groups and clusters (0.54%). Pushing these numbers to offsets larger than 1.5 kpc, we find 15 field galaxies (0.20%) and 2 satellites in groups and clusters (0.06%). A much larger sample of galaxies would,

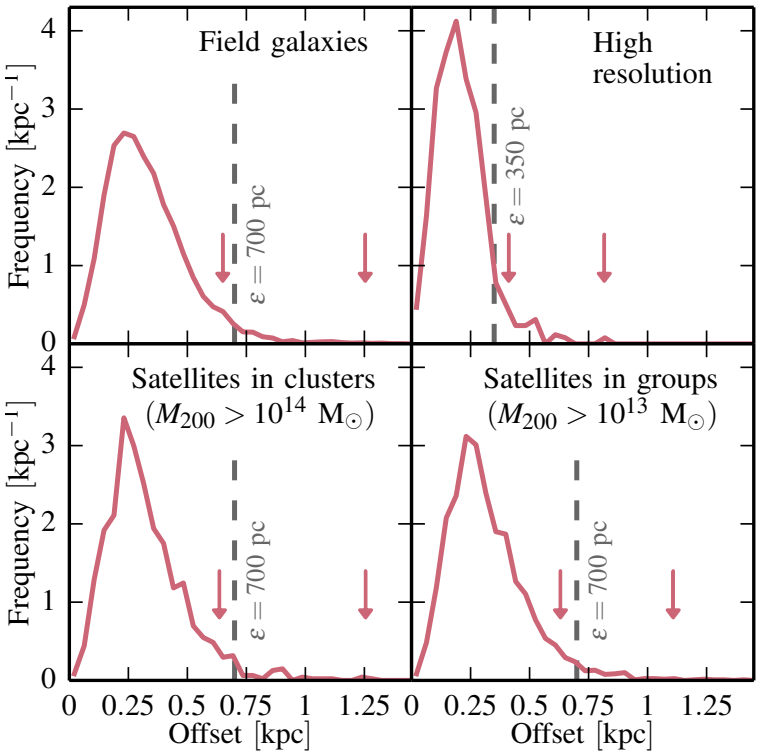

Figure 6.1: The offset between the centre of the dark matter distribution and stellar distribution for galaxies with a stellar mass $M_* > 10^9 \mathrm{M}_\odot$. The different panels correspond to field galaxies in the reference simulation (top left), the field galaxies in the higher resolution simulation (top right), satellites in clusters (bottom left) and in groups (bottom right). In each panel the vertical dashed line indicates the softening length used in the simulation. The arrows indicate the position of the 95% and 99.7% percentiles of each distribution. The offset seen is similar in field galaxies and clusters and is of the order of the softening scale of the simulation. Offsets larger than 1.5 kpc correspond to fluctuations greater than 3σ.

however, be required to characterise robustly the tail of the distribution.

Offsets in the higher resolution Recal-L025N0752 simulation (top right panel) are smaller, with 95% of the galaxies displaying an offset smaller than 410 pc. Unfortunately, the smaller number of galaxies in that simulation volume does not allow for a thorough discussion of the position of larger percentiles. The results from this simulation indicate that the offsets seen in the main simulation are probably overestimated (at least for field galaxies) and that simulations run at a higher resolution (i.e. with a smaller softening length) would lead to galaxies with smaller offsets between dark matter and stars. However, the decrease in softening length by a factor of 2 between our two simulations has only led to a decrease in median offset by a factor of 1.5, indicating that even higher resolution simulations might not converge towards a negligible offset between components[4]. We nevertheless caution that the softening length is not the only scale setting the resolution of a simulation. Changes in the subgrid parameters and, sometimes, models between different simulations at different resolution are necessary to account for the newly resolved scales and have a non-trivial impact on the analysis of convergence.

6.3.2 Offset along the direction of motion

If the dark matter-stellar offset in Abell 3827 is due to SIDM, then not only will the centres of the galaxies and dark matter halos be offset but this offset should also be aligned with the direction of motion of the galaxy with the dark matter trailing the stars. Although the offsets observed in the EAGLE simulation are approaching the resolution limit set by the scale of gravitational softening, it is worth measuring whether the dark matter might be trailing or leading the galaxies in their motion.

[4]The offset of 300-400 pc found by Kuhlen et al. (2013) in high resolution zoom-in simulation of a single Milky Way-like galaxy is consistent with our findings. That offset from the centre of their dark matter distribution is ~ 3 times larger than their softening, indicating that a small but non-zero offset might be found with sufficiently high resolution adopted in the simulations. We note, however, that the dark matter density profile of their galaxy is not monotonic; a result different from what is seen in other simulations.

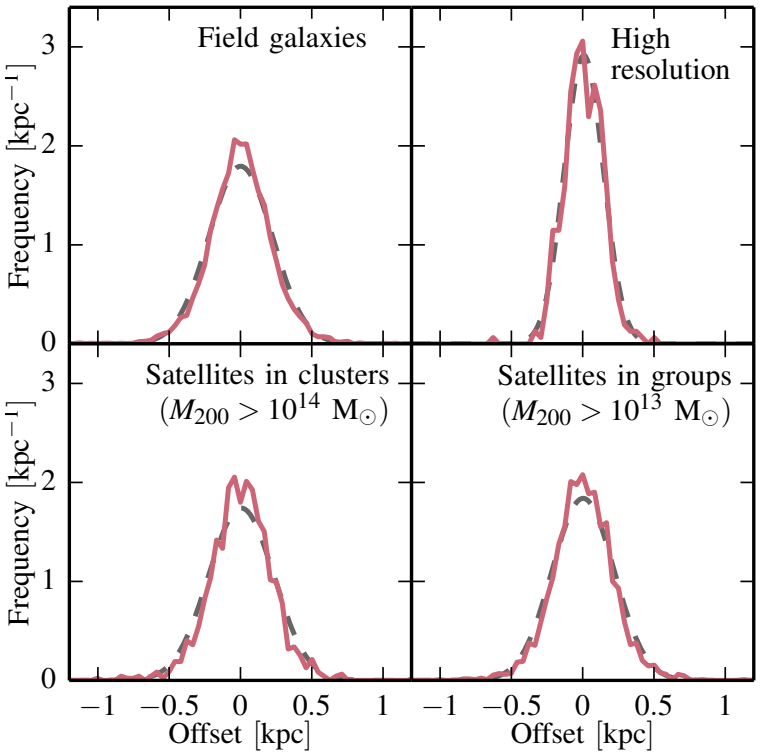

Figure 6.2: The offset between the centre of the dark matter distribution and stellar distribution along the axis of motion of the stellar distribution for galaxies with a stellar mass $M_* > 10^9 \mathrm{M}_\odot$. The different panels correspond to the same subsets of galaxies as in Fig. 6.1. The dashed grey curves in the background show a Gaussian distribution with the same mean and standard deviation as the offset distributions. The distribution of offsets displays no bias towards trailing or leading motion of the dark matter centre with respect to the luminous centre and only deviates from a normal distribution by displaying a positive kurtosis.

The offset between dark matter and stars, projected along the velocity vector of the stars, is shown in Fig. 6.2. In all four galaxy sub-samples, the distribution is symmetric and shows no bias towards leading or trailing motion of the dark matter. The distribution and its mirror image are indistinguishable in a Kolmogorov-Smirnov (KS) test, with a p-value larger than 0.9. The scatters are $\sigma \approx 210\,\mathrm{pc}$ (main simulation) or $\sigma \approx 128\,\mathrm{pc}$ (high resolution simulation), in agreement with those for the Maxwellian 3D offsets. The dashed lines in the figure show Gaussians with the same mean and width as the measured distributions. The distributions of projected offsets are leptokurtic, making large offsets rarer than predicted by a Gaussian with the same standard deviation. The offsets are, thus, consistent with being randomly orientated and unaffected by the motion of the galaxy. Indeed, we find no preferred direction of offset, repeating the experiment by projecting the offset onto other axes like the dark matter velocity, direction to nearest neighbour, direction to cluster centre, etc. All offsets are consistent with random scatter.

6.3.3 Detailed examination of satellite galaxies in the tail of the distribution

In our sample of satellite galaxies, we found 17 (2) objects out of 3111 presenting an offset larger than $1\ \mathrm{kpc}$ ($1.5\ \mathrm{kpc}$). It is hence worth exploring whether these are just random fluctuations in the population or whether these larger offsets are seen as the result of an astrophysical process. The offsets of the 17 galaxies display no preferred direction with respect to the direction of motion, with a flat distribution of $\cos(\theta)$, where θ is the angle of the offset from the velocity vector of the galaxy.

The first of the two extreme outliers is a low mass ($M_* = 3.9 \times 10^9\ \mathrm{M}_\odot$) extended galaxy ($r_{50} = 6.9\ \mathrm{kpc}$). This galaxy is too diffuse at the resolution of the simulation for the centre-finding algorithm to return a sensible answer. Similarly, it would be difficult to find the centre of the light distribution of a galaxy with such a flat profile in real observations. A galaxy like the one for which an offset has been observed in Abell 3827 is much more massive and less diffuse, making the presence of this

specific outlier in our catalogue irrelevant for the scenario we are considering.

The second extreme outlier is a giant elliptical galaxy with stellar mass $M_* = 1.5 \times 10^{11}\ \mathrm{M}_\odot$, located $130\ \mathrm{kpc}$ from the centre of its cluster. This galaxy experienced a recent merger with a smaller very concentrated satellite ($M_* \approx 2 \times 10^9\ \mathrm{M}_\odot$).

The dark matter from the two galaxies has mixed, forming a smooth, virialised halo. The stars from the elliptical lie at the centre (within $200\ \mathrm{pc}$) of this dark matter. However, the tightly-bound stars from the centre of the former satellite have not yet had time to mix with the stars from the elliptical. They instead remain as a peak in the outskirts of the stellar light distribution. This merger remnant is thus affecting the measurement of the peak of the light distribution but, at the time of measurement, it does not carry any dark matter. The large perceived offset is a temporary phenomenon due to the difference between the time taken to mix the stars in interacting galaxies and the time needed to mix their dark matter. This is the first merger scenario discussed in the Introduction, and is not consistent with details of the observations (except perhaps a short time window might exist during which distinct dark matter peaks still exist, but are offset from the light. This time window would make Abell 3827 even more rare.)

6.3.4 Detailed examination of satellite galaxies in the cores of clusters

The simulation contains 50 (11) $M_* > \times 10^{10}\ \mathrm{M}_\odot$ satellite galaxies within the central $100\,\mathrm{kpc}$ of groups (clusters). The statistics for this small sample is noisier, but they have a similar offset distribution and distribution of angles between offset and velocity vector as the full sample. The distribution of angles is consistent with uniform and the distribution of offsets has a mean of $310\,\mathrm{pc}$ with a 95 percentile at $690\,\mathrm{pc}$, in remarkable agreement with the whole population. This sub-sample and the whole population are virtually indistinguishable in a KS test (p-value >0.6).

The closest non-BCG galaxy with $M_* \gtrsim 10^{10}\mathrm{M}_\odot$ in the six simulated $M_{200} > 10^{14}\ \mathrm{M}_\odot$ clusters are at clustercentric radii $26\,\mathrm{kpc}$, $92\,\mathrm{kpc}$, $22\,\mathrm{kpc}$, $58\,\mathrm{kpc}$, $82\,\mathrm{kpc}$ and

54 kpc. These have offsets between their stars and dark matter of 182 pc, 223 pc, 252 pc, 198 pc, 320 pc and 284 pc, in apparently random directions. Looking in more detail at the two objects with the smallest clustercentric position, we find two elliptical galaxies of mass 1.5×10^{10} and $4 \times 10^{10} \mathrm{M}_{\odot}$ with low star formation rate and gas content. They both present an offset between their dark and luminous component smaller than 250 pc, unaligned with their direction of motion nor aligned with the radius to the centre of the cluster. We thus find no feasible analogues for Abell 3827 in the EAGLE simulation.

6.4 Summary & Conclusion

Motivated by the measurement of a $1.62^{+0.47}_{-0.49}$ kpc offset between the stars and dark matter of a galaxy in Abell 3827 (Massey et al., 2015), we investigated the relative location of these matter components in galaxies from the ΛCDM EAGLE simulation suite. Our results can be summarised as follows:

1. More than 95% of simulated galaxies have an offset between their stars and dark matter that is smaller than the simulation's gravitational softening length ($\epsilon = 700$ pc). The offsets are smaller still in our higher resolution simulation, indicating that our measured values are likely upper limits. Even this state-of-the-art cosmological simulation has only just sufficient resolution to compare to the observations.

2. Of the extreme objects with resolved offsets, fewer than 0.54% (0.20%) of satellite galaxies in groups and clusters present a separation larger than 1 kpc (1.5 kpc).

3. We find no systematic alignment between the direction of the offset and the direction of motion of the galaxies. Dark matter is statistically neither trailing nor leading the stars.

4. We find no difference between field galaxies and satellite galaxies in

groups and clusters. Astrophysical effects related to a galaxy's local environment play no significant role in producing or enhancing offsets.

5. We find two types of outliers with extreme offsets: faint galaxies for which the resolution of the simulations does not allow for the robust identification of a centre, and massive galaxies that have recently absorbed a smaller galaxy but haven't yet mixed their stellar distributions. Neither of these outlier types match what is observed in Abell 3827.

Astrophysical effects produce no feasible analogue in the entire EAGLE simulation, for the galaxy observed in Abell 3827. Taking the best-fitting value for its observed offset, the galaxy is a $>3\sigma$ outlier in a ΛCDM universe with collisionless dark matter. Larger simulations will be needed to improve the sampling of the tail of the offset distribution.

The observation is so far unique, and finding more systems in which similarly precise measurements can be obtained will be challenging. If more large offsets can be found, the case for an alternative dark matter model (e.g. SIDM) would be compelling. High resolution simulations including these models of dark matter would also be useful, to understand the processes that might have led to the observed offset in Abell 3827.

Chapter 7

Morphology of the dark matter annihilation signal around the galactic centre of simulated Milky Way galaxies

7.1 Introduction

Uncovering the unknown nature of dark matter is one of the biggest task of modern cosmology and particle physics. Since Peebles (1982)'s original suggestion that the dark matter consists of massive, weakly interactive, neutral particles a large set of evidence has consolidated that picture but this could, only be ultimately confirmed by the detection of such a particle in an experiment. Among the possible candidates, supersymmetric particles (see Jungman et al., 1996, for a review) and in particular neutralinos are attractive options that current particle accelerator based experiments might detect. An interesting property of most exotic particle candidates for dark matter is the possibility for these particles to annihilate into a pair of photons. This opens the door for experiments attempting to detect such photons in space. Given the properties of the dark matter particles that are expected from observations of the cosmic microwave background and other cosmology ex-

periments, the expected particle mass is of order $m_\chi = 10 - 1000$ GeV, leading to the emission of gamma-ray photons in that energy range when two dark matter particles annihilate (see review by Bertone et al., 2005).

The Large Area Telescope aboard the Gamma-Ray Space Telescope (*Fermi*) (Gehrels & Michelson, 1999) has, over the last few years, produced the most detailed maps of the γ-ray sky, covering a large energy range (20 MeV $- 500$ GeV) with a resolution of a few arcmin at the highest energy end of the spectrum. Analysing the Fermi data around the galactic centre (GC), a number of groups (Hooper & Goodenough, 2011; Hooper & Linden, 2011; Abazajian & Kaplinghat, 2012; Gordon & Macías, 2013; Hooper & Slatyer, 2013; Macias & Gordon, 2014; Daylan et al., 2014; Abazajian et al., 2014) have claimed the discovery of an extended diffuse excess emission above the other know astrophysical sources. This excess emission, peaking at $E \approx 2$ GeV was found to be broadly consistent with the expected signal from dark matter annihilation. Furthermore, the emissivity was found to decrease with distance from the GC as $r^{-\Gamma}$ with $\Gamma = 2.2 - 2.4$, only slightly steeper than the asymptotic inner slope ($\Gamma = 2$) obtained for the flux originating from Navarro et al. (1996b) (NFW) density profiles found in dark matter only simulations of halos.

Alternative explanations have been proposed for the excess near the GC. As the modelling of the Galactic diffuse emission (GDE) is rather uncertain in the inner few degrees ($r \lesssim 500$ pc), the excess could potentially explained by systematics such as point source subtraction (Boyarsky et al., 2011; Ackermann et al., 2012), Bremsstrahlung from electrons scattering off neutral molecular clouds (Yusef-Zadeh et al., 2013), the interaction between protons accelerated by the supermassive black hole and gas (Linden et al., 2012), a population of yet unresolved millisecond pulsars (MSP) (Abazajian, 2011; Gordon & Macías, 2013; Yuan & Zhang, 2014) or young pulsars (O'Leary et al., 2015). However, more recent analysis of the γ-ray spectra seem to disfavour these last two interpretations (Hooper et al., 2013; Calore et al., 2014; Cholis et al., 2015) and place limit on the contribution of pulsars to the excess to 10% of the observed flux.

Besides the analysis of the spectral shape, another way to distinguish the poten-

tial sources of γ-ray contributing to the excess is to analyse the morphology of the signal. A dark matter origin would imply that the excess should extend over tens of degrees (Serpico & Zaharijas, 2008; Nezri et al., 2012). An excess with the same spectral shape over a large angular range (but with emissivity decreasing with distance from the GC) would strengthen the interpretation of the excess as originating from dark matter annihilation. Using multiple regions between 2° and 20° from the GC and a large range of GDE models, Calore et al. (2015a) found that the excess emission is consistent with a dark matter particle of mass $m_\chi = 49^{+6.4}_{-5.4}$ GeV annihilating into a $b\bar{b}$ pair and distributed following a generalised NFW profile (gNFW, see equation 7.1 below) with a slope $\gamma = 1.26$. A similar spatial distribution was found by Daylan et al. (2014) who suggested a slope of the inner profile in the range $\gamma = 1.1 - 1.3$. With the increasing precision of these measurements and of the foreground modelling, it has become crucial to refine the theoretical models for the distribution of dark matter at the centre of galaxies in a ΛCDM context. Characterising the dark matter profile slope and sphericity as well as investigating the potential offset between the dark matter and the GC are all important tasks given to theorists.

Work based on dark matter only simulations has shown that the dark matter is distributed following an NFW distribution with a scale-length, r_s, varying with halo mass (e.g. Navarro et al., 1996b; Neto et al., 2007; Dutton & Macciò, 2014). Higher resolution simulations (Springel et al., 2008a) have shown that the very inner part of dark matter profiles might be slightly shallower than an asymptotic slope of $\gamma = 1$ (Navarro et al., 2010). Similarly, predictions for the signal coming from subhaloes have also been made using these simulations (Kuhlen et al., 2008; Springel et al., 2008b), effectively proposing to test the cold dark matter paradigm. At the other end of the halo mass range, Gao et al. (2012a) argued that nearby rich clusters could provide a cleaner signal than the Milky Way's satellites. Thus far observational results have proved inconclusive and the only claimed detection comes from the centre of our own Milky Way, where precise predictions from simulations have been made (Springel et al., 2008b).

However, all these studies have a ignored the effects that baryons might have on dark matter. Mechanisms such as dark matter contraction (Blumenthal et al., 1986; Gnedin et al., 2004) can potentially drag more dark matter towards the centre, steepening the profile. Conversely, perturbations to the potential, due for instance to feedback from stars or the formation of a bar, can lead to a flattening of the very central regions (Navarro et al., 1996a; Weinberg & Katz, 2002; Mashchenko et al., 2006; Pontzen & Governato, 2012). The correct balance between all those mechanisms can only be obtained by performing high resolution simulations of Milky-Way-like galaxies with a model that reproduces a large variety of other observables, hence validating the physical model.

In this study we use two zoom-in simulations of local groups (Sawala et al., 2015) performed within the framework of the "Evolution and Assembly of GaLaxies and their Environments" (EAGLE) project (Schaye et al., 2015; Crain et al., 2015). These simulations have been shown to reproduce observables in the low redshift Universe and the satellite luminosity function with unprecedented accuracy. Furthermore, Schaller et al. (2015a) showed the remarkable agreement between observed rotation curves and the ones extracted from the simulation, showing that the matter distribution in the simulated galaxies is in agreement with observed ones, implying that the correct balance between the various effects of baryons on dark matter has been achieved. These simulations are hence the ideal test beds to assess the effects of baryons on the inner dark matter profile of Milky Ways.

This chapter is structured as follows. In Section 7.2 we introduce the simulation setup used. In Section 7.3, we investigate the dark matter density profiles of our halos and analyse the morphology of the annihilation signal in Section 7.4. We summarise our findings and conclude in Section 7.5.

Throughout this chapter, we assume a *WMAP7* flat ΛCDM cosmology (Komatsu et al., 2011) ($h = 0.704$, $\Omega_b = 0.0455$, $\Omega_m = 0.272$ and $\sigma_8 = 0.81$), express all quantities without h factors and assume a distance from the GC to the Sun $r_\odot = 8.5$ kpc.

7.2 The simulations

The simulations used in this study are based on the EAGLE simulation code (Schaye et al., 2015) . We summarize here the parts of model relevant to our discussion.

7.2.1 Simulation code and subgrid models

The EAGLE code is based on a substantially modified version of the GADGET code, last described in (Springel, 2005). The modifications include the use of a state-of-the-art implementation of Smoothed Particle Hydrodynamics (SPH), labelled ANARCHY (Dalla Vecchia (in prep.)), based on the Pressure-Entropy formulation of SPH (Hopkins, 2013). Gravitational interactions are computed using a Tree-PM scheme.

The subgrid models employed are an evolution of the ones used in the GIMIC (Crain et al., 2009) and OWLS (Schaye et al., 2010) simulations and we summarise here their main features. Cooling of gas and its interaction with the background radiation is implemented following the recipe of Wiersma et al. (2009a) who tabulated photo-heating and cooling rates element-by-element (for the 9 most important elements) in the presence of the UV and X-ray backgrounds inferred by Haardt & Madau (2001).

To prevent artificial fragmentation, the cold and dense gas is placed on an equation of state $P_{\rm eos} \propto \rho^{4/3}$ that is designed to mimic the mixture of phases in the interstellar medium (ISM) (Schaye & Dalla Vecchia, 2008). Star formation is implemented using a pressure-dependent prescription that reproduces the observed Kennicutt-Schmidt star formation law (Schaye & Dalla Vecchia, 2008) and uses a threshold that captures the metallicity dependence of the transition from the warm, atomic to the cold, molecular gas phase (Schaye, 2004). Star particles are treated as single stellar populations with a Chabrier (2003) IMF evolving along the tracks provided by Portinari et al. (1998). Metals from supernovae (SNe) and AGB stars are injected into the ISM following the model of Wiersma et al. (2009b) and stellar feedback is implemented by injecting thermal energy into the gas as described in Dalla

Vecchia & Schaye (2012). Galactic winds hence form naturally without having to impose a direction, velocity or mass loading factor. The amount of energy injected into the ISM per SN event is dependent on the local gas metallicity and density in an attempt to take into account the unresolved structure of the ISM (Schaye et al., 2015; Crain et al., 2015). Supermassive black hole seeds are injected in halos above $10^{10}h^{-1}\mathrm{M}_{\odot}$ and grow through mergers and accretion of low angular momentum gas (Rosas-Guevara et al., 2015; Schaye et al., 2015). AGN feedback is performed by injecting thermal energy into the gas directly surrounding the black hole (Booth & Schaye, 2009; Dalla Vecchia & Schaye, 2012). Halos are identified using the FOF algorithm (Davis et al., 1985) and substructures within them are later extracted using the SUBFIND code (Springel et al., 2001).

The subgrid model was calibrated (mostly by adjusting the intensity of stellar feedback and the accretion rate onto black holes) so as to reproduce the present day stellar mass function and galaxy sizes (Crain et al., 2015).

7.2.2 Selection of Milky-Way halos

The two volumes used in this work are zoom-in re-simulations of regions extracted from a dark matter only simulation of 100^3 Mpc^3 with 1620^3 particles. The halos were selected to match the observed dynamical constraints of the Local Group (Sawala et al., 2015; Fattahi et al., 2015). Each volume contains a pair of halos in the mass range $M_{200} = 5 \times 10^{11}\mathrm{M}_{\odot}$ to $M_{200} = 2.5 \times 10^{12}\mathrm{M}_{\odot}$ that will host analogues of the Milky Way and M31. The high-resolution region encloses a sphere larger than 2.5 Mpc around the centre of mass of the two halos at $z = 0$. The dark matter particle mass in the zoom regions was set to $5 \times 10^4\mathrm{M}_{\odot}$, whilst the primordial gas particle mass was set to $1 \times 10^4\mathrm{M}_{\odot}$. The initial conditions were generated from ΛCDM power-spectra using 2$^{\mathrm{nd}}$ order Lagrangian perturbation theory (Jenkins, 2010) and linear phases taken form the Gaussian white noise field PANPHASIA (Jenkins, 2013) with the exact descriptors given in the appendix of Schaye et al. (2015). The gravitational softening length was set to $\epsilon = 134$ pc (Plummer equivalent) at $z < 2.8$ and was kept fixed in co-moving units at higher redshifts. Simulations without

baryonic components were run with the exact same setup and are labelled as DMO in what follows.

7.3 Dark matter distribution in the centre of the halos

In this section, we analyse the dark matter distribution inside the simulated Milky-Way galaxies. We consider both galaxies in each of the two simulation volumes as Milky-Way like galaxies.

7.3.1 Profiles without baryon effects

The analysis of the GC excess is often performed using an assumed density profile shape for the dark matter. This profile is a generalisation of the NFW profile for which the asymptotic inner slope is a free parameter γ:

$$\rho_{\rm DM}(r) = \frac{\rho_{\rm s}}{(r/r_{\rm s})^{-\gamma}\,(1+r/r_{\rm s})^{3-\gamma}} \tag{7.1}$$

The NFW profile is recovered when $\gamma = 1$. This generalized form for the density profile is not supported by numerical simulations of collisionless dark matter (e.g. Navarro et al., 2010) but is a useful way to parametrise the deviation from the NFW shape in the very centre of halos as a result of baryonic effects. As the measurements of the GC excess only cover a range of a few kilo-parsecs, the value of the scale radius $r_{\rm s}$ cannot be constrained by the observation and is typically set to $r_{\rm s} = 20$ kpc, in broad agreement with simulation results for Milky-Way-like halos (e.g. Neto et al., 2007; Dutton & Macciò, 2014). The normalisation of the profile, $\rho_{\rm s}$, is degenerate with other particle physics parameters (see Section 7.4) and is usually fixed by requesting that the density of dark matter at the location of the Sun is $\rho_{\rm DM}(r_\odot) = 0.4\ {\rm GeV}\cdot{\rm cm}^{-3}$ [1], in agreement with local dynamical constraints (Catena & Ullio, 2010; Iocco et al., 2011).

[1] Note that for simplicity we use units convenient for particle physics applications. Units more friendly to astronomers are recovered using the conversion $1\ {\rm M}_\odot\cdot{\rm kpc}^{-3} = 3.795\times10^{-8}\ {\rm GeV}\cdot{\rm cm}^{-3}$.

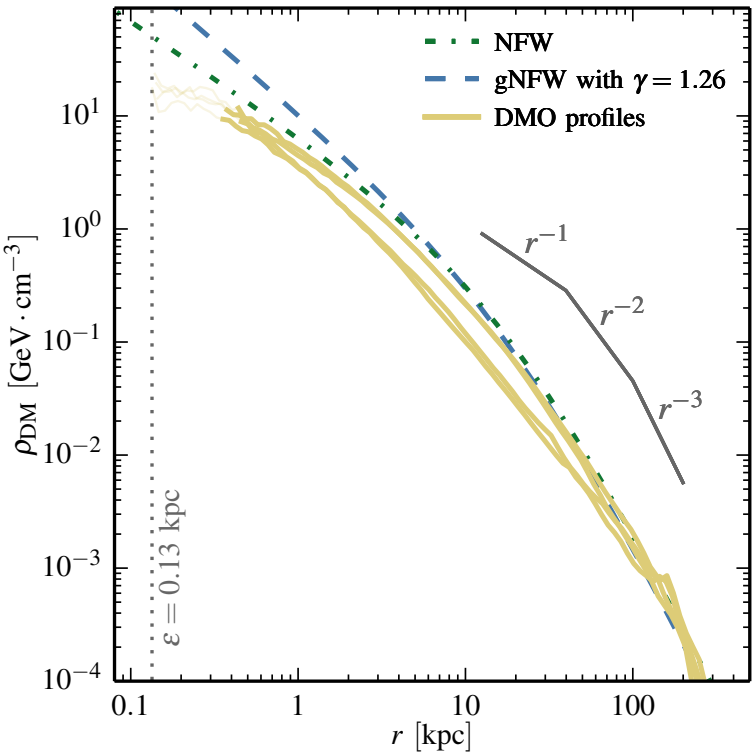

Figure 7.1: The density profiles of the four halos in the simulations without baryons (yellow solid lines). Thinner lines are used at radii smaller than the convergence radius of the simulation. The vertical dotted line indicates the simulation's gravitational softening length. The green dot-dashed and blue dashed lines correspond to an NFW and gNFW with $\gamma = 1.26$ profiles respectively, both normalised to $\rho(r_\odot) = 0.4$ GeV $\cdot$ cm^{-3} and with a scale-length $r_{\rm s} = 20$ kpc. As expected, the simulated profiles display a shape similar to the plotted NFW model, but with a lower normalisation than the standard halos.

Table 7.1: Properties of the four simulated halos and the best-fitting NFW parameters to their dark matter density profiles.

Halo	M_{200} [$\mathrm{M}_\odot$]	R_{200} [kpc]	R_{P03} [pc]	r_s [kpc]	$\rho_{\mathrm{DM}}(r_\odot)$ [$\mathrm{GeV}\cdot\mathrm{cm}^{-3}$]
1	1.65×10^{12}	243.2	435	22.4	0.290
2	1.09×10^{12}	212.0	445	20.1	0.132
3	1.35×10^{12}	226.9	344	23.2	0.162
4	1.39×10^{12}	229.4	358	19.8	0.281

In order to quantify the effects of baryons on the dark matter distribution, it is worth considering the profiles extracted from the simulations without baryonic physics first. In Fig. 7.1, we show the dark matter density profiles of our four halos. Thick lines are used at radii larger than the resolution limit ($R_{\mathrm{P03}} \approx 350 - 450$ pc depending on the halo) set by the criterion of (Power et al., 2003) and thin lines are used at smaller radii. The softening length is indicated by the vertical dotted line. The green dot-dashed and blue dashed lines correspond to an NFW and gNFW with $\gamma = 1.26$ (the best-fitting value of Calore et al. (2015a) to the excess) profiles respectively, both normalised, as discussed above, to $\rho_{\mathrm{DM}}(r_\odot) = 0.4\,\mathrm{GeV}\cdot\mathrm{cm}^{-3}$ and with a scale-length $r_\mathrm{s} = 20$ kpc. As expected, the profiles are in good agreement with the NFW model albeit with a lower normalisation. The best-fitting NFW profile parameters to our halos are given in table 7.1. The usual choice of $r_\mathrm{s} = 20$ kpc is in good agreement with our simulated halos but the normalisation of our halos is lower than what is often assumed in the literature. When baryon effects are neglected, an inner slope close to $\gamma = 1.26$ is clearly ruled out by our simulations.

7.3.2 Profiles in the simulations with baryons

We now turn towards the dark matter profiles in the simulations including baryons. In Fig. 7.2, we show the dark matter density profiles of the four halos simulated

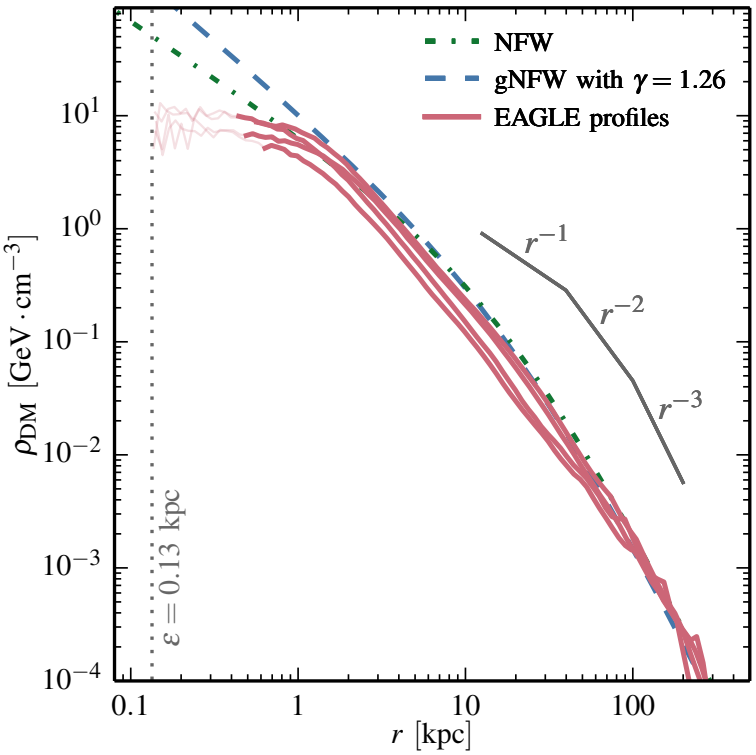

Figure 7.2: The dark matter density profiles of the four halos in the simulations with baryons physics (red solid lines). Thinner lines are used at radii smaller than the convergence radius of the simulation. The vertical dotted line indicates the simulation's gravitational softening length. The green dot-dashed and blue dashed lines correspond to an NFW and gNFW with $\gamma = 1.26$ profiles respectively, both normalised to $\rho(r_\odot) = 0.4\ \mathrm{GeV} \cdot \mathrm{cm}^{-3}$ and with a scale-length $r_\mathrm{s} = 20\ \mathrm{kpc}$. The profiles display a logarithmic slope steeper than -1 between $r \approx 1.5\ \mathrm{kpc}$ and $r \approx 10\ \mathrm{kpc}$ in broad agreement with the profiles inferred from observations by Calore et al. (2015a). At radii $r \leq 1\ \mathrm{kpc}$ the profile is significantly shallower than NFW profiles are.

with the full baryonic model. As for the previous figure, the lines are thin at radii smaller than the convergence radius of the simulation $R_{\rm P03}$ and the dashed lines correspond to the NFW and gNFW profiles normalised to $\rho(r_\odot) = 0.4\ {\rm GeV}\cdot{\rm cm}^{-3}$. The simulated profiles present two interesting features when compared to the DMO results. In the range $1.5 - 10$ kpc, the profile is significantly steeper than an NFW model and at radii $r \lesssim 1$ kpc, the profiles display a significant flattening. Our profile display a combination of dark matter contraction and a flattening of the very central regions.

These halos are obviously not well described over the entire radial range by any of the profiles commonly found in the literature. The main properties of the halos are given in table 7.2. Note that in agreement with the findings of Schaller et al. (2015a), the halo masses M_{200} (and hence radii R_{200}) are lower than in the simulation that did not include baryon physics. A consequence of the steepening of the profile due to contraction is the slight increase in the local dark matter density $\rho_{\rm DM}(r_\odot)$ (column 6 of the tables), which, however, remain lower than the commonly adopted value of $0.4\ {\rm GeV}\cdot{\rm cm}^{-3}$. Clearly, the simulated profiles will not be well described by a gNFW profile at radii $r \lesssim 1.5$ kpc. It is, however, instructive to find the best-fitting profile at larger radii for comparison with the models used to characterise the Fermi excess. The best-fitting asymptotic slopes are given in column 5 of table 7.2. For all four halos, the slopes are larger than the value ($\gamma = 1.26$) found by Calore et al. (2015a) when modelling of the GC excess. We note, however, that the simulated profiles are in broad agreement with the gNFW profile of (Calore et al., 2015a) (blue dashed line), if the overall normalisation is, once again, ignored. The baryons have significantly steepened the profiles at radii $r \gtrsim 1.5$ kpc.

At radii $r \lesssim 1.5$ kpc, the density profiles deviate significantly from the cusp seen in the DMO simulation. At the resolution limit $R_{\rm P03} = 450 - 600$ pc, the simulated profiles display a density between 2.5 and 4.2 times lower than the gNFW profile inferred from observations.

Table 7.2: Properties of the four simulated halos and the best-fitting gNFW asymptotic slope γ to their dark matter density profiles in the radial range $r > 1.5\,\mathrm{kpc}$.

Halo	M_{200} $[\mathrm{M}_\odot]$	R_{200} [kpc]	R_{P03} [pc]	γ $[-]$	$\rho_{\mathrm{DM}}(r_\odot)$ $[\mathrm{GeV}\cdot\mathrm{cm}^{-3}]$
1	1.56×10^{12}	238.8	559	1.38	0.310
2	1.01×10^{12}	206.8	592	1.47	0.160
3	1.12×10^{12}	213.7	438	1.73	0.204
4	1.16×10^{12}	216.2	462	1.49	0.280

7.3.3 Origin of the central flattening

The flattening in the inner $\approx 1.5\,\mathrm{kpc}$ of the four simulated halos is a very important feature of the profiles since they will determine the intensity of the γ-ray emission around its peak. This flattening is very well resolved by the simulation since it occurs at radii much larger than the convergence radius $R\mathrm{P03} = 450 - 600\,\mathrm{pc}$. In all four cases, the halos display a cuspy central profile at high redshift. As a result of violent star formation events (in some cases multiple times) in the inner few kiloparsecs, stellar feedback has expelled the densely packed gas from the centre of the haloes. Since this gas was locally dominating the potential its sudden removal will impact the other matter components and drag some of the dark matter out by unbinding it. This is a practical application of the mechanism proposed by Navarro et al. (1996a) with the perturbation to the potential originating from star formation activity. Similar flattenings have been observed, mostly in dwarf galaxies, as a consequence of feedback by various simulation groups (e.g. Governato et al., 2010; Pontzen & Governato, 2012; Teyssier et al., 2013; Oñorbe et al., 2015), using different simulation techniques and subgrid models. Our findings are hence consistent with results from the literature.

7.3.4 Sphericity of the distribution

In order to characterise the morphology of the dark matter annihilation signal at the centre of the Milky Way, it is interesting to study the shape of the distribution. The profiles described so far assumed a spherically symmetric dark matter density profile. With the higher precision of the measurements of the excess and the increasing understanding of the GDE, it will soon be possible to measure deviations from a perfect sphere. For instance, the presence of a "dark disc" (Read et al., 2008) would enhance the signal in the plane of the galactic disk and hence break the symmetry of the signal. This would also make the signal more difficult to disentangle from the GDE models since these are also strongly asymmetric.

In order to test this, we computed the inertia tensor of our four halos using all

Table 7.3: Axis ratios ($a > b > c$) inferred from the inertia tensor of the matter within 500 pc from the centre of the galaxies for both the halos in the DMO and EAGLE simulations.

	DMO		EAGLE	
Halo	b/a	c/b	b/a	c/b
1	0.828	0.969	0.974	0.952
2	0.866	0.951	0.974	0.959
3	0.823	0.967	0.987	0.962
4	0.840	0.939	0.968	0.959

the dark matter within a spherical aperture of 500 pc from the centre. This distance corresponds to $\approx 3^\circ$ on the sky and is hence encapsulating the majority of the γ-ray flux. We then computed the three eigenvalues $a > b > c$ of the inertia tensor and report the values in table 7.3 for both simulations with and without baryons.

As can be seen, the axis ratios are very close to unity, indicating only very small variations from sphericity and hence no obvious feature in the signal. We also find no alignment between the main axis of the dark matter distribution in the inner 500 pc and the plane of rotation of the stars. It is interesting to note that the simulation with baryons yields more spherical distributions close to the centre than its counterpart without baryons. We verified that repeating the exercise with apertures of 1 and 2 kpc yields similar results.

7.3.5 Position of the centre

Another potential source of systematics in the analysis of the GC excess is the position of the centre of the dark matter distribution. If the highest density part of the dark matter profile is offset from the centre of the stellar distribution then this offset should appear in the data. In their simulation of a single Milky Way halo Kuhlen et al. (2013) found a sizeable offset of $300 - 400$ pc between the centre of the stellar distribution and the peak of their dark matter distribution. If such an offset was

indeed present in the Milky Way, then a offset of $\approx 2^\circ$ between the GC and the peak of the dark matter annihilation signal should be found. In their study based on the EAGLE simulations, Schaller et al. (2015b) found that the offset between the peak of the dark matter density distribution and the centre of the light emission is typically smaller than the softening length of the simulation ($\epsilon = 700$ pc in their case). Repeating their analysis on our four simulated Milky Way halos, we find offsets between 22 and 43 pc, well below the size of the softening length ($\epsilon = 134$ pc), indicating that the offsets are consistent with zero. For all practical purposes and given the current resolution of instruments, the centre of the dark matter distribution is hence at the position of the centre of the light distribution.

7.4 Dark matter annihilation signal

Now that the dark matter profiles have been characterised we turn to the derivation of the corresponding annihilation signal.

7.4.1 J-factor for the simulated halos

In the case of a dark matter particle that annihilates into photons, the photon flux (in units of $\mathrm{GeV}^{-1} \cdot \mathrm{cm}^{-2} \cdot \mathrm{s}^{-1} \cdot \mathrm{sr}^{-1}$) at a given angle, Ψ, on the sky away from the GC is given by

$$\frac{\mathrm{d}N}{\mathrm{d}E}(\Psi) = \frac{\langle \sigma v \rangle}{8\pi m_\chi^2} \frac{\mathrm{d}N_\gamma}{\mathrm{d}E} I(\Psi), \tag{7.2}$$

where m_χ is the mass of the dark matter particle, $\langle \sigma v \rangle$ is its velocity averaged total annihilation cross-section, $\mathrm{d}N_\gamma/\mathrm{d}E$ is the averaged energy spectrum of photons produced per annihilation and $I(\Psi)$ is the integral along the line of sight of the square of the dark matter density. This so-called "J-factor" reads

$$I(\Psi) = \int_{\mathrm{l.o.s.}} \rho^2_{\mathrm{DM}}(r(s, \Psi))\, \mathrm{d}s, \tag{7.3}$$

with the variable s running on the line of sight axis from $s = 0$ to $s = \infty$ and

$$r(s, \Psi) = \sqrt{(r_\odot - s\cos\Psi)^2 + (s\sin\Psi)^2} \tag{7.4}$$

giving the distance from the GC for a particular angle on the sky Ψ and distance to the GC, $r_\odot$. Note that this form of the J-factor is only valid in the cases where the dark matter density is spherically symmetric, as is the case in our simulations. In a more general case the J-factor becomes a function of the galactic latitude b and longitude l. The differential intensity dN/dE is hence the product of the J-factor, given by the distribution of dark matter, and the particle physics model assumed. As a consequence, the normalisation of the J-factor is largely irrelevant since a similar signal can be recovered by altering the particle physics model. To ease the comparison with the analysis of the GC excess, we have, thus, normalised our simulated profiles such that $\rho_{\rm DM}(r_\odot) = 0.4\ {\rm GeV}\cdot{\rm cm}^{-3}$.

On the top panel of Fig. 7.3 we show the J-factor (Eq. 7.3) as a function of galactic latitude b (at galactic longitude $l = 0°$) for our four simulated profiles normalised to the same local dark matter density. The red and yellow lines correspond to the the dark matter profiles in the simulations with and without baryons respectively. The green dot-dashed and blue dashed lines correspond to an NFW and gNFW with $\gamma = 1.26$ profiles respectively with a scale-length $r_{\rm s} = 20\ {\rm kpc}$ and the same normalisation local dark matter density than our normalised halos. The morphology of the J-factor is different in the runs with and without baryons. The contraction of the dark matter due to baryons has increased the J-factor by a factor of ≈ 2 at angles $b \gtrsim 4°$ from the GC, when compared to an NFW halo. In that angular range, the J-factor is also larger than the one obtained for a gNFW with a slope $\gamma = 1.26$ (Calore et al., 2015a). Closer to the GC, the simulated J-factors display a shallower slope and values lower than the gNFW model.

7.4.2 Extrapolation of the profiles towards the centre

As most of the dark matter annihilation signal originates from the inner few hundreds of parsecs, it is necessary to extrapolate our findings from section 7.3.2 to

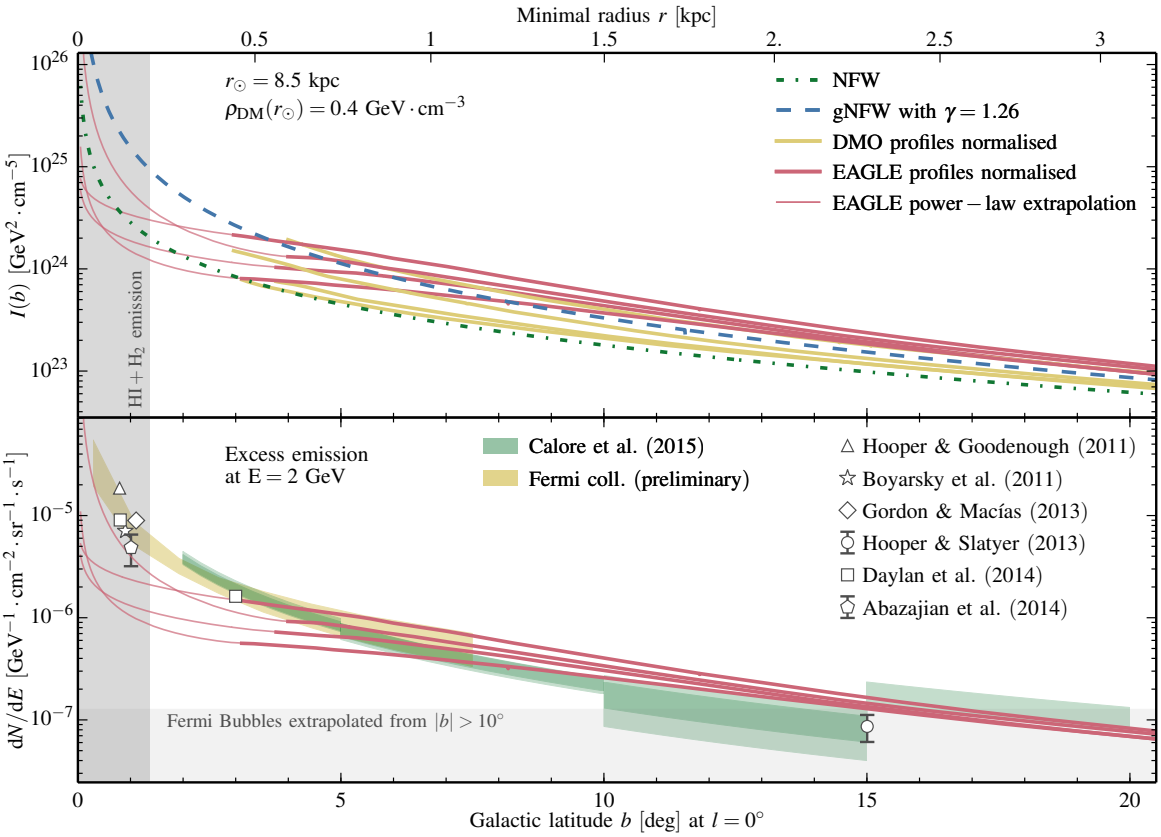

Figure 7.3: *Top panel:* The J-factor as a function of galactic latitude b inferred from our simulated halos both with (red lines) and without (yellow lines) baryon effects. The green dot-dashed and blue dashed lines correspond to an NFW and gNFW with $\gamma = 1.26$ profiles respectively with a scale-length $r_{\rm s} = 20$ kpc. To ease comparison, all profiles have been normalised to yield $\rho_{\rm DM}(r_\odot) = 0.4\,{\rm GeV}\cdot{\rm cm}^{-3}$. The thin lines correspond to the power-law extrapolation of our simulated profiles (see text). The scale at the top indicates the minimal radius intersected by a line of sight at the given galactic latitude b. *Bottom panel:* Emission at $E = 2$ GeV for our halos assuming the best-fitting particle physics model from Calore et al. (2015b). Data points with error bars show the best-fitting models of Hooper & Goodenough (2011), Boyarsky et al. (2011), Gordon & Macías (2013), Hooper & Slatyer (2013), Daylan et al. (2014) and Abazajian et al. (2014) to the Fermi GeV excess. The green shaded regions indicate the excess emission and its statistical uncertainty for a fixed gNFW profile derived by Calore et al. (2015a) and the yellow shaded region indicates the preliminary results of the Fermi-LAT team. The vertical grey shaded region indicates the radial range where uncertainties in the GDE modelling due to HI and H_2 emission dominate. Similarly, the shaded region at the bottom indicates the flux intensity of the Fermi bubbles.

smaller radii. As the annihilation signal increases with the square of the local density, one can ask what is the highest density that can be reached in the inner regions given the constraints on the density and enclosed mass at the smallest converged radius. Assuming that the profile is not hollow and that the logarithmic slope is monotonic, it is straightforward to show that the only asymptotic power-law that can be used to extrapolate the profiles from a given radius r towards the centre has a slope $\gamma_{\rm max} = 3(1 - 4\pi r^3 \rho(r)/3M(r))$ (Navarro et al., 2010). Setting r to the convergence radius of the halos $R_{\rm P03}$, we obtain slopes in the range $\gamma_{\rm max} = 0.55 - 1.22$ for our four halos. The J-factors resulting from these extrapolations are shown on Fig. 7.3 using thin lines. They allow us to set upper-bounds on the J-factor for angles $b \lesssim 3^\circ$. Even with this power-law extrapolation, the flux is lower than the gNFW profile with a slope $\gamma = 1.26$.

7.4.3 Gamma-ray flux morphology

In the bottom panel of Fig. 7.3, we show the emission at $E = 2$ GeV for our J-factors, assuming the best-fitting particle physics model of Calore et al. (2015a)[2]. For comparison, we show the flux inferred from the GC excess by Hooper & Goodenough (2011),Boyarsky et al. (2011), Gordon & Macías (2013), Hooper & Slatyer (2013), Daylan et al. (2014) and Abazajian et al. (2014) with the error bars indicating the $\pm 1\sigma$ statistical error (not shown when smaller than the symbols). The observed intensities were re-scaled following the procedure highlighted in Calore et al. (2015b), taking into account the assumed excess profiles. Note that individual measurements are more than 3σ discrepant with each others. The green shaded regions indicate the best-fitting model of Calore et al. (2015a). Their model assumed a gNFW profile for the dark matter profile and used 60 GDE templates in their likelihood analysis. The width of the green regions on the figure indicates both the statistical uncertainty and the posterior range of the GDE modelling around the best-fitting profile. The uncertainty on the slope of the profile is not shown. A similar analysis, performed by Calore et al. (2015b), of the preliminary results of

[2] $m_\chi = 46.6$ GeV, $\langle \sigma v \rangle = 1.60 \times 10^{-26}$ cm^3 s^{-1}

the Fermi collaboration is shown as a yellow shaded region. The grey shaded region on the left of the plot indicates the radial range over which the galactic diffuse emission models are dominant (Calore et al., 2015b). Similarly, the grey shaded region at the bottom of the panel indicates the level of γ-ray flux expected from the extended "Fermi Bubbles" (Su et al., 2010), thought to be the remnant of past AGN activity. We use the extrapolation, assuming a constant density, to lower latitudes of the flux estimated by Ackermann et al. (2014). The flux originating from the annihilation of dark matter is higher than the contribution of the Fermi Bubbles at angles $b < 15^\circ$, making the radial range $2^\circ < b < 15^\circ$ ideal for the study of the excess. The resolution of our simulations is, hence, well matched to this requirement.

Our simulated profiles (red lines) are in good agreement with the observational results at angles $b > 3^\circ$. This is expected since, over the relevant radial range, our profiles resemble the gNFW profiles with asymptotic inner slope $\gamma = 1.2 - 1.3$, that are inferred from observations. At smaller angles, three of the four extrapolation of the halo profiles towards the centre are significantly lower than the observed data points, whilst the fourth one is in agreement with the data. As this is the simple extrapolation giving the largest signal at the GC, it is reasonable to assume that part of the observed signal can be due to other sources. The simulated halos could be reconciled with the data at $b < 2^\circ$ if the particle physics model is changed to increase the flux. This would, however, violate the constraints at larger angles.

7.5 Summary & Conclusion

In this study we investigated the dark matter density profiles of four simulated Milky Way galaxies using a state-of-the-art hydrodynamics code and subgrid model. We specifically focused on the inner few kiloparsecs of the dark matter distribution in order to refine the earlier predictions for a potential dark matter annihilation signal. The careful treatment of baryons in our simulation allows us to understand and analyse the effects baryons have on the dark matter distribution. We can summarise our findings as follows

- The distribution of dark matter in the inner 500 pc of our halos is very close to spherical with axis ratios $b/a > 0.96$ in all cases. The baryons have made the dark matter more spherical.

- There is no offset between the position of the GC and the peak of the dark matter distribution. The largest offset found in our halos is 45 pc, much smaller than the softening length of the simulation ($\epsilon = 134$ pc), indicating that the offset is consistent with zero.

- The profiles extracted from the simulation with baryon physics display a steeper profile than NFW in the radial range $r = 2 - 10$ kpc as a consequence of dark matter contraction.

- In the inner 1.5 kpc, the dark matter profiles present a well resolved flattening as a consequence of violent star formation events that have taken place at early stages of the formation of the halos.

- The resulting dark matter annihilation signal is in good agreement with the observations of the *Fermi* excess at galactic latitudes $b \gtrsim 3^{\circ}$. An extrapolation of our profiles to smaller angles lead in three of the four cases to a γ-ray flux significantly lower than the observed one. In the fourth halo, the annihilation signal from the extrapolation is in broad agreement with the measurements performed close to the GC.

The analysis of the *Fermi* excess have thus far been performed assuming a gNFW profile for the dark matter. Future, more precise studies, would probably benefit from the use of a more realistic profile shape. The use of such profiles might help disentangle the signal from the dark matter annihilation from the galactic diffuse emission and hence help shade some light on the nature of the dark matter particle.

Chapter 8 | *Conclusions*

8.1 Summary of the results

In the next decade, cosmological probes and surveys such as DESI (Levi et al., 2013), LSST (LSST Dark Energy Science Collaboration, 2012) or EUCLID (Laureijs et al., 2011) will attempt to measure cosmological parameters in the low-redshift Universe with a precision better than $1\ \%$ and will hopefully shed some light on the nature of dark energy. These surveys rely extensively on mock catalogues generated in simulations to control their systematics and correlation matrices. Thus far these mock catalogues have been generated using SAMs, i.e. using DMO simulations in which the baryons cannot act on the dark matter distribution. It is hence crucial to address, using simulations that do incorporate all the relevant processes, whether this approximation is sufficient or not. Similarly, experiments attempting to detect dark matter particles both directly (e.g. XENON 100 Xenon100 Collaboration et al. (2012), LUX Akerib et al. (2013)) and indirectly (e.g. Fermi telescope Gehrels & Michelson, 1999) also rely on assumptions, inferred partially from simulations, about the dark matter distribution within the Galaxy. Understanding whether cooling processes, feedback from star formation or AGN has had an impact on the dark matter is necessary to put limits on the detection or non-detections coming from these experiments. Running and analysing state-of-the-art simulations of galaxy formation able tor reproduce the local Universe is hence crucial for the quest that cosmologists have embarked on.

In this thesis, we have analysed simulations from the EAGLE suite (Schaye et al., 2015; Crain et al., 2015), which have been shown to reproduce a wealth of low-redshift observations as well as reproduce the cosmic evolution of the galaxy stellar mass function, to address some of these questions. The simulation code and

the philosophy behind the calibration of the model parameters were described in chapter 2 where a summary of the main published results was also presented. The EAGLE code relies on a series of subgrid model, evolved from the OWLS and GIMIC (Schaye et al., 2010; Crain et al., 2009) simulations, whose parameters have been calibrated such that the $z = 0.1$ stellar mass function and relations between galaxy mass and size as well as between galaxy and black hole masses are reproduced. This matching implies that the right balance between all the effects that baryons can have on the dark matter distribution might have been found, allowing for a detailed analysis of the changes in the dark matter distribution.

The simulation also used a state-of-the-art implementation of SPH (called ANARCHY) as its hydrodynamics solver. Chapter 3 was dedicated to the description of this new solver and to the analysis of the changes brought to it (compared to the standard GADGET solver) on the simulated population of galaxies. We found that the galaxy properties such as mass or sizes are unaffected by the choice of hydrodynamics solver but that the star formation rate in the most massive objects is affected by the lack of phase mixing in the GADGET-based simulation. This directly impacts the efficiency with which AGN activity can quench star formation in these galaxies. The new solver also leads to differences in the intra-group medium properties that affect X-ray emission from these objects. The differences seen could, however, potentially be cured by changing some of the subgrid prescriptions and are less important at lower resolution. We also found that the use of a time step limiter is crucial to achieve the feedback efficiency required to match observations of the low mass end of the stellar mass function.

Having assessed the importance of the hydrodynamics solver on our results, we moved to the analysis of the halo profiles in the EAGLE simulation. In chapter 4, we investigated the internal structure and density profiles of halos of mass $10^{10} - 10^{14}\,\mathrm{M}_{\odot}$. We found significant differences between the masses of halos in the EAGLE simulations and in the DMO simulations. Nevertheless, halos are well described by the Navarro-Frenk-White (NFW) density profile at radii larger than $\sim 5\%$ of the virial radius but, closer to the centre, the presence of stars can produce cuspier

profiles. Central enhancements in the total mass profile are most important in halos of mass $10^{12} - 10^{13}\mathrm{M}_{\odot}$, where the stellar fraction peaks. Over the radial range where they are well resolved, the resulting galaxy rotation curves are in very good agreement with observational data for galaxies with stellar mass $M_* < 5 \times 10^{10}\mathrm{M}_{\odot}$. We also presented an empirical fitting function that describes the total mass profiles and show that its parameters are strongly correlated with halo mass.

Pushing this analysis further, we focused on the effect of baryons on the density profiles of rich galaxy clusters in chapter 5. We focused on clusters with $M_{200} > 10^{14}\mathrm{M}_{\odot}$ of which we had six examples. We found that the central brightest cluster galaxies (BCGs) in the simulation have steep stellar density profiles, $\rho_*(r) \propto r^{-3}$. Stars dominate the mass density for $r < 10\,\mathrm{kpc}$, and, as a result, the *total* mass density profiles are steeper than the Navarro-Frenk-White (NFW) profile, in remarkable agreement with observations. The dark matter halo itself closely follows the NFW form at all resolved radii ($r \gtrsim 3.0\,\mathrm{kpc}$). By mimicking observations, we found that the EAGLE BCGs have similar surface brightness and line-of-sight velocity dispersion profiles as the BCGs in the sample of Newman et al. (2013a), which have the most detailed measurements currently available. After subtracting the contribution of the stars to the central density, Newman et al. infer significantly shallower slopes than the NFW value, in contradiction with the EAGLE results. We then discussed possible reasons for this discrepancy, and conclude that an inconsistency between the kinematical model adopted by Newman et al. for their BCGs, which assumes isotropic stellar orbits, and the kinematical structure of the EAGLE BCGs, in which the orbital stellar anisotropy varies with radius and tends to be radially biased, could explain at least part of the discrepancy.

In chapter 6, we used the simulations to measure offsets between the centres of stellar and dark matter components of galaxies. We found that the vast majority ($> 95\%$) of the simulated galaxies display an offset smaller than the gravitational softening length of the simulations ($\epsilon = 700\,\mathrm{pc}$), both for field galaxies and satellites in clusters and groups. We also found no systematic trailing or leading of the dark matter along a galaxy's direction of motion. The offsets are hence consistent with

being randomly drawn from a Maxwellian distribution with $\sigma \leq 196\,\mathrm{pc}$. Since astrophysical effects produce no feasible analogues for the $1.62^{+0.47}_{-0.49}$ kpc offset recently observed in Abell 3827, this observational result is in tension with the collisionless cold dark matter model assumed in EAGLE.

Finally, in chapter 7, we used zoom-in re-simulations of Milky Way halos to analyse the dark matter profile near their galactic centres. We found that the profiles present a slope steeper than a Navarro-Frenk-White profile between $r \approx 1.5\,\mathrm{kpc}$ and $r \approx 10\,\mathrm{kpc}$ due to contraction whilst at smaller radii, the profiles display a significant flattening. The inner regions of our halos are almost perfectly spherical (axis ratios $b/a > 0.96$ at $r = 500\,\mathrm{pc}$) and no significant offset ($\gtrsim 45\,\mathrm{pc}$) is found between the centre of the stellar distribution and the centre of the dark halo. The resulting dark matter annihilation signal morphology into γ-ray is in broad agreement with observations at large galactic latitudes ($b \gtrsim 3^\circ$). At smaller angles, we found that the inferred signal is significantly lower than what observations suggest, indicating a possible contribution from other sources to the observed galactic centre excess.

8.2 Future work

The work presented in this thesis shows that baryons play a crucial role and can modify the predictions from DMO simulations significantly. Future surveys and dark matter experiments should consider baryons in order to achieve the precision they expect. Our results, however, suffer from limitations that future simulations should attempt to alleviate. There are:

- The simulation volume $100^3\ \mathrm{Mpc}^3$ is far too small to perform cosmological tests of the size of planned surveys. It is also too small to contain the rarest objects (large clusters, high redshift quasars, ...). Effects of baryons on scales of the BAO or on rare objects can not be probed.

- At the same time, the simulations are too low resolution for some applica-

tions. When properly resolved by the hydro and gravity solvers some of the processes, currently simulated via subgrid models, might impact the dark matter or couple to the other parts of the calculation in an unexpected fashion.

- There are only two zoom-in simulations of local group environments performed at the highest resolution in our suite. Many more similar environments will be needed to understand the scatter in the observables and give better estimates for the dark matter detection experiments.

Despite these limitations, there are many more measurements and differences that can be analysed out of the current simulations. Analysis of the power spectrum and of its differences between the DMO and EAGLE simulations could give limits on the precision achievable by cosmology probes relying on SAMs only. Similarly, performing mock lensing measurements could lead to interesting differences and help understand some of the biases and systematics that could plague observations. In terms of dark matter detection, the simulations could also be used to infer the rate of events for a given experiments, by improving on earlier results based on DMO simulations.

The EAGLE simulation suite has proved to be an invaluable tool to understand the effects of baryons on the dark matter. The next generation of simulations will improve on this and make precise predictions that will hopefully help cosmologists shed some light on the nature of the dark matter.

Appendix A

Uncertainties due to the subgrid models

As discussed by Schaye et al. (2015), cosmological hydrodynamical simulations require subgrid models whose parameters have to be calibrated against a set of observables. In the case of the EAGLE suite of simulations, the observations used are the $z = 0$ galaxy stellar mass function, the galaxy mass-size relation and the stellar mass-black hole mass relation. Using only a subset of these observables, it is possible to find different values of the subgrid model parameters that match the galaxy stellar mass function (Crain et al., 2015). Hence, it is important to assess whether the results presented here depend on these parameters or on the resolution of the simulation.

A.1 Changes in the AGN model parameters

One of the models that matched the selected set of observables is the EAGLE model AGNdT9-L050N0752, which is very similar to the EAGLE-Ref model used in the rest of this paper but whose parameters have been calibrated to match the group gas fractions and X-ray luminosities better (Schaye et al., 2015). In this model, the galaxy masses and sizes are very similar to the Ref model and we have verified that the dark matter halo profiles extracted from that model are very close to the ones shown in Section 4.4.2 for the halo mass range represented in this simulation ($M \lesssim 2 \times 10^{13} \mathrm{M}_{\odot}$).

In Section 4.3.1 we discussed the difference in halo masses between the AGNdT9 simulation and its DMO equivalent and showed that the ratio reached unity only for more massive halos than in EAGLE-Ref model. This is, in part, caused

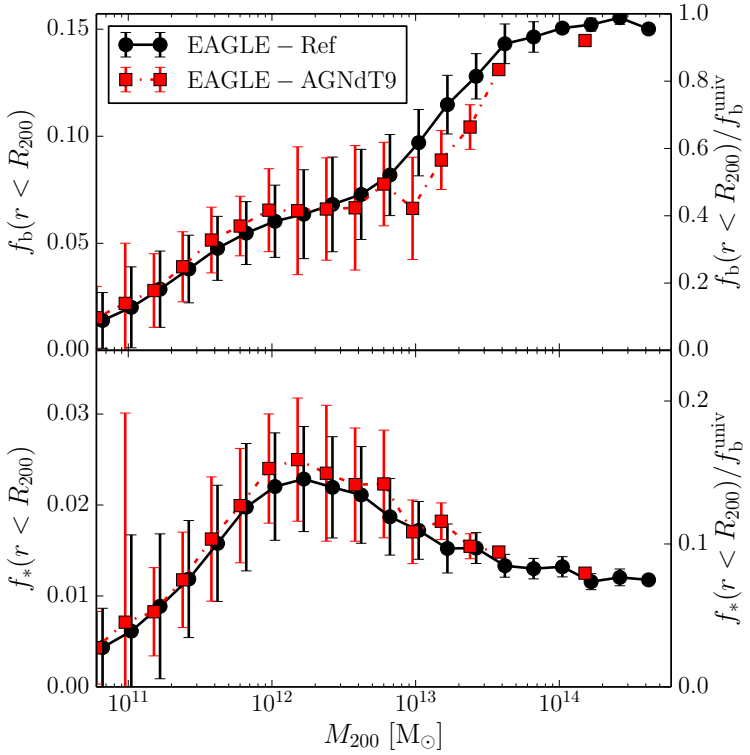

Figure A.1: Baryon fraction, $f_{\rm b} = M_{\rm b}/M_{200}$ (top panel), and stellar fraction, $f_* = M_*/M_{200}$ (bottom panel), within R_{200}, as a function of halo mass for the EAGLE-Ref model (black circles) and the EAGLE-AGNdT9 model (red squares). The error bars show the RMS halo-to-halo scatter in each mass bin. The baryon fractions in the halos more massive than 10^{13}M$_\odot$ are lower in the AGNdT9 model.

by the lower baryon fractions that these halos have. Fig. A.1 shows the baryon (top panel) and stellar (bottom panel) fractions for halos extracted from the EAGLE-Ref simulation (black circles) and from the EAGLE-AGNdT9 model (red squares). The stellar fractions are comparable in both models, with any differences laying well within the large halo-to-halo scatter. The baryon fractions in group-like halos ($10^{13}\mathrm{M}_{\odot} < M_{200} < 10^{14}\mathrm{M}_{\odot}$), however, are systematically lower, by as much as 20%, in the EAGLE-AGNdT9 model. This difference is reflected in the observed shift in the best fitting parameter, M_{23}, in Eqn. 4.10 between the two models. The difference vanishes for the central regions of the halos. The baryon and stellar fractions within $0.05R_{200}$ are similar in both simulations indicating that the difference in the AGN treatment has mostly lead to a change in the structure of the gas outside galaxies, impacting on the inferred X-ray luminosities (Schaye et al., 2015).

Bibliography

Abazajian K. N., 2011, J. Cosmology Astropart. Phys., 3, 10

Abazajian K. N., Kaplinghat M., 2012, Phys. Rev. D, 86, 083511

Abazajian K. N., Canac N., Horiuchi S., Kaplinghat M., 2014, Phys. Rev. D, 90, 023526

Ackermann M., et al., 2012, ApJ, 750, 3

Ackermann M., et al., 2014, ApJ, 793, 64

Agertz O., et al., 2007, MNRAS, 380, 963

Agnello A., Evans N. W., Romanowsky A. J., Brodie J. P., 2014, MNRAS, 442, 3299

Akerib D. S., et al., 2013, Nuclear Instruments and Methods in Physics Research A, 704, 111

Avila-Reese V., Firmani C., Klypin A., Kravtsov A. V., 1999, MNRAS, 310, 527

Bagla J. S., 2002, Journal of Astrophysics and Astronomy, 23, 185

Baldry I. K., et al., 2012, MNRAS, 421, 621

Balsara D. S., 1995, Journal of Computational Physics, 121, 357

Barnes J., Hut P., 1986, Nature, 324, 446

Bauer A. E., et al., 2013, MNRAS, 434, 209

Beck A. M., et al., 2015, preprint, (arXiv:1502.07358)

Behroozi P. S., Wechsler R. H., Conroy C., 2013, ApJ, 770, 57

Bell E. F., McIntosh D. H., Katz N., Weinberg M. D., 2003, ApJS, 149, 289

Berlind A. A., Weinberg D. H., 2002, ApJ, 575, 587

Bertone G., Hooper D., Silk J., 2005, Phys. Rep., 405, 279

Bigiel F., Leroy A., Walter F., Brinks E., de Blok W. J. G., Madore B., Thornley M. D., 2008, AJ, 136, 2846

Binney J., Tremaine S., 1987, Galactic dynamics. Princeton, NJ, Princeton University Press, 1987, 747 p.

Blumenthal G. R., Faber S. M., Flores R., Primack J. R., 1986, ApJ, 301, 27

Boddy K. K., Feng J. L., Kaplinghat M., Tait T. M. P., 2014, Phys. Rev. D, 89, 115017

Bode P., Ostriker J. P., Xu G., 2000, ApJS, 128, 561

Bondi H., Hoyle F., 1944, MNRAS, 104, 273

Booth C. M., Schaye J., 2009, MNRAS, 398, 53

Bouwens R. J., et al., 2012, ApJ, 754, 83

Bower R. G., Benson A. J., Malbon R., Helly J. C., Frenk C. S., Baugh C. M., Cole S., Lacey C. G., 2006, MNRAS, 370, 645

Boyarsky A., Malyshev D., Ruchayskiy O., 2011, Physics Letters B, 705, 165

Brook C. B., et al., 2012, MNRAS, 426, 690

Bruzual G., Charlot S., 2003, MNRAS, 344, 1000

Bryan G. L., Norman M. L., 1998, ApJ, 495, 80

Budzynski J. M., Koposov S. E., McCarthy I. G., Belokurov V., 2014, MNRAS, 437, 1362

Bullock J. S., Kolatt T. S., Sigad Y., Somerville R. S., Kravtsov A. V., Klypin A. A., Primack J. R., Dekel A., 2001, MNRAS, 321, 559

Calore F., Di Mauro M., Donato F., 2014, ApJ, 796, 14

Calore F., Cholis I., Weniger C., 2015a, J. Cosmology Astropart. Phys., 3, 38

Calore F., Cholis I., McCabe C., Weniger C., 2015b, Phys. Rev. D, 91, 063003

Cappellari M., 2008, MNRAS, 390, 71

Carrasco E. R., et al., 2010, ApJ, 715, L160

Catena R., Ullio P., 2010, J. Cosmology Astropart. Phys., 8, 4

Chabrier G., 2003, PASP, 115, 763

Charlot S., Fall S. M., 2000, ApJ, 539, 718

Cholis I., Hooper D., Linden T., 2015, J. Cosmology Astropart. Phys., 6, 43

Claeskens J.-F., Sluse D., Riaud P., Surdej J., 2006, A&A, 451, 865

Cline J. M., Liu Z., Moore G. D., Xue W., 2014, Phys. Rev. D, 90, 015023

Clowe D., Gonzalez A., Markevitch M., 2004, ApJ, 604, 596

Clowe D., Bradač M., Gonzalez A. H., Markevitch M., Randall S. W., Jones C., Zaritsky D., 2006, ApJ, 648, L109

Cole S., Lacey C. G., Baugh C. M., Frenk C. S., 2000, MNRAS, 319, 168

Cole S., et al., 2005, MNRAS, 362, 505

Correa C. A., Wyithe J. S. B., Schaye J., Duffy A. R., 2015a, MNRAS, 450, 1514

Correa C. A., Wyithe J. S. B., Schaye J., Duffy A. R., 2015b, MNRAS, 450, 1521

Crain R. A., et al., 2009, MNRAS, 399, 1773

Crain R. A., et al., 2015, MNRAS, 450, 1937

Cucciati O., et al., 2012, A&A, 539, A31

Cui W., Borgani S., Dolag K., Murante G., Tornatore L., 2012, MNRAS, 423, 2279

Cui W., Borgani S., Murante G., 2014, MNRAS, 441, 1769

Cullen L., Dehnen W., 2010, MNRAS, 408, 669

Cusworth S. J., Kay S. T., Battye R. A., Thomas P. A., 2014, MNRAS, 439, 2485

Dalla Vecchia C., Schaye J., 2012, MNRAS, 426, 140

Davis M., Efstathiou G., Frenk C. S., White S. D. M., 1985, ApJ, 292, 371

Daylan T., Finkbeiner D. P., Hooper D., Linden T., Portillo S. K. N., Rodd N. L., Slatyer T. R., 2014, preprint, (arXiv:1402.6703)

Dehnen W., 2005, MNRAS, 360, 892

Dehnen W., Aly H., 2012, MNRAS, 425, 1068

Dehnen W., Read J. I., 2011, European Physical Journal Plus, 126, 55

Di Cintio A., Brook C. B., Dutton A. A., Macciò A. V., Stinson G. S., Knebe A., 2014, MNRAS, 441, 2986

Dietrich J. P., Böhnert A., Lombardi M., Hilbert S., Hartlap J., 2012, MNRAS, 419, 3547

Doi M., et al., 2010, AJ, 139, 1628

Dolag K., Borgani S., Murante G., Springel V., 2009, MNRAS, 399, 497

Driver S. P., et al., 2011, MNRAS, 413, 971

Duffy A. R., Schaye J., Kay S. T., Dalla Vecchia C., 2008, MNRAS, 390, L64

Duffy A. R., Schaye J., Kay S. T., Vecchia C. D., Battye R. A., Booth C. M., 2010, MNRAS, 105, 2161

Durier F., Dalla Vecchia C., 2012, MNRAS, 419, 465

Dutton A. A., Macciò A. V., 2014, MNRAS, 441, 3359

Dutton A. A., et al., 2011, MNRAS, 410, 1660

Einasto J., 1965, Trudy Astrofizicheskogo Instituta Alma-Ata, 5, 87

Eisenstein D. J., et al., 2005, ApJ, 633, 560

Eke V. R., Cole S., Frenk C. S., 1996, MNRAS, 282, 263

Eke V. R., Navarro J. F., Steinmetz M., 2001, ApJ, 554, 114

Elíasdóttir Á., et al., 2007, preprint, (arXiv:0710.5636)

Fattahi A., et al., 2015, preprint, (arXiv:1507.03643)

Ferland G. J., Korista K. T., Verner D. A., Ferguson J. W., Kingdon J. B., Verner E. M., 1998, PASP, 110, 761

Foot R., 2014, International Journal of Modern Physics A, 29, 30013

Frenk C. S., White S. D. M., Davis M., Efstathiou G., 1988, Astrophysical Journal, 327, 507

Frenk C. S., et al., 1999, ApJ, 525, 554

Furlong M., et al., 2015, MNRAS, 450, 4486

Gao L., Navarro J. F., Cole S., Frenk C. S., White S. D. M., Springel V., Jenkins A., Neto A. F., 2008, MNRAS, 387, 536

Gao L., Frenk C. S., Jenkins A., Springel V., White S. D. M., 2012a, MNRAS, 419, 1721

Gao L., Navarro J. F., Frenk C. S., Jenkins A., Springel V., White S. D. M., 2012b, MNRAS, 425, 2169

Gavazzi R., Treu T., Rhodes J. D., Koopmans L. V. E., Bolton A. S., Burles S., Massey R. J., Moustakas L. A., 2007, ApJ, 667, 176

Gehrels N., Michelson P., 1999, Astroparticle Physics, 11, 277

Genel S., et al., 2014, MNRAS, 445, 175

George M. R., et al., 2012, ApJ, 757, 2

Gilbank D. G., Baldry I. K., Balogh M. L., Glazebrook K., Bower R. G., 2010, MNRAS, 405, 2594

Gilmore G., Wilkinson M. I., Wyse R. F. G., Kleyna J. T., Koch A., Evans N. W., Grebel E. K., 2007, ApJ, 663, 948

Gingold R. A., Monaghan J. J., 1977, MNRAS, 181, 375

Gnedin O. Y., Kravtsov A. V., Klypin A. A., Nagai D., 2004, ApJ, 616, 16

Gnedin O. Y., Ceverino D., Gnedin N. Y., Klypin A. A., Kravtsov A. V., Levine R., Nagai D., Yepes G., 2011, preprint, (arXiv:1108.5736)

Gonzalez A. H., Sivanandam S., Zabludoff A. I., Zaritsky D., 2013, ApJ, 778, 14

Gordon C., Macías O., 2013, Phys. Rev. D, 88, 083521

Governato F., et al., 2010, Nature, 463, 203

Gray M. E., Ellis R. S., Lewis J. R., McMahon R. G., Firth A. E., 2001, MNRAS, 325, 111

Guo Q., et al., 2011, MNRAS, 413, 101

Gustafsson M., Fairbairn M., Sommer-Larsen J., 2006, PhRvD, 74, 123522

Haardt F., Madau P., 2001, in Neumann D. M., Tran J. T. V., eds, Clusters of Galaxies and the High Redshift Universe Observed in X-rays. (arXiv:astro-ph/0106018)

Haas M. R., Schaye J., Booth C. M., Dalla Vecchia C., Springel V., Theuns T., Wiersma R. P. C., 2013, MNRAS, 435, 2931

Hanany S., et al., 2000, ApJ, 545, L5

Harvey D., et al., 2014, MNRAS, 441, 404

Harvey D., Massey R., Kitching T., Taylor A., Tittley E., 2015, Science, 347, 1462

Haynes M. P., et al., 2011, AJ, 142, 170

Henriques B. M. B., White S. D. M., Thomas P. A., Angulo R., Guo Q., Lemson G., Springel V., Overzier R., 2015, MNRAS, 451, 2663

Hernquist L., Katz N., 1989, ApJS, 70, 419

Hezaveh Y., Dalal N., Holder G., Kuhlen M., Marrone D., Murray N., Vieira J., 2013, ApJ, 767, 9

Hochberg Y., Kuflik E., Volansky T., Wacker J. G., 2014, arXiv:1402.5143,

Hoekstra H., 2003, MNRAS, 339, 1155

Hooper D., Goodenough L., 2011, Physics Letters B, 697, 412

Hooper D., Linden T., 2011, Phys. Rev. D, 84, 123005

Hooper D., Slatyer T. R., 2013, Physics of the Dark Universe, 2, 118

Hooper D., Cholis I., Linden T., Siegal-Gaskins J. M., Slatyer T. R., 2013, Phys. Rev. D, 88, 083009

Hopkins P. F., 2013, MNRAS, 428, 2840

Hopkins P. F., 2015, MNRAS, 450, 53

Host O., 2012, MNRAS, 420, L18

Hu W., Dodelson S., 2002, ARA&A, 40, 171

Hu C.-Y., Naab T., Walch S., Moster B. P., Oser L., 2014, MNRAS, 443, 1173

Iocco F., Pato M., Bertone G., Jetzer P., 2011, J. Cosmology Astropart. Phys., 11, 29

Jackson N., 2008, MNRAS, 389, 1311

Jaffe W., 1983, MNRAS, 202, 995

Jenkins A., 2010, MNRAS, 403, 1859

Jenkins A., 2013, MNRAS, 434, 2094

Jing Y. P., 2000, ApJ, 535, 30

Jungman G., Kamionkowski M., Griest K., 1996, Phys. Rep., 267, 195

Kahlhoefer F., Schmidt-Hoberg K., Frandsen M. T., Sarkar S., 2014, MNRAS, 437, 2865

Kahlhoefer F., Schmidt-Hoberg K., Kummer J., Sarkar S., 2015, MNRAS, 452, L54

Karim A., et al., 2011, ApJ, 730, 61

Kaufmann T., Bullock J. S., Maller A. H., Fang T., Wadsley J., 2009, MNRAS, 396, 191

Kennicutt Jr. R. C., 1998, ApJ, 498, 541

Kennicutt Jr. R. C., et al., 2007, ApJ, 671, 333

Kereš D., Vogelsberger M., Sijacki D., Springel V., Hernquist L., 2012, MNRAS, 425, 2027

Khoze V. V., Ro G., 2014, Journal of High Energy Physics, 10, 61

Klypin A. A., Shandarin S. F., 1983, MNRAS, 204, 891

Klypin A. A., Trujillo-Gomez S., Primack J., 2011, ApJ, 740, 102

Komatsu E., et al., 2011, ApJS, 192, 18

Koopmans L. V. E., Treu T., Bolton A. S., Burles S., Moustakas L. A., 2006, ApJ, 649, 599

Koopmans L. V. E., et al., 2009, ApJL, 703, L51

Kormendy J., Richstone D., 1995, ARA&A, 33, 581

Kravtsov A., Vikhlinin A., Meshscheryakov A., 2014, preprint, (arXiv:1401.7329)

Kuhlen M., Diemand J., Madau P., 2008, ApJ, 686, 262

Kuhlen M., Guedes J., Pillepich A., Madau P., Mayer L., 2013, ApJ, 765, 10

LSST Dark Energy Science Collaboration 2012, preprint, (arXiv:1211.0310)

Lagos C. d. P., et al., 2015, MNRAS, 452, 3815

Laporte C. F. P., White S. D. M., 2015, MNRAS, 451, 1177

Laureijs R., et al., 2011, preprint, (arXiv:1110.3193)

Le Brun A. M. C., McCarthy I. G., Schaye J., Ponman T. J., 2014, MNRAS, 441, 1270

Levi M., et al., 2013, preprint, (arXiv:1308.0847)

Li C., White S. D. M., 2009, MNRAS, 398, 2177

Lin Y.-T., Stanford S. A., Eisenhardt P. R. M., Vikhlinin A., Maughan B. J., Kravtsov A., 2012, ApJ, 745, L3

Linden T., Lovegrove E., Profumo S., 2012, ApJ, 753, 41

Lucy L. B., 1977, AJ, 82, 1013

Ludlow A. D., et al., 2013, MNRAS, 432, 1103

Ludlow A. D., Navarro J. F., Angulo R. E., Boylan-Kolchin M., Springel V., Frenk C., White S. D. M., 2014, MNRAS, 441, 378

Lupton R., Blanton M. R., Fekete G., Hogg D. W., O'Mullane W., Szalay A., Wherry N., 2004, PASP, 116, 133

Macciò A. V., Dutton A. A., van den Bosch F. C., Moore B., Potter D., Stadel J., 2007, MNRAS, 378, 55

Macias O., Gordon C., 2014, Phys. Rev. D, 89, 063515

Magorrian J., et al., 1998, AJ, 115, 2285

Mamon G. A., Boué G., 2010, MNRAS, 401, 2433

Marigo P., 2001, A&A, 370, 194

Marri S., White S. D. M., 2003, MNRAS, 345, 561

Martizzi D., Teyssier R., Moore B., Wentz T., 2012, MNRAS, 422, 3081

Martizzi D., Teyssier R., Moore B., 2013, MNRAS, 432, 1947

Mashchenko S., Couchman H. M. P., Wadsley J., 2006, Nature, 442, 539

Massey R., Kitching T., Nagai D., 2011, MNRAS, 413, 1709

Massey R., et al., 2015, MNRAS, 449, 3393

Maughan B. J., Jones C., Forman W., Van Speybroeck L., 2008, ApJS, 174, 117

McCarthy I. G., et al., 2010, MNRAS, 406, 822

McCarthy I. G., Schaye J., Font A. S., Theuns T., Frenk C. S., Crain R. A., Dalla Vecchia C., 2012, MNRAS, 427, 379

McKee C. F., Ostriker J. P., 1977, ApJ, 218, 148

Mitchell N. L., McCarthy I. G., Bower R. G., Theuns T., Crain R. A., 2009, MNRAS, 395, 180

Mo H. J., Mao S., White S. D. M., 1998, MNRAS, 295, 319

Monaghan J. J., 1992, Annual Review of Astronomy and Astrophysics, 30, 74

Monaghan J. J., 1997, Journal of Computational Physics, 136, 298

Morris J. P., Monaghan J. J., 1997, Journal of Computational Physics, 136, 41

Moster B. P., Naab T., White S. D. M., 2013, MNRAS, 428, 3121

Moustakas J., et al., 2013, ApJ, 767, 50

Navarro J. F., Eke V. R., Frenk C. S., 1996a, MNRAS, 283, L72

Navarro J. F., Frenk C. S., White S. D. M., 1996b, ApJ, 462, 563

Navarro J. F., Frenk C. S., White S. D. M., 1997, ApJ, 490, 493

Navarro J. F., et al., 2004, MNRAS, 349, 1039

Navarro J. F., et al., 2010, MNRAS, 402, 21

Neto A. F., et al., 2007, MNRAS, 381, 1450

Newman A. B., Treu T., Ellis R. S., Sand D. J., Nipoti C., Richard J., Jullo E., 2013a, ApJ, 765, 24

Newman A. B., Treu T., Ellis R. S., Sand D. J., 2013b, ApJ, 765, 25

Nezri E., Lavalle J., Teyssier R., 2012, Phys. Rev. D, 86, 063524

Oñorbe J., Boylan-Kolchin M., Bullock J. S., Hopkins P. F., Kerěs D., Faucher-Giguère C.-A., Quataert E., Murray N., 2015, preprint, (arXiv:1502.02036)

O'Leary R. M., Kistler M. D., Kerr M., Dexter J., 2015, preprint, (arXiv:1504.02477)

O'Shea B. W., Nagamine K., Springel V., Hernquist L., Norman M. L., 2005, ApJS, 160, 1

Okabe N., Smith G. P., Umetsu K., Takada M., Futamase T., 2013, ApJL, 769, L35

Okamoto T., Jenkins A., Eke V. R., Quilis V., Frenk C. S., 2003, MNRAS, 345, 429

Okamoto T., Shimizu I., Yoshida N., 2014, PASJ, 66, 70

Oman K. A., et al., 2015, MNRAS, 452, 3650

Oppenheimer B. D., Davé R., Kereš D., Fardal M., Katz N., Kollmeier J. A., Weinberg D. H., 2010, MNRAS, 406, 2325

Pearce F. R., Jenkins A., Frenk C. S., White S. D. M., Thomas P. A., Couchman H. M. P., Peacock J. A., Efstathiou G., 2001, MNRAS, 326, 649

Pedrosa S., Tissera P. B., Scannapieco C., 2009, MNRAS, 395, L57

Peebles P. J. E., 1982, ApJ, 263, L1

Perlmutter S., et al., 1999, ApJ, 517, 565

Planck Collaboration et al., 2014, AA, 571, A16

Pointecouteau E., Arnaud M., Pratt G. W., 2005, AAP, 435, 1

Pontzen A., Governato F., 2012, MNRAS, 421, 3464

Pontzen A., Governato F., 2014, Nature, 506, 171

Portinari L., Chiosi C., Bressan A., 1998, AAP, 334, 505

Power C., Navarro J. F., Jenkins A., Frenk C. S., White S. D. M., Springel V., Stadel J., Quinn T., 2003, MNRAS, 338, 14

Pratt G. W., Croston J. H., Arnaud M., Böhringer H., 2009, A&A, 498, 361

Price D. J., 2004, PhD thesis, Institute of Astronomy, Madingley Rd, Cambridge, CB2 0HA, UK

Price D. J., 2008, Journal of Computational Physics, 227, 10040

Price D. J., 2012, Journal of Computational Physics, 231, 759

Puchwein E., Springel V., 2013, MNRAS, 428, 2966

Rafferty D. A., McNamara B. R., Nulsen P. E. J., Wise M. W., 2006, ApJ, 652, 216

Rahmati A., Pawlik A. H., Raičevič M., Schaye J., 2013, MNRAS, 430, 2427

Rahmati A., Schaye J., Bower R. G., Crain R. A., Furlong M., Schaller M., Theuns T., 2015, MNRAS, 452, 2034

Randall S. W., Markevitch M., Clowe D., Gonzalez A. H., Bradač M., 2008, ApJ, 679, 1173

Read J. I., Gilmore G., 2005, MNRAS, 356, 107

Read J. I., Lake G., Agertz O., Debattista V. P., 2008, MNRAS, 389, 1041

Read J. I., Hayfield T., Agertz O., 2010, MNRAS, 405, 1513

Reyes R., Mandelbaum R., Gunn J. E., Pizagno J., Lackner C. N., 2011, MNRAS, 417, 2347

Riess A. G., et al., 1998, AJ, 116, 1009

Ritchie B. W., Thomas P. A., 2001, MNRAS, 323, 743

Rocha M., Peter A. H. G., Bullock J. S., Kaplinghat M., Garrison-Kimmel S., Oñorbe J., Moustakas L. A., 2013, MNRAS, 430, 81

Rodighiero G., et al., 2010, A&A, 518, L25

Rosas-Guevara Y. M., et al., 2015, MNRAS, 454, 1038

Rosswog S., Davies M. B., Thielemann F.-K., Piran T., 2000, A&A, 360, 171

Saitoh T. R., Makino J., 2009, ApJ, 697, L99

Saitoh T. R., Makino J., 2013, ApJ, 768, 44

Sales L. V., Navarro J. F., Schaye J., Dalla Vecchia C., Springel V., Booth C. M., 2010, MNRAS, 409, 1541

Sand D. J., Treu T., Ellis R. S., 2002, ApJL, 574, L129

Sand D. J., Treu T., Smith G. P., Ellis R. S., 2004, ApJ, 604, 88

Sanderson A. J. R., O'Sullivan E., Ponman T. J., Gonzalez A. H., Sivanandam S., Zabludoff A. I., Zaritsky D., 2013, MNRAS, 429, 3288

Sawala T., Frenk C. S., Crain R. A., Jenkins A., Schaye J., Theuns T., Zavala J., 2013, MNRAS, 431, 1366

Sawala T., et al., 2014a, preprint, (arXiv:1412.2748)

Sawala T., et al., 2014b, preprint, (arXiv:1406.6362)

Sawala T., et al., 2015, MNRAS, 448, 2941

Scannapieco C., et al., 2012, MNRAS, 423, 1726

Schaller M., et al., 2015a, MNRAS, 451, 5765

Schaller M., Robertson A., Massey R., Bower R. G., Eke V. R., 2015b, MNRAS, 453, L58

Schaye J., 2004, ApJ, 609, 667

Schaye J., Dalla Vecchia C., 2008, MNRAS, 383, 1210

Schaye J., Theuns T., Rauch M., Efstathiou G., Sargent W. L. W., 2000, MNRAS, 318, 817

Schaye J., et al., 2010, MNRAS, 402, 1536

Schaye J., et al., 2015, MNRAS, 446, 521

Sembolini F., et al., 2015, preprint, (arXiv:1503.06065)

Serpico P. D., Zaharijas G., 2008, Astroparticle Physics, 29, 380

Shaw L. D., Weller J., Ostriker J. P., Bode P., 2006, ApJ, 646, 815

Shen S., Mo H. J., White S. D. M., Blanton M. R., Kauffmann G., Voges W., Brinkmann J., Csabai I., 2003, MNRAS, 343, 978

Sijacki D., Vogelsberger M., Kereš D., Springel V., Hernquist L., 2012, MNRAS, 424, 2999

Smoot G. F., et al., 1992, ApJ, 396, L1

Spergel D. N., Steinhardt P. J., 2000, Physical Review Letters, 84, 3760

Springel V., 2005, MNRAS, 364, 1105

Springel V., 2010a, ARA&A, 48, 391

Springel V., 2010b, MNRAS, 401, 791

Springel V., Hernquist L., 2002, MNRAS, 333, 649

Springel V., Hernquist L., 2003, MNRAS, 339, 312

Springel V., White S. D. M., Tormen G., Kauffmann G., 2001, MNRAS, 328, 726

Springel V., Di Matteo T., Hernquist L., 2005, MNRAS, 361, 776

Springel V., Frenk C. S., White S. D. M., 2006, Nature, 440, 1137

Springel V., et al., 2008a, MNRAS, 391, 1685

Springel V., et al., 2008b, Nature, 456, 73

Stinson G. S., Brook C., Macciò A. V., Wadsley J., Quinn T. R., Couchman H. M. P., 2013, MNRAS, 428, 129

Strigari L. E., Frenk C. S., White S. D. M., 2010, MNRAS, 408, 2364

Strigari L. E., Frenk C. S., White S. D. M., 2014, preprint, (arXiv:1406.6079)

Su M., Slatyer T. R., Finkbeiner D. P., 2010, ApJ, 724, 1044

Sun M., Voit G. M., Donahue M., Jones C., Forman W., Vikhlinin A., 2009, ApJ, 693, 1142

Teyssier R., Pontzen A., Dubois Y., Read J. I., 2013, MNRAS, 429, 3068

Thielemann F.-K., et al., 2003, in Hillebrandt W., Leibundgut B., eds, From Twilight to Highlight: The Physics of Supernovae. p. 331

Trayford J. W., et al., 2015, MNRAS, 452, 2879

Tremonti C. A., et al., 2004, ApJ, 613, 898

Tulin S., Yu H.-B., Zurek K. M., 2013, Physical Review Letters, 110, 111301

Umetsu K., et al., 2014, ApJ, 795, 163

Velliscig M., van Daalen M. P., Schaye J., McCarthy I. G., Cacciato M., Le Brun A. M. C., Vecchia C. D., 2014, MNRAS, 442, 2641

Velliscig M., et al., 2015, MNRAS, 453, 721

Vikhlinin A., Kravtsov A., Forman W., Jones C., Markevitch M., Murray S. S., Van Speybroeck L., 2006, ApJ, 640, 691

Vogelsberger M., Zavala J., Loeb A., 2012, MNRAS, 423, 3740

Vogelsberger M., Genel S., Sijacki D., Torrey P., Springel V., Hernquist L., 2013, MNRAS, 436, 3031

Vogelsberger M., et al., 2014, Nature, 509, 177

Wadsley J. W., Veeravalli G., Couchman H. M. P., 2008, MNRAS, 387, 427

Walker M. G., Penarrubia J., 2011, ApJ, 742, 20

Weinberg M. D., Katz N., 2002, ApJ, 580, 627

Weinberg D. H., Bullock J. S., Governato F., Kuzio de Naray R., Peter A. H. G., 2015, Proceedings of the National Academy of Sciences

Wendland H., 1995, Advances in Computational Mathematics, 4, 389

Wetzstein M., Nelson A. F., Naab T., Burkert A., 2009, ApJS, 184, 298

White S. D. M., Frenk C. S., 1991, ApJ, 379, 52

White S. D. M., Rees M. J., 1978, MNRAS, 183, 341

White S. D. M., Frenk C. S., Davis M., 1983, ApJ, 274, L1

Wiersma R. P. C., Schaye J., Smith B. D., 2009a, MNRAS, 393, 99

Wiersma R. P. C., Schaye J., Theuns T., Dalla Vecchia C., Tornatore L., 2009b, MNRAS, 399, 574

Williams L. L. R., Saha P., 2011, MNRAS, 415, 448

Xenon100 Collaboration et al., 2012, Astroparticle Physics, 35, 573

Yuan Q., Zhang B., 2014, Journal of High Energy Astrophysics, 3, 1

Yusef-Zadeh F., et al., 2013, ApJ, 762, 33

Zhao D. H., Jing Y. P., Mo H. J., Börner G., 2003, ApJL, 597, L9

Zwaan M. A., et al., 2003, AJ, 125, 2842

de Bernardis P., et al., 2000, Nature, 404, 955